Sample Delivery Enabled by 3D Printing for Reduced Sample Consumption and Mix-and-Inject Serial Crystallography at X-ray Free Electron Lasers

by

Austin Echelmeier

A Dissertation Presented in Partial Fulfillment
of the Requirements for the Degree
Doctor of Philosophy

Approved November 2019 by the
Graduate Supervisory Committee:

Alexandra Ros, Chair
Marcia Levitus
Uwe Weierstall

ARIZONA STATE UNIVERSITY

December 2019

ABSTRACT

Serial femtosecond crystallography (SFX) with X-ray free electron lasers (XFELs) has enabled the determination of damage-free protein structures at ambient temperatures and of reaction intermediate species with time resolution on the order of hundreds of femtoseconds. However, currently available XFEL facility X-ray pulse structures waste the majority of continuously injected crystal sample, requiring a large quantity (up to grams) of crystal sample to solve a protein structure. Furthermore, mix-and-inject serial crystallography (MISC) at XFEL facilities requires fast mixing for short (millisecond) reaction time points (t_r), and current sample delivery methods have complex fabrication and assembly requirements.

To reduce sample consumption during SFX, a 3D printed T-junction for generating segmented aqueous-in-oil droplets was developed. The device surface properties were characterized both with and without a surface coating for improved droplet generation stability. Additionally, the droplet generation frequency was characterized. The 3D printed device interfaced with gas dynamic virtual nozzles (GDVNs) at the Linac Coherent Light Source (LCLS), and a relationship between the aqueous phase volume and the resulting crystal hit rate was developed. Furthermore, at the European XFEL (EuXFEL) a similar quantity and quality of diffraction data was collected for segmented sample delivery using ~60% less sample volume than continuous injection, and a structure of 3-deoxy-D-manno-octulosonate 8-phosphate synthase (KDO8PS) delivered by segmented injection was solved that revealed new structural details to a resolution of 2.8 Å.

For MISC, a 3D printed hydrodynamic focusing mixer for fast mixing by diffusion was developed to automate device fabrication and simplify device assembly. The mixer was characterized with numerical models and fluorescence microscopy. A variety of devices were developed to reach reaction intermediate time points, t_r, on the order

of 10^0 – 10^3 ms. These devices include 3D printed mixers coupled to glass or 3D printed GDVNs and two designs of mixers with GDVNs integrated into the one device. A 3D printed mixer coupled to a glass GDVN was utilized at LCLS to study the oxidation of cytochrome *c* oxidase (CcO), and a structure of the CcO Pr intermediate was determined at t_r = 8 s.

DEDICATION

I dedicate this work to my sister for inspiring me to be a kind, brilliant brother who can shine as brightly as she does.

ACKNOWLEDGMENTS

I would like to thank my advisor, Dr. Alexandra Ros, for the guidance and wisdom she has provided me over the years. Thank you for encouraging me to be a better scientist and to push further than I thought possible.

Thank you to my family for always believing in me even when I didn't believe in myself. Your love and support have gotten me through some difficult moments! I'm incredibly grateful for all of the laughs and hugs, the nights spent on the couch with the Gilmores, the ice cream and cookie cakes, the happy dog days, the outdoor adventures, and all of the little moments that light up my memories.

Thank you to the lab members who have supported me through all the travels of my PhD. Whether it was during lab inspection, discussing an experiment, or at a 24+ hour beamtime shift, I don't think I could have made it this far without you.

My friends, both near and far, I don't think I can thank you enough! For grounding me, for encouraging me. For laughing, drinking, talking, dancing, gaming, walking with me. For the night outs, the nights in, the days in the pool, the days abroad. For the adventures that lead to discovery, for the setbacks that opened new doors, for the triumphs that empowered me. For all of it, for all of you, thank you!

I would also like to thank the following people for their invaluable contributions: Richard A. Kirian, Reza Nazari, Sahba Zaare, Caleb Madsen, Garrett Nelson, Daniel James, John Spence, Stella Lisova, and Uwe Weierstall for their contributions towards GDVNs, 3D printing, and injection; Jesse Coe, Chelsie Conrad-Smith, Shangji Zhang, Chris Gisriel, Zach Dobson, and Petra Fromme for their contribution with crystal sample preparation; Izumi Ishigami, Syun-ru Yeh, and Denis Rousseau for everything involved in the cytochrome c oxidase beamtimes; Bob Sublett, Raymond Sierra, and the MFX team for their contributions at MFX beamtimes; Adrian Mancuso and the EuXFEL team for their contributions at EuXFEL beamtimes; Sabine

Botha, Nadia Natsepin, and the ASU data analysis team for their expertise in solving protein structures; Bill Bauer and the BioXFEL team for their contribution towards collaboration and knowledge transfer.

TABLE OF CONTENTS

Page

APPENDIX Page

LIST OF TABLES

LIST OF FIGURES

CHAPTER 1

INTRODUCTION

1.1 Structural Biology

In the past 80 years, groundbreaking understanding of how biology is affected by molecular structures has been achieved due to the advances in visualization techniques to study the structures of biological components such as DNA and proteins.[1, 2] Advances such as X-ray crystallography have ushered in an era of structural biology to gain insight into the relationship between a protein's structure and its function within biological organisms for applications such as rational drug design. In the field of structural biology, there are several different methods to determine a protein structure.

The most common method to determine a protein structure is with X-ray crystallography. Indeed, by late 2019, of the >150,000 protein structures in the Protein Databank,[3] >139,000 were determined by X-ray crystallography. In this method, a protein crystal is irradiated by X-rays, and, in accordance with Bragg's law,[4] the angle, phase, and intensity of the X-rays that diffract off the electrons in the protein crystal yields a diffraction pattern that provides information about the placement of the atoms within the protein. A protein crystal is comprised of unit cells which are many repeating protein molecules. Unit cells are composed of one or more asymmetric units: the building blocks of the protein crystal. The arrangement of the atoms within the asymmetric units and the overall symmetry of the crystal lattices allows the scattered X-rays to interfere either constructively or destructively. Constructively interfered diffraction is then amplified, increasing the signal-to-noise such that a reflection or "Bragg peak" is recorded on a detector in accordance with

Bragg's law. [5] Irradiating a crystal will result in one set of reflections (a diffraction pattern) that contains structural information from one angle of the protein crystal. However, one diffraction pattern only samples a section of the protein crystal (a portion of the Ewald sphere[6]) and does not reveal the complete structure. To fully sample the Ewald sphere and construct a three-dimensional (3D) structure,[7] the protein crystal is incrementally rotated and irradiated to obtain reflections at multiple angles. Due to symmetry within the crystal, it is often not necessary to scan a full 360°.[5, 6] After the collection of a rotating data set, the resulting diffraction patterns can be analyzed to solve the protein structure.[6]

When irradiating a protein crystal with X-rays, two types of damage occur. Primary radiation damage is the ionization of an atom due to absorbing an X-ray photon (the photoelectric effect) or inelastic scattering (Compton scattering).[8] Primary radiation damage can result several artifacts such as decreased diffraction intensity and increased unit cell size to name a few.[8, 9] Each incident of primary radiation damage produces one photoelectron, but each photoelectron can produce up to 500 secondary electrons that can diffuse through the crystal and create secondary radiation damage.[8] The secondary electrons can produce radicals both in the protein molecules and the neighboring water or solvent molecules (hydroxy and oxygen radicals, for example), and the radicals can then diffuse through the crystal and can damage covalent bonds. Effects of secondary radiation damage include cleavage of disulfide bonds and decarboxylating carboxylic acids.[5, 8, 10] To mitigate the effects of secondary radiation damage, traditional crystallography methods require a large protein crystal (>100 μm) to be cryo-cooled (~100 K) to prevent the spread of radicals through the crystal.[5, 8] At cryo-temperatures, the majority of radicals are prevented from diffusing, but the secondary electrons can diffuse even at 77K.[11] Since secondary damage due to radical diffusion is mitigated at cryo-temperatures,

the crystal can be rotated to an area an unexposed area free of primary damage. At microfocus beamlines, smaller cryo-cooled crystals (on the order of 10 μm) can be studied without excessive secondary X-ray damage.[12] However, the effects of primary X-ray damage are not avoided, thus placing limits on which proteins can be studied to those that crystallize into large crystals.[13, 14]

Nuclear magnetic resonance (NMR) uses radio waves to determine the proximity of atoms in a protein to one another and is useful for determining protein structures of proteins in solution without the need for a crystallization step.[15, 16] This method benefits from being able to study proteins that do not readily crystallize (with much success seen with intrinsically disordered proteins) and from studying protein-protein reactions in physiological conditions with time resolution on the picosecond-millisecond scale.[16] While this works well for small proteins, specifically for identifying the flexible and rigid regions of a protein, larger proteins can have a problem of overlapping signals, limiting the structure determination ability for NMR.[16]

Another emerging method of protein structure determination is cryo-electron microscopy (Cryo-EM),[17] which has made significant gains in recent years in its ability to determine protein structures at high resolution. In Cryo-EM, single proteins within vitreous ice are imaged by an electron beam. With advances in sample preparation, imaging components and detectors, and computational methods, Cryo-EM has undergone a "resolution revolution" and can now reach near-atomic resolutions similar to crystallography.[17]

Information from each of these three techniques can be viewed in conjunction with one another and with additional characterization methods to obtain a thorough view of the protein structure, composition, and dynamics. Additionally, there have been significant advancements in X-ray crystallography with the development of serial femtosecond crystallography with X-ray free electron lasers.

1.2 Serial Femtosecond Crystallography

With the advent of the X-ray free electron laser (XFEL),[18] crystallography using extremely bright femtosecond X-ray pulses became possible.[19, 20] The X-ray pulses are intense enough to destroy an irradiated crystal, but are fast enough to outrun radiation damage and yield a diffraction pattern "snapshot" in a process termed "diffraction before destruction."[19, 21] In order to determine a 3D structure of the protein, this process must be done in serial, with a new crystal replenishing the destroyed sample between X-ray pulses.[22] As such, it quickly becomes impractical to mount a single protein crystal one at a time, so crystals are frequently injected continuously into the path of the X-ray.[23] From thousands to tens of thousands of randomly oriented snapshots, an electron density for the protein can be calculated.[24] This method, termed serial femtosecond crystallography (SFX), has allowed the use of micro- and nanocrystals in crystallography, further opening the way to study proteins that have difficulty yielding large crystals or are limited by X-ray damage. Specifically, membrane proteins account for a large portion of all proteins, yet traditionally have difficulty forming large crystals due to the complex membrane environment in which they are stable.[25] Sample delivery methods to mimic a membrane environment such as an injector for lipidic cubic phase (LCP, detailed in Chapter 3.6) have been developed, resulting in a dramatic increase in the number of membrane protein structures determined.[25-29] Additionally, SFX does not require cryogenically cooled conditions to mitigate X-ray damage. There is evidence that cryo-cooling crystals can impact their conformational heterogeneity,[30, 31] so permitting the crystals to be present in a more biologically relevant ambient temperature can yield more accurate structures.

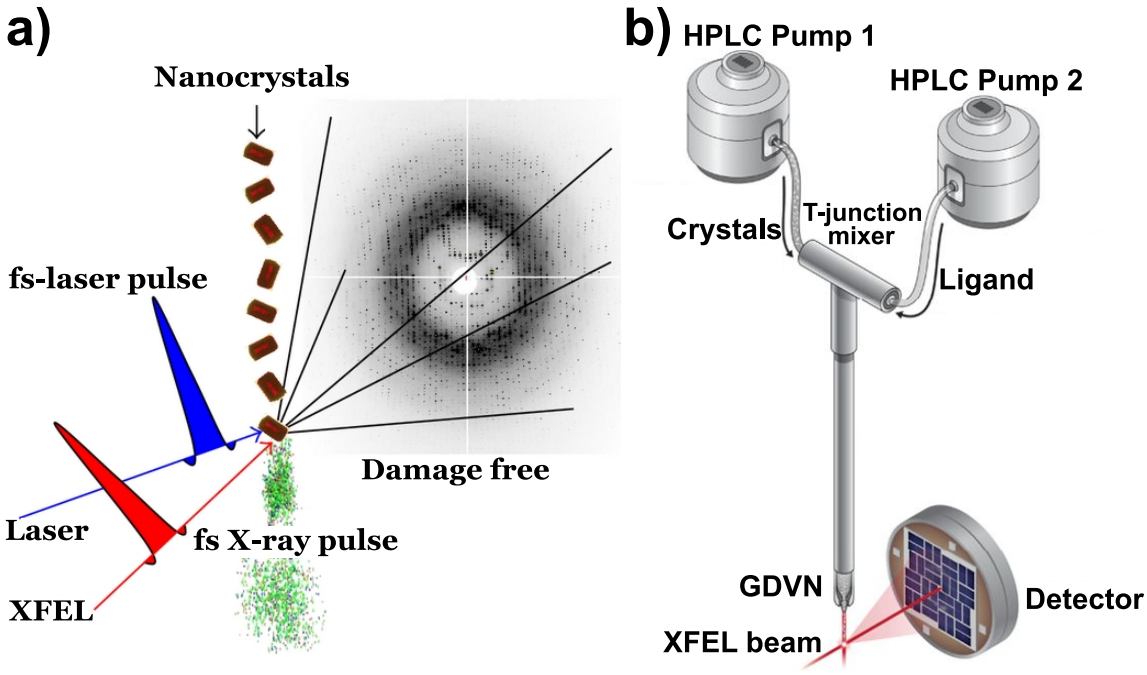

Figure 1.1 Illustrations of time-resolved serial femtosecond crystallography. (a) A fs-pump laser excites the photoactive nanocrystals just before they are probed by the X-ray beam, yielding a time-resolved diffraction pattern. Reprinted and adapted with permissions by Schmidt et al. [32]. (b) A crystal suspension and a corresponding ligand meet at a T-junction mixer, mix and react while traveling the delay line, and are injected into the X-ray beam for MISC. Reprinted and adapted by permission from Stagno et al. [33].

In addition to obtaining static protein structures, an exciting frontier for protein crystallography is the ability to determine the crystal structure of a reaction intermediate. Due to the ultrashort femtosecond pulses of the XFEL,[18] femtosecond or greater time resolution can be achieved in a method termed time-resolved serial femtosecond crystallography (TR-SFX).[34] By determining the structures of multiple reaction intermediates, one can piece together a "molecular movie" to essentially visualize the structure of a protein as it undergoes a reaction, providing further information relating to reaction mechanisms that have been hotly debated.[35, 36] For instance, the spatial resolution for structure determination with SFX is potentially greater than with solution scattering.[34]

There are two main experimental methods for studying reaction intermediates by TR-SFX. The first and most widely used method is a pump-probe photoactivation (Figure 1.1a).[37-39] In this method, an injected protein crystal is exposed to a short laser pulse before it is irradiated by the X-ray beam. The time between the laser flash "pump" and the X-ray irradiation "probe" determines the time point, and thus structure, of the photoactivated reaction intermediate. Several applications of this style of TR-SFX are detailed in Chapter 3. A second method for TR-SFX relies on mixing a protein crystal with a substrate that reacts with the aforementioned protein, and subsequently injecting the mixed crystal suspension into the X-ray beam (Figure 1.1b).[32, 33, 40] The time between completed mixing of the crystal and substrate and the X-ray irradiation determines the reaction intermediate time point probed. The time-resolution of mix-and-inject serial crystallography (MISC) is generally limited to millisecond or greater reaction intermediates, which is much slower than the hundreds of femtosecond resolution achievable by pump-probe. A drawback for pump-probe methods is that they are generally limited to photoactivated reactions, although there has been success utilizing photocaged compounds to, upon laser illumination, release a substrate the reacts with the protein.[41, 42] There are some challenges when using photocages for TR-SFX. Design of the photocage can be resource intensive: each photocage must be tailored to a specific substrate such that the intermolecular forces (e.g. hydrogen bonds), covalent bonds, or steric forces of the cage-substrate complex prevent the substrate from reacting with the protein.[43, 44] This means a new photocage has to be designed and synthesized (frequently complex multistep synthesis) for new protein-substrate pairings, both of which are nontrivial processes. It is difficult to achieve 100% caging,[43] which can lead to free substrate in solution and cause uncertainty in the probed intermediate. Additionally, the bond between the cage and the substrate must be weak enough so that the

substrate is sufficiently removed from the cage during photoactivation and also strong enough to prevent free dissociation, further complicating cage design and implementation. Because of the challenges involved with photocaged compounds, MISC is a more all-purpose method for mixing a protein and substrate for TR-SFX.

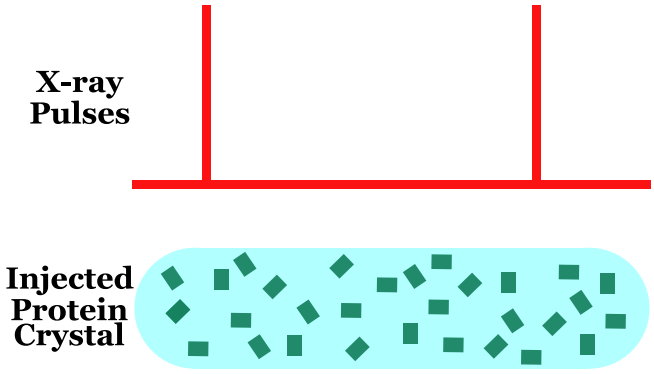

Figure 1.2 Illustration of protein crystal sample wasted between X-ray pulses.

As further detailed in Chapter 3, there are several notable drawbacks with SFX and MISC. One of the most common methods of introducing protein crystals into an XFEL is continuously injecting a stream of protein crystals by way of a liquid jet.[45] Due to the pulsed nature of the XFEL, protein crystal injected between pulses or pulse trains (Figure 1.2, see Chapter 3.2 for details on XFEL facility pulse frequencies) is not probed by the X-ray, resulting in >95% of the injected sample being wasted.[26] This requires milligrams to grams of protein to be crystallized in order to obtain enough diffraction patterns to construct a 3D structure of a protein; thus, protein crystallization can become a significant bottleneck to the SFX method. The current methods of sample delivery are detailed in Chapter 3, many of which strive to reduce the amount of protein crystal sample required to conduct an SFX experiment.[23] While each has their advantages and drawbacks, most methods for reducing sample waste are incompatible with the current setup at the European XFEL (EuXFEL) due to its

unique pulse structure. While the other XFEL facilities operate at a constant X-ray pulse frequency, with maximum frequencies ranging from 30 – 120 Hz, the EuXFEL has 10 Hz pulse trains with intratrain MHz X-ray pulse repetition.[46] Replenishing the protein crystal between intratrain pulses requires a high jet velocity,[47] but continuously injected sample during the ~ 99 ms between pulse trains is wasted.[46] Thus, a method of sample delivery that permits the high jet velocities of a GDVN with minimal crystal sample waste between pulse trains is necessary.

Separate from sample waste problems, current MISC sample delivery methods have a tradeoff. The first mixing methods employed for TR-SFX were simple to develop as they consisted of a commercial T-junction connector for introducing the protein crystal suspension to the substrate solution.[33, 48] However, the mixing was slow and required a long distance and time in order for the two to completely mix which limits time resolution to seconds or greater. To facilitate faster mixing, a MISC injector was developed by Calvey, et al.[49] that permits mixing on the order of micro- to milliseconds, thus allowing reaction intermediates to be determined on the millisecond time scale.[50] A drawback to this method is the complex design and assembly requirements for the injector, requiring laser milling and technical precision with manual assembly.[51] A MISC sample delivery method that has simpler construction and assembly is necessary to increase the availability of MISC.

1.3 Dissertation Overview

The main objectives of this thesis are as follows:

1. Summarize the currently available sample delivery methods for SFX and TR-SFX.
2. Demonstrate a method for reducing sample waste by generating aqueous-in-oil droplets for segmented injection during an SFX experiment.

3. Develop a method for fast mixing within a 3D printed device for TR-SFX.
4. Illustrate instances in which these microfluidic technologies have been utilized at XFEL facilities to characterize protein crystal structures by SFX.

The thesis is split into eight chapters. Chapter 1 gives an introduction to background and motivation for developing improved sample delivery methods for SFX, and Chapter 2 gives a more in-depth physical explanations of how these microfluidic devices operate. Chapter 3 gives a review of the sample delivery methods used for SFX at hard XFEL beamlines and the benefits of each method. In Chapter 4, the device for generating aqueous-in-oil droplets is detailed, and its surface properties and hydrophobic surface treatments are explored. Furthermore, initial diffraction data at a hard XFEL is reported. Chapter 5 describes the application of the segmented injection at the European XFEL to reduce the amount of protein crystal sample required for a complete dataset, and a structure for 3-deoxy-D-*manno*-octulosonate 8-phosphate synthase (KDO8PS) is determined during segmented sample delivery. In Chapter 6, 3D printed mixers for MISC are described, with a focus on device characterization. Chapter 7 details additional experiments at which I utilized the developed microfluidic devices to assist with sample delivery at a hard XFEL beamtime, and a summary of the thesis, impact my work has had on the field, and future directions are the components within Chapter 8.

CHAPTER 2

BACKGROUND THEORY

2.1 Microfluidics

The unique properties of microfluidic devices have many advantages compared to those of their macroscale counterparts.[52, 53] One of the more obvious advantages is the reduction in sample volume consumed during an experiment: as microfluidic devices are defined by length scales from 100s of nanometers to less than 100 micrometers, sample volumes on the order of nanoliters or less can be used.[54] This minimal sample volume is ideal in the context of SFX; as mentioned in the previous section, obtaining enough crystal sample to collect a complete dataset is the major bottleneck, hence, techniques that reduce the amount of sample consumed are required for broader applications of this emerging crystallography method. Indeed, since the first developed injector for SFX, the gas dynamic virtual nozzle (GDVN, detailed in Chapter 3.3.1)[55] utilized liquid delivery lines with inner diameters ≤ 100 μm. Subsequent sample delivery methods, from viscous media injection to fixed-target arrays, incorporate small crystal suspension volumes and microscale structures;[23, 56] thus, all sample delivery methods for SFX can be thought of as microfluidic devices. Additionally, microfluidic technologies have seen use in the development of MISC methods for TR-SFX.[40, 49, 57]

In a microfluidic environment, the surface and interfacial forces play a large role and the role of gravity, which dominates on the macroscale, is negligible.[53] To take advantage of these microscale effects, microfluidic droplets have been an area of great interest as they can serve as a high-throughput production of individualized reaction or transportation vessels that can reduce sample volume requirements.[58-61]

An aqueous phase suspended in an oil phase will tend to form a sphere in order to minimize the free surface energy; and within a microfluidic device, an aqueous phase containing an analyte can be intersected by an oil carrier phase to generate discrete aqueous-in-oil droplets.[60, 62] By controlling the flow parameters of the immiscible liquids and the geometry of the droplet generator, the droplets can be uniformly generated for discrete sample vessels.[60] Each isolated droplet can serve as a reaction chamber to perform thousands of parallel experiments in minutes,[63] for applications such as enzyme-kinetics,[64, 65] synthesis of biomolecules and nanoparticles,[66, 67] and individual crystal growth environments.[68, 69] In relation to SFX, microfluidic droplets can be utilized to reduce the amount of sample wasted between X-ray pulses,[70, 71] as is detailed in Chapter 2.3 and Chapter 3 through Chapter 5. Due to the tunability of microfluidic droplet generation parameters, this method has the potential to be useful at all currently available XFEL beamlines.

Another characteristic of microfluidic devices is their propensity to operate at low Reynolds number. The Reynolds number[72], Re, is a relationship between the inertial forces and viscous forces in a system (Equation 2.1)

$$Re = \rho u L / \mu \tag{2.1}$$

where ρ is the density, u is the velocity, L is a characteristic length, and μ is the viscosity. At Re < 2000, the flow is in a laminar regime where the flow profile is absent of perturbations such as vortices that occur in turbulent conditions (i.e. Re > 2500).[53, 73, 74] This allows for highly predictable and repeatable mixing scenarios that are dominated by diffusion. Due to their characteristically small length scales (L ~ 10^{-5} μm), laminar flow is common for microfluidic devices, including those used for sample delivery at XFELs. Diffusion is governed by the root mean square (RMS) displacement (Equation 2.2):[75, 76]

$$\sqrt{\langle \chi^2 \rangle} = \sqrt{2nDt} \tag{2.2}$$

In Equation 2.2, χ is the distance traveled by a particle, n is the number of dimensions allowed for diffusion (i.e. n = 1, 2, 3), D is the diffusion coefficient, and t is the time required for a particle to diffuse the RMS distance. In order to decrease the amount of time required for mixing, it is clear that decreasing the mixing distance, here the RMS of χ, must also decrease.

There have been several methods suggested to increase the speed and efficiency of mixing on the microscale. Active methods include acoustic, electric, thermal, and magnetic perturbations of the mixing system, and passive methods include a wide variety of channel geometries meant to perturb the flow fields and decrease the mixing distance. [77-79] There are several considerations to take into account when selecting a method for fast mixing in TR-SFX, as will be discussed further in Chapter 2.4. For instance, in passive mixers, the channel geometry is designed to decrease diffusion time for aqueous solutions instead of protein crystal suspensions. These geometries include serpentines,[80] crossing layers,[81] grooves,[82] and variously shaped blocks.[83] Each of these geometrical structures perturbs the flow field, allowing the two mixing liquids to effectively fold over one another. This phenomenon both increases the surface area for diffusion to occur and decreases the mixing distance; however, many of these structures are incompatible with SFX as the geometry can increase the likelihood of crystal clogging. Additionally, active mixing components present in magnetic, thermal, and electric active mixers have the potential to damage the crystals or interfere with the crystallography setup. Thus, passive diffusive mixing has been the most explored method for MISC as there are no active components and the channel geometry is free of obstacles to reduce crystal clogging.[33, 49, 50] When mixing protein crystals with an aqueous substrate for MISC,

the crystals are rather large in comparison to the substrates which affects their diffusion coefficient.

$$D = \frac{k_b T}{6\pi\mu r} \quad (2.3)$$

A general equation for a particle's diffusion coefficient due to Brownian motion, the Stokes Einstein equation (Equation 2.3),[74] where k_b is Boltzmann's constant, T is temperature, and r is the radius of the particle, illustrates that the larger a particle's size, the slower it diffuses. Fortunately, an aqueous substrate is typically a small molecules, thus will diffuse faster than the protein crystal. So, in order to enable fast mixing by diffusion, a microfluidic mixer must decrease the mixing distance between the quickly-diffusing substrate molecules and the slowly-diffusing protein crystals, as will be discussed in Chapter 2.4 and Chapter 6.

2.2 Microfabrication

There are a variety of methods used to fabricate microfluidic devices.[74] In addition to etching methods,[84] a common method for designing microfluidic devices is by using photolithography followed by soft lithography.[53, 85, 86] For example, a photoresist that has been spin-coated onto a substrate (e.g. silicon) is exposed to UV light through a mask (either a glass plate with patterned chromium or a plastic sheet with printed patterns) containing the desired structure. The exposure light has enough energy to excite the photoiniator to generate radicals that trigger polymerization,[87] resulting in all of the exposed photoresist being polymerized while the unexposed regions are not. In the case of a negative photoresist, the exposed portions of the photoresist remain after the non-exposed photoresist is washed away during a development step, while the reverse is applicable for positive photoresists.[74] Photolithography is a two-dimensional (2D) process that works well for planar structures and can be used for multilayer devices, but designing the proper masks and exposure conditions for

more complex, nonplanar 3D geometry microfluidic devices is challenging. Additionally, the subsequent soft lithography step must be taken into consideration, adding additional complexity.

To fabricate microfluidic 3D designs, there are several 3D printing methods available including inkjet 3D printing, stereolithography, extrusion printing, and two-photon polymerization (2PP).[88] Except for 2PP which has a resolution on the order of 10^2 nm, 3D printing methods are limited in resolution.[88] In order to print the small features (≤ 100 μm) necessary for SFX liquid jet injectors (see Chapter 3.3), 3D printing using 2PP is utilized.[87-90] The microfluidic devices described in this thesis are printed using a Photonic Professional GT (Nanoscribe, GmbH, Germany) 3D printer that operates with the principle of 2PP,[91] as illustrated in Figure 2.1.

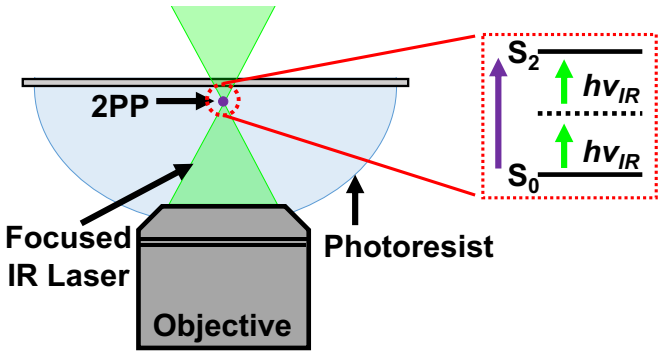

Figure 2.1 Illustration of 2PP 3D printing. A laser is focused by an objective to a small voxel within the photoresist (here represented as a violet dot). In this focused volume, two photons at one wavelength (hv_{IR}) are simultaneously absorbed by the photoinitiator in the photoresist. As seen in the pop-out, one photon will excite an electron's ground state (S_0) to a virtual state (dashed black line) and the second photon will excite from the virtual state to the excited state (S_2). Thus, at this focused volume is where the photoresist becomes polymerized.

In 2PP, an individual photon does not have enough energy to excite an electron. However, when a high photon density is present, two photons whose total energy is high enough to excite the electron can be absorbed simultaneously (Figure 2.1). One of the absorbed photons will excite the electron to a virtual state between the

electron's ground state and the excited state, and the other absorbed photon can then provide enough energy to reach the excitation band of the electron.[87] To supply such a high photon density, femtosecond laser pulses can be utilized, which have an added benefit of increasing the precision of the exposed region.[87]

For the Nanoscribe Photonic Professional GT, the laser (780 nm wavelength) is focused by an objective to a small point (approximately 200 nm^3). At this focused voxel, there is a high probability of two photons being simultaneously absorbed by an electron in the photoresist's photoiniator for 2PP at a wavelength of 390 nm. The excited photoinitatior will generate radicals that initiate monomer polymerization.[88, 91] The photoresist and photoiniator are chosen so that the lower energy photons cannot trigger the excited state for polymerization without a two-photon absorption process. Since two-photon absorption has a low probability of occurring outside of the focused voxel (where the probability of a two-photon absorption is high), 2PP permits complex 3D structure design in a space-selective manner.[87] The desired structure can be designed in a 3D CAD program and imported into the printing software. Following the blueprints of the CAD file, the xy-stage on which the photoresist and substrate are mounted is translated during the femtosecond pulsed exposure, and the objective is mobile in the z-direction; thus, a complex nonplanar structure can be printed layer by layer from the bottom (attached to the substrate, a glass slide in Figure 2.1) to top. The printing mode shown in Figure 2.1 is dip-in laser lithography (DiLL) as the objective is immersed in the photoresist.[92] Other printing modes have the photoresist on top the substrate and the objective below the substrate. In this mode of printing, the objective is immersed in either air or another liquid (e.g. oil) for refractive index matching. Designs that would be challenging or impossible to fabricate with one photon processes like photolithography are printed

with ease using 2PP 3D printing. Once the device has been printed, a development step is necessary to remove not polymerized resist.

2.3 Droplet Generation

Microfluidic droplets can be formed when two immiscible liquids intersect in a microchannel as a result of the instabilities between the two liquids.[60] The aqueous phase (for SFX applications, the protein crystal suspension) is hydrophilic while the oil carrier phase is hydrophobic; thus, the two liquids are immiscible. Microfluidic droplets can be passively or actively generated. In passive generation, the channel geometry, liquid properties (e.g. viscosity and interfacial tension), and flow conditions determine the resulting droplet parameters such as droplet volume and frequency. Many geometries for passive droplet generation have been developed for various applications[59, 60, 62, 93] with three main types of geometries[62] (Figure 2.2): T-junction (or cross-flow),[58] flow-focusing,[94, 95] and coaxial injection, [96] with the simplest being the T-junction or cross-flow geometry (Figure 2.3). The simplicity of T-junction geometries has led to a significant amount of characterization of droplet generation parameters and resulting droplets.[60] Flow-focusing geometries have a more complex geometry that has been less characterized but have a higher maximum frequency and minimum droplet size in comparison to T-junctions. Coaxial injection geometry can have simple fabrication requirements (e.g. a cylindrical capillary aligned within a square capillary). Additional geometries such as step-emulsification, microchannel emulsification, and membrane emulsification can passively produce droplets.[60] This thesis focuses mainly on T-junction geometry whose benefits include simplicity for design, assembly, and quantification, and its propensity for monodispersed droplets.

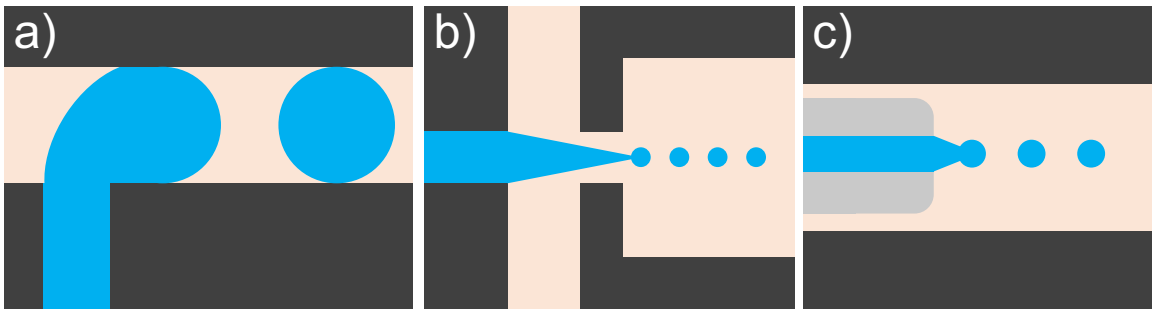

Figure 2.2 Passive droplet generation geometries. The dispersed phase (blue) intersects the continuous phase (orange) to form droplets. The walls of the device are black. (a) T-junction, or cross-flow, (b) flow-focusing, and (c) coaxial injection, with the coaxial capillary in gray.

In active generation, an external force triggers droplet generation and affects the resulting droplet volume and frequency. Active components can include, piezoelectric components (e.g. a piston), acoustic components to release a defined volume of aqueous sample into the oil phase, valves that pinch off droplets, or an electrical trigger to produce an aqueous droplet on-demand.[60] From an SFX sample delivery perspective, active methods may have difficulty incorporating protein crystals in the aqueous phase due to either clogging effects or potential damage to the crystal, although as discussed in Chapter 3 this is not always the case.[23]

A competition of forces, influenced by geometrical constraints and fluid properties, can lead to instabilities that generate droplets. The forces in consideration include the viscous drag force, interfacial forces (or capillary forces), pressure forces, inertial forces, and any external forces such as gravity.[60] One can tune these forces by adjusting the channel geometry, the viscosity ratio between the two liquids, and the flow rate ratio between the two liquids.

The interfacial force arises from the opposing intermolecular forces between the immiscible phases – the energy required for a polar molecule (e.g. the dispersed phase) to transfer from its homogenously polar environment into a volume of intermolecular forces that oppose it is thermodynamically unfavorable, and the same

is true for a nonpolar molecule (e.g. the continuous phase) transferring into a polar environment. As such, at the phase boundary each phase will have a net force inward, minimizing the surface area and surface energy. [97]

The viscous forces describe the transfer of momentum through a liquid and are related to the liquid viscosities and velocities.[97] A liquid with high viscosity has a high degree of internal friction and will better transfer momentum through its internal layers. For Newtonian fluids, increasing the velocity of one liquid (e.g. the continuous phase) will result in a greater shear force exerted on the other liquid.

The inertial forces describe the ability of a flow to take on the momentum of an object or flow field without altering its original flow path. The Reynold's Number (Equation 2.1) relates the inertial forces to the viscous forces, and frequently illustrates that inertial forces are small in microfluidic devices, although there are notable exceptions where inertia is a contributing force, as discussed below. Pressure forces arise from the fluid's driving force, generally a syringe pump, high-pressure liquid chromatography (HPLC) pump, or constant pressure pump. There can also be increased pressure forces due to temporary blockages in the channels. For passive droplet generation, the external force is gravity, and it plays a negligible role in droplet formation.[60]

When describing the competing forces, some dimensionless values are handy. As previously mentioned, the Reynold's Number relates the contribution of inertial forces to viscous forces. The contribution of viscous forces to interfacial forces is described with the capillary number, Ca .

$$Ca = \frac{\mu_c u_c}{\gamma} \tag{2.4}$$

In Equation 2.4, μ_c is the viscosity of the continuous phase, u_c is the velocity of the continuous phase, and γ is the interfacial tension.

There are three primary regimes of droplet generation in the T-junction geometry: squeezing, dripping, and jetting, as shown in Figure 2.2.

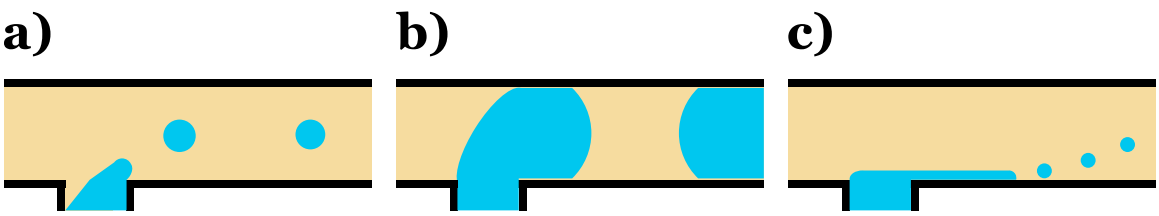

Figure 2.3 Illustrations of droplet breakup regimes. (a) dripping, (b) squeezing, and (c) jetting.

At mid-range Ca ($0.01 < Ca < 0.3$), droplets are generated in the dripping regime (Figure 2.3a).[98, 99] In the dripping regime, the viscous shear forces overcome the dispersed phase interfacial forces before the dispersed phase can fill the outlet channel.[60, 100] This regime creates spherical droplets that have a diameter smaller than the channel dimensions.

At $Ca < 0.01$, droplets are generated in a squeezing regime (Figure 2.3b).[98, 101-103] In the squeezing regime, the dispersed phase fills the main channel as the shear forces are not sufficient to initiate breakup.[60] A thin layer of oil can pass around the droplets when the channel walls are hydrophobic. The growing aqueous plug acts as a blockage for the continuous phase which then builds pressure as a result.[60, 103] Eventually the pressure in the continuous phase overcomes the pressure within the droplet and initiates breakup, with the dispersed phase forming a neck of decreasing width until pinching off into a droplet. Instead of being spherical, the droplets in the squeezing regime are plug-shaped, longer than the width of the channel, and have hemispherical end caps.

At high Capillary Number, $Ca > 0.3$, droplets are generated in the jetting regime (Figure 2.3c).[102] In the jetting regime, the inertial forces are balanced with the interfacial forces and viscous shear forces. The dispersed phase extrudes along the

wall of the channel until the continuous phase viscous forces and dispersed phase inertial forces overcome the interfacial forces, and droplet break up occurs due to Rayleigh instability.[97, 104] Jetting tends to produce small, spherical droplets, similar in diameter to the width of the jet.

As discussed in Chapter 4, the surface properties of the channel walls in a microfluidic device can be crucial to the success of uniformly generated droplets.[70] For water-in-oil droplets, this may require the channel walls to be hydrophobic (i.e. have a contact angle >90°, Figure 4.1)[74] such that oil wets the walls and has a constant thin layer present. In this way, the aqueous phase does not come in contact with the walls and does not have an opportunity to adsorb on the device channels. As discussed in Chapter 4, hydrophilic channel walls can cause non-uniformity in droplet generation due to adsorbed aqueous phase.

There are several considerations for SFX when deciding on a method of droplet generation to reduce the amount of sample wasted between pulses or pulse trains.[23, 56] The first is the frequency of the X-ray laser: to reduce the greatest amount of sample wasted while maintaining a similar hit rate to continuous injection, droplets should be generated at a frequency matching the XFEL. In the same line of thought, the phase of the generated droplets needs to match the phase of the X-ray pulses. If droplet generation matches the frequency but is out of phase with respect to the X-ray pulses, it is unlikely that droplets containing the crystal sample will be present during an X-ray pulse. Active droplet generation methods have the benefit of directly controlling the frequency and phase of the generated droplets;[60] however, the added periphery required for active droplet generation may be incompatible with SFX setups. For instance, a piezoelectric piston may have difficulty with the high back pressures of the long capillary lengths (discussed in Chapter 5.4), and the force of the piston may damage the protein crystals. Furthermore, as discussed in Chapter

3.4,[23] acoustically generated droplets can require significant adjustments to the sample delivery setup at a hard XFEL facility, and the generated droplets may have difficulty supporting high X-ray pulse frequencies or the pulse structure at the EuXFEL. As such, a passive droplet generation method has advantages due to its ease of use but faces challenges when it comes to synchronizing the phase of the droplet with the X-ray pulses. As described in Kim et al. [105], a combination of an active droplet generation technique, electrowetting, with a passive droplet generation setup can allow one to adjust the phase of droplet generation and maintain its frequency.

Additional considerations for droplet generation at XFELs are the droplet size and liquid flow rates. At all beamlines, it is necessary to repopulate a crystal in the X-ray beam between pulses, and depending on the beamline this can require a high jet velocity. For instance, the EuXFEL requires a jet velocity ≥50 m/s [47] and thus frequently uses high total flow rates to accomplish this velocity. For droplet generation, this requires the use of high oil flow rates and an adjustment of the channel dimensions to reach the 10 Hz pulse train frequency as described in Chapter 5. In contrast, beamlines such as LCLS and SACLA that function at lower X-ray pulse frequencies of 120 or 100 Hz respectively can utilize lower flow rates for sample refresh rates, and thus an adjusted channel geometry is ideal for reaching these higher droplet generation frequencies.

The jetting regime also has use for SFX outside of droplet generation: if the parallel-flowing oil and aqueous crystal sample (Figure 2.4) reach the end of the injection nozzle before the aqueous phase reaches the Rayleigh instability point, the two phases may be concurrently injected.[106, 107] In this co-flow injection, a low flow rate aqueous crystal sample and a high flow rate oil phase are continuously injected, thus permitting less crystal sample to be utilized while maintaining a high jet velocity.

This is particularly useful at the EuXFEL as the high jet velocity can refresh the crystal sample between pulses while reducing the amount of sample injected between pulse trains without requiring synchronization that is necessary during droplet injection.

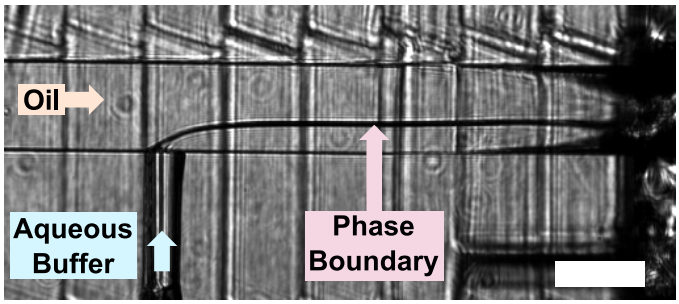

Figure 2.4 Optical microscopy image of a 3D printed T-junction operating in the co-flow regime. The oil flow rate is 15 µL/min and the aqueous buffer flow rate is 5 µL/min. The boundary between the aqueous and oil flor rate is highlighted by the pink arrow. Scale bar is 100 µm.

2.4 Microscale Mixing

As described in Chapter 2.1, the Reynolds number can be indicative of whether flow conditions are laminar or turbulent. In microfluidic devices, the small channel dimensions lend to $Re \ll 2000$ characteristic of laminar flow.[74] As such, species transport is governed by the laminar flow profile and diffusion.

The flow within the microfluidic channels can be described with the Navier-Stokes equation for a Newtonian incompressible liquid (Equation 2.5)[74, 108]

$$0 = -\nabla p + \mu \nabla^2 \boldsymbol{u} \tag{2.5}$$

that satisfies conservation of momentum. In Equation 2.5, u is velocity, p is pressure, and μ is viscosity. As $Re \ll 1$, the left-hand side of the equation that describes the inertial forces present is zero. On the right-hand side, the first term includes the pressure forces and the second term is the viscous forces. There is no

external force acting on the system (gravity is negligible) so no additional term is included.

In addition to conservation of momentum, conservation of mass must be satisfied. This is described in the continuity equation for a Newtonian incompressible liquid (Equation 2.6).

$$\nabla \cdot u = 0 \tag{2.6}$$

By solving Equation 2.5 and 2.6, the velocity within a microfluidic device, and thus the laminar flow profile, can be determined. In order to determine a particle's motion due to diffusion, movement corresponding to Brownian motion must be described. Fick's first law[109] (Equation 2.7) describes the flux, $\boldsymbol{J}$, of a particle due to diffusion.[74, 110]

$$\boldsymbol{J} = -D\nabla c \tag{2.7}$$

In Equation 2.7, D is the diffusion coefficient (Equation 2.3) and c is the concentration.

A simple example of mixing by diffusion in a microfluidic channel can be illustrated by two miscible liquids flowing parallel to one another in a channel (Figure 2.5). When the solution containing species A (red) meets the solution containing species B (blue) at x_0, the two species are completely separate. As the solutions proceed along the channel, the red species A diffuses into the blue species B. In Figure 2.5, line plots of the cut lines (dashed black lines) depict the concentration profile of species A along the channel at specified x-positions. At the end of the channel, x_4, the solution is uniformly green across the channel width, and the concentration profile is 0.5 across the channel length, both indicating a uniform concentration of species A throughout the channel due to diffusive mixing.

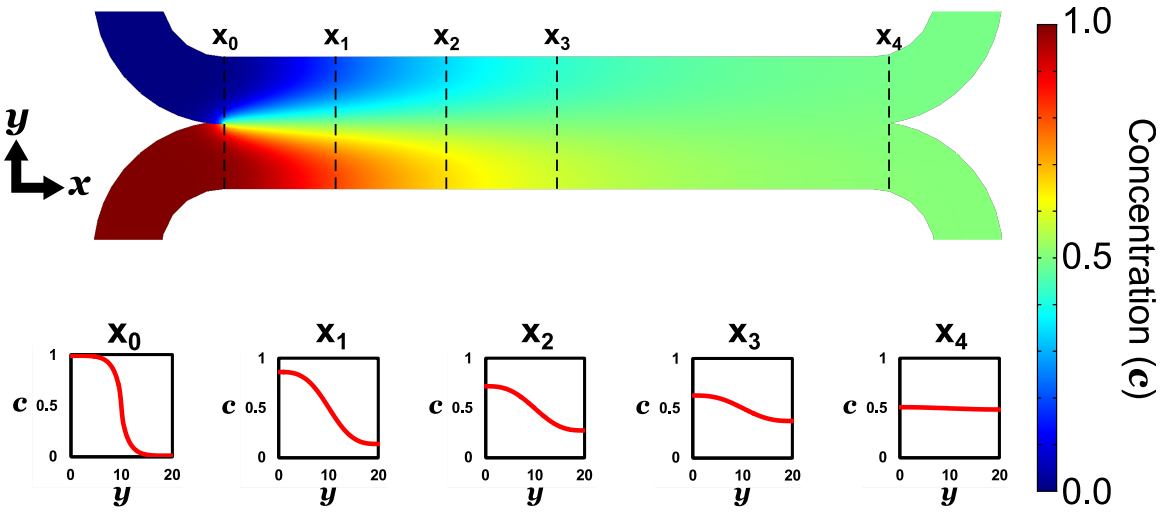

Figure 2.5 Illustration of mixing by diffusion within a microfluidic device. At point x_0, the two liquids are completely separated (red and blue), and as they continue traveling down the channel the liquids begin to mix by diffusion (green), until the species concentration for both liquids is uniform throughout the channel width at the end of the channel, x_4. Line plots of the cut lines (dashed black lines) illustrate the concentration profile perpendicular to the flow direction at defined positions (x) along the mixing channel. Concentration plot generated in COMSOL Multiphysics 5.3 based off the H-mixer application library file.

The Peclet number, Pe, compares the relative importance of convection and diffusion in regard to species transport.[97]

$$Pe = uL/D \tag{2.8}$$

In Equation 2.8, L is the characteristic length. When Pe < 1 diffusion is dominant, and when Pe > 1 convection is dominant. Mixing by diffusion still occurs when Pe > 1, as can be the case with large liquid velocities in a microfluidic device; in that case, a long channel would be necessary to allow the particles enough time to diffuse and mix. For the microfluidic devices described in Chapter 6, Pe > 1 and convection is the dominant means of species transport, resulting in negligible transport by diffusion in the direction of flow. The diffusion occurs in one dimension (i.e. normal to the direction of flow) due to Brownian motion.

As discussed in Chapter 2.1, the time required for mixing to occur by diffusion is quadratically related to the distance over which a particle must diffuse (Equation

2.2). When flowing two miscible liquids parallel with one another as in Figure 2.5, the mixing distance is equivalent to the channel width. Thus, to decrease this mixing distance the channel width must be decreased. While this is relatively simple to accomplish with microfabrication methods, a small channel width can impose limitations such as high flow resistance, low sample throughput, and clogging effects. The latter is of particular concern when working with protein crystals as the channel needs to be at least as wide as the protein crystals. Furthermore, even when the channel is on the same length order as the crystal size, crystals can agglomerate and form blockages in the channel. Due to this potential for clogging, decreasing the channel width is not always a viable option for decreasing the mixing distance.

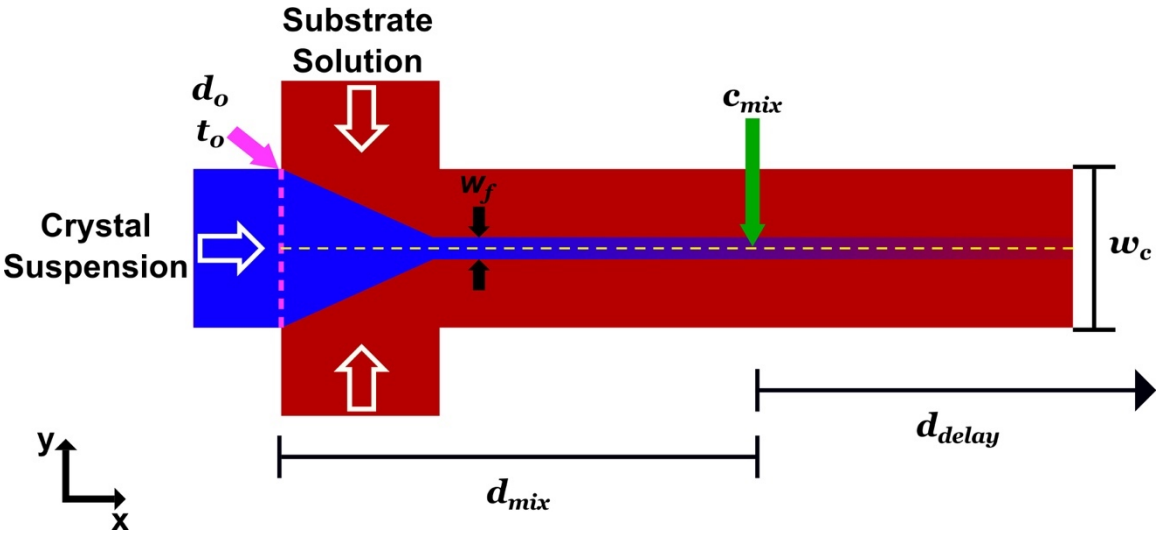

Figure 2.6 Illustration of hydrodynamic focusing in a cross mixer. The crystal suspension (blue) is focused on two sides by a substrate solution (red) into a narrow stream for mixing by diffusion over a short distance. The two species are mixed at a point, x_{mix}, in the outlet, which corresponds to c_{mix} (violet). Figures of merit, defined in Table 2.1, are displayed. The initial mixing point, d_0, is represented as a dashed pink line. The yellow dashed line represents the center concentration line that is used for determining the mixing distance, d_{mix}, and the mixing time, t_{mix}. The delay distance, d_{delay}, extends downstream until the mixture reaches the X-ray (not pictured). Flow direction indicated by white arrows. Not to scale.

To decrease the mixing distance without altering the channel size, the principle of hydrodynamic focusing can be exploited (Figure 2.6).[111-116] By increasing the number of inlets in the mixing device from two (Figure 2.5) to three (Figure 2.6), flow from two side inlets can focus the liquid from the center inlet into a narrow stream. For instance, a solution containing a substrate that binds to a protein is introduced in the two side inlets, and a protein crystal suspension is introduced in the center inlet, as seen in Figure 2.6. Hydrodynamic focusing has the added benefit that, in a planar device like Figure 2.6 diffusion occurs on two interfaces of the center stream as opposed to just one interface in Figure 2.5, effectively decreasing the mixing distance by half the hydrodynamically focused stream width.

The width of the center stream can be expressed by:[110]

$$w_f/w_c = Q_c/Q_{tot} \tag{2.9}$$

where w_f is the width of the focused stream (Figure 2.6), w_c is the width of the outlet, Q_c is the average flow rate in the center inlet, and Q_{tot} is the total flow rate in the outlet.[110] It can be seen from Equation 2.9 that for a given outlet width, the flow rates are critical for determining the diffusion distance for mixing by diffusion. Since Q_{tot} is the sum of the flow rate from the side channels (Q_{sides}) and Q_c, the flow ratio, φ, can be defined as Equation 2.10.

$$\varphi = (Q_{tot} - Q_c)/Q_c = 2Q_{sides}/Q_c \tag{2.10}$$

As φ increases, w_f decreases, thus resulting in a decreased diffusion distance, χ, and, from Equation 2.2, a decreased mixing time, t.

Aside from passive mixing methods, there are several notable active mixing methods within microfluidic devices,[77, 110] such as electrokinetic control of the liquids, mixing within microfluidic droplets, controlling magnetic particles within the device to elicit a stirring effect, utilizing pressure control to create a type of segmented flow, and applying acoustic perturbations. Active mixing methods have not been explored for

MISC, although they may face challenges when using delicate protein crystals as damaging the crystals is a concern in addition to device clogging.

Table 2.1 Figures of merit for a MISC experiment.

Figure of Merit	*Symbol*
Mixing time	t_{mix}
Reaction time point	t_r
Reaction time point uncertainty	$t_{r,spread}$
Time for diffusion into a crystal	t_{cryst}
Mixed concentration	c_{mix}
Mixing distance	d_{mix}
Delay distance	d_{delay}
Channel width	w_c
Focused stream width	w_f
Total flow rate	Q_{tot}
Flow ratio	φ
Velocity in the center of the channel	u_{max}
Diffusion coefficient	D

2.4.1 Mixing Time, t_{mix}

In a MISC experiment, the main goal is to determine reaction intermediates for a protein-substrate reaction. In order to reach a reaction intermediate time point, t_r, there are several figures of merit (Table 2.1) for the sample, microfluidic mixer, and operating parameters (Figure 2.6). Before a reaction can begin, the protein crystal suspension and substrate solution need to mix. The crystal suspension is designated

as fully mixed with a substrate when there are enough substrate molecules to react with each protein molecule in the crystal. This is conveyed by the concentration of the substrate, c_{mix}, at which the crystal suspension stream is fully mixed. The time it takes for the entire crystal stream to reach c_{mix} is the mixing time, t_{mix}.

The mixing time is influenced by several factors. First, as the hydrodynamic flow is in the laminar flow regime, mixing by diffusion is dominant. The substrate D (Equation 2.3) determines on average how quickly the substrate molecules will diffuse through the crystal stream. The distance (y-direction in Figure 2.6) over which the substrate must diffuse (χ in Equation 2.2) is determined by w_f, depicted in Figure 2.6. To determine w_f, both the channel geometry and flow rate conditions are important (Equation 2.9). For short t_{mix}, w_f should be minimized which can be accomplished by decreasing w_c or increasing φ. For MISC, w_c is often several-fold larger than the crystal size as decreasing w_c comes with a risk of crystal clogging (crystal size is rarely uniform[117] and crystals can agglomerate). Thus, a large flow ratio, φ, is used to focus the center crystal suspension into a narrow stream for a short w_f. With D and w_f, Equation 2.2 can be used to determine t_{mix}.

Alternatively, numerical models can be solved to calculate the velocity and concentration profiles along the center line of Figure 2.6. After determining the mixing distance (Chapter 2.4.2), the time it takes to reach c_{mix} can be calculated using the velocity profile (further detailed in Chapter 6.4.2).

2.4.2 Mixing distance, d_{mix}

While the substrate is diffusing in the y-direction, the crystals and substrate are also transported in the x-direction (Figure 2.6) by convection. The x-direction distance from the initial mixing point, d_0 in Figure 2.6, to c_{mix} is the mixing distance, d_{mix}. The concentration profile in a mixing device (Chapter 6) can be solved using numerical

models, and d_{mix} can be determined from the center concentration line (Figure 2.6). Alternatively, to calculate d_{mix} for the center crystal stream, the velocity along the center line (yellow dashed line in Figure 2.6) and t_{mix} can be utilized. In Figure 2.6, the center velocity profile relates to the yellow dashed line. In the outlet, the velocity in the center of the channel is u_{max} (Equation 2.11).

$$u_{max} = 1.5\, u_{tot} = 1.5(Q_{tot}/A) \tag{2.11}$$

In Equation 2.11, A is the cross-sectional area of the channel and u_{tot} is the average velocity in the outlet channel. Due to the parabolic flow profile in the outlet, u_{max} is 1.5 time u_{tot}.[118] Since the protein crystals are relatively large, $D_{crystal}$ will be small, on the order of 10^{-14} m^2/s for 20 μm crystals, and the crystals will remain localized to the focused stream and experience u_{max}. However, the velocity increases from d_0 to the outlet when u_{max} is achieved. The velocity in this region can be roughly estimated[49] as a linear increase from the velocity in the center inlet to u_{max} or more accurately determined using numerical models, as is done in Chapter 6. With t_{mix} and a velocity profile, d_{mix} can be calculated.

2.4.3 Delay distance, d_{delay}

An additional delay distance (x-direction), d_{delay}, is required after d_{mix} to allow the substrate to diffuse into the protein crystal and to permit the protein-substrate reaction to proceed until the intermediate at t_r is probed by the X-ray (Figure 2.6). Assuming a constant A after c_{mix}, u_{max} is constant in the outlet and d_{delay} can be calculated using Equation 2.12

$$d_{delay} = u_{max}\left(t_{cryst} + t_r\right) \tag{2.12}$$

where t_{cryst} is the time required for the substrate molecules to diffuse into the crystal. To determine t_{cryst}, it is important to know the size of the crystal,[32] and the availability of solvent channels in the crystal for substrate diffusion. Crystal size is

determined during crystallization. The solvent content of the protein crystal,[119] Φ, and D can be used to calculate the effective diffusion coefficient, D_{eff}, (Equation 2.13)[49] within the crystal.

$$D_{eff} = \Phi^2 D \tag{2.13}$$

To calculate t_{cryst}, Equation 2.2 can be utilized, with D_{eff} as the diffusion coefficient and the crystal size as the diffusion distance. For microcrystals, t_{cryst} can range from microseconds to milliseconds depending on crystal size and solvent channel availability, with small crystals minimizing t_{cryst}. After calculating t_{cryst} and with a designated t_r for a desired reaction intermediate, d_{delay} can be calculated with Equation 2.12. With d_{delay}, one can determine the required outlet dimensions (i.e. length and A) for the connection between the mixer and the injection nozzle. Several designs of 3D printed mixers with variable outlet dimensions are discussed in Chapter 6.

CHAPTER 3

MICROFLUIDIC SAMPLE DELIVERY FOR SERIAL CRYSTALLOGRAPHY USING XFELS

3.1. Abstract

Serial femtosecond crystallography (SFX) with X-ray free electron lasers (XFELs) is an emerging field for structural biology. One of its major impacts lies in the ability to reveal the structure of complex proteins previously inaccessible with synchrotron-based crystallography techniques and allowing time-resolved studies from femtoseconds to seconds. The nature of this serial technique requires new approaches for crystallization, data analysis, and sample delivery. With continued advancements in microfabrication techniques, various developments have been reported in the past decade for innovative and efficient microfluidic sample delivery for crystallography experiments using XFELs. This article summarizes the recent developments in microfluidic sample delivery with liquid injection and fixed-target approaches, which allow exciting new research with XFELs.

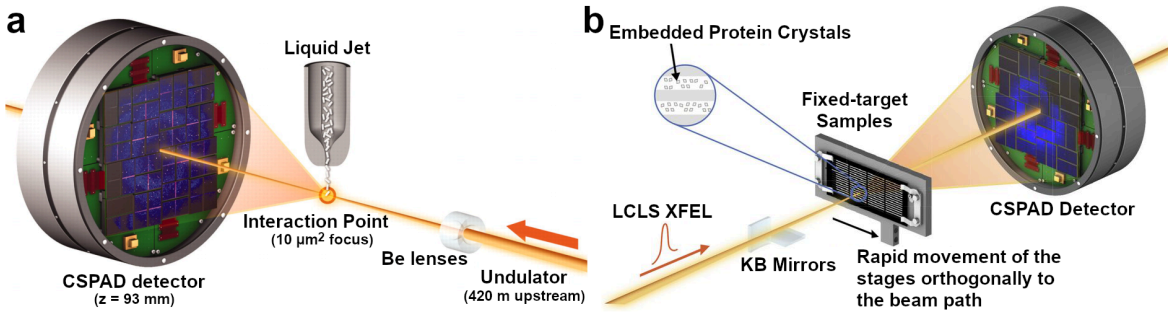

Figure 3.1 (a) Overview of an SFX experiment with an XFEL delivering sample with a liquid jet. Reprinted by permission from Boutet et al.[120]. (b) Overview of an SFX experiment with an XFEL employing a fixed-target. Reprinted with permission from Hunter et al. [121].

3.2. Introduction

X-ray crystallography has enabled the determination of high-resolution protein structures that are essential in predicting a protein's function. With the development of serial femtosecond crystallography (SFX) with an X-ray free electron laser (XFEL), crystallographers now have a powerful tool to study proteins and reactions, overcoming limitations of traditional crystallography[19, 20, 22]. Due to the ultrafast, highly brilliant X-ray pulses, a protein crystal exposed to a short XFEL pulse can yield a diffraction pattern before the onset of destructive radiation damage, a process termed "diffraction before destruction"[21]. However, since the crystal experiences extensive damage or destruction after a single X-ray exposure, new crystals must be introduced into the path of the XFEL in order to construct a complete electron density map of the protein's structure[22]. Several thousands of diffraction patterns, each pattern obtained from one crystal, are typically needed to obtain a full data set that enables the determination of electron density for a protein structure. Powerful data analysis techniques have been developed in the past years for this purpose,[122-124] to cope with the requirement of SFX with XFELs. This new field has opened the door to studying proteins that do not readily crystallize into large crystals but can crystallize as micro- and nanocrystals[21]. There is even the potential to forgo crystallization altogether and study single particles in solution such as large viruses [125, 126]. Another benefit is that SFX can be performed at ambient temperature and pressure which can more closely model physiological conditions [36]. Furthermore, the short exposure time coupled with the serial introduction of crystals makes SFX a prime target for time-resolved (TR-) studies that elucidate previously unresolved reaction intermediates with the ultimate goal of putting together a "molecular movie" that tracks a reaction as it progresses in time [127].

Currently, there are five operational hard XFEL beamlines: Spring 8-Angstrom Compact free electron Laser (SACLA), Linac Coherent Light Source (LCLS), Pohang Accelerator Laboratory XFEL (PAL-XFEL), European XFEL (EuXFEL), and SwissFEL. The femtosecond X-ray pulse structure varies between beamlines: SACLA, PAL-XFEL, and SwissFEL operate at a maximum of 100 Hz, LCLS operates at up to 120 Hz, and EuXFEL has a 10-Hz bunch train structure, with a projected maximum 4.5-MHz frequency within each 0.6-ms bunch [128, 129]. The current pulse structure at the EuXFEL has a 1.1-MHz frequency with < 1 μs spacing between pulses [47] with about 300 pulses per bunch (which is constantly being improved to meet the final specs of the instrument). As each pulse will destroy the irradiated crystal, new crystals must be delivered at or exceeding the frequency of the XFEL pulses, which makes the traditional setup of a single looped crystal mounted on a goniometer impractical. To this end, many sample delivery methods have been developed [130], with two main categories: liquid injection or fixed-target approaches, as schematically depicted in Figure 3.1. Essentially, all approaches qualify as microfluidic techniques as the critical dimensions of sample delivery are adapted to the size of the crystals used in SFX with XFEL experiments, which ranges from a few micrometers to a few tens of micrometers for most reported experiments. Additionally, since many protein crystals are injected into the path of the XFEL, there is a significant effort to optimize sample delivery methods to reduce sample waste and reduce the time required to collect sufficient data to fully characterize a protein structure. Here, we describe the advancements in sample delivery technology and how they have been applied for SFX and TR-SFX.

3.3. Liquid injection devices

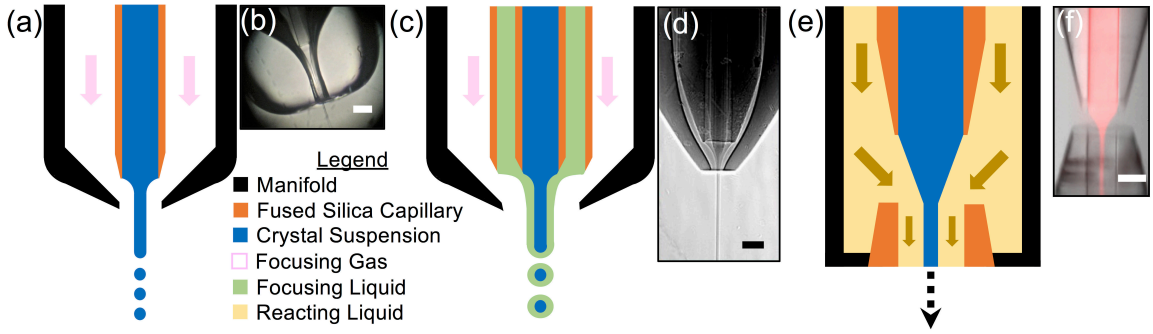

Figure 3.2 (a) Schematic and (b) optical microscopy image of a gas dynamic virtual nozzle (GDVN). Adapted and reprinted from Weierstall et al. [45]. (c) Schematic and (d) radiograph of a double flow focusing nozzle (DFFN). Adapted and reprinted with permission from Oberthuer et al. [131]. (e) Schematic and (f) optical microscopy image with an overlaid fluorescence microscopy image of the hydrodynamic focusing region of the mix-and-inject serial crystallography (MISC) injector. Adapted and reprinted from Calvey et al. [49] under a Creative Commons Attribution (CC BY) License. Scale bar for (b) and (d) is 100 μm, and (f) is 50 μm.

3.3.1. Gas dynamic virtual nozzle

Due to the high-intensity X-ray pulses, microcrystals are largely damaged or destroyed when exposed to the X-ray, and a new crystal must be delivered into the X-ray beam by the next pulse. One way to accomplish this high crystal replenish rate is to inject a continuous stream of protein crystal suspension into the X-ray (Figure 3.1a). Rayleigh jets were first explored [132] but encountered difficulties: high flow rates (mL/min) and small nozzle orifices are required to create stable jets with a small jet diameter to reduce background scattering from the carrier buffer. The result is an easily clogged nozzle. Furthermore, the Rayleigh jets have a high propensity for ice formation in vacuum, and the intense diffraction from the ice crystals can damage the detector [132].

To overcome the drawbacks, a gas dynamic virtual nozzle (GDVN) was developed that utilizes a coaxially flowing gas to accelerate and focus a liquid stream into a liquid jet [55] (Figure 3.2a, b). Pressurized water (frequently from high-pressure liquid

chromatography (HPLC) pumps) is used to apply a constant flow rate on a piston within a steel sample reservoir such that the loaded crystal suspension on the opposite side of the piston travels into a fused silica capillary that is interfaced to the GDVN [133]. While nitrogen can be used as a focusing gas, helium is frequently used as it has fewer issues with ice formation in vacuum and results in more stable jet formation, and the lower molecular weight results in less background scattering from X-rays [22]. The first GDVNs were developed using commercially available fused silica capillaries [55]. The smaller liquid capillary is aligned in the center of the larger gas capillary. The end of the gas-focusing capillary is flame polished to decrease the diameter of the gas aperture in order to focus the liquid into a thin jet (< 10 μm) [45]. To decrease the background scattering from the gas-focusing capillary, the nozzle tip is polished into a rounded cone shape [45]. These glass GDVNs were utilized for the early serial crystallography experiments at LCLS [19] and continue as one of the most common injection methods of protein crystals in low-viscosity media, both in vacuum and in ambient pressure [134].

Construction of the outer portion of the GDVN with ceramic materials instead of glass has been explored to increase the nozzle's uniformity and durability [135]. Here, the tip of the nozzle is fabricated by micro-injection molding while the inner capillaries for the gas and liquid lines are polished as in the fused silica GDVNs. The minimum flow rate for stable jetting with ceramic nozzles is similar to that of a glass GDVN, and ceramic nozzles have recently been used for the injection of crystallized fibrils into an XFEL [136]. To further simplify assembly, ceramic nozzles manufactured with powder injection molding [137] have been developed for increased reproducibility of the liquid capillary alignment. Despite their successful use in many XFEL experiments, GDVNs are still mostly assembled manually and require skilled technicians for reliable functioning.

3.3.2. Microfabricated injectors

In an effort to simplify and automate fabrication, several microfabrication methods for GDVN construction have emerged. For instance, soft lithography was utilized to construct a multilayer polydimethylsiloxane (PDMS) nozzle[138]. The device operates both in vacuum and in ambient pressure, and liquid flow rates are similar to the glass GDVNs, operating between 2 and 8 µL/min, with jet diameters that can extend into the sub-micrometer range. Microfluidics with PDMS has been extensively explored [139, 140], and this fabrication technique has the potential to be coupled to a myriad of microfluidic techniques such as hydrodynamic mixing. However, the elastomer material PDMS may break down or show leaking effects at the high pressures required for GDVN injections at XFEL facilities.

For further fabrication automation, 3D-printed nozzles have been developed [47, 90]. The first custom nozzle designs were realized by computer-aided design (CAD) software in combination with 3D-printing based on the process of two-photon polymerization of a specific resin. Additionally, the nozzles have been utilized at the EuXFEL as the high jet velocities (50–100 m/s) permit sample to be refreshed in the 0.9 µs between pulses within a pulse train (10 Hz) [47]. Even at these velocities, sample consumption can be as low as 13 µL/min depending on nozzle geometry and gas flow rates [47], although between the pulse trains much sample is wasted. Further development was reported by Bohne et al. where 3D-printed nozzles were printed onto a silicon-glass microfluidic device for reduced complexity during assembly, increased repeatability, and interfacing well to the existing on-chip microfluidic applications such as microfluidic mixers and microfilters [141]. This 3D-printing approach eases the layered construction and planar constraints of photolithography; however, the requirements of the printed device geometry require high-resolution

3D-printers, which can currently only be accomplished through two-photon polymerization.

3.3.3. Mix and react injectors

Mixing for time-resolved mix and inject serial crystallography (MISC) is of great interest as the focus of crystallography with XFELs shifts from static structures to dynamic structures of reaction intermediates. MISC experiments have been explored with fused silica GDVNs and an upstream commercial T-junction for mixing and studying reactions on the minute [33] to second time scale [48]. In the former, a ligand binding to a riboswitch RNA is observed with four different structures over the course of the reaction points, including a reaction intermediate, and in the latter studies, the conformational changes that occur when ß-lactamase reacts with the antibiotic ceftriaxone. To reach shorter time points in the millisecond range, MISC injectors with a microfluidic hydrodynamic focusing mixer built into the nozzle have been developed [40]. Here, an inner capillary is aligned coaxially within another liquid capillary. The most central capillary contains the crystal suspension, the outer liquid capillary contains a solution to react with the protein crystals, and a final outermost capillary supplies the focusing gas. More recently, a MISC device with the hydrodynamic focusing mixer at a short distance before the injection nozzle was developed [49] (Figure 3.2e, f). The construction of these MISC devices requires access to laser cutting hardware for crafting the device components as well as technical skill for precise manual assembly. Based on the flow rates of the central and focusing liquid as well as the distance from the mixing region to the nozzle aperture, which is tunable during device construction, the reaction time can be adjusted from milliseconds to seconds. This MISC device was utilized at SLAC to mix ß-lactamase with ceftriaxone to study reaction intermediates from 30 ms–2 s [50].

Recently, a MISC method was described that utilized an upstream 3D-printed hydrodynamic mixer coupled to a glass GDVN by a fused silica capillary to study the PR-intermediate during the catalytic oxidation of cytochrome c oxidase [57]. A time point of 8 s was achieved with a long delay line between the mixer and nozzle. The automation of 3D-printing decreases the variability between devices, and a decreased length between the mixer and nozzle will enable reaction time points on the millisecond time scale.

3.3.4. Other approaches

To maintain a stable jet with lower flow rates, a double flow focusing nozzle (DFFN) has been developed that uses a coaxially flowing liquid to accelerate the flow of the inner crystal-containing liquid, both of which are subsequently accelerated by gas focusing to create a jet [131] (Figure 3.2c, d). Since the flow rate of the central liquid can be lower than the outer sheath liquid, a thin crystal-containing jet forms within the sheath jet. Due to the reduced volume of the crystal suspension matrix, background scattering can be reduced. Furthermore, the outer sheath liquid has a lower surface tension than the protein crystal suspension; this injection method has increased stability in comparison to injecting the crystal suspension only. Perhaps the greatest benefit of this injection method is the reduced crystal sample flow rate as one of the major drawbacks for GDVNs is the continuous sample injection between X-ray pulses which leads to a majority of the injected sample being wasted. The central sample stream of the DFFN can operate at ~ 5 µL/min, effectively reducing the sample waste by about half.

3.4. Pulsed injection

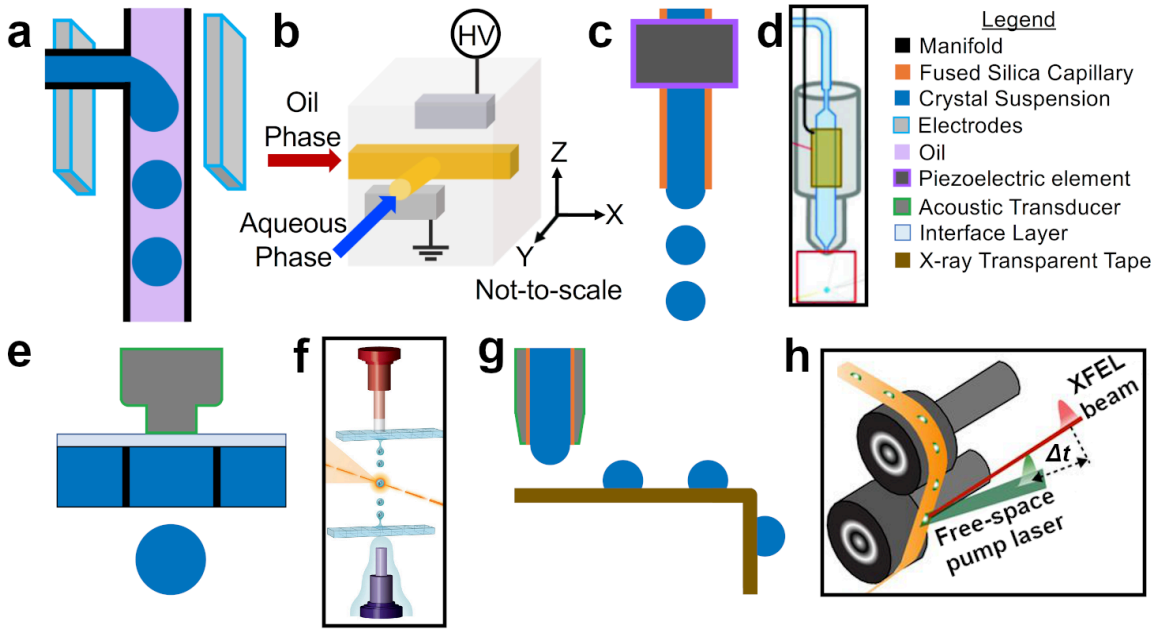

Figure 3.3 (a) Schematic of droplet generation and (b) 3D layout of the geometry for the electrically triggered microfluidic droplet generator. Adapted from Kim et al. [105]. (c, d) Schematics of the piezoelectrically actuated droplet injector. Adapted and reproduced from Mafune et al. [142] with permission of the International Union of Crystallography. e Schematics of an acoustic droplet ejection (ADE) injector. (f) Schematic illustrating ADE injection from below and above the sample well. Adapted and reprinted from Roessler et al. [143]. (g, h) Schematics of ADE combined with droplets on tape (DOT) for sample delivery. Adapted and reprinted by permission from Fuller et al. [144].

3.4.1. Segment flow droplet injection

The five currently active hard XFEL beamlines—SLAC, SACLA, PAL-XFEL, SwissFEL, and EuXFEL—utilize a pulsed structure to deliver X-rays. As mentioned above, for continuously flowing sample from GDVNs, there is considerable sample waste between X-ray pulses. Depending on the pulse structure of the beamline and the flow rate of the liquid, this can result in > 99% of protein crystals being unseen by the X-rays and therefore not provide diffraction information. Indeed, it has been estimated that 1 out of 10,000 crystals injected using a traditional GDVN results in a diffraction pattern [26]. Given the complexity of protein purification and crystallization,

this leads to one of the most severe limitations of SFX with XFELs and has therefore been addressed by several groups. Thus, a way to pulse the injection method such that a sample is present during an X-ray pulse and absent when the laser is "off" is highly desirable.

One method of pulsed injection utilizes a microfluidic droplet generator upstream of the GDVN to segment the aqueous crystal suspension with an oil carrier phase [71]. By varying the liquid flow rates, the frequency of the generated water-in-oil style droplets can be controlled to match the frequency of the XFEL to reduce the amount of sample between droplets (Figure 3.3a). The main challenge moving forward will be synchronizing the phase of the droplets with that of the X-ray pulses or pulse trains. To this aim, a 3D-printed droplet generator with built-in electrodes has been developed [105], see Figure 3.3b. This device allows droplet generation which can be electrically triggered in a drop-on-demand mode (one trigger pulse yields one droplet generated), a phase shift mode (to shift the phase of the droplet generation while maintaining the frequency), or an acceleration mode (to increase the frequency of the droplet generation). The first and second modes can be used to synchronize sample droplets with the phase of the XFEL pulses to further optimize sample introduction.

3.4.2. Piezoelectric droplet ejection

Instead of continuously injected segmented flow, approaches including piezoelectric elements have demonstrated drop-on-demand ejection into the X-ray beam [142]. The crystal suspension is pressure driven such that a meniscus of the sample is primed to be ejected when agitated by the piezoelectric element that is triggered by an electric pulse generator at the frequency and phase of the XFEL (Figure 3.3c, d). This has been demonstrated with a repetition rate of 30 Hz and a crystal suspension of

lysozyme crystals in a helium environment [142]. Considerable savings in sample amount (1–2 orders of magnitude) can be accomplished using this droplet injection method and it has been applied for crystallographic studies on lysozyme [142] and bacteriorhodopsin [145]. The droplet diameter of ~ 80 μm is large in comparison to typical GDVN jet diameters (< 10 μm), which can result in higher background scattering, and this method may have difficulties with ice formation in vacuum. However, a study comparing the piezo-electrically pulsed droplet injection to GDVN injection found that there was no significant difference in the limiting diffraction resolution when studying a photochromic fluorescent protein [134].

3.4.3. Acoustic droplet ejection (ADE)

Similar to the previous method, crystal suspension in ambient pressure conditions can be acoustically ejected as a droplet from a well plate into the path of the X-ray [143] (Figure 3.3e, f). The acoustic pulse is synchronized to the X-ray frequency, resulting in a high droplet hit rate (here defined as the number of droplets hit divided by the total number of X-ray pulses) of up to 88% and up to two orders of magnitude less volume of protein crystal suspension required to solve a complete electron density structure. The main benefit is the reduction in protein crystal consumption: on average, for every two crystals injected, one diffraction pattern is recorded which corresponds to a crystal hit ratio up to 50% (defined as the number of images containing Bragg peaks from crystals per droplet probed). In ADE, the crystal hit ratio is still determined by the crystal density, although the concentration can be increased by allowing the crystals to settle in the meniscus of a droplet and ejecting the droplets downward. However, if the crystal density is too high, clogging can occur caused by insufficient acoustic forces to eject a droplet, therefore care must be taken to balance high crystal hit ratios with effective droplet ejection.

Additionally, by adjusting the acoustic frequency, the droplet size can be tuned, and this method works for crystal suspensions in a range of buffer compositions and viscosities [143]. While ADE works for crystals as small as 5 μm, it is optimized for larger crystals (>50 μm) as the ejected droplet has a large diameter (~60–170 μm) that yields higher background scattering than the thin jets of a GDVN.

3.4.4. Droplet on tape

An X-ray transparent conveyor belt can be coupled with ADE to make a DOT method of delivering crystals to the XFEL [144]. The droplets are deposited onto the conveyor belt tape on which they are transported into the path of the X-ray (Figure 3.3g). Droplet synchronization with the XFEL and any upstream time-resolved excitation periphery is accomplished with a complex combination of the conveyor belt tape speed, the ADE trigger (attained from the XFEL master clock), and micromanipulation of upstream optical fibers aided by inline cameras (Supplemental Information of Fuller, F. D. et al. [144]). Indeed, the setup of the DOT method is non-trivial and required three experts to devote 5 days toward DOT assembly and optimization (Supplemental Information of Fuller, F. D. et al. [144]). The X-ray beam itself is parallel to the tape, thereby intersecting the crystal-containing droplet without damaging the tape (Figure 3.3h). After a cleaning step, the tape is recycled allowing this method to work continuously for long periods of time. With an X-ray frequency of 10 Hz, DOT has demonstrated up to 100% droplet hit rate [144], with the crystal hit ratio still dependent on crystal concentration in the droplet. Droplet delivery of up to 60 Hz has been demonstrated for X-ray emission spectroscopy (XES) at an XFEL [144] and can extend up to 120 Hz. On the way to the beam, the droplets can be photoactivated by a series of optical pump probe lasers, and based on the tape velocity, a TR-SFX experiment can be performed. For example, the

structural changes for the various intermediate states of photosystem II (PSII) after photoexcitation were observed [146]. Instead of a pump probe setup, a gas chamber can be installed for chemically triggered reactions such as oxygen reacting with ribonucleotide reductase R2. The reaction time points capable of being probed with this method range from hundreds of milliseconds to seconds [144]; however, the time resolution may not be suitable for fast reactions and is currently limited to gaseous reactants.

3.5. Electrospinning

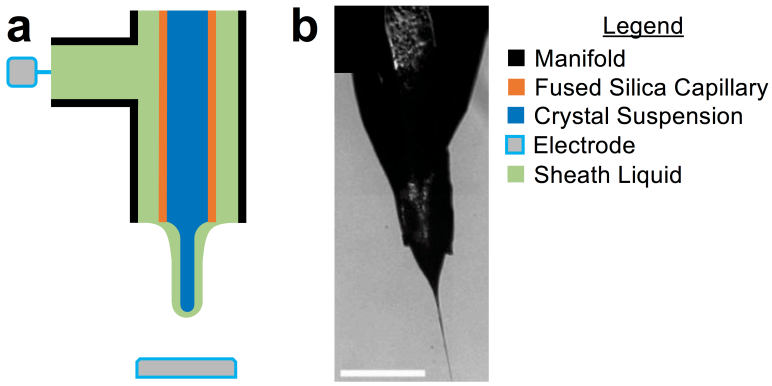

Figure 3.4 (a) Schematic of the CoMESH injector and (b) an optical microscopy image of injected PSII crystals. Adapted and reprinted by permission from Sierra et al. [147]. Scale bar is 360 μm.

3.5.1. Microfluidic electrokinetic sample holder

By applying a potential between a liquid and an electrode, a liquid stream can become a liquid jet in a process called electrospinning [148]. The neck of the jet is similar to the jet produced by the GDVN and can be used as a continuous injection method for SFX [149]. The microfluidic electrokinetic sample holder (MESH) injector [149] is gentle on the crystals as there is no traditional Rayleigh nozzle, and the capillary delivering the crystals can be larger than those found in a GDVN which sidesteps the

need for crystal filtering. The original design for the MESH injector required the crystal suspension to include glycerol in order to extend the neck of the jet and decrease the likelihood of dehydration and freezing after the liquid has exited the orifice. While a benefit is that glycerol would decrease the speed at which crystals settled in a reservoir, the drawback is that not all crystals remain stable when mixed with glycerol.

3.5.2. Concentric MESH

In order to solve this problem, a concentric MESH (CoMESH) injector was developed [147]. Operating off the same principle as the MESH injector, the CoMESH has a capillary containing a sheath liquid that concentrically surrounds the capillary containing the crystal suspension (Figure 3.4). This sheath liquid contains components such as 2-methyl-2,4-pentanediol to prevent dehydration and freezing due to the vacuum environment. In this way, the crystals can stay in the preferred mother liquor while a jet is maintained due to the stability of the sheath liquid. Additionally, since the sheath liquid only comes in contact with the crystal suspension immediately before jetting, not enough time is present for the sheath liquid to destabilize the crystals. A potential of up to 5000 V is applied to generate a jet, and the flow rates required for jetting (0.8–3.0 μL/min) are about an order of magnitude smaller than jetting with a GDVN.

The CoMESH has been used to study both static structures and time-resolved structures at XFEL facilities. The structure of a bacterial 30S ribosomal subunit was determined with SFX with electrospinning injection and subsequently compared to the structure obtained by cryo-crystallography [150, 151]. In the same study [151], the structures of several aminoglycosides bound to the ribosome were determined, and the effect of temperature on the protein structures was revealed. For photoactivated

TR-SFX with MESH injection, the Mn4CaO5 cluster in PSII was studied by simultaneous X-ray diffraction with an XFEL and XES with an optical laser [152]. Photoactivated TR-SFX of PSII injected by electrospinning (this time using the CoMESH) was later revisited to further study the production of oxygen [146]. High-resolution structures for the dark state and one of the photoexcited states were obtained.

3.6. Viscous media injection

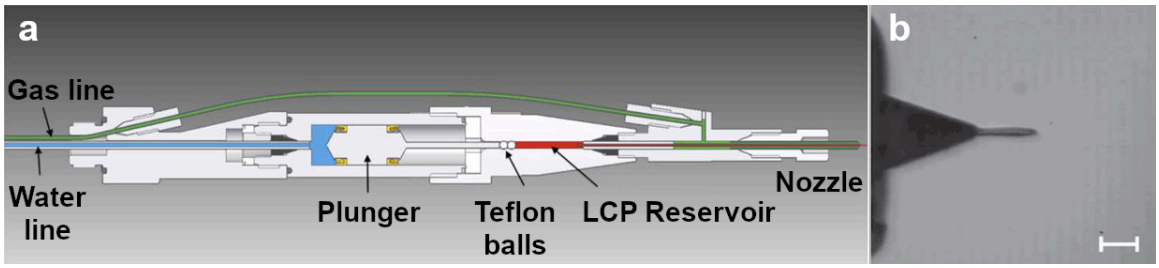

Figure 3.5 (a) Schematic of the LCP injector and (b) optical microscopy image of a jet of 9.9 MAG LCP in vacuum. Both (a) and (b) are adapted and reprinted by permission from Weierstall et al. [26]. Scale bar is 100 μm.

3.6.1. Lipidic cubic phase

For a typical GDVN, the vast majority of the injected sample volume is unseen by the X-ray and is wasted [26]. Therefore, another route for reducing sample consumption is to decrease the flow rate of the jet, and consequently the jet velocity, so that less sample is injected between pulses. To reduce the liquid flow rate below what has been demonstrated with a DFFN and electrospinning, high-viscosity crystal-containing media that maintain a jet-like extrusion even at sub-μL/min flow rates have been explored. One of the most widely applied high-viscosity crystal media is lipidic cubic phase (LCP), which is especially useful for membrane proteins: LCP can mimic the lipid bilayer in which the proteins are natively embedded, and some

proteins can also be crystallized in LCP and remain in their natural crystallization environment during X-ray diffraction as successfully demonstrated by Cherezov and coworkers for various membrane proteins [153, 154]. Furthermore, the crystals grown in LCP are typically microcrystals that are well suited for SFX with XFELs, and the high viscosity prevents crystal settling in the reservoir, avoiding the need for an anti-settling device. One of the most noteworthy successes of SFX using LCP has been the structure determination of G protein-coupled receptors (GPCRs), proteins that are vital for regulating many biological processes in humans, which were challenging to study with third-generation synchrotron sources due to their dynamic nature that leads to complex crystallization and stabilization conditions [155, 156]. Of particular note, SFX with LCP has been used to obtain higher resolution structures than previous synchrotron diffraction experiments, and novel GPCR structures have been solved with de novo phasing methods [155, 156]. It should be noted that the composition of the LCP is crucial as the transition to any other phase, such as to the lamellar phase must be avoided to protect the detector from too strong diffraction [26]. In addition, the high viscosity of the LCP will typically rapidly clog the GDVN and thus requires specialized injectors.

To overcome this limitation, Weierstall et al. [26] developed an injector which extrudes the viscous LCP at a pressure between 2000 and 10,000 psi, therefore requiring a modification to the sample reservoir. Water pressurized through an HPLC pump exerts a force on a large steel plunger that is connected by a narrow rod to two Teflon balls present before the LCP in the reservoir (Figure 3.5). In this way, the applied pressure is amplified by a factor of 34, so lower upstream pressures can be utilized to extrude the LCP. The sample reservoir is built into the LCP injector and is located immediately before the nozzle. The extruded LCP is stabilized by a focusing gas, typically nitrogen or helium, and the flow rate of the LCP is chosen to match the

frequency of the XFEL so that new sample is refreshed between X-ray pulses and excess sample injected is minimized. Ultimately, LCP injection can result in up to two orders of magnitude less protein used than with typical GDVN injection to acquire the same amount of data. A drawback of using this method is the large jet diameter (~ 50 μm) in comparison to the GDVN (< 10 μm) which increases the background scattering and complicates data analysis.

3.6.2. Alternative high viscosity media

As not all proteins grow into crystals in LCP, other viscous media have been explored. By mixing crystals in their mother liquor with a grease matrix, the crystals stay within media sustaining their integrity while being suspended in the highly viscous grease. The grease mixture can be extruded from a narrow-bore tip (e.g., 110-μm inner diameter) into the XFEL at flow rates as low as 120 nL/min for a 30-Hz X-ray frequency [157]. Using this same method of mixing and extrusion, hyaluronic acid has been used as a water-based viscous medium for protein crystals that are grease-sensitive [158]. Additionally, hyaluronic acid has demonstrated weaker background scattering in comparison to grease methods.

Other media, such as agarose, can also be used with the LCP injector [159]. While grease methods have only been demonstrated in ambient pressure, agarose can be employed as a medium for crystals that are not compatible with LCP and, when mixed with a cryoprotectant like glycerol, can be used to extrude a high viscosity jet at low flow rates in vacuum. An additional benefit is the reduced background scattering with agarose in comparison to LCP or a grease matrix; working in vacuo further reduces background. Conrad et al. obtained a structure of phycocyanin at 2.5 Å with agarose as the viscous medium combined with an LCP injector.[159]

Recently, polyacrylamide has been studied for use as a high-viscosity carrier matrix for protein crystals [160]. When compared to the monoolein in LCP, polyacrylamide shows less maximum background scattering. Both lysozyme and thermolysin crystals were injected using a carrier matrix delivery injector (similar to the LCP injector) at PAL-XFEL, and structures were solved to 1.7 Å and 1.8 Å, respectively [160].

3.6.3. TR-SFX applications for viscous media

The LCP injector has been successfully employed for TR-SFX, with photoactivated proteins as a prime target. The protein crystals extruded in the LCP jet are irradiated by an optical laser just before being intersected by the X-ray beam. For instance, bacteriorhodopsin (bR) can act as a proton pump when triggered by light and has been a key target for TR-SFX in LCP [161, 162]. The time delay between the optical laser pump probe and the X-ray determines the intermediate species of the protein. The time delays can be from the millisecond [161] over nanosecond [162] down to picosecond time range [163], although the sample flow rate must be increased above 5 µL/min for the shorter time delays. The ultimate goal of such time-resolved studies is a "molecular movie," that allows researchers to follow the structural changes upon light excitation.

Similar to LCP, grease has been used for TR-SFX studies at SACLA. Structural changes for PSII on the millisecond time scale were observed out to 2.35 Å using a grease jet extruded from a syringe [164]. Another avenue for pump probe style TR-SFX is using photocaged compounds. Photocaged nitric oxide (NO) was injected in a hydroxyethyl cellulose matrix by an LCP injector, and upon irradiation with UV light, it was released to react with the P450, a protein that catalyzes NO to nitrous oxide, for 20 ms before X-ray exposure [42]. From this, an ambient temperature 2.1 Å structure of the P450nor intermediate was determined.

3.7. Aerosol injection

3.7.1. Aerodynamic Lens stack

As a result of the ultrashort pulses and high brightness of XFELs, another frontier is the ability to obtain diffraction from large single particles, for instance, viruses [125, 165]. A benefit of using non-crystalline samples is that protein samples do not need to be crystallized which eliminates much of the sample preparation required in crystallography with the previously mentioned methods. However, since single particles have very weak diffraction intensity in comparison to crystals, background from a liquid jet would dwarf any signal obtained from the analyte [166]. As such, aerosolized samples are a promising method of sample introduction for non-crystalline samples at XFELs. An aerodynamic lens stack that focuses an aerosol into a thin particle beam has been developed and employed to obtain diffraction at a synchrotron [126]. The diameter of these particle beams can range from hundreds to tens of micrometers. The aerodynamic lens stack was utilized at the atomic, molecular and optics (AMO) end station at LCLS to study carboxysomes [167, 168]. Hit rates (here defined as the number of images containing Bragg peaks per total number of X-ray pulses) were about 79%, and the sample volume used was only 36 µL.

3.7.2. Convergent nozzle aerosol injector

In an effort to minimize both the setup and the diameter of the focused aerosol, a single orifice convergent nozzle aerosol injector (CNAI) was developed [169]. In this case, a GDVN upstream of the convergent nozzle generates an aerosol at ambient pressures, and the geometry of the nozzle accelerates the aerosol particles along convergent gas streamlines as they transverse the orifice into the vacuum chamber.

The result is an aerosol with a sub-ten-micrometer diameter focal point that is several hundred micrometers from the nozzle orifice. This CNAI was utilized at the coherent X-ray imaging (CXI) beamline at LCLS to image granulovirus (200 × 200 × 370 nm^3) surrounded by a crystalline shell [170]. In comparison to liquid jets such as the GDVN, one would expect a decreased hit rate since the particles injected by the CNAI have a velocity ~ 25× greater and have a reduced liquid flow rate. The predicted particle hit rate for the CNAI was 0.04– 0.4%; however, the experimental particle hit rate was substantially lower at 0.006%. Currently, the very low hit rate is a bottleneck for single particle imaging work at XFELs with CNAIs.

3.7.3. Aerosolization by desorption

An innovative method that combines fixed-target with aerosolized injection is desorption by impulsive vibrational excitation (DIVE) with a picosecond IR laser (PIRL) [171]. In this method, crystal sample in solution deposited on a substrate is irradiated by a PIRL and the contents are ejected in a plume upwards into the path of the X-ray. The PIRL is relatively gentle on the crystals, with the crystal diffraction quality essentially unaffected by this injection method. The authors also mention that the sample does not need to have crystals, opening the door for single-particle diffraction if the aerosol has sufficiently low background signal intensity to differentiate the analyte signal.

3.8. Sample delivery for fixed-target experiments

While liquid delivery at XFEL experiments has been the method of choice in the early years, delivery of crystals on a solid support or so-called fixed-target has also been explored recently. Typically, fixed-target crystallographic experiments refer to the case where crystals are loaded on a solid matrix in the path of an X-ray source to

obtain the diffraction data, as shown in Figure 3.1b [21, 56]. These matrices are often microfabricated and micropatterned chips that allow fast and reproducible loading of thousands of crystals in a reproducible manner. This highly efficient method of crystal delivery not only significantly decreases the amount of required sample in comparison with liquid injection methods discussed above (typically a few μL) but can also be readily modified for crystals ranging from sub-micrometer to 100 μm in size. These chips can also be developed to support room and cryo temperature conditions. Furthermore, such microfabricated devices offer spatial control over crystal location and orientation on-chip, and they can be exploited for high-throughput automated serial crystallographic applications using high-speed translation stages at various XFEL and synchrotron beamlines [56, 172]. In the case of XFELs, fixed-target applications offer further potential as high energy femtosecond X-ray pulses can be used to gather diffraction data prior to onset of radiation damage on the crystal [19, 21]. Other than holding crystals, microfluidic devices have also gained immense interest recently for integrated on-chip crystallization and fixed-target applications, eliminating the cumbersome and error-prone process of harvesting crystals from conventional crystallization methods prior to X-ray diffraction. Recently, a number of such microfluidic fixed-target devices have surfaced for both on-chip crystallization and diffraction studies at XFEL sources and are discussed below.

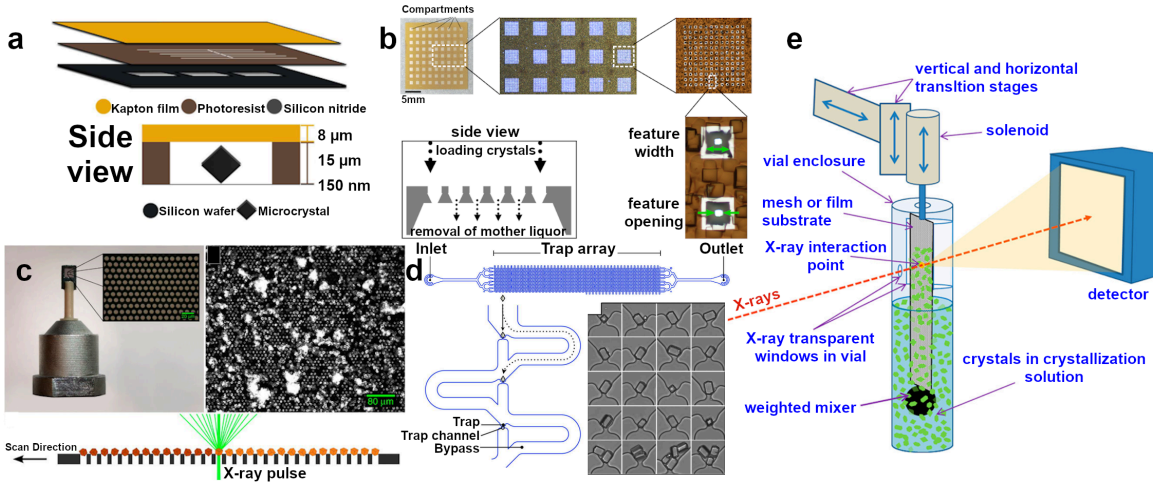

Figure 3.6 Sample delivery for fixed-target diffraction experiments. (a) A schematic of the three-layer microchip crystal holder device fabricated from a silicon wafer, photoresist, and Kapton. Adapted and reprinted with permission from Murray et al. [173]. (b) A Silicon chip with an array of tapered holes for holding crystals to conduct time-resolved crystallographic experiments. Reprinted from Mueller et al. [174] under a CC BY License. (c) A silicon chip with micropores for holding crystals (right) mounted on a "Roadrunner" Goniometer (left) along with crystal scanning strategy for high-speed fixed-target viral crystallography (bottom). Adapted and reprinted with permission from Roedig et al. [175]. (d) A schematic of a PDMS-PMMA microfluidic device with Trap-and-Bypass array for crystal capture with a micrograph of trapped HEWL microcrystals. Adapted and reprinted with permission from Lyubimov et al. [176]. (e) An overview of a fixed-target serial crystallography experiment using a nylon mesh-based crystal extractor positioned through translation stages. Reprinted with permission from Mathews et al. [177].

3.8.1. Silicon micropatterned chips

Silicon-based micropatterned chips and trap arrays, offering low background scattering, have been widely exploited for fixed-target X-ray diffraction studies. Hunter et al. [121] reported an etched silicon nitride membrane chip as a fixed-target solid support for microcrystals of rapid encystment protein (24 kDa, REP24) embedded in Paratone-N for crystallographic studies at LCLS. The device was used to perform SFX at a high resolution of ~ 2.5 Å with an acquisition rate of 10 Hz and a hit rate of ~ 38% (Figure 3.1b). Murray et al. [173] also reported a three-layer microdiffraction device made from silicon nitride, photoresist and polyimide film for studying Hen egg-white lysozyme (HEWL) microcrystals, as shown in Figure 3.6a.

HEWL microcrystals (~ 10–15 μm in size) were used for room temperature X-ray diffraction experiments at the LCLS X-ray Pump Probe (XPP) end station and other synchrotron beamlines. Diffraction experiments were performed using a 3–30 μm unattenuated beam with 40-fs pulses, and microcrystal images were taken manually by focusing on the silicon nitride window present on the chip. Using this chip, a high-resolution (~ 1.5 Å) diffraction data set was reported from 324 diffraction images. Mueller et al. [174] reported another silicon-based crystal holder chip as a fixed-target matrix for room temperature serial crystallographic applications at XFEL and synchrotron sources. The crystal holder chip was microfabricated from a silicon wafer using photolithographic, plasma etching, and wet etching techniques to create a matrix of tapered through holes to filter crystals of 30–60-μm size from their mother liquor prior to fixed-target experiments, as shown in Figure 3.6b. Using this device, crystals of sperm whale myoglobin bound with carbon monoxide (SWMb-CO) were used to conduct time-resolved crystallographic experiments at LCLS. Recently, the same group reported additional improvements to the first-generation chip by combining spectroscopic mapping of crystals prior to X-ray diffraction to achieve an overall hit rate up to 85%, further decreasing the required sample volume [178]. Using this device, SWMb-CO crystals were used to obtain an X-ray diffraction data set with a resolution of ~ 1.3 Å at the XPP end station. Nam et al. [179] reported a silicon nitride membrane-based fixed-target diffraction chip for single-shot imaging of biological and non-biological specimen. The chip was composed of an array of 200 μm × 200 μm windows of 100-nm-thick negatively charged silicon nitride membrane, and monodisperse metallic nanoparticles were either air dried or spin coated on the chip. Employing the same device, RNAi microsponges could be sandwiched between two silicon nitride membranes. These fixed-target diffraction experiments were conducted at SACLA with a 1.5-μm focused beam (10-fs pulses) at 30 Hz.

Recently, Roedig et al. [175] reported a micropatterned silicon chip mounted on a high-speed goniometer—termed the "Roadrunner"—for serial X-ray crystallography at XPP end station. As shown in Figure 3.6c, the silicon chip contained a grid of micropores (size 4–8 μm) to accommodate crystals of picornavirus bovine enterovirus 2 (BEV2) and cytoplasmic polyhedrosis virus type 18 polyhedrin (CPV18). The chip was mounted on the Roadrunner goniometer for high-speed raster scanning at a repetition rate of 120 Hz. Using this high-speed setup, a maximum hit rate of ~10 and ~70% and resolution of 2.3Å and 2.4Å was reported for BEV2 and CPV18 crystals, respectively.

3.8.2. Alternative materials for micropatterned fixed-target chips

Due to the nature of fixed-target X-ray diffraction experiments, there is constant need for microfabrication materials exhibiting high X-ray permeability and low background scattering. Thus, numerous new device fabrication materials (other than micropatterned silicon chips) like PDMS, poly (methyl methacrylate) (PMMA), and cyclic olefin copolymer (COC) have also been explored. Lyubimov et al. [176] reported a microfluidic trap array chip fabricated from PDMS on a PMMA substrate for trapping microcrystals for X-ray diffraction studies. Two types of crystal trapping array designs were explored (weir-type and trap-and-bypass designs). After initial testing, the trap-and-bypass design was chosen for crystal trapping due to its comparatively high trapping efficiency, shown in Figure 3.6d. Using this microcrystal trapping device, HEWL microcrystals were trapped and used for room temperature X-ray diffraction studies at XPP and synchrotron beamlines with resolutions up to 1.8 Å. Mathew et al. [177] recently reported a nylon mesh-based crystal extractor for serial crystallography experiments also at XPP end station. The nylon mesh extractor contained diamond-shaped holes and was dipped in solution of trans-acyltransferase

crystals to extract the crystals prior to X-ray exposure using translation stages, as shown in Figure 3.6e. Out of ~ 23,000 images collected in ~ 40 min, about 2000 images contained sufficient diffraction information (a hit rate of ~ 10%) to obtain a full data set with a resolution of 2.5 Å. Very recently, Górzny et al. [180] proposed a hybrid microfluidic device capable of forming on-chip lipid bilayers to perform fixed-target experiments on membrane proteins in their native state using XFELs. The device integrated etched silicon nitride windows sandwiched between two channels formed by PDMS layers for introducing electrolyte solution and lipids resulting in the formation of a lipid bilayer at silicon nitride windows. The presence of the lipid bilayer was verified using impedance spectroscopy as the measured impedance increased from kΩ to GΩ for empty chip and chip containing lipid bilayer, respectively. Such a conceptual microfluidic device may offer great potential for diffraction experiments on membrane proteins in the future. Additionally, a number of hybrid COC-PDMS devices have been recently reported by several research groups for fixed-target X-ray diffraction experiments at Synchrotron beamlines that may also be modified for XFEL-based diffraction experiments [56, 130, 181, 182].

3.8.3. Chip-less fixed-target

Despite low sample requirements for the aforementioned fixed-target chips, microfabrication of such platforms and crystal loading may still pose some challenges. Thus, some researchers are working on thin film adaptation of fixed-target chips. Very recently, Doak et al. [183] reported a "chip-less" approach for fixed-target crystallization experiments using crystal solution sandwiched between two Mylar sheets (2.5-µm thickness). Microcrystals of carboxyhemoglobin and lysozyme were used for SFX data collection at SACLA using this sheet-on-sheet setup with a hit rate of 10–30% and resolutions down to ~ 2.1 Å. Such "sheet-on-sheet"

platforms may require larger sample volumes as compared to micropatterned chips but are comparatively inexpensive and may eliminate cumbersome microfabrication processes requiring a cleanroom facility as well as challenges with on-chip crystal loading.

3.9. Conclusion and outlook

Due to the many variations in beamline parameters, crystal stability, and experimental design, there has yet to be a catch-all sample delivery method for the exciting field of SFX and TR-SFX with XFELs. Optimization continues for methods such as the GDVN and viscous media injectors that see widespread use and have shown to support exciting new insight into protein structure. Previously inaccessible crystal samples are also being explored with methods such as electrospinning and ADE, and efforts are being conducted in the community to even explore TR-mixing experiments with viscous LCP injectors. With the increased resolution of 3D printers, microfluidics coupled to various injection methods is a rapidly developing frontier. This may eventually allow integration of various functionalities, such as mixers, injectors, and droplet generators, to name a few and greatly facilitate sample delivery for challenging experiments such as TR studies. Advancements in fixed-target devices, requiring low sample volumes and eliminating the crystal harvesting processes, have also paved the path for high-efficiency X-ray diffraction experiments for proteins that are difficult to crystallize in suitable concentrations and volumes. Furthermore, recently explored novel device fabrication materials offering low background scattering and high X-ray transparency may offer high-resolution diffraction data. Such devices can also offer crystal mapping prior to diffraction experiments ensuring high crystal hit rate which is crucial considering the scarcity of protein crystal samples and beamtime availability. While the lack of access to XFEL

facilities remains one of the major bottlenecks, such advancements in sample delivery technology may allow researchers to collect more data with less sample volume in a shorter time in the future.

CHAPTER 4

3D PRINTED DROPLET GENERATION DEVICES FOR SFX ENABLED BY SURFACE COATING

4.1 Abstract

The role of surface wetting properties and their impact on the performance of 3D printed microfluidic droplet generation devices for serial femtosecond crystallography (SFX) are reported. SFX is a novel crystallography method enabling structure determination of proteins at room temperature with atomic resolution using X-ray free-electron lasers (XFELs). In SFX, protein crystals in their mother liquor are delivered and intersected with a pulsed X-ray beam using a liquid jet injector. Owing to the pulsed nature of the X-ray beam, liquid jets tend to waste the vast majority of injected crystals, which this work aims to overcome with the delivery of aqueous protein crystal suspension droplets segmented by an oil phase. For this purpose, 3D printed droplet generators that can be easily customized for a variety of XFEL measurements have been developed. The surface properties, in particular the wetting properties of the resist materials compatible with the employed two-photon printing technology, have so far not been characterized extensively, but are crucial for stable droplet generation. This work investigates experimentally the effectiveness and the long-term stability of three different surface treatments on photoresist films and glass as models for our 3D printed droplet generator and the fused silica capillaries employed in the other fluidic components of an SFX experiment. Finally, the droplet generation performance of an assembly consisting of the 3D printed device and fused silica capillaries is examined. Stable and reproducible droplet

generation was achieved with a fluorinated surface coating which also allowed for robust downstream droplet delivery. Experimental XFEL diffraction data of crystals formed from the large membrane protein complex photosystem I demonstrate the full compatibility of the new injection method with very fragile membrane protein crystals and show that successful droplet generation of crystal-laden aqueous droplets intersected by an oil phase correlates with increased crystal hit rates.

4.2 Introduction

X-ray crystallography is one of the most powerful tools to elucidate protein structures. High-intensity femtosecond X-ray free-electron lasers (XFELs) allow for the investigation of protein structure and dynamics with atomic resolution. Unlike traditional X-ray crystallography where a single protein crystal is rotated and irradiated with X-rays, in serial femtosecond crystallography (SFX) a protein structure is determined by merging thousands of diffraction patterns from individual micro- and nanometer-sized crystals being 'hit' by the XFEL pulses in random orientations[19]. The crystals need to be rapidly replenished because they are destroyed by the XFEL beam in less than a picosecond. A major method to accomplish crystal delivery is by jetting an aqueous suspension of protein crystals across the beam path using a gas dynamic virtual nozzle (GDVN) [138, 184]. Although the femtosecond X-ray pulses of XFELs either have varying repetition rates from 30 Hz up to 120 Hz or arrive in 10 Hz bunch trains with each bunch containing up to 2700 X-ray pulses [166, 185], every XFEL beamline has a common problem: crystals injected between pulses or bunch trains are not irradiated and are therefore wasted. The sample cannot be recycled as the radicals formed by the XFEL beam exposure spread the damage in the solution. Large protein amounts, up to milliliters of protein crystal suspension, or tens of milligrams to grams of protein, are then required to

obtain a complete data set [14]. Methods for producing and crystallizing proteins in such large amounts are highly resource and time intensive and can be a serious limiting factor for protein crystallography with XFELs. Thus, methods for reducing protein crystal waste in serial femtosecond crystallography are of the utmost importance. Examples of sample-introduction methods with reduced sample consumption [14, 130] are viscous media injection [132, 157-159], electrospinning with a microfluidic electrokinetic sample holder injector [147], double flow-focusing nozzles [131], acoustic droplet ejection [142, 143], droplet on tape [144] and fixed target [121, 173-177, 186]. In addition, recirculating jets that recycle the injected sample have been developed and employed at the Linac Coherent Light Source (LCLS) [187] and the SPring-8 Ångstrom Compact Free Electron Laser (SACLA) [188, 189]. However, the recirculating jet setup at LCLS is not designed for experiments under vacuum, and jet diameters are typically ≥20 μm, both contributing to higher background scattering than non-recirculating jets under vacuum. Furthermore, SACLA requires a minimum sample volume of 5 mL in order to use the recirculating jet, a volume which can be prohibitive for samples that are difficult to crystallize in large volumes. The exposure to the XFEL beam also leads to ionization and radical formation, inducing damage in the recycled sample even if the protein crystals have not been exposed to a laser pulse. Such radiation damage defers the goal of SFX for near-damage-free X-ray diffraction collection from protein crystals at room temperature such as metal proteins like photosystem I (PSI), but recycling jets may still be applied for radiation-hard samples.

Microfluidic devices have been explored in traditional crystallography applications typically coupled with synchrotron irradiation [69, 172, 190], and also in crystallography with XFELs including microfabricated liquid jet injectors [135, 138], crystal sorters [191] and time-resolved crystallography with microfluidic mixers [49]. We have recently proposed using water-in-oil microfluidic droplets to reduce the protein crystal suspension

volume for SFX with XFELs [71]. For droplet generation we fabricated a device using two-photon polymerization 3D printing. This approach involves a polymerization reaction initiated by near-infrared femtosecond laser pulses focused into a photosensitive material volume, followed by the removal of non-photopolymerized material, with advantages including micrometer resolution, availability of transparent photoresists and fast design modification [88, 192]. This 3D printing approach has been utilized to develop nozzles for SFX sample delivery [47, 90, 141]. Although droplets can be generated using devices with different geometries, we have focused on a T-junction geometry because of its simplicity and well characterized droplet formation physical parameters [58, 60, 68, 103, 193-197]. In T-junction droplet generators, the continuous-phase channel orthogonally intersects the dispersed-phase channel, and the resulting droplets proceed down the continuous-phase channel outlet [197].

Generation of multiphase flows in XFEL experiments poses unique challenges unlike those in droplet generation in microfluidic devices at low pressure. Firstly, the sample is placed in a reservoir which frequently requires a few meters of liquid lines to connect to the GDVN. This connection is established through fused silica capillaries with small inner diameters (50–100 μm) and is required for accommodating protein crystal suspension anti-settling devices necessary to avoid clogging. Therefore, fluidic resistance is high, and pressures comparable to those typical in high performance liquid chromatography (HPLC) are usually required for the crystal suspension injection. Polyether ether ketone (PEEK) devices withstand high operating pressures and have been used for droplet generation with controlled droplet frequency by adjusting the flow rate ratios of the two phases employed for droplet generation, from hundreds of microliters to milliliters per minute [102, 198]. However, because of their relatively large internal diameters they do not allow for adjustment of droplet volumes and frequencies within the much lower flow rates typical for SFX

(tens of microliters down to hundreds of nanoliters per minute), as we noted in preliminary tests. In addition, PEEK devices are not transparent and do not allow visual monitoring of the droplet generation.

Second, wetting properties are crucial for reproducible and long-term droplet generation in an SFX experiment and have not been fully investigated. An ideal coating should render hydrophobic both the 3D printed photoresist droplet generator and the upstream and downstream fused silica capillary surfaces. Also, it is highly desirable to collect diffraction data uninterruptedly for typically 6–12 h over the course of one shift at the XFEL beamline. Surface coatings should therefore be stable over long periods at flow rates of tens of microliters per minute.

A huge variety of coating methods on photoresists and glass have been developed, addressing surface composition, chemical functionality, wettability, charge, porosity/roughness and coating durability, including coating methods to impart specific wetting properties in microfluidic droplet generation devices [88, 199]. Droplet formation occurs when the drag force, with a minor contribution from inertia, overcomes the interfacial tension. However, coating the inner surface of an SFX device assembly consisting of a 3D printed droplet generator with internal dimensions of a few tens of micrometers connected to several meters-long fused silica capillaries with internal diameters between 50 and 100 µm can be extremely challenging and time consuming. Chemical approaches for surface modification such as self-assembled monolayers [200] and gas-phase silanization methods [200, 201] typically require an activation step [200, 201], e.g. acid or plasma treatment, for rendering desired surface chemical functionality prior to the linking reaction. Silanization under a vapor environment in addition involves a relatively complicated setup [201] (e.g. vacuum and ventilation system) and protocol. Fluorophilic surface coatings in cyclic olefin copolymer microfluidic devices for fixed-target crystallography were achieved using a

simple protocol [202]. All these surface coating methods, while effective for microfluidic devices with dimensions of a few millimeters, would be highly impractical to use with our device assemblies, which include a glass nozzle, meters of silica capillaries and the 3D printed droplet generator device, and too cumbersome to perform if needed during beamtime experiments. Therefore, we explored simpler physical adsorptive coatings and tested them on various surfaces, including photoresists used in two-photon polymerization 3D printing approaches as well as on glass surfaces [47, 90, 203-205].

We have addressed challenges in droplet generation for SFX by developing a 3D printed microfluidic droplet generator with a size <2 mm in every dimension, which can withstand high pressures (up to approximately 2500 psi; 1 psi = 6.89 kPa), is transparent and can be rapidly prototyped. In addition, our device is compatible with both low and high X-ray pulse frequencies (from 10 to 120 Hz), supports micro- to nano-sized crystals, does not ionize the protein crystal, and is suitable for time-resolved serial crystallography. Here we investigate different adsorptive surface coatings that can produce and maintain stable droplet streams for several hours under high pressure in device assemblies for droplet generation in SFX experiments and assess the ability to collect XFEL diffraction data from droplets of PSI protein crystal suspensions.

4.3. Materials and methods

4.3.1. Reagents and materials

Silicon wafers (p-type ⟨100⟩, 4 inches) were obtained from University Wafer, USA. Glass slides (76 x 25 x 1 mm) were purchased from Fisher Scientific, USA. The negative photoresist SU-8 2007 for surface coating and SU-8 developer were purchased from Microchem, USA. The ultraviolet sensitive photoresist (IP-S) was

purchased from Nanoscribe GmbH, Germany. (Tridecafluoro-1,1,2,2-tetrahydrooctyl) dimethylchlorosilane (TDTS) was purchased from Gelest Corp., USA. Novec 1720 electronic grade was a generous gift from 3M, USA. Aculon AL-B was purchased from Aculon Inc., USA. Ethanol, acetone, potassium chloride, magnesium sulfate, Tris base, 2-(*N*-morpholino)ethanesulfonic acid (MES), β-mercaptoethanol, poly(ethylene glycol) methyl ether (mPEG, MW = 5000 amu), perfluorodecalin (PFD) and 1H,1H,2H,2H-perfluoro-1-octanol (perfluorooctanol, PFO) were purchased from Sigma–Aldrich, USA. *n*-Dodecyl-β-maltopyranoside was purchased from Glycon, Germany. Deionized water (18 MΩ) was supplied from a Synergy purification system (Millipore, USA). Fused silica capillaries (360 μm outer diameter, 100 μm inner diameter and 50 μm inner diameter) were purchased from Molex, USA. Hardman extra-fast setting epoxy was purchased from All-Spec, USA.

4.3.2. Preparation of photoresist film model surfaces

Silicon wafers and glass slides were sonicated in isopropanol and acetone for 5 min and immediately rinsed thoroughly with deionized water and dried with a stream of nitrogen gas before the surface coating. A previously described SU-8 coating method was used [206]. In brief, an Si wafer was spin-coated at 1000 r min^{-1} with a Laurell spinner (WS-650–8, Laurell, USA) for 30 s by dispensing 3 mL of negative photoresist SU-8, UV-exposed for 30 s (350 W, 10.32 mW cm^{-2}, HTG Mask Aligner, JM Industries, USA) and developed in a developer bath. The thickness of the SU-8 film was 12 μm as measured by a profilometer (Dektak II, USA). The IP-S photoresist was spin-coated at 1000 r min^{-1} for 60 s on a silicon wafer and then cured by a high-power UV (365 nm) curing LED system (CS2010, Thorlabs, USA) under an inert N2 atmosphere. The thickness of the IP-S layer on the Si wafer was 62 μm as measured by the Dektak profilometer.

4.3.3. Hydrophobic coatings on photoresists and glass

SU-8 or IP-S films on silicon wafers and bare glass slides were coated with hydrophobic agents as follows. The surfaces were rinsed with deionized water and dried with a stream of nitrogen gas and placed in glass Petri dishes. A volume of 200 µL of either Novec 1720 or Aculon AL-B was placed on the substrate and allowed to evaporate at room temperature. Subsequently, the substrates were baked in an oven at 423 K for 30 min. For the surface coating with a fluorinated silane, gas-phase deposition of TDTS was performed in a desiccator connected to a vacuum source by evaporating 40 µL of TDTS in an incubator with SU-8 and IP-S substrates. A vacuum was applied for 1 min then turned off and the TDTS was allowed to deposit for 30 min.

4.3.4. Contact angle measurement

All substrates were rinsed with deionized water and dried with compressed air or nitrogen gas before measurement. Contact angles were measured with a goniometer (drop shape analyzer DSA25, Kruss, Germany) under ambient conditions. To measure the static water contact angle, a sessile drop (2 µL) of deionized water was dispensed onto bare and treated photoresist films and glass slides, and a side image was captured with the camera when the droplet was stabilized on the substrate. Three different samples for each material and surface treatment were measured.

4.3.5. Stability of hydrophobic coatings

To explore the long-term coating stability we measured the contact angles on Novec 1720-treated SU-8, IP-S and glass slides before and after immersion in either a mixture of PFD:PFO (10:1 *v:v*%) oil for up to 24 h or ethanol or deionized water for

up to 16 h. In addition, the contact angles of the Novec-treated samples were measured before and after immersion in deionized water in an ultrasonic bath (JP-031B 180W, 40KHz, 6.5L, USA) for 3, 10 and 30min at room temperature followed by drying under pressurized N_2 gas.

4.3.6. 3D printed devices for droplet generation

Devices were designed in AutoCAD (AutoDesk, USA) and imported into the DeScribe software of the Nanoscribe GT instrument (Nanoscribe GmbH, Germany). A drop of IP-S was deposited onto a clean indium tin oxide-coated boroaluminosilicate glass slide. The 3D structure was printed on the glass slide upon the two-photon polymerization of IP-S. The structure was printed using the standard Meso Scale protocol: IP-S 25x solid (ITO) recipe, with 100 000 μm s^{-1} scan speed, 100% laser power, 0.9 power scaling, 1 μm slice distance and 0.5 μm hatch distance. Printing was complete after 4–7 h depending on the device version. After printing, the device was developed by one or more cycles of a 40 min sonication in SU-8 developer followed by an isopropyl alcohol rinse until development completion was determined by visual inspection using an optical microscope. After development, the dry 3D printed device was immobilized on a glass slide with tape, and 360 μm outer diameter fused silica capillaries with polished flat ends were inserted into the two inlets and the outlet of the device. The diameters of the two inlet and the outlet ports were 370 μm. Fused silica capillaries were permanently affixed to the device with fast-curing epoxy for high-pressure operation.

4.3.7. T-junction and capillary coating with Novec 1720

For hydrophobic surface treatment, Novec 1720, as provided by the manufacturer, was slowly injected into one of the T-junction assembled capillaries using a

disposable syringe and fittings (P-629, F-300, F-142N and F-262) (IDEX-HS, USA) until it could be seen exiting the other two fused silica capillary ends. The entire Novec-filled assembled device was placed in a ventilated oven at 423 K overnight to allow for vaporization of any excess solvent.

4.3.8. Droplet generation and monitoring

The oil-phase mixture was PFD:PFO (10:1 *v:v*%). The aqueous phase was either water, mPEG buffer (82 mM potassium chloride, 14 mM Tris base pH = 7.3, 1.4 mM β-mercaptoethanol and 7% mPEG, used as mother liquor for the protein of interest for SFX studies) or low ionic strength PSI buffer [5 mM MES pH = 6.4 and 0.02%(*w/v*) *n*-dodecyl-β-maltopyranoside] for delivery of PSI crystals. In the X-ray diffraction experiments the aqueous phase was a suspension of 1–5 μm PSI protein microcrystals prepared as described previously [19, 117, 207], and the aqueous phase reservoir was mounted on a custom-made device that slowly oscillates to prevent microcrystals from settling while keeping the crystal suspension at 277 K [133]. The aqueous and oil phases were each driven by an HPLC pump (LC-20AD, Shimadzu, Japan) operating in constant-flow-rate mode into a custom-made stainless-steel syringe-like reservoir[133]. The reservoirs were connected to the 3D printed T-junction microfluidic droplet generator by fused silica capillaries. Oil-phase flow rates (Q_{oil}) ranged from 6 to 45 μL min^{-1}, and aqueous-phase flow rates ($Q_{aqueous}$) from 0.5 to 20 μL min^{-1}. The outlet capillary was mounted in a droplet detector about 30 cm downstream of the droplet generator, and about 20 cm further downstream was connected to the GDVN inlet liquid capillary. For preliminary studies at the laboratories at Arizona State University prior to the first experiments at the Linac Coherent Light Source (LCLS) at SLAC National Accelerator Laboratory, the T-junction droplet generation was imaged by immobilizing the 3D printed device onto a

glass slide with tape and using an inverted microscope (IX71, Olympus, USA) in bright-field imaging mode in conjunction with a high-speed camera (FASTCAM SA4, Photron, Japan). The droplet detector was used to monitor the frequency of the droplets in real time in the fused silica capillary and consisted of a 1550 nm laser diode and a photodetector connected to an oscilloscope, which detected a signal based on the difference in transmittance between the oil and the aqueous phase.

4.3.9. X-ray diffraction

The SFX experiments were carried out at the macromolecular femtosecond crystallography (MFX) instrument at LCLS (proposal ID: LQ70) at an X-ray energy of 9.5 keV with 40 fs pulse duration at a pulse rate of 120 Hz [208]. The X-ray diffraction experiments were carried out at ambient pressure in a helium atmosphere to reduce background scattering from air. The X-ray diffraction data were recorded using a Rayonix MX170-HS detector in the 2 x 2 binning mode, leading to 1920 x 1920 pixels, each 89 x 89 µm. In this mode, the rate of data collection was detector-limited to 10 Hz. For online data collection monitoring and live real-time crystal hit rates, we used *OnDA* [209]. Further analysis was performed on a single experimental run where we observed droplet generation as detected by the above-mentioned droplet detector during beamtime. The images were preprocessed to detect the crystal hits using *Cheetah* [122]. To identify when aqueous-phase droplets formed, based on the X-ray scattering, we used radial profiles calculated from each 2D image to distinguish the aqueous-phase scattering from the largely different oil-phase scattering. The radial profiles from oil-only and water/aqueous-buffer-only data were calculated and used for estimating volume fractions of oil and water in each PSI diffraction image (where volume fraction of water + volume fraction of oil = 1.0). Volume fractions [210] were estimated using a linear combination of oil and water

scattering profiles with custom Python scripts. Images were sorted by increasing fractions of water and the crystal hit rate was calculated by binning the sorted images into groups of 100 images.

4.4. Results and discussion

The wetting properties of the channels are crucial for the quality and reproducibility of droplet generation. For producing water-in-oil droplets, the device walls need to be hydrophobic, whereas oil-in-water droplets require hydrophilic channels [59, 93, 211]. Since the wetting properties of the employed Nanoscribe proprietary photoresist have not been studied in detail, we investigated the effect of different hydrophobic surface treatments on 3D printed device assemblies with regards to droplet generation performance in SFX.

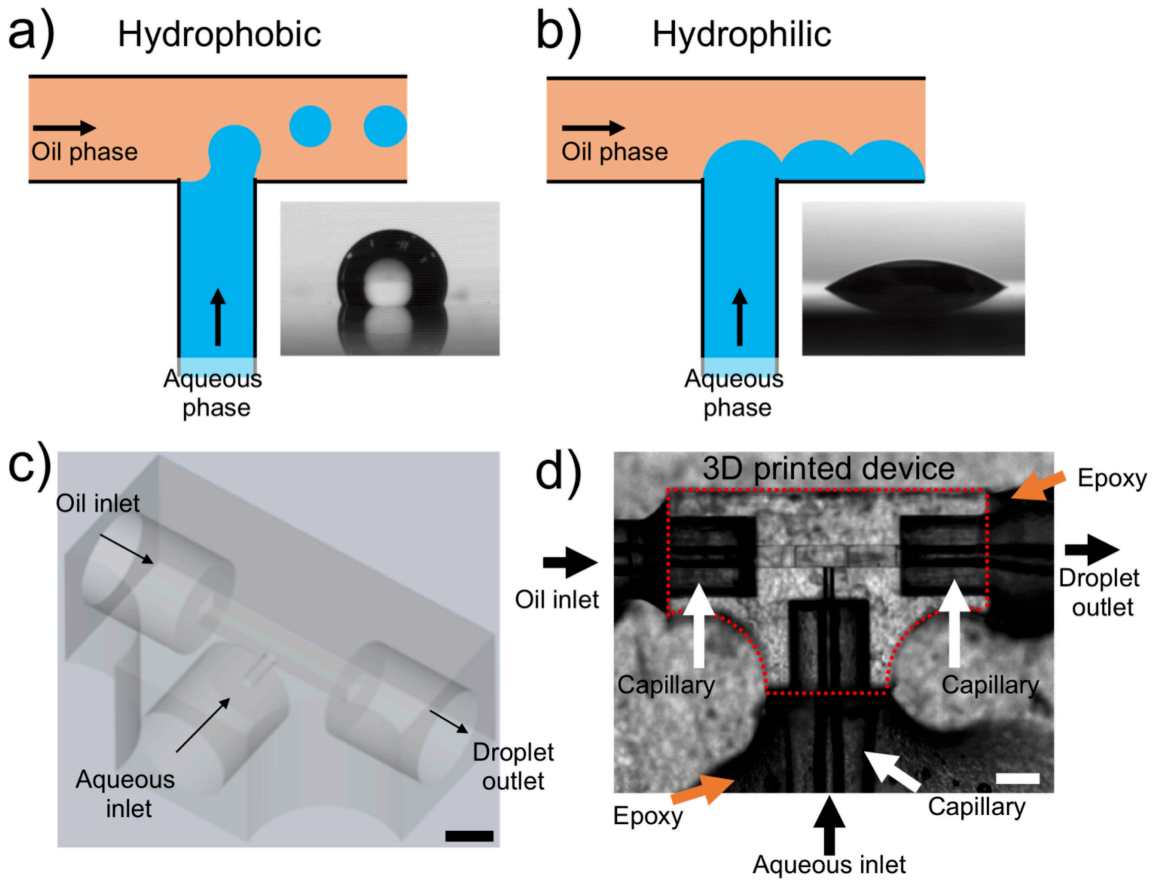

Figure 4.1 (a) Schematic of ideal water-in-oil droplet generation in a T-junction device with hydrophobic walls. Inset: image of a water droplet sitting on glass treated with a hydrophobic coating agent. (b) Schematic of a hydrophilic T-junction droplet generation device. The aqueous phase adheres to the walls and oil flows beside it; no droplets are generated. Inset: image of a water droplet on a hydrophilic glass slide. Panels (a) and (b) are not to scale. (c) CAD drawing of the 3D printed droplet generator. The black arrows indicate the various inlets and outlet. (d) Bright-field microscopy image of a 3D printed droplet generator (red dotted outline), epoxy-bonded and connected to fused silica capillaries. White arrows indicate capillaries and orange arrows indicate epoxy bonding material. The gray speckled background is due to tape used to attach the device onto a glass slide for microscopy. Scale bars in (c) and (d) are 200 μm.

4.4.1. Device fabrication and characteristics

A schematic of droplet generation in a microfluidic T-junction is shown in Figure 4.1. In a hydrophobic channel Figure 4.1a the oil coats the walls of the T-junction and prevents aqueous-phase adherence and, as the aqueous phase extends into the oil channel, droplets pinch off the bulk and proceed downstream to the outlet. In

contrast, in a hydrophilic channel Figure 4.1b the aqueous phase adheres to the walls and co-flows with the oil without breaking into droplets. These effects can also be seen in a fused silica capillary (as demonstrated below in Figure 4.5d). A computer-aided design (CAD) drawing and an optical microscopy bright-field image of the 3D printed droplet generator are shown in Figure 4.1c and Figure 4.1d, respectively. The oil enters through the left side of the device into the large rectangular channel of the T-junction (width = 100 μm, height = 75 μm), while the aqueous phase enters through a circular channel (radius = 25 μm) orthogonal to the oil channel. Flow proceeds down the large channel toward the outlet port (right). All three ports are connected to 360 μm fused silica capillaries and are sealed with epoxy to withstand high pressures. This seal can typically withstand sustained pressure of several hundred psi over a time period of 12 h, with short-durations of increased pressure up to 2500 psi, as demonstrated during an SFX shift.

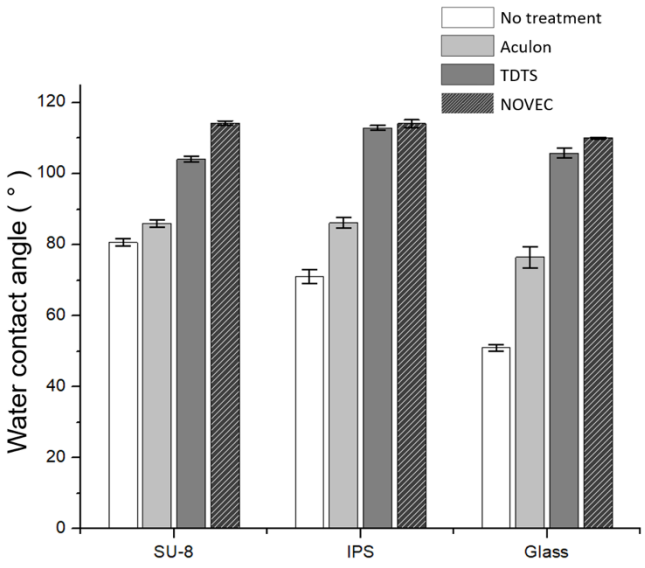

Figure 4.2 Static water contact angle (θ) measurements on SU-8, IP-S and glass substrates before and after treatment with three fluorinated chemicals. Error bars represent the standard deviations of the mean contact angle measurements.

4.4.2. Glass and photoresist treatment with different fluorinated agents

Fluorinated agents for treatment of microfluidic droplet generators include perfluorinated polymers [212-214], long fluorinated hydrocarbon compounds such as polyfluoropolyethers [215, 216] and commercialized adsorptive fluoropolymer surfactants [217-219]. Our goal was to investigate the stability of the droplet streams in a serial crystallography setup using a 3D printed droplet generator with three different adsorptive surface coatings. Owing to their geometry and small dimensions, it is not possible to measure contact angles inside fused silica capillaries and 3D printed devices using a sessile droplet. Instead, we investigated static water contact angles on borosilicate glass slides as well as on SU-8 and IP-S films spin-coated on silicon wafers before and after applying three different fluorinated hydrophobic surface treatments to mimic the coating effect within fused silica capillaries and 3D printed T-junction channels, respectively.

Novec and Aculon are two commercially available long-chain fluorinated hydrocarbons, both dissolved in methyl nonafluorobutyl ether and methyl nonafluoroisobutyl ether. Aside from solvent composition, they presumably also differ in the fluorinated compound content, which is a trade secret. Both are specified for water repellent treatment and can be flowed through microfluidic channels and capillaries for easy application (Novec 1720 EGC Technical Data Sheet and Aculon AL-B Technical Data Sheet; available at https:// www.3m.com). The third agent, TDTS, was applied through chemical vapor deposition. All treatment agents produced an increase in contact angle on the three surfaces tested, but to a different extent. The contact angle measurements and corresponding droplet images are shown and listed in Figure 4.2a and the supporting information.

For our application, Novec was the most advantageous treatment. It was easiest to handle – specifically as simply flushing it through the device treats the inner surfaces

of the 3D printed droplet generator assembled with silica capillaries. Furthermore, it produced the largest contact angles θ ≥ 110° for all three substrates and demonstrated good long-term stability, as detailed in the following section. Silanization with TDTS produced contact angles almost as large as Novec, although for our particular application this method presented several disadvantages. Introducing TDTS in the gas phase into 3D printed devices with a few hundred micrometer-sized inner diameters coupled to long fused silica capillaries is cumbersome to accomplish. In addition, for optimum results silanization requires an activation step with plasma [220] or acid [201] to increase the number of hydroxyl groups on the surface before surface modification. Since activation of the inner surface of our assembled devices with plasma is not feasible, and activation with acid would be cumbersome and could damage our devices, we did not further consider this method. Finally, the Aculon treatment did not produce hydrophobic (θ > 90°) surfaces on any of the substrates.

Compared with smooth spin-coated films, the walls of the IP-S 3D printed device may present a higher surface roughness depending on printing parameters such as the objective magnification, slicing distance and hatching distance. For the described 3D printed T-junctions, the root-mean-square roughness amplitude is estimated to be on the order of 100 nm [221]. The effect of roughness on the wetting properties in the meso-scale (several hundreds of micrometers to millimeters) typically amplifies the hydrophilic or hydrophobic character of the corresponding smooth surface [222]. For two-phase flows in hydrophilic microfluidic channels, such as the 3D printed devices without surface treatment or with Aculon coating, the effect of the contact line pinning at surface irregularities can decrease its intrinsic hydrophilicity [223]. In a hydrophobic channel, such as Novec-coated IP-S devices (Figure 4.2), the effect of

the surface roughness is always further increased by the surface hydrophobicity [224] and thus is advantageous for the generation of water-in-oil droplets.

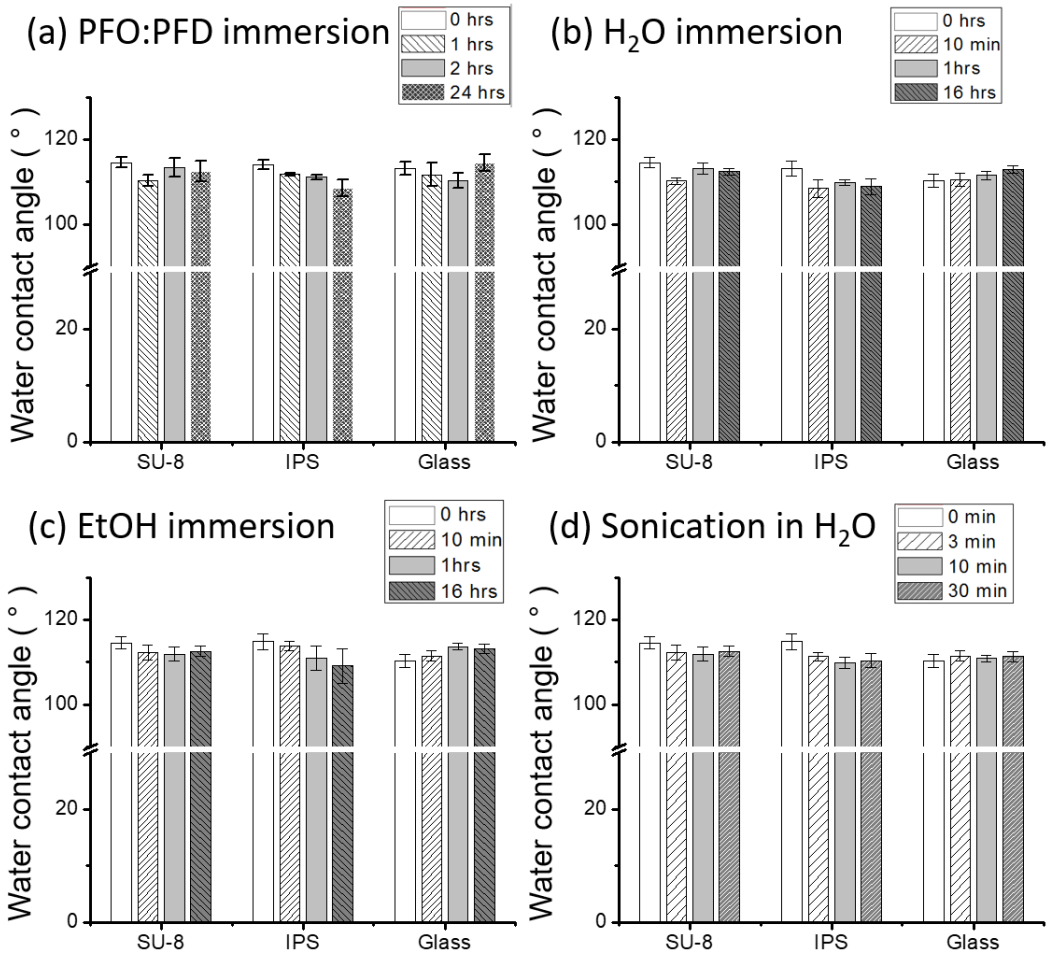

Figure 4.3 Stability of Novec coating on SU-8, IPS and glass substrates subject to various conditions. The measurements were obtained by immersing the Novec-coated substrates in (a) PFD:PFO (10:1 *v:v*%) for up to 24 h, (b) deionized water for up to 16 h and (c) ethanol (EtOH) for up to 16 h and (d) ultrasonication in deionized water for up to 30 min.

4.4.3. Long-term hydrophobic coating stability tests

In SFX experiments with XFELs, protein crystal suspensions are delivered to the X-ray beam for several hours, and thus the surface coating stability is critical for sustained droplet generation. To determine whether the Novec-modified surfaces can

retain their hydrophobicity, we investigated the treatment stability under various conditions. We mimicked the flow conditions in a droplet generator by immersing Novec-coated SU-8, IP-S and glass surfaces in various solvents, and also by sonicating the samples for 3–30 min in water. Figure 4.3 shows contact angle measurements on Novec-treated SU-8, IP-S and glass surfaces before and after various immersion times in oil, deionized water and ethanol, and after sonication in water. The measured contact angles did not exhibit noticeable changes, which indicates that the Novec treatment is effective in rendering SU-8, IP-S and glass surfaces hydrophobic, with excellent long-term stability. The excellent stability of the surface coating with Novec was also observed during droplet generation in an SFX experiment, as discussed below.

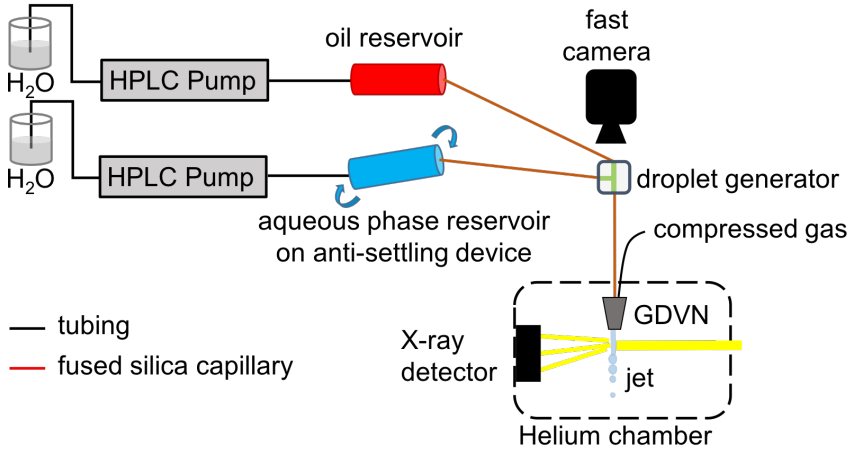

Figure 4.4 Experimental setup for droplet generation. Two HPLC pumps were used to drive two stainless steel reservoirs containing the oil and aqueous phases. The aqueous phase reservoir was mounted in a slowly oscillating holder (represented by curved arrows) to prevent the crystals from settling. The reservoirs were connected to the T-junction droplet generator using fused silica capillaries. Droplet generation at the T-junction was imaged using bright-field microscopy coupled to a fast camera. The outlet of the droplet generator was connected to a droplet detector and subsequently to the GDVN using a fused silica capillary. Helium gas was used in the GDVN to form a stable jet. The droplet detector consisted of a 1550nm laser diode and a photodetector connected to an oscilloscope. Based on the differences in transmittance between oil and water at this wavelength, the droplet frequency was monitored.

4.4.4. Effects of surface treatment on droplet generation

Next, we compared the effects of the hydrophobic surface treatment on the droplet generation behavior of T-junction devices assembled with fused silica capillaries. The experimental setup used at the MFX instrument is described in detail in the experimental section and schematically shown in Figure 4.4. This setup was mimicked in laboratory experiments, with similar flow rates, pressures, tubing and capillary lengths, and coupling the droplet generator and GDVN. In this setup, droplets of protein crystal suspensions could be generated reproducibly using a single T-junction device for periods of ~8 h under applied pressures from ~200 psi up to 2500 psi (for short periods of pressure spikes), with protein crystal suspension flow rates of 1–5 μL min^{-1} and total flow rates of 20–40 μL min^{-1}. The high pressure arises from the long lengths of small-inner-diameter capillaries and the viscosity of the oil phase; for example, for a conservative length of 1 m, an inner diameter of 50 μm and viscosity of 5.1 cP for PFD, the pressure drop required is approximately 1500 psi. The frequency of the droplets ranged from 30 to 150 Hz depending on the flow rates of the aqueous and oil phases.

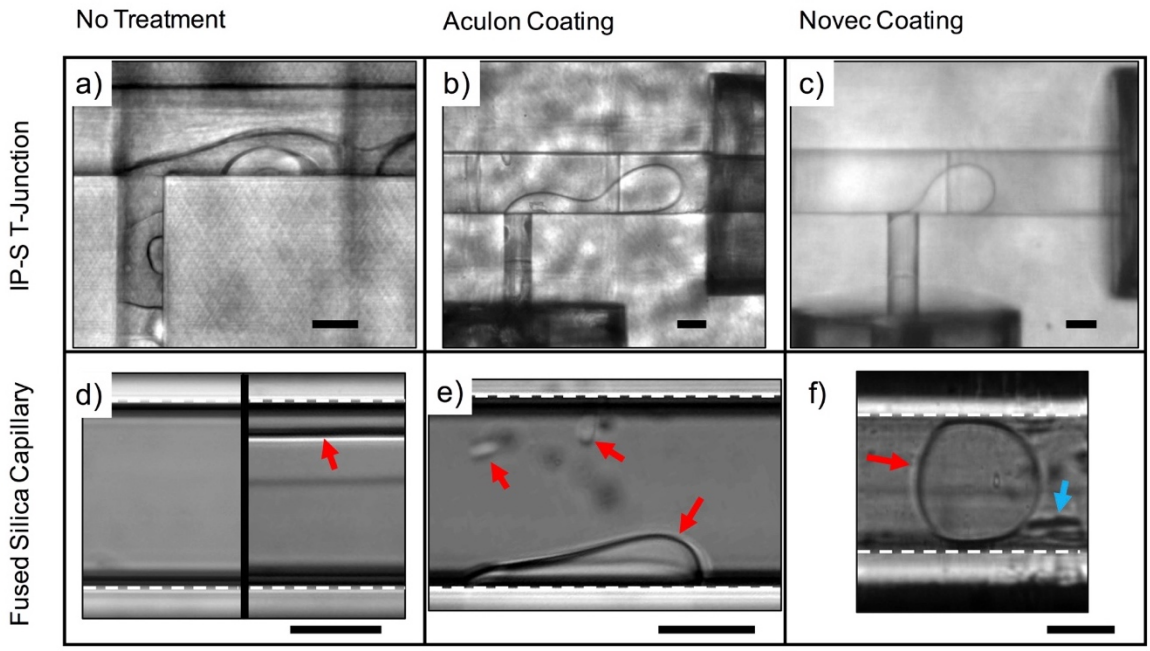

Figure 4.5 Effect of surface treatment on IP-S (a)–(c) and fused silica (d)–(f) capillaries on water-in-oil droplet generation. For IP-S: (a) no surface treatment (θ < 90°) results in the aqueous phase forming streamlines instead of droplets (Q_{oil} = 10 μL min^{-1}; $Q_{aqueous}$ = 5 μL min^{-1}), (b) surface treatment with oil aqueous Aculon (θ < 90°) results in adherence of the aqueous phase to IP-S until it pinches off into a droplet at the T-junction capillary joint (Q_{oil} = 12 μL min^{-1}; $Q_{mPEG\ buffer}$ = 5 μL min^{-1}), and (c) surface treatment with Novec (θ > 90°) results in droplet formation at the T-junction with no aqueous phase adherence to the IP-S surface (Q_{oil} = 6 μL min^{-1}; $Q_{PSI\ buffer}$ = 0.5 μL min^{-1}). For fused silica capillaries: (d) Right panel: the aqueous phase co-flows next to the oil (red arrow indicates phase boundary) when flowing both oil and water. The faded line below the red arrow is the same phase boundary from an out-of- focus wall of the capillary (Q_{oil} = 45 μL min^{-1}; $Q_{PSI\ buffer}$ = 5 μL min^{-1}). (d) Left panel: an untreated fused silica capillary surface (θ < 90°) with only the aqueous phase which fully wets the walls, provided for comparison. (e) After coating a fused silica capillary with Aculon (θ < 90°), aqueous drops adhere to the capillary wall (red arrows indicate adhered drops) (Q_{oil} = 35 μL min^{-1}; $Q_{PSI\ buffer}$ = 5 μL min^{-1}). (f) Surface treatment with Novec (θ > 90°) prevents droplets from adhering to the fused silica surface (Q_{oil} = 12 μL min^{-1}; $Q_{mPEG\ buffer}$ = 5 μL min^{-1}). The blue arrow indicates debris on the outside of the capillary. Dashed white lines indicate the cylindrical fused silica capillary walls. The scale bars are 50 μm in all images.

We first characterized the fluid-flow behavior on the IP-S and fused silica capillary portions of the fully assembled device, as summarized in Figure 4.5. When the droplet generator assembly was left untreated, no droplets could be generated. The aqueous phase streamlines along the surfaces, randomly making contact with the

device walls, and varying the flow rate Q did not disrupt the stability of the streamlines. This situation is depicted in Figure 4.5a for Q_{oil} = 10 μL min^{-1} and $Q_{aqueous}$ = 5 μL min^{-1}. When the droplet generator assembly was treated with Aculon, droplets usually appeared in the 3D printed device initially; however, after a few minutes under flow, the aqueous phase began adhering to the wall, streamlining and producing droplets that occasionally pinch off approximately at the T-junction and capillary joint, thus preventing control over the droplet generation, as shown in Figure 4.5b for Q_{oil} = 12 μL min^{-1} and $Q_{aqueous}$ = 5 μL min^{-1}. This limitation can be ascribed to the contact angle on the Aculon coating, which does not reach the hydrophobic regime, and to incomplete coverage, low stability of the coating or a combination of these. Lastly, when the surface was treated with Novec, as shown in Figure 4.5c (see Supplementary Video D.1), the aqueous phase did not stream along the wall and instead pinched off into droplets in the device itself (Q_{oil} = 6 μL min^{-1}; $Q_{aqueous}$ = 0.5 μL min^{-1}). This situation was only achieved with a surface treatment capable of rendering the IP-S surface hydrophobic.

Similar effects were observed on fused silica capillary surfaces. When flowing both water and oil phases in untreated surfaces (Figure 4.5d, right), the hydrophilic fused silica walls resulted in the aqueous phase flowing as a stream next to the oil phase (Q_{oil} = 45 μL min^{-1}; $Q_{aqueous}$ = 5 μL min^{-1}). When only flowing an aqueous phase, the inner fused silica capillary was fully wetted (Figure 4.5d, left). For cases of contact angles <90° after the surface treatment, or for cases of inhomogeneous surface treatment (Figure 4.5e), a similar situation to that shown in Figure 4.5b is observed in the fused silica capillary (Q_{oil} = 35 μL min^{-1}; $Q_{aqueous}$ = 5 μL min^{-1}). The aqueous phase interacts with the hydrophilic regions and may adhere to the surface. Eventually, a large droplet pinches off from this hydrophilic spot and the droplet progresses until it is captured by the next hydrophilic region. Ultimately, this results

in unstable non-uniform droplet generation. Lastly, when the surface is coated with Novec and uniformly hydrophobic (Figure 4.5f),

the aqueous droplets do not interact with the walls and maintain their shape, size and spacing (Q_{oil} = 12 µL min^{-1}; $Q_{aqueous}$ = 5 µL min^{-1}). With flow rates in the range 0.5–20 µL min^{-1} for the aqueous phase and 5–40 µL min^{-1} for the oil phase, droplets could be generated for periods of up to 8 h with no observable degradation of the Novec surface coating. Furthermore, droplets containing PSI crystal suspension were generated in a Novec-coated device under similar flow rate conditions (Figure 4.6c). In this example, <1 nL droplets were generated at a frequency of ~90 Hz (Q_{oil} = 14 µL min^{-1}; $Q_{aqueous}$ = 3 µL min^{-1}). In addition, the droplets could be transported through capillaries of up to 2 m in length, and the droplet generator was tested at an XFEL as shown in the next section.

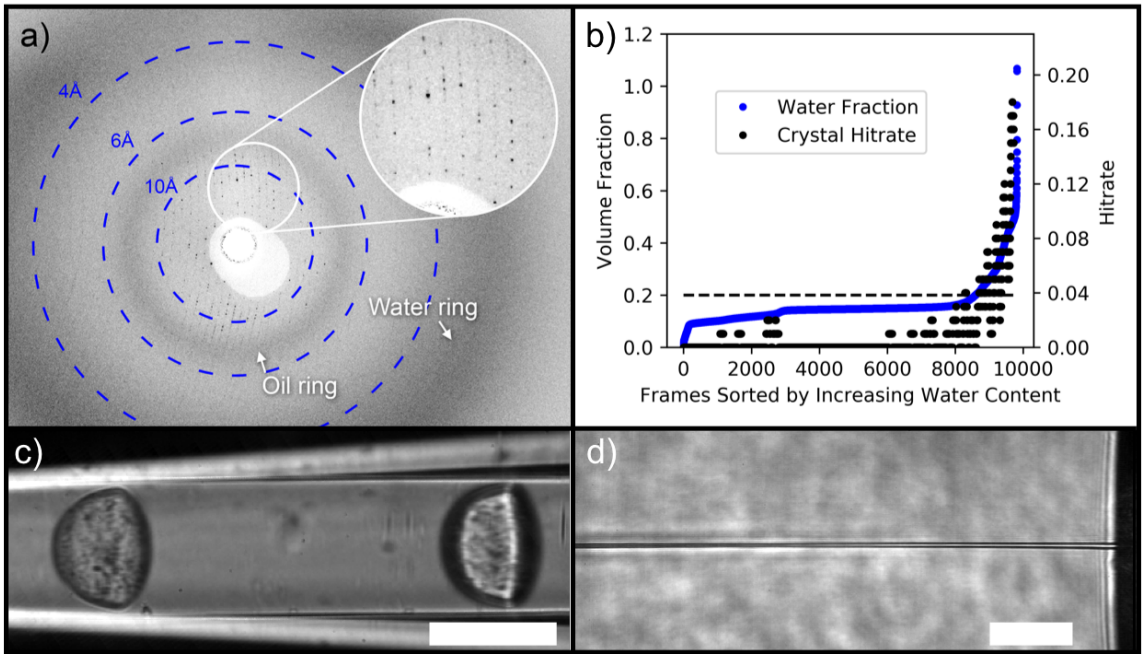

Figure 4.6 XFEL diffraction from PSI microcrystals injected with a 3D printed microfluidic droplet generation device. (a) Single XFEL diffraction pattern showing Bragg diffraction and diffuse scattering from oil (inner ring) and water. Diffraction peaks were observed to ~3.5 Å. (b) Volume fraction of water calculated per pattern,

sorted by increasing fraction of water (blue). An effective crystal hit rate calculated from binning the sorted patterns into groups of 100 shows a clear correlation between crystal hit rate and water volume fraction. Water fraction values below the dashed line cannot be distinguished from pure oil. (c) Droplets containing PSI crystals in an outlet capillary. The capillary was imaged 'free standing' at an angle through the image plane resulting in the right droplet being out of focus. (d) Still image of a Novec-coated GDVN jetting oil. Flow rates were 10 µL min^{-1} for PSI buffer solution and 20 µL min^{-1} for oil. Scale bars in (c) and (d) are 100 µm.

4.4.5. Experimental diffraction from XFELs

To assess the ability to collect XFEL diffraction data using the droplet generator, we performed SFX experiments at the MFX instrument at LCLS (see also Figure 4.4 for the entire fluidic setup and the discussion above). The droplet generator was configured for a 120 Hz operation, which is the maximum X-ray pulse repetition rate at LCLS. In these initial tests, droplet synchronization with the XFEL was not realized, although it is the focus of ongoing work. Also, diffraction images were collected at the lower rate of 10 Hz, which is the X-ray detector maximum frequency in 2 x 2 binning mode with an effective pixel size of 89 µm suitable for Bragg peak identification at a detector-to-sample distance of 160 mm.

Microcrystals (0.2–1 µm in size) of the large membrane protein complex PSI were prepared as described previously [19, 207] and delivered using the droplet generator as described above. During the run where we observed droplet generation at the beamline with the droplet detector, we were able to collect 10124 images, of which 94 (1%) were identified as hits by *Cheetah* (see Figure 4.6a for an example diffraction pattern). Of these 94 images, *CrystFEL* [225] was able to index 46 (50%). The average resolution of these patterns was 6.3 Å , with some patterns showing diffraction peaks to 3.5 Å as estimated by *CrystFEL*. There were not enough higher-resolution images collected to generate a complete data set for structure determination. Initial data analysis showed that the proportion of oil and water in the X-ray-illuminated volume varies from image to image, and correspondingly, the

likelihood of hitting a crystal in the water droplet fluctuates as well. This may be attributed to small instabilities in the position of the liquid jet (~5 μm diameter) when aqueous droplets in oil are injected with reference to the position of the X-ray beam (~3 μm diameter), resulting in the X-ray beam intersecting the liquid jet in different locations with each XFEL pulse.

In the GDVN, a water droplet carried by the oil stream is focused by a sheath of He gas, leading to droplet stretching. For example, a 0.8 nL droplet could be stretched to a length of 40 mm in a 5 μm diameter jet. This may result in a thin column of water (~3 μm thick) of finite length enveloped by an oil sheath (~1 μm thick), additionally contributing to the fluctuation in water content. The likelihood of hitting a crystal in the water droplet also fluctuated, as is commonly observed in SFX experiments with GDVN sample delivery, and as expected for randomly distributed crystals.

In addition, the angle of the liquid jet can flicker between two positions when jetting alternates between only oil or an aqueous droplet, further contributing to varied hit proportions of oil and water. This was observed in laboratory tests and to some extent at the MFX instrument. However, good jet stability when the fluorinated oil was present as shown in Figure 4.6d was observed in the laboratory experiments. Additional detailed characterization of micrometer-scale jets of water in oil suspensions is beyond the scope of this chapter.

Oil and water scattering patterns are distinguishable by their diffuse rings. As can be seen in Figure 4.6a, oil has a relatively narrow diffuse ring with a peak at $q \simeq 8.0$ Å, whereas water has a very broad diffuse ring with a peak at $q \simeq 3.3$ Å. Exposures containing both oil and water may arise when the X-ray pulse hits the spheroidal end of a droplet. Furthermore, as described above, a thin layer of oil around the droplets prevents wetting of the capillary walls (hence the hydrophobic surface treatment)

which may extend into the liquid jet and interaction region causing simultaneous exposure of oil and water. Several example images of diffraction patterns in varying fractions of oil/water are shown in Figure A.2. A correlation between the diffraction resolution limit and volume fraction of water was not observed. To assess the correlation between the likelihood of hitting a crystal and the volume fraction of water illuminated by the X-ray beam (and thus successful droplet generation), we analyzed the one-dimensional radial scattering profiles calculated for each image. Using oil-only and water-only scattering profiles, the volume fractions of oil and water in each image were estimated using a simple linear combination fitting procedure (Figure 4.6b). Owing to the diffuse nature of the oil and water rings, low volume fractions of water below ~20% (dashed line in Figure 4.6b) cannot be distinguished from pure oil. This probably refers to the regime where synchronization between the droplet generator and the XFEL pulse sequence is not achieved. After sorting the images by increasing the volume fraction of water, crystal hit rates were calculated by binning the images into groups of 100 and calculating the average hit rate within each group. The results show a clear correlation between the effective crystal hit rate and the increasing volume fraction of water (Figure 4.6b), and correspondingly successful droplet generation. This demonstrates that, despite the lack of synchronization of droplets with the X-ray pulses in this prototype, the 3D printed droplet generation device successfully injected crystal-containing aqueous droplets into the oil stream, and delivered the resulting liquid jet into the X-ray beam path for serial micro-crystallography data collection.

4.5. Conclusions

Current liquid injection methods for SFX typically waste the majority of injected crystals as a result of the mismatch between XFEL pulse repetition rate and jet

speed. Because of this mismatch, most of the sample flows into waste without interacting with the X-ray beam. We address this problem with a microfluidic droplet generator that effectively stops the flow of sample between X-ray pulses by interleaving crystal-laden aqueous droplets within an oil jet. Our device consists of a 3D printed T-junction droplet generator coupled to fused silica capillaries interfacing with liquid handling periphery and sample injectors. The wetting properties of bare 3D printed devices did not allow reproducible droplet generation. We therefore investigated the effect of the two commercially available coatings Novec and Aculon as well as gas phase silanization with TDTS in the performance of the droplet in oil generation. While the two commercially available coatings can be applied by simple filling methods, the gas phase silanization method was impractical for this application because of the intricate geometry and small dimensions of the surfaces that need to be coated. Of the three surface treatments investigated under conditions mimicking the flow in an XFEL experiment, Novec provided the most hydrophobic surface and most stable coating on both photoresist films and glass. Importantly, we demonstrated that Novec-treated droplet generation devices produce stable droplets of aqueous buffers employed in an SFX experiment over several hours, suitable for use in an entire shift at an XFEL facility. In contrast, coatings rendering lower hydrophobicity resulted in flow conditions unsuitable for robust droplet generation such as co-flowing of the oil and aqueous phases, intermittent surface attachment of the aqueous phase or random droplet generation. We also demonstrated the successful application of the novel droplet generator at an SFX experiment at LCLS and showed a correlation between crystal hit rate and volume fraction of water during droplet generation. Robust droplet generation with a 3D printed device and Novec surface coatings will be utilized for the synchronization of crystal suspension droplets with the frequency and phase of XFELs in the future.

CHAPTER 5

SEGMENTED FLOW GENERATOR FOR SFX AT THE EUROPEAN XFEL

5.1. Abstract

Serial femtosecond crystallography with X-ray free electron lasers (XFELs) has made great advancements in recent years, including the structure determination of complex membrane proteins as well as time-resolved serial protein crystallography. When conducted with common liquid sample delivery, which continuously jets the crystal suspension into the path of the XFEL beam, a vast amount of sample is wasted due to the pulsed nature of all current XFEL sources. The European XFEL (EuXFEL) currently requires very large sample amounts as it delivers femtosecond (fs) X-ray pulses in pulse trains separated by 100 ms, but with pulses within trains currently separated by only 1 microsecond. Therefore, in continuous liquid delivery, fast jet speeds are required to replenish the sample between pulses, but more than 99% of sample flows to waste in between pulse trains without interaction with the XFEL beam. Here, we introduce a microfluidic device to deliver aqueous protein crystal laden droplets segmented with an immiscible oil that reduces sample waste significantly. We demonstrate droplet injection at the EuXFEL during the first commissioning experiments, showing that this approach is compatible with the high-pressure liquid delivery of a serial crystallography experiment including sample jetting for more efficient data collection. While achieving ~ 60% reduction in sample waste, we determined the structure of the enzyme 3-deoxy-D-*manno*-octulosonate 8-phosphate synthase from microcrystals delivered in segmented droplets revealing distinct structural features not previously reported.

5.2. Introduction

The emergence of X-ray free electron lasers (XFELs) has significantly advanced X-ray crystallography in the past decade by circumventing many of the limitations of traditional goniometer-based synchrotron X-ray crystallography. Traditional macromolecular X-ray crystallography collects full data sets from irradiation of a single crystal as it is rotated during X-ray exposure to obtain a structure. Radiation-induced structural damage[19, 226] can be mitigated, but not eliminated, by data collection under cryogenic conditions, using relatively large crystals or spreading the dose over a few crystals.[227] While decreasingly small protein crystals can be used for high-resolution structure determination at modern microfocus synchrotron beamlines, protein crystallography is typically achieved for static structures that are not highly prone to radiation damage.[226] Furthermore, time-resolved synchrotron macromolecular crystallography is currently limited to 100 ps time resolution and almost exclusively carried out on reversible, light-initiated reactions in large crystals. In serial femtosecond crystallography (SFX) with XFELs, each diffraction pattern is obtained before the crystal is destroyed by the intense XFEL pulse, enabling high-resolution structure determination at room temperature from radiation-sensitive samples (such as metalloproteins),[19, 226, 227] and reaction intermediates with unprecedented time resolution.[19, 164, 228-230] SFX datasets consist of thousands of single snapshot diffraction patterns collected from microcrystals in random orientations interacting with single femtosecond-scale XFEL pulses.[36]

The European XFEL (EuXFEL) is designed to deliver trains of fs X-ray pulses with MHz repetition rates within such trains. The trains repeat at 10 Hz effectively switching off the beam >99% of the time, causing a tremendous sample waste problem if sample is delivered continuously (even if the EuXFEL runs at the full capacity of 4.5 MHz pulse repetition rate within trains in the future). Thus, a large amount of protein

needs to be produced and crystallized for structure determination, creating a bottleneck where hundreds of milligrams to grams of protein are required for a complete data set.[14]

The EuXFEL MHz pulse repetition rate requires fast sample replenishing which can only be accomplished with high jet velocities ≥ 50 m/s.[47, 231] Suitable injectors for crystal suspension sample injection are the gas dynamic virtual nozzle (GDVN)[45] or liquid focusing with a double-flow focusing nozzle (DFFN).[131] The GDVN has been demonstrated to generate high velocity jets able to replenish the sample jet between MHz pulses at the EuXFEL,[47] and the DFFN also utilizes a GDVN. Sample delivery with viscous media injectors[159] such as the lipidic cubic phase injector[26] or fixed target approaches[23] cannot keep up with the MHz repetition rate of the EuXFEL despite their advantages in reducing sample waste. Similar issues arise for the microfluidic electrokinetic sample holder (MESH)[149] and its updated version, the concentric MESH injector (coMESH).[147]

Droplet injection methods have the potential to overcome the limitations due to sample waste, but in order to be compatible with MHz repetition rates of the EuXFEL they must be compatible with the fast replenishing requirements. Additionally, any method for reducing sample waste, should also be compatible with time-resolved (TR) crystallography with the ultimate goal of constructing molecular movies.[232] TR-SFX is relatively straightforward to be combined with droplet injection for photoactivated reactions. However, biomolecular reactions with ligands or substrates require crystals to be mixed with reactants in solution prior to injection into the path of an XFEL. Acoustic droplet ejectors (ADEs) have demonstrated delivery of drops-on-demand for SFX with a high hit fraction[143, 144] usually in conjunction with a conveyor belt that transfers the droplets into the X-ray beam. However, the ADE technique is incompatible with the short spacing of pulses at the EuXFEL, so this

technique could only use one pulse in the pulse train thereby reducing the repetition rate to effectively 10 Hz. In addition, this approach is limited to photoinitiated TR-SFX studies and reactions involving gas-phase substrates delivered to aqueous media on millisecond time scales or above, excluding a large class of enzyme-substrate reactions. Similarly, piezoelectric droplet injectors[142] suffer from large droplet volumes increasing background scattering and are not compatible with the MHz repetition rates required by the EuXFEL.

Here, we introduce a novel approach to reduce sample waste in SFX experiments at the EuXFEL. It is based on the generation of sub-nL crystal suspension droplets embedded in an immiscible oil, allowing injection with a traditional GDVN. We demonstrate droplet generation of 3-deoxy-D-*manno*-octulosonate 8-phosphate synthase (KDO8PS) crystal suspensions with a microfluidic droplet generator and show that the droplet generation frequency can be controlled by the flow rates of the aqueous and oil streams. The diffraction quality of crystals of KDO8PS is similar both when injected in aqueous droplets surrounded by oil or by continuous injection with a GDVN, with ~ 60% reduction in sample consumption achieved with droplet injection. The determined structure revealed new detail in a previously undefined loop region of KDO8PS, an important target for antibiotic studies.

These results from commissioning the EuXFEL advocate for future routine integration of droplet generation by segmented oil flow at other XFELs around the world. This includes the Linac Coherent Light Source at SLAC National Accelerator Laboratory (SLAC) operating from 30-120 Hz[18] and other XFELs such as the Spring-8 Angstrom Compact Free Electron Laser (SACLA) pulsed at 30-60 Hz,[233] the Pohang Accelerator Laboratory (PAL) at 60 Hz [234] and the SwissFEL at up to 100 Hz.[235] All these instruments waste the majority of sample during continuous liquid injection[132] which could be significantly reduced with the here presented approach.

5.3. Materials and Methods

5.3.1. Chemicals and Materials

IP-S photoresist was purchased from Nanoscribe GmbH (Germany); SU-8 developer, from Microchem (USA); Novec 1720, from 3M (USA); isopropyl alcohol, from VWR Analytical (USA); epoxy (#04001) from Hardman Inc. (USA); perfluorodecalin (PFD), from Sigma-Aldrich (USA); 1H,1H,2H,2H-perfluorooctanol (PFO), from Alfa Aesar Co. Inc. (USA); KDO8PS genes, from GenScript Inc. (USA); *E. Coli,* from New England Biolabs (USA); Sigma Fast tablets, β-mercaptoethanol, Tris, HCl, ethylenediaminetetraacetic acid (EDTA), protamine sulfate, KCl, and protease inhibitor cocktail, from Sigma-Aldrich (USA); and poly(ethylene glycol) 5000 methyl ether (PEG5000 MME), from Hampton Research (USA). Fused silica capillaries were obtained from Molex LLC (USA); tubing and capillary union connectors, from IDEX Health & Science LLC (USA); PicoClear unions, from New Objective, Inc. (USA); PEEK tubing, from Zeus (USA); double sided tape, from 3M (USA); and 10 kDa cutoff filters, from Centricon, Millipore (USA).

5.3.2. Sample Preparation

The wild-type KDO8PS gene was cloned into a pET-23d plasmid and subsequently transformed into LEMO23(DE3) competent *E. coli* cells and expressed as described previously[236, 237]. Cells were harvested by centrifugation and lysed by sonication after resuspension in 300 mM Tris-HCl pH 7.3, 75 mM KCl, 5 mM EDTA, 2 mM β-mercaptoethanol, SigmaFast protease inhibitor cocktail and 2 mg/mL of hen egg white lysozyme in the lysis buffer. The lysate was centrifuged to separate the lysate from intact cells and debris and subsequently stirred with dropwise addition of 2.2% w/v protamine sulfate, 20 mM Tris pH=5, 300 mM KCl, 2 mM β-mercaptoethanol,

and SigmaFast protease inhibitor cocktail until precipitation of the genetic material, followed by centrifugation. The supernatant was dialyzed through a 3 kDa cutoff dialysis membrane overnight into 20 mM Tris-HCl pH=7.3, 75 mM KCl, and 2 mM β-mercaptoethanol. After centrifugation, the supernatant was filtered using a 0.22 μm syringe filter. Aliquots were injected into an anion exchange column (900 mm x 16 mm, DEAE-sepharose) equilibrated with 20 mM Tris-HCl pH=7.3, 75 mM KCl, and 2 mM β-mercaptoethanol. The salt concentration was increased to 125 mM KCl to elute KDO8PS fractions. Purity was determinded by sodium dodecyl sulfate polyacrylamide gel electrophoresis (SDS-PAGE) and a thiobarbituric acid assay was used to confirm KDO8PS functional activity. Additionally, mass spectrometry by MALDI-TOF/TOF and dynamic light scattering (DLS) were used to confirm the identity of KDO8PS and to characterize the monodispersity of the sample prior to crystallization. Pure fractions of KDO8PS were pooled and concentrated with a 10 kDa cutoff centrifugal filter until an absorbance value of A_{205} = 0.645 was achieved. The concentrated solution was frozen and stored at -80°C until crystallization. KDO8PS microcrystals were grown using a stirred batch method[238] where the concentration of KDO8PS was adjusted to 8.75-12 mg/mL. Crystallization was induced by dropwise addition of 16-20% w/v PEG 5000 MME. Crystal batches were monitored and inspected under a stereo microscope and characterized by dynamic light scattering to select the most uniform batches for desired size and size homogeneity. Crystal batches used for this experiment consisted of uniform crystals of the size range between 8 and 10 μm.

5.3.3. Droplet generator fabrication

The continuous oil phase was prepared by mixing PFD and PFO in a 10:1 v/v ratio. Droplet generator devices were fabricated as described previously.[70] Briefly, models were designed in AutoCAD (AutoDesk, USA) and 3D printed using IP-S photoresist

and the Photonic Professional GT 3D printer (Nanoscribe GmbH, Germany). Printing was accomplished in solid mode using dip-in laser lithography two-photon polymerization. Once printed, devices were developed in SU-8 developer and rinsed in isopropyl alcohol. Each device was then immobilized on a glass slide with tape, and fused silica capillaries with polished ends were inserted and glued into the device inlets and outlet with epoxy. Lastly, the device, GDVN, and capillaries were surface treated using Novec 1720 as described previously.[70] The fused silica capillary outer diameter (OD) was 360 μm and the inner diameter (ID) varied (either 50, 75, or 100 μm). The T-junction was defined by the intersection of a 100 μm x 75 μm x 650 μm rectangular channel and a 50 μm diameter cylindrical channel (see Figure 5.1c).

5.3.4. Fluidic set-up

Positive pressure was applied using HPLC pumps (LC-20AD from Shimadzu Co., Japan) to initiate and control the fluid flow. Each HPLC pump delivered water to a custom made or commercial reservoir containing a piston from which either crystal suspension or oil phase was dispensed.[133] For XFEL experiments, the crystal suspension reservoir was mounted on a rotating anti-settling device with temperature control at 4°C.[133] PEEK tubing and fluidic connections were used to connect components upstream of the droplet generator device, while fused silica capillaries and PicoClear unions were used to connect the droplet generator to the downstream GDVN. Liquid flow meters SLI-0430 and SLG-0075 (Sensirion, Switzerland) were used to monitor the flow rates after the reservoirs (see Figure 5.1a,b for a schematic).

5.3.5. Droplet detection

All components were purchased from Thorlabs, USA, unless stated otherwise. Briefly, a 1550 nm 5 mW laser beam (a L1550P5DFB laser diode and a LTC56B Controller Kit) was transmitted across the fused silica capillary connecting the T-junction droplet generator with the GDVN, and the transmitted light was detected with an amplified photodetector (PDA20CS). A collimating lens (C230TMD-C) on kinematic mount (KC1-T), a fused silica capillary custom built holder, and a 200 µm pinhole were aligned between the laser diode and the detector using x-y translators (SCPO5T) within a 30 mm cage system. The signal (Figure 5.1f) was displayed and recorded on an oscilloscope (TDS 2024, Tektronix). Droplet experiments outside of an XFEL facility were additionally monitored with brightfield optical microscopy (IX71, Olympus, USA) and a Photron high speed camera (FASTCAM SA4, Japan). MicroManager (ver 1.4.22, UCSF, USA) and ImageJ (ver 1.48v, NIH, USA) software were used for image acquisition, processing, and analysis, and Origin (OriginLab Corp., USA) was used to generate plots.

5.3.6. XFEL Instrument Setup

Experiments were conducted at the EuXFEL (Schenefeld, Germany) upstream interaction region of the SPB/SFX instrument[46] during the beamtime P2042. The pulse structure of the XFEL was composed of 10 Hz trains, with 32 pulses per bunch train. The pulse duration was ≤100 fs[239] with a photon energy of 9.31 keV. The beam was focused with compound refractive lenses to a beam diameter of 15 x 20 μm^2. The average pulse energy was 280 µJ. Diffraction data was collected using an AGIPD 1 Mpx detector[240] at a detector distance of 173.5 mm.[241, 242] The GDVN was attached to the end of a nozzle rod (~ 1 m in length) that was inserted through an airlock system into the 10^{-5} mbar vacuum chamber. Helium gas pressure of 150 psi

was used to operate the GDVN and was controlled by GP1 electronic pressure regulators (Equilibar, USA).

5.3.7. Data Processing

The KDO8PS diffraction patterns collected were identified and calibrated using Cheetah.[122] For hit-finding, a minimum of 2 pixels with a count above a threshold of 500 with a minimum signal-to-noise ratio of 8 was considered a peak, and an image containing at least 10 such peaks was classified as a hit. From the ~ 4,100,000 images collected, 37,000 were classified as hits, which corresponds to an average hit rate of 0.9%.

Approximately 46 % of the identified hits could be indexed and the Bragg reflections integrated using the software package CrystFEL (version 0.8.0),[123] based on the peak locations found by Cheetah. Indexing was performed by CrystFEL's indexamajig sequentially trying XGANDALF,[243] DirAx,[244] MOSFLM[245] and XDS[246] requiring a cubic body-centered lattice and unit cell parameters of a=b=c=118 Å and $\alpha=\beta=\gamma=90°$ (Figure B.3). The indexamajig integration radii were set to 2, 3, 4 pixels and indexing solutions were checked by ensuring that they accounted for at least 50% of the observed peaks (option "check-peaks").

The indexed patterns were further processed with ambigator[225] to resolve the indexing ambiguity inherent to the cubic space group for serially collected data. The number of correlation coefficients per crystal was limited to 1000 for speed, and 10 passes of ambiguity resolution were made over all crystals. This resulted in 8315 indexing assignments being changed, corresponding to roughly 50 % of the data as expected. The indexed reflections were subsequently scaled and merged using partialator,[124] applying the unity model (without partiality modeling) over 3 iterations. The intensities were converted to structure factor moduli using the

truncate program of the CCP4 suite[247], and a fraction of 0.1 reflections were included in the generated Rfree set. The L-test implemented in truncate was used to ascertain successful de-twinning of the data (Figure B.4).

5.3.8. Structure Solution and Refinement

Phasing was done using molecular replacement with Phaser[248] of the CCP4i program suite[247] using the PDB code 1X8F [249] as search model. The obtained model was refined using alternate cycles of automated refinement with REFMAC[250] and manual inspection was performed with COOT.[251] The final refined structure was assessed using the web server PDB-REDO,[252] which indicated that the Rfree value is biased. The Rfree value reported in the results is therefore the unbiased Rfree value, as defined by PDB-REDO.[253] All Figures of the protein structure presented in this manuscript were generated in PYMOL.[254] The final refined structure was validated using the wwwPDB Validation Service and submitted to the Protein Data Bank for deposition. (PDB ID 6U57).

5.4. Results and Discussion

5.4.1. Droplet Generator Setup at XFEL

We present a droplet generator providing sub-nL sized droplets of crystal suspensions intersected by a continuous oil phase for experiments at the EuXFEL, which is depicted in Figure 5.1. To integrate it in a typical SFX liquid injection setup employing a GDVN to deliver the sample in a vacuum chamber, we employed a 3D printed microfluidic droplet generator, as previously described.[70] Here, we adapted this approach for a workflow compatible with the early user experiments at the EuXFEL as depicted in Figure 5.1a. Positive pressure was applied to drive water at a constant flow rate from the HPLC pumps to the fluidic reservoirs. The HPLC pumps

and flow rate sensors were remotely accessible to allow real-time adjustment of the flow rate conditions for the oil phase and crystal suspension during the experiment. The reservoir containing the crystal suspension was mounted in an anti-settling device to prevent crystal settling and was maintained at 4°C to minimize crystal degradation.[255] Teflon pistons in the reservoirs displaced the sample or oil, and the flow rates were monitored with flow rate sensors mounted shortly after the reservoir. The crystal suspension leaving the sample reservoir flowed into the droplet generator inlet for the aqueous phase with flow rates, Q_{aq}, ranging from 3 – 15 µL/min. The oil leaving the respective reservoir entered the droplet generator at the continuous phase inlet (Figure 5.1c), with oil flow rates, Q_{oil}, ranging from 5 – 50 µL/min. Thus, the total flow rate, Q_{tot}, varied from 8 – 65 µL/min, with various combinations of flow rate ratios of Q_{oil} to Q_{aq} utilized for droplet generation. Droplets exited the droplet generator through the outlet and associated capillary. Figure B.1 shows a representative image of droplets containing crystals generated at Q_{aq} = 4.5 µL/min and Q_{oil} = 12 µL/min imaged in the capillary after the droplet generator. The capillary was connected to the GDVN by a union.

The capillary leaving the droplet generator was connected to another capillary passing through the droplet detector which was located about 30 cm downstream from the droplet generator. The droplet detector was crucial for this experiment as it allowed real-time feedback of the droplet generation frequency. The photodetector delivered a scalable voltage signal that allowed recording of the droplet frequency with an oscilloscope. Figure 5.1d shows the functioning principle of the droplet detector, taking advantage of the transmission differences between oil and aqueous solutions upon excitation at 1550 nm. Droplets were continuously observed with the droplet detector as shown in Figure 5.1e. The same capillary directly served as the inlet capillary of the GDVN to inject the segmented flow into the X-ray beam. The

total capillary length after the droplet generator was ~ 2 m to accommodate the droplet detector mounted near the top of the vacuum chamber and the full length of the nozzle rod required to insert the GDVN into the SPB/SFX vacuum chamber (Figure 5.1b). At total flow rates larger than 8 µL/min, we observed a stable and robust jet with a jet diameter of about 5-10 µm (see Figure B.2). The sample was hit by the X-rays in the vacuum chamber and diffraction data was collected with the AGIPD detector[240] (see Methods Section for details).

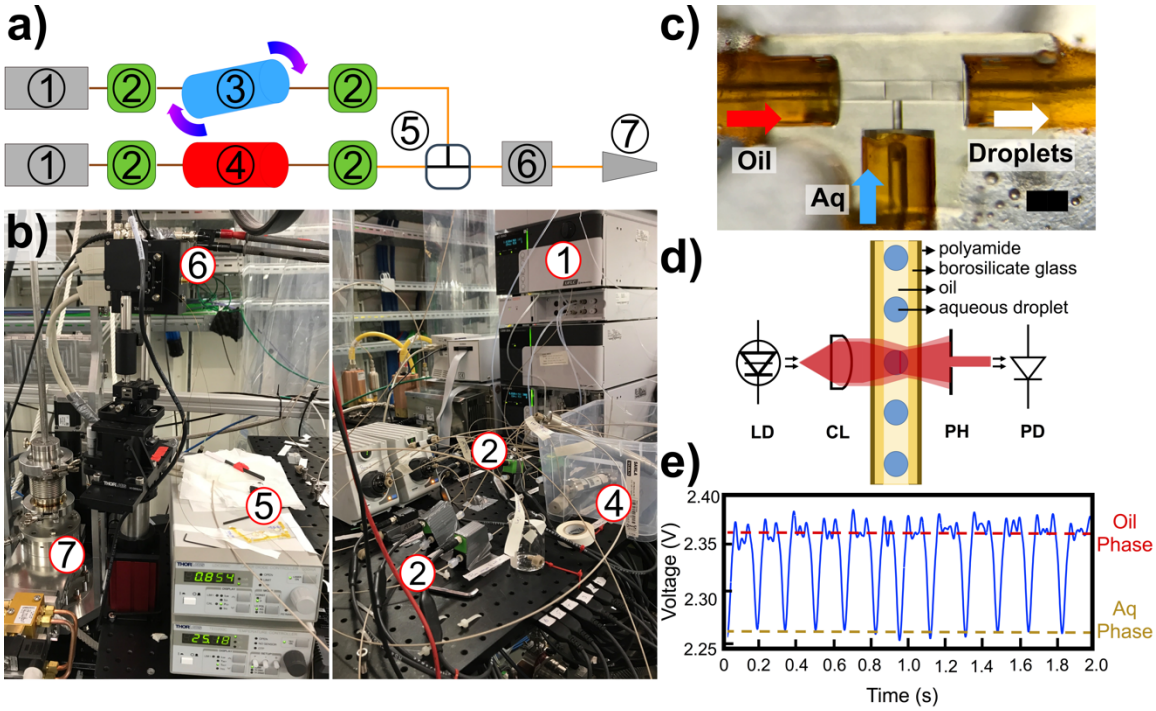

Figure 5.1 (a) Schematic of the workflow used at the EuXFEL SPB/SFX end station. The components are: 1. HPLC pumps, 2. flow rate sensors, 3. crystal suspension reservoir in an anti-settling device, 4. oil reservoir, 5. droplet generator, 6. droplet detector, 7. GDVN. (b) Representative images of the fluidic setup on top of the SPB/SFX sample chamber at the EuXFEL, with numbers matching those in (a). (c) Brightfield optical microscopy image of an assembled droplet generator. (d) Schematic of the droplet detector and representative components: laser diode (LD), collimating lens (CL), pinhole (PH), and photodetector (PD). (e) Representative voltage plot of aqueous-in-oil droplets. Scale bar is 100 µm in (c).

5.4.2. Droplet Generation Frequency

The droplet generator was tested prior to the experiment using a fluorinated oil as continuous phase (10:1 PFD:PFO) and the KDO8PS mother liquor as dispersed phase to characterize the achievable droplet generation frequencies. Many factors may affect droplet generation, including the channel dimensions, liquid flow rates and velocities, liquid viscosities, and interfacial tension between the two immiscible liquids. A comprehensive equation that takes into account the aforementioned physical parameters to characterize the droplet generation frequency, f_d, was given by Zhang et al.[102]:

$$f_d = \frac{K \times Ca^{4/3}}{W} \times \frac{u_d}{u_{tot}} \quad (5.1)$$

where u_d is the velocity of the dispersed (aqueous) phase, u_{tot} is the total velocity, Ca is the capillary number, W is the width of the continuous phase channel, and K is a pre-factor characteristic for the system. The capillary number describes the relationship between viscous shear and interfacial forces, and equals the product of the viscosity (η = 13.3 mPa s) and velocity of the continuous phase divided by the interfacial tension (σ = 12 mN/m) between the two immiscible liquids. Note that the only variable term in Ca is the continuous phase velocity.

The velocities of both continuous and dispersed phases were varied by changing their flow rates, while maintaining the channel geometry, fluid viscosity, and interfacial tension constant, with the total flow rate, u_{tot}, between 10 – 20 mm/s. As illustrated in Figure 5.2, the obtained droplet frequencies follow the relationship described in eq 5.1 in excellent agreement. For the flow rates tested, $Ca \sim 10^{-2}$, which closely corresponds to both the transient droplet generation regime between dripping and squeezing as reported by Xu et al.[98] and Christopher et al.,[99] for which the relationship of eq 5.1 holds.[102] The best fit to the experimental data was obtained with K = 3.7 ± 0.2 m/s, which differs from the pre-factor described by Zhang et

al.[102] We attribute this to the differences in geometry of the T-junction, which was reported by Gupta and Kumar[256] and Wehking et al.[101] to affect the droplet generation frequency. We further note that the target 10 Hz droplet generation frequency to match the EuXFEL pulse train frequency is achievable at $Ca^{4/3} \times \frac{u_d}{u_{tot}} = 3\times10^{-4}$.

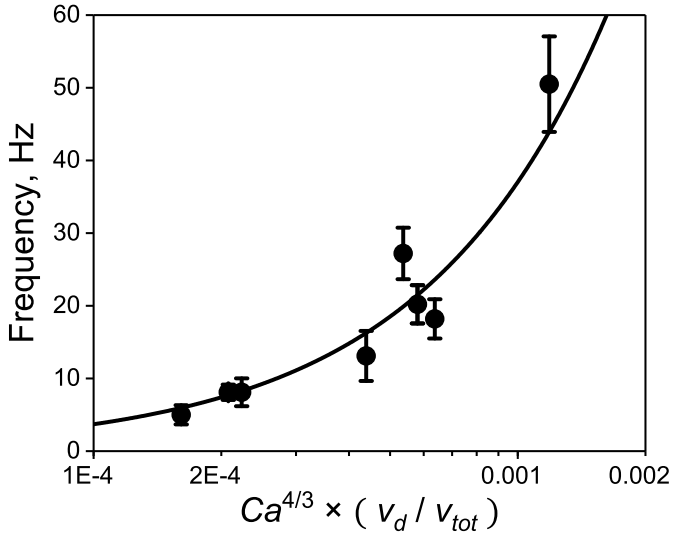

Figure 5.2 Droplet frequency vs. $Ca^{4/3} \times \frac{u_d}{u_{tot}}$. The black circles represent experimentally determined data by varying Q_{oil} and Q_{aq} while maintaining a constant channel geometry. The curve is a fit of the data with eq 5.1 where K = 3.7 ± 0.2 m/s.

5.4.3. Correlations between Flow Rates, Crystal Hit Fraction and Diffraction Quality

During the beam time experiment, we investigated the influence of the aqueous and oil flow rates on the crystal hit fraction, defined here as the number of diffraction patterns from crystals divided by the total number of X-ray pulses. In these experiments, the droplet generation was not synchronized with the EuXFEL pulse trains. If we assume a plug-flow model for the liquid jet, measurement conditions in which the droplets are unsynchronized with respect to the X-ray pulses, a constant nozzle sheath gas pressure, and an X-ray beam larger than the segmented jet

diameter, we expect the hit fraction to be proportional to the ratio $p_{aq} = \frac{Q_{aq}}{Q_{tot}}$, which represents the probability that an aqueous segment is illuminated by the X-rays in a randomly selected X-ray pulse. Moreover, we expect the hit fraction to be proportional to the total X-ray-illuminated volume of liquid, which is proportional to the square of the jet diameter, d_{jet}. The jet diameter in turn is proportional to $\sqrt{Q_{tot}}$ because the jet speed is nearly fixed by the sheath gas pressure drop.[257] The probability of hitting a crystal, p_{xtal}, is proportional to the X-ray beam diameter and d_{jet}^2. Multiplying the two probabilities, we expect the hit fraction to simply be proportional to Q_{aq}.

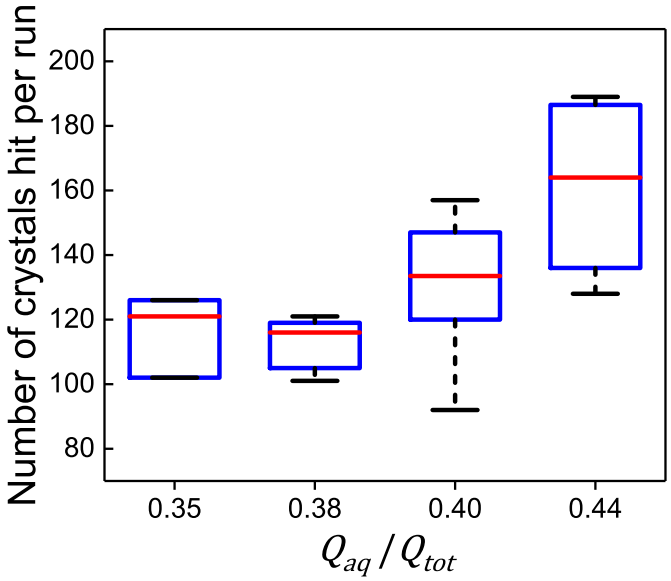

Figure 5.3 Comparison of the number of crystals hit per run at different oil and crystal suspension flow rate ratios. The oil flow rate is fixed at 15 μL/min, and crystal suspension flow rate is varied. The box plots show the number of crystals hit per run at each condition: the box contains 50% of the data, whiskers include 5-95% of the data, and the red line in the box shows the median value. An average 5 runs per data point are included.

In Figure 5.3, several flow rate conditions are summarized underlining this behavior with the oil flow rate fixed at Q_{oil} = 15 μL/min whereas Q_{aq} is varied. The number of

hits is increased as $\frac{Q_{aq}}{Q_{tot}}$ increases, indicative of more crystal suspension present in the segmented jet, and thus an increased hit fraction as discussed above. Our observations were thus in agreement with expected dependencies for aqueous and oil flow rates when synchronization with the EuXFEL was not achieved.

KDO8PS diffraction data quality was further compared for crystals suspended in droplets of a segmented jet with the same sample suspended in a continuous jet (no oil present). A subset of data containing 13 runs for continuous injection and 67 runs for droplet injection was selected for this analysis obtained from the same crystallization batch (1 run = 2 min). The crystal suspension was continuously injected with a flow rate of 10 µL/min for a total of 26 min (13 runs), generating an injected volume of 260 µL and resulting in 577 crystal hits. This continuously injected sample was compared to segmented flow injection of the same sample batch over the same amount of time. In the segmented case, droplets were generated at different flow rate conditions, varying from 5 µL/min to 3 µL/min for Q_{aq}, summing up to a total volume of 110 µL of crystal suspension injected over 13 runs. The average Q_{aq} during this time was 4.2 µL/min, resulting in 735 crystal hits. During continuous crystal suspension injection, 2.2 hits/µL were collected while 6.6 hits/µL were collected during segmented flow injection (see also Table 5.1).

Despite the observed hit fraction being small compared to previous SFX experiments at the LCLS,[26, 258] it is similar to that observed in other SFX experiments conducted during the early user beam times at the EuXFEL.[47, 259] This decreased hit fraction is caused by the large beam diameter of ~20 µm (compared to 2 µm at LCLS and 1 µm at SACLA for example) combined with the low pulse energy of 0.25 mJ (compared to the higher pulse energy of up to 4 mJ at LCLS). In order to measure higher resolution data, much larger crystals would be required for these experiments compared with other XFELs. These larger crystals are more prone to clogging and

thereby much less crystal density can be reached. However, we also note that in comparison to continuously injected sample, the number of crystal hits per sample volume is increased by 3-fold and the sample consumption is reduced by ~ 60% during the segmented flow injection. Concomitantly, the diffraction quality is comparable for both cases with regard to average resolution, highest resolution, average number of peaks per pattern for all hits, and average number of peaks per indexed pattern, as listed in Table 5.1. Overall, KDO8PS crystal suspension was injected using segmented flow for a total of 134 minutes summed over the entire beam time, where data collection was possible. Within this time, the crystal suspension flow rate ranged between 3 and 12 µL/min injecting a total volume of 962 µL of suspension. An average of 6.0 hits per µL of sample was obtained with an average resolution of 4 Å. This clearly indicates that the surrounding oil did not impact crystal quality and did not affect the data quality for structure determination. A representative diffraction pattern for KDO8PS is shown in Figure B.5.

Table 5.1 Data collected from continuous crystal suspension injection and crystal suspension injected with segmented flow

Condition	*Continuous Flow*	*Segmented Flow Injection*	
Collection total time (min)	26	26 (out of 134)	134
Volume injected (µL)	260	110	962
Total hits	577	735	5770
Average number of hits per µL	2.2	6.6	6.0
% indexed	53.6%	44.8%	51.9%
Average number of peaks per pattern	16.6	21.0	38.3
Average number of peaks per indexed pattern	23.1 ± 10.4	25.5 ± 17.5	35.5 ± 23.9
Average resolution (Å)	4.12	4.40	4.00

Note: Crystals were from the same crystallization batch for both continuous and segmented flow.

5.4.4. SFX structure of KDO8PS

The SFX structure of KDO8PS was solved based on all collected data where droplet formation was confirmed *via* the in-line droplet detector. The mean of unit cell constant distributions (Figure B.3) were calculated to be a=b=c=118.4 Å and $\alpha=\beta=\gamma=90^\circ$ by cell_explorer, part of the CrystFEL package.[123] Of the 37,000 patterns classified as hits, 16,777 could be indexed and 15,777 patterns were included in the final set of merged reflections (1000 crystals were rejected by partialator during the merging) and used for structure determination. Detected diffraction peaks reached a resolution of 2.8 Å (Figure B.5). An overview of the data collection and processing parameters and statistics is presented in Table B.1 and Table B.2.

It has been reported previously[249, 260] that refinement of the KDO8PS structure is particularly difficult due to the inherent heterogeneity of the arrangement of

monomers in the KDO8PS tetramer, and three 2-fold symmetry axes intersecting in the center of the tetramer. This was observed for the data presented here, with the structure refining to a final Rwork/Rfree of 18.8/26.1. This is in good agreement with the structure published previously by Vainer et al.[249] which was also solved by applying molecular replacement, but at cryogenic temperatures using conventional data collection methods. Furthermore, the structures reported by both Radaev et al.[260] and Vainer et al.[249] have a missing, unstructured loop region ranging from residues 205 to 218. In our case residue CYS-206 showed clear electron density and was therefore included in the model (Figure 5.4a,b). A further deviation to the previously published model by Vainer[249] was found in the loop region ranging from residue 246 through to 251, which was modified from the 1X8F search model in accordance with the clear deviation present in the electron density (Figure 5.4c). This loop is completely omitted from the structure published by Radaev et al.,[260] indicating that it is a highly flexible loop. Radaev further reports that each monomeric unit making up the tetramer binds up to 3 sulfate ions with varying occupancies. We could however not reliably place any sulfate ions in our model, and only 2 potential solvent molecules were visible in the calculated electron density.

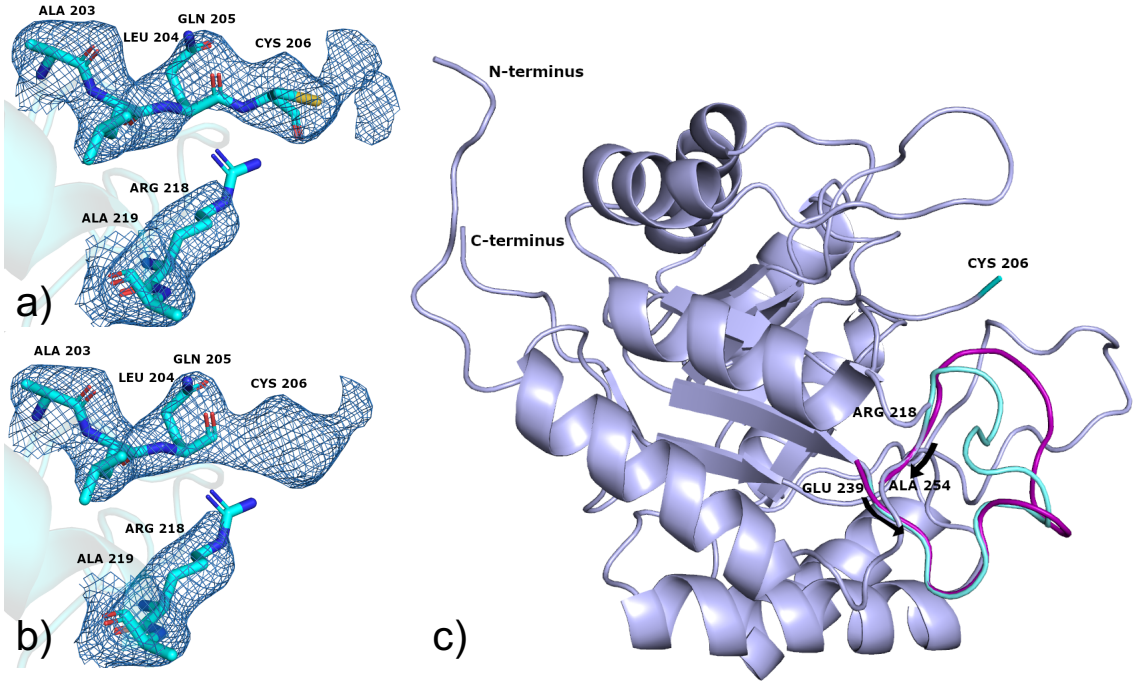

Figure 5.4 Structural differences between our refined model and the pdb entry 1X8F used as the search model. (a,b) 2Fo-Fc electron density map contoured at 1.0 σ in the undefined loop region ranging from amino acids 205 through 218 missing in the search model 1X8F. Residule electron density can clearly be seen extending beyond GLN-205 (b) and a cysteine was built into position 206 and refined (a). (c) Cartoon plot of the refined model superimposed on pdb entry 1X8F. The different loop placement (residue range 246-251) is highlighted in cyan (refined model) and magenta (pdb entry 1X8F).

5.5. Conclusion

We have presented an effective way to mitigate the sample waste inherent to continuous liquid sample injection for SFX at pulsed XFEL sources, a challenge exacerbated by the unique pulse structure of the EuXFEL. We demonstrated that a 3D printed microfluidic droplet generator can be integrated into the workflow of an SFX experiment at the SPB/SFX instrument at the EuXFEL and have successfully injected droplets containing protein crystals into the MHz repetition rate X-ray beam. In comparison to continuous injection from a GDVN, segmented flow injection resulted in a higher number of crystal hits per volume, while maintaining the same quality of SFX data.

A room temperature structure of KDO8PS was determined from microcrystals delivered with the segmented flow generator. The electron density revealed additional detail compared to previously-reported KDO8PS structures determined at cryogenic temperatures,[249, 260] such as the CYS-206 residue as well as a different loop placement in the residue range 246-251 (Figure 5.4c). The results outlined in this article paint a promising future for segmented flow sample delivery mitigating the sample waste problem of the unique pulse structure of the EuXFEL. With droplets synchronized with the frequency and phase of the X-ray pulses, we expect a further reduction in the volume of sample consumed, allowing one to explore new crystal samples that do not crystallize readily in large volumes. Such efforts to synchronize droplets in a 3D printed droplet generator *via* electrical triggering are currently being explored.[105] Furthermore, the droplet generation frequency is tunable, presenting a promising future for segmented flow sample delivery of scarce, hard-to-crystallize samples and more efficient data collection for studying macromolecular dynamics at other current and future XFELs.

CHAPTER 6

3D PRINTED MIXERS FOR MIX-AND-INJECT SERIAL CRYSTALLOGRAPHY

6.1 Introduction

One of the exciting avenues exploitable by serial femtosecond crystallography (SFX) with an X-ray free electron laser (XFEL) is the potential to obtain crystal structures of reaction intermediates with time-resolved (TR-) SFX.[20, 36] As detailed in Chapter 1.2, there are two main methods for TR-SFX: the pump-probe method that utilizes an excitation laser pulse to trigger a photoactivated reaction before the protein crystal is probed by the X-ray, and mix-and-inject serial crystallography (MISC) that mixes a protein crystal suspension with an aqueous substrate before injection into the X-ray beam.[70] While pump-probe TR-SFX has been pivotal in structure determination for reaction intermediates on time scales of hundreds of femtoseconds or greater,[228] the method is typically limited to photoactive proteins. There are many protein reactions that are not triggered by light, but instead occur when a substrate interacts with the protein such as the antibiotic ceftriaxone binding to a β-lactamase protein[50], or the 3-deoxy-*D*-manno-octulosonate 8-phosphate synthase (KDO8PS) protein catalyzing a condensation reaction of phosphoenolpyruvate and *D*-arabinose 5-phosphate.[261] For these non-photoactivated reactions, MISC is an ideal TR-SFX method.

One simple way to accomplish MISC is by using a commercial T-junction to intersect a protein crystal suspension with a substrate solution. This method permits reaction intermediate time points, t_r, on the order of seconds or greater.[33, 48] To reach smaller t_r, a MISC injector has been developed by Calvey et al.[49, 51] This injector uses the principle of hydrodynamic focusing for fast mixing by diffusion as detailed in Chapter 2.4. It then becomes feasible to reach $t_r \sim 10^1$ ms or greater with a short mixing

time, t_{mix}, in this example, t_{mix} ≤ 3.3 ms.[50, 51] A drawback to this MISC injector is its complex fabrication and assembly (>100 steps), as it requires specialized setups that include a custom-built UV-curing station and a laser cutting setup, and technical skill in microassembly and nozzle polishing.[51] Additionally, since the mixer and nozzle are handmade, there is likely interdevice performance variation.

To address these drawbacks, a 3D printed mixing device that utilizes hydrodynamic focusing for mixing by diffusion on the millisecond timescale has been proposed. With advances in 3D printing technology from the Photonic Professional GT (Nanoscribe) printer that permit printing resolution of > 500 nm, it is possible to design and fabricate a custom microfluidic mixing device based on the requirements of the protein crystal suspension and substrate solution. It has also been demonstrated that nozzles can be 3D printed,[47, 90, 141] and the automated construction of critical components like the mixing region and nozzle can decrease variations in device performance.

In order to determine the appropriate operating parameters (e.g. flow rate, channel geometry, delay length, etc.) to achieve a specific t_{mix} and t_r, numerical models can be used to solve the Navier-Stokes and convection-diffusion equations. The Navier-Stokes equation is solved to determine the velocity flow profile within the device, and the convection-diffusion equation is solved to determine the concentration profile within the device. With the results from this model, t_{mix} can be calculated without the need to experimentally use precious protein crystal suspension or substrate solution. By varying the flow rates of the center, Q_c, and side inlets, Q_{sides}, and flow ratios (Equation 2.10), φ, t_{mix} and t_r can be varied in real time to probe multiple reaction intermediates. In this way, progress can be made towards assembling a molecular movie of a protein reaction.

Fluorescence microscopy experiments can be performed to verify that the numerical models reflect experimental conditions. In these experiments, a fluorescent solution hydrodynamically focuses a non-fluorescent solution. The fluorescence intensity profile along the center focused stream (Figure 2.6) in the microscopy experiment can be compared to the numerical model for verification. There are still challenges regarding the fluorescence microscopy experiments, as will be discussed in Chapter 6.4.3, and thus far the fluorescence experiments have not agreed with the numerical models. To this extent, potential explanations for the discrepancies are provided and potential solutions are proposed.

In addition to device characterization with numerical modeling and fluorescence microscopy, four main types of mixers have been developed for a variety of t_r ranging from 10^0 – 10^3 ms. These devices include 3D printed mixers connected to a nozzle by a fused silica capillary and a 3D printed mixer with an integrated nozzle. The long capillary-coupled mixer (CCM) device was utilized at the MFX end station at LCLS to determine a structure for the Pr intermediate of the oxidation of cytochrome c oxidase (t_r = 8 s).[57]

6.2 Materials and Methods

6.2.1 Chemicals and Materials

IP-S photoresist and ITO-coated glass slides were purchased from Nanoscribe GmbH (Germany); SU-8 Developer from Microchem (USA); isopropyl alcohol, rhodamine B, pentaerythritol triacrylate (PETA), Phenylbis(2,4,6-trimethylbenzoyl)phosphine oxide (BAPO), fluorescein sodium salt, potassium phosphate monobasic, and sodium phosphate dibasic from Sigma (USA); polydimethylsiloxane (PDMS) from Dow Corning (USA). Alexa Fluor 488 dye was purchased from Fisher Scientific Company (USA). Fused silica capillaries were purchased from Polymicro (Molex, USA);

Double/Bubble® red extra fast drying epoxy adhesive from Hardman (USA); 3 μm aluminum oxide lapping film from Allied High tech products, Inc. (USA); Polyetherether ketone (PEEK) tubing from Zeus (USA); 5 mL plastic syringes from BD (USA); syringe filters (0.2 μm) from Thermo Scientific (USA). Ultrapure water from Millipore (USA) and Elga (UK) water purification systems. Fluidic connections were from IDEX Health & Science (USA).

6.2.2 3D Printing

A 3D CAD drawing was created using AutoCAD (Autodesk Inc., USA) and SolidWorks (Dassault Systèmes, France), which was then imported into DeScribe (Nanoscribe GmbH, Germany) to create a printing file. The file was composed in solid mode for structural integrity. Since the device was too large to print in one continuous piece, the solid was split into blocks (240x240x150 μm^3) such that each block has a slight overlap (3 μm) with adjacent blocks to stitch together a complete solid device. The range of the piezo motor is 300 μm, so any design larger than that must be split into blocks to ensure accurate printing. Each block is set to print individually, and each subsequently printed block progresses such that one plane of the full device is printed before the z-drive of the Nanoscribe lowers the objective and begins printing the next plane of blocks. During the block splitting process, the position of the blocks was modified to ensure blocks edges did not overlap any critical portions of the mixer such as the cross intersection. The device was printed using a Photonic Professional GT (Nanoscribe GmbH, Germany) two-photon 3D printer using a 25x objective (numerical aperture (NA) 1.4), with photoresist on an ITO-coated glass slide operating in dip-in laser lithography mode. The photoresist was either IP-S or PETA with 1.2% (w/w) BAPO as the photoinitiator (PETA photoresist).[262-264] A detailed printing description is provided in Appendix C.

After printing, the non-polymerized photoresist was removed using SU-8 Developer followed by rinsing with isopropyl alcohol. When using the PETA photoresist, ethanol was used instead of SU-8 developer. Wetted with isopropyl alcohol, the device was imaged under a stereomicroscope (Olympus, USA) to visualize the channels. Since the material is transparent, the meniscus of the vaporizing alcohol in the channels was monitored to ensure that the channels were free of debris and defects. The device was allowed to dry before assembly.

6.2.3 Device Assembly

For handling, the mixing device was temporarily immobilized between two pieces of polydimethylsiloxane (PDMS) with the inlets exposed and accessible. With the aid of a stereomicroscope, fused silica capillaries were manually inserted into the inlets of the mixing device and permanently affixed with epoxy. Once the epoxy was set (~10 min), the device and PDMS were adjusted to expose the outlet, and a capillary was inserted and affixed with epoxy.

For devices utilized in SFX experiments, a nozzle was coupled to the outlet capillary. For a short CCM, the liquid line capillary of a 3D printed GDVN was attached to the mixer's outlet through the same insert-and-affix procedure with an additional step of inserting and affixing the capillary for the helium gas in the 3D printed nozzle. For a long CCM, the liquid line of a traditional glass GDVN was connected by a union to the mixer's outlet capillary. When assembling a hybrid device, the capillaries for the liquid lines and gas line are inserted and affixed at the same time, and there is no outlet capillary as the nozzle is integrated with the mixer.

6.2.4 Fluorescence Detection

For experiments using Rhodamine B, a 110 μM solution of aqueous Rhodamine B in 50 mM pH 7.4 phosphate buffer was used to visualize hydrodynamic focusing within the device. Water from an HPLC pump (LC-20AD, Shimadzu, Japan) was driven through PEEK tubing at a constant flow rate and applied positive pressure to a Teflon piston within a steel reservoir[133] that contained a solution of phosphate buffer. The displaced liquid was then driven through the fused silica capillary and into the center inlet of the mixing device. Plastic 5 mL syringes containing the rhodamine B solution were driven by a dual syringe pump (Pump 11 Pico Plus Elite, Harvard Apparatus, USA). The center flow rate was monitored using an in-line flow rate sensor (SLG0075, Sensirion, Switzerland) between the HPLC pump and the steel reservoir. Fluidic connections were made with IDEX fittings, Zeus tubing, and fused silica capillaries. For experiments that used Alexa Fluor 488, 10 μL aliquots of 10 mM Alexa Fluor 488 in 50 mM pH 7.4 phosphate buffer were prepared and frozen. Before each experiment, a single aliquot was thawed, diluted to the working concentration, and loaded into the plastic 5 mL syringes. The remaining fluidic setup was identical to Rhodamine B experiments. For fluorescein experiments, the setup was the same as Alexa Fluor 488 experiments, but with 1 μM fluorescein in 50 mM pH 7.4 phosphate buffer. All solutions were filtered with 0.2 μm surfactant-free cellulose acetate membrane filters (Thermo Scientific, USA) before use.

Optical brightfield and fluorescence microscopy of the hydrodynamic focusing were accomplished with an Olympus IX71 microscope (Olympus, Japan) using a 20x objective (NA 0.45) (Olympus, Japan) for Rhodamine B experiments and a 40x objective (NA 0.6)(Olympus, Japan) for Alexa Fluor 488 experiments. Light from a mercury lamp (U-LH100HG, Olympus, Japan) passed through a filter cube to excite the fluorescent dye and the resulting emission was detected with an EMCCD camera

(iXon X3, Andor, Ireland). For Rhodamine B experiments, the filter cube setup was as follows: excitation filter: 531/40 nm (FF01-531/40-25, Semrock, USA), emission filter: 607/36 nm (FF01-607/36, Semrock, USA), dichroic mirror: 593 nm (FF01-593/40-25, Semrock, USA). For Alexa Fluor 488 and fluorescein experiments, the filter cube setup was as follows: excitation filter: 470/40 nm (ET470/40 X 204556, Chroma, USA), emission filter: 525/50 nm (ET525/50 M 204808, Chroma, USA), dichroic mirror: 495 nm (U-N49002, Chroma, USA). Images were acquired with MicroManager (Fiji, USA) and processed with Fiji (Fiji, USA) and Matlab (MathWorks, USA).

Mixers designated for fluorescence microscopy experiments were immobilized on a 1 mm glass slide with epoxy applied between the capillaries and the glass slide. The mixing device was flat on the glass slide. Before imaging IP-S mixing devices, they were photobleached for ≥ 2 hours by exposure to the excitation light.

6.3 Numerical Modeling

Using COMSOL Multiphysics 5.3 (COMSOL Inc., Sweden), the flow profile and concentration profile within a microfluidic device were modeled. The following is a detailed description of the modules and components within the module.

Two-dimensional and three-dimensional stationary studies using the laminar flow and transport of diluted species modules were developed in COMSOL Multiphysics 5.3. The 2D study was used to model mixing devices with square channels. As the channels and flow profile are symmetric in the square channels, a 2D study is representative of the center xy-plane of the device and was used to reduce the computational power and time. Three-dimensional studies were used to model mixing devices with cylindrical channels as the curvature is not necessarily well modeled in a 2D study. Additionally, three-dimensional studies were also used to

model square channels (Figure 6.6) for comparison with the 2D models. As the hydrodynamic focusing profile operates at steady state in a laminar flow regime, a stationary study is useful for reducing computational power while maintaining results representative of experimental conditions. In a MISC experiment, the profile would not be steady state due to the protein crystals that pass through. This discrepancy between model and experiment can be reconciled in two ways depending on crystal size. If the crystals are smaller than w_f, then the impact the crystals have on the shape of the hydrodynamic focusing profile should be minimal. If the crystals are larger than w_f, then the presence of a crystal will cause a disturbance in the flow profile. Since crystals tend to stay in the center of w_f,[49] the flow profile will be similar to the modeled hydrodynamic focusing profile on average.

In the parameters tab, the following parameters were defined: initial concentration (1×10^{-3} mol/m^3, equivalent to 1 μM), density (1000 kg/m^3 for water at room temperature), viscosity (8.0×10^{-4} Pa s for water at room temperature), the hydrodynamic radius of the dye (for Alexa Fluor 488, 5.8×10^{-10} m),[265] and the flow rate for each inlet. The temperature defined in the Common Model Inputs tab was 293.15 K for room temperature. The diffusion coefficient of the dye was calculated using Equation 2.3 with the previously defined radius, viscosity, and temperature as inputs for the equation and was found to be $4.2\text{x}10^{-10}$ m^2/s, in good agreement with the literature.[265]

The geometry node was used to create a blank 2D geometry plane. A rectangular cross intersection of the device was constructed with channel widths of 120 μm using built-in geometry functions. The corners of the intersection were filleted by 5 μm to avoid any corner effects. The inlets were 150 μm in length, with a 120 x 120 μm cross intersection, and the outlet was 1 mm in length.

In the materials node, a material was created that used the same density and viscosity as defined in the parameters section. This was representative of the phosphate buffer solution as the ions of the phosphate buffer do not significantly affect the viscosity and density of the aqueous solution.

The laminar flow module solves the Navier-Stokes equation for a Newtonian incompressible fluid (Equation 2.5)[74] within the device as detailed in Chapter 2.4. In addition to the conservation of momentum represented in the Navier-Stokes equation, conservation of mass must also be satisfied, so Equation 2.6 was solved as well in this module. The discretization of fluids was set to P2 + P1, and the density and dynamic viscosity were as defined in the parameters node. Initial values for velocity and pressure throughout the geometry were zero, and the walls were no slip boundaries. Inlet boundaries were set as fully developed flow, with the flow rate being defined as listed in the parameters section. An entrance thickness of 120 μm was defined to model the flow profile within a 3D printed device. The outlet boundary was set to a pressure of zero and suppressed backflow.

The transport of diluted species (TDS) module solves the convection-diffusion equation (Equation 6.1) to determine the concentration profile within the mixer as detailed in Chapter 2.4.

$$\nabla \cdot \boldsymbol{J} + \boldsymbol{u} \cdot \nabla c = 0 \tag{6.1}$$

In Equation 6.1, $\boldsymbol{u}$ is the velocity vector, $\boldsymbol{J}$ is the molar flux (Equation 2.7), and c is the concentration. Since there is no reaction modeled, the right-hand side of the equation is zero. As the flow is laminar and with a high Pe (see Equation 2.8), the species transport in the x-direction of Figure 2.6 (i.e. the direction of the bulk flow) is dominated by convection, but in the y- and z-directions convection is negligible; thus, in the y- and z-direction, the species transport is dominated by diffusion (Fick's first law, Equation 2.7). The discretization in the TDS module was set to quadratic,

and the velocity profile was the result of the laminar flow module. The diffusion coefficient used was as defined in the parameters node. The wall boundaries were set to no flux and the initial concentration was zero throughout the geometry. Inlet boundaries for the side inlets were set to the initial concentration defined in the parameters node, while the center inlet boundary was set to zero, and an outflow boundary was set for the outlet.

The free triangular mesh was segmented into several parts. The base mesh throughout the geometry and the wall boundaries were defined with the preset extremely fine fluid dynamics mesh. In the intersection of the cross, extending 20 μm into each inlet and the outlet, the mesh was preset to the same extremely fine mesh, but the maximum and minimum element size were reduced to 0.5 and 0.001 μm, respectively. This altered extremely fine mesh was also used for the wall boundaries on the filleted corners of the intersection.

The study was split into two steps: first, the laminar flow module was solved, then, using the velocity results from the first step, the TDS module was solved. Breaking the study into two steps reduces computation time while maintaining the same results as computing the laminar flow and TDS modules simultaneously.

By varying the inlet flow rate magnitudes and flow rate ratios, φ (Equation 2.10), the mixing time, t_{mix}, was studied. The resulting velocity profile yields u_{max} in the outlet, and can thus be used when calculating d_{delay} (Equation 2.12) for a specified t_r. Center flow rates were varied from 1 – 10 μL/min, with φ from 2 – 80.

In addition to 2D models, stationary 3D models were investigated. The parameters for the 3D model were identical to the 2D model with the exception of the geometry and the mesh settings. In the geometry node, two intersecting cylinders (120 μm diameter) were constructed using the built-in geometry functions. As with the 2D model, the Navier-Stokes equation was first solved to determine the velocity flow

profile and then the convection-diffusion equation was solved to determine the concentration profile within the device. To compute the results in a reasonable amount of time, a coarser mesh than the 2D model was used: instead of extremely fine, the mesh was set to normal.

6.4 Results

6.4.1 3D Printed Mixer

Mixing devices (Figure 6.1) were designed to couple with existing SFX sample delivery setups, as well as to optimize print time and structural stability. First, the channel dimensions were selected to prevent clogging of microcrystals within the device. A large inner diameter relative to the average crystal size reduces the likelihood that a crystal will get stuck and clog the device, which then would require time-consuming cleaning or device replacement. At a time-sensitive XFEL experiment, device robustness is of great importance. For working with protein crystals with an average size of 20 x 20 x 4 μm^3, such as the cytochrome *c* oxidase crystals used in Ishigami, et al.,[57] a channel width, w_c, of 120 μm was selected to minimize clogging risk. The outlet length (400 μm) within the 3D printed device was not crucial as the capillary connecting the mixing device with the GDVN was three orders of magnitude longer, and thus would be the main factor in determining the reaction intermediate time point, t_r. The fluidic channels were cylindrical for the majority of printed devices, although devices with square channels to eliminate lensing effects during fluorescence microscopy were developed later. The square devices maintained the same w_c.

Next, the device must interface to sample reservoirs and injection nozzles. These connections are commonly accomplished with PEEK tubing and fused silica capillaries. Since the PEEK tubing (1/16” outer diameter (OD)) is too large for a

Nanoscribe 3D printed device, the inlets and outlet were designed to interface with 360 µm OD fused silica capillary instead. In earlier designs, the transition from capillary to 3D printed fluidic channels used a cone that decreased from 360 µm OD of the capillary down to w_c (Figure 6.1a). Later iterations instead had an increasing cone with the base positioned flush with the 100 µm fluidic hole in the capillary and transitioning to the larger w_c (Figure 6.1).

Some iterations of the CCM omitted much of the unused space in the device (i.e. no fluidic channels or capillary ports) to reduce printing time. The walls of the device were all connected and thick enough (≥100 µm) to maintain structural stability during handling.

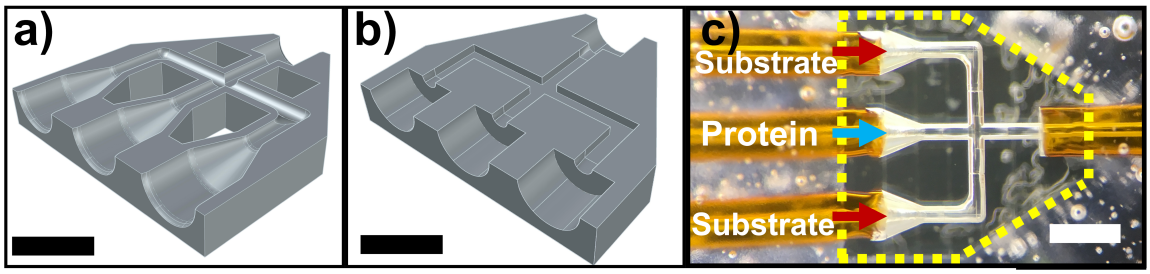

Figure 6.1 Design of the mixing device. (a-b) CAD drawings of a horizontal slice halfway through the mixing device for visualization of the channels. The channels are (a) cylindrical or (b) square. (c) A brightfield microscopy image of an empty, assembled device surrounded by epoxy. The device outline is highlighted with yellow dashes, and the inlets are labeled with their corresponding liquid. The channel geometry is identical to (a) without the holes cut out to reduce printing time. Scale bars are 0.5 mm.

6.4.2 Numerical Models

Numerical models were performed to calculate the flow velocity profile and the concentration profile within the cross intersection of the mixing device (Figure 6.2). A detailed description of the model was described in Chapter 6.3.1. The parameters of Q_c and φ were varied to study the effects on t_{mix}, d_{mix}, and u_{max}. Q_c ranged from 1 – 10 µL/min and φ ranged from 2 – 80. The side inlet species is representative of

Alexa Fluor 488 dye, Rhodamine B, or fluorescein as all have essentially the same D.[265-267]

As can be seen in Figure 6.2, as φ is increases, the focus stream width, w_f, decreases. In these models, c_{mix} is defined as the concentration that is half the initial normalized concentration. The numerical model is defined as fully mixed once the concentration in the center of the outlet has reached c_{mix}, as the center is the furthest distance for the side solution to diffuse to (the yellow dashed line in Figure 2.6). In Figure 6.2a, the center of the focused stream does not reach c_{mix} at φ = 4 within the modeled outlet distance (1000 µm, extending past the viewing region of Figure 6.2a). In Figure 6.2b, φ = 16, and the center line is approaching c_{mix} at the end of the outlet, but only reaches a normalized concentration of ~0.3 at the end of the 1000 µm outlet (which extends past the viewing region in Figure 6.2b). In Figure 6.2c, φ = 40, and c_{mix} is reached at 160 µm after the center and sides solutions meet at the end of the center inlet.

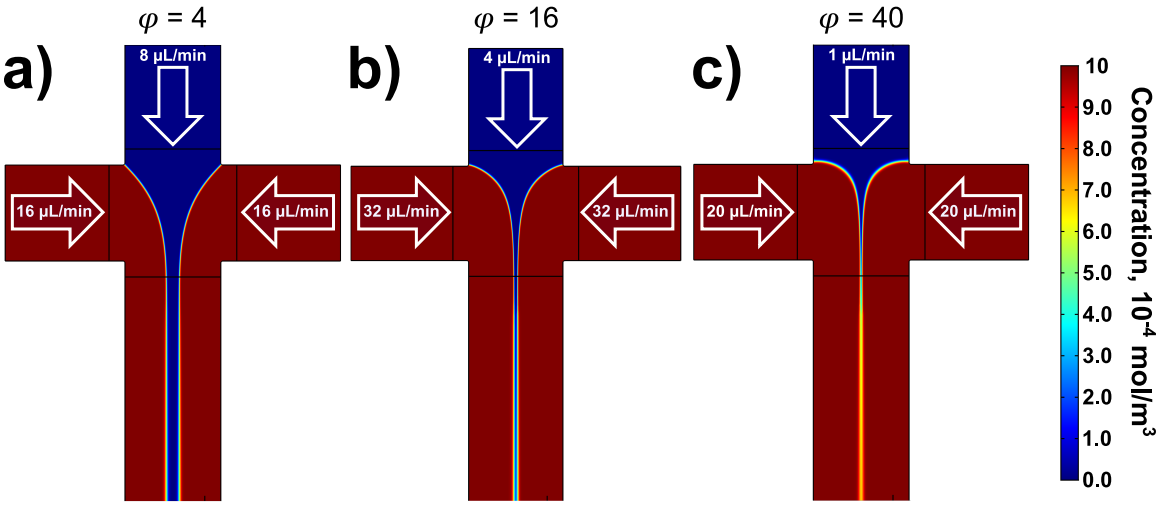

Figure 6.2 Concentration surface plots calculated from the transport of diluted species module in COMSOL Multiphysics 5.3. The plots are ordered by increasing φ. (a) Q_c = 8 µL/min, Q_{sides} = 16 µL/min, Q_{tot} = 40 µL/min, (b) Q_c = 4 µL/min, Q_{sides} = 32 µL/min, Q_{tot} = 68 µL/min, (c) Q_c = 1 µL/min, Q_{sides} = 20 µL/min, Q_{tot} = 41 µL/min. Larger φ results in a smaller w_f. Channel widths are 120 µm.

The velocity at the center of the outlet, u_{max}, is determined from the result of the velocity profile, and is used when calculating t_{mix} (Equation 6.2) and d_{delay} (Equation 2.12).

$$t_{mix} = \sum_{n=0}^{d_{mix}} [(d_{n+1} - d_n)/u_n] \tag{6.2}$$

In Equation 6.2, d_n is the distance along the center velocity profile (white dashed line in Figure C.1) with corresponding velocity, u_n. Equation 6.2 is the sum of discrete time steps between d_0 and d_{mix} that are calculated using the velocity at each step. A cut line that proceeds from the center of the d_0 until the end of the modeled outlet (Figure 2.6) can be dictated in the Results node of COMSOL. From this cut line, the concentration and velocity profiles at discrete points along the line can be extracted. Using Equation 6.2, t_{mix} is calculated using the velocity and distance values from the extracted velocity line plot. Some examples of modeled mixing times are illustrated in Figure 6.3.

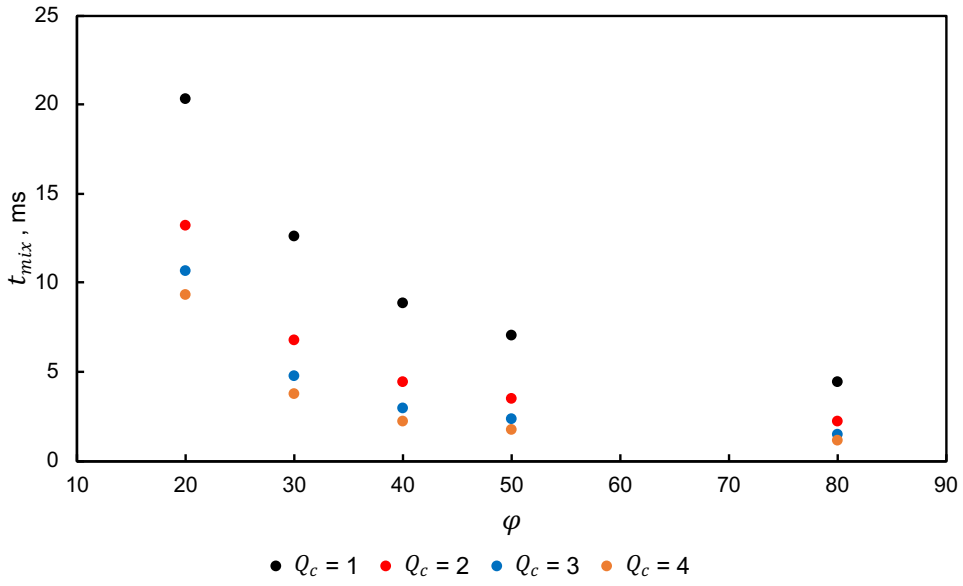

Figure 6.3 Projected mixing times, t_{mix}, for flow rate ratios, φ, at various center flow rates, Q_c.

For every Q_c, as φ increases, t_{mix} decreases (Figure 6.3). This relationship is expected as Equation 2.9 and 2.10 illustrate that w_f decreases with φ, and with Equation 2.10 the relationship between φ and t_{mix} can be seen. Q_c and Q_{tot} also contribute to the t_{mix}. As the flow rate increases, so does the velocity, and thus it takes less time to get from d_0 to d_{mix}. This relationship can be seen in the decreasing t_{mix} for increasing Q_c at a constant φ.

6.4.3 Experimental mixing time determinations

Mixing with a fluorescent dye was performed experimentally with an inverted fluorescence microscope in order to validate the accuracy of the numerical modeling. A mixing device made from IP-S photoresist was used for the first mixing tests. The assembled device affixed to a glass slide was inverted when mounted on the microscope's xy-stage such that only air was present between the objective and the 3D printed mixing device. This setup allowed the inlet and outlet capillaries to extend past the microscope stage and connect to the liquid reservoirs. The 110 μM Rhodamine B fluorophore solution entered from the side inlets and focused the phosphate buffer solution from the center inlet (Figure 6.4a). The device was visualized using a 20x objective.

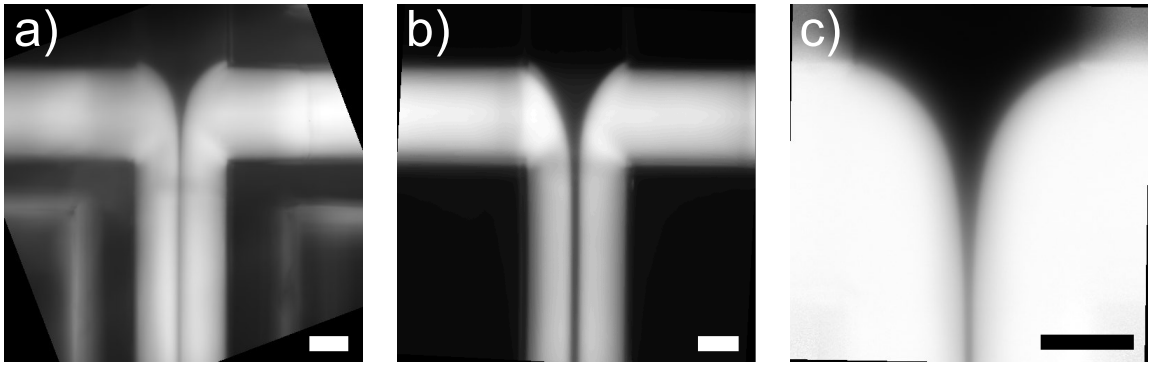

Figure 6.4 Fluorescence microscopy images of the intersection of a mixing device. Flow rates in each condition are Q_c = 4 µL/min, Q_{sides} = 32 µL/min, Q_{tot} = 68 µL/min. (a) IP-S mixing device with the 110 µM Rhodamine B solution in the side inlets and phosphate buffer in the center inlet. (b) PETA photoresist mixing device with the same solutions as (a). Magnification for (a-b) is 20x and channels are cylindrical. (c) PETA photoresist mixing device with 0.1 µM Alexa Fluor 488 in the side inlets and phosphate buffer in the center inlet. Magnification is 40x and the channels are square. The black corners in (a,c) are due to rotation during image processing. Scale bar is 50 µm.

While the hydrodynamic focusing profile can be seen in Figure 6.4a, the device material contributed a significant amount of background fluorescence. This is most notable in Figure 6.4a at the edges of the device where the holes are cut out to reduce printing time (see Figure 6.1a). To address this background, the images were normalized with Equation 6.3.

$$I_{Normalized} = (I - I_{min})/(I_{max} - I_{min}) \tag{6.3}$$

In Equation 6.3, the minimum intensity, I_{min}, was an image of the channel filled with buffer (absent of fluorophore) and the maximum intensity, I_{max}, was an image of the channel filled with the fluorophore solution. Even after each pixel was normalized, the resulting center intensity curve (Figure 6.5) did not align with the results from the numerical model. The experimental intensity curve began increasing at d_0, which is earlier than the model and earlier than when one would predict with Equation 2.2. A potential explanation for the early fluorescence increase and shorter d_{mix} was that the emitted light from the fluorescing Rhodamine B molecules was acting as an

excitation light source for the photoinitiator within the IP-S photoresist of the 3D printed mixing device. The resulting autofluorescence from the device would result in an increased I (Equation 6.3) where no fluorophore is present and I_{min} would be insufficient for the background correction. Furthermore, the photoinitiator within IP-S has a high autofluorescence which contributes to a large I_{min}.

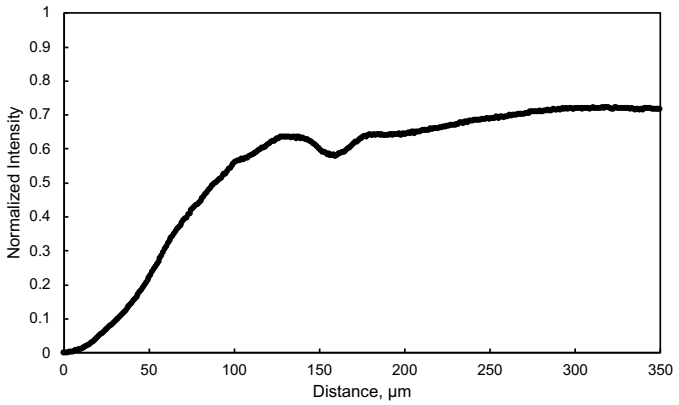

Figure 6.5 Plot of the normalized fluorescence intensity along the center of the device from d_0 to the end of the outlet for the flow conditions in Figure 6.4a.

To address the background fluorescence and autofluorescence from the IP-S device, an alternative photoresist was utilized. The device was printed in the PETA photoresist, which has been shown to have low autofluorescence with common fluorescence microscopy filter cube setups.[264] The experiment was repeated in the PETA photoresist device with the same fluorophore solution and buffer solution (Figure 6.4b), and the background fluorescence was two orders of magnitude lower than with IP-S. However, the issues of early fluorescence intensity increase and short d_{mix} persisted. A potential explanation was that the cylindrical channels were causing a lensing effect or reflecting the fluorophore light such that the focused stream appeared to have intensity where there was no fluorophore present. An additional concern was that the concentration of Rhodamine B was too high, and that

fluorophores were forming dimers and quenching which could affect the mixing profile.[268]

To eliminate the potential sources of error associated with cylindrical channels, a device with square channels was developed. Additionally, the dye in the fluorophore solution was changed to Alexa Fluor 488 or fluorescein to address the dimerization concern.[269] With the PETA photoresist device with square channels and 1 μM fluorescein dye, the experiment was repeated using a 40x objective for visualization (Figure 6.4c). While the shape of the focusing profile matches well with the numerical model, the center normalized intensity profile does not match with the models (Figure 6.6).

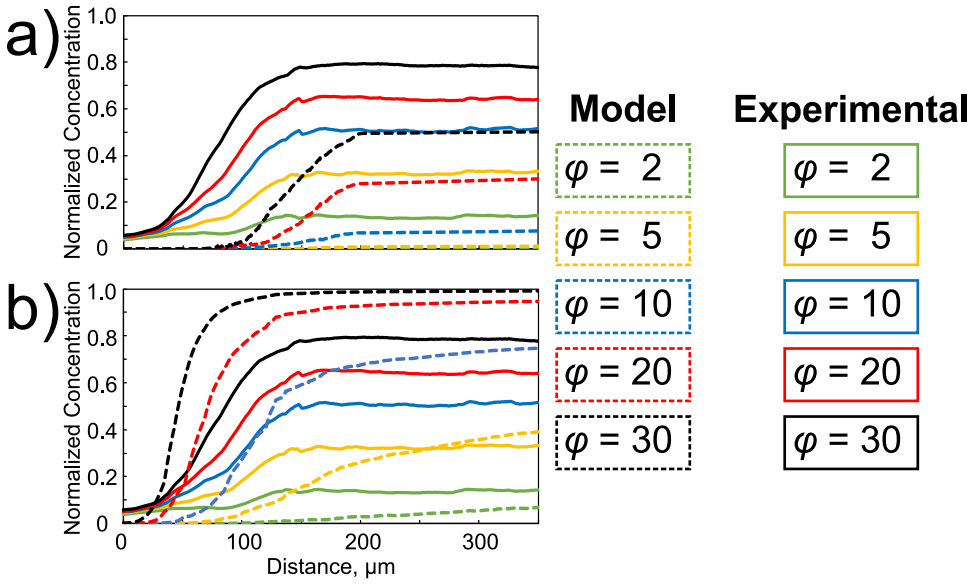

Figure 6.6 Plot of the center normalized concentration curves from (a) 2D and (b) 3D numerical models (dashed lines) and the corresponding normalized intensity curves from fluorescence microscopy data. Both the numerically modeled channels and the channels used experimentally are rectangular. In all conditions, Q_c = 10 μL/min.

There are three main mismatches between the normalized experimental results and the 2D model (Figure 6.6a). First, the experimental results start at a higher

fluorescence intensity than the model even after normalization. This suggests that the fluorescence emission is affecting a region where the fluorophore is not present. A potential explanation could be related to the point spread function (PSF) of the fluorophores. The focal plane is centered on the middle of the device, but since the channel is relatively large (120 μm channel height) there is likely a contribution of light from fluorophores above and below this central focal plane. For in-focus fluorophores, the PSF radius in the x and y directions is ~0.5 μm (using a 40x objective and 470 nm excitation). For fluorophores that are out of focus, their PSF would increase, and thus the fluorophores at the focusing profile boundary may potentially contribute fluorescence intensity to regions where no fluorophore is present.

Second, the fluorescence intensity increase (indicative of mixing) begins ~75 μm before the concentration begins increasing in the numerical model. The PSF of the out of focus fluorophores could also be responsible for this early fluorescence increase. As the hydrodynamic focusing profile narrows, more fluorophores get closer to the center. The increased number of out of focus fluorophores may then contribute to a higher fluorescence intensity. An alternate explanation could be due to the concentration of fluorophore being too low. If the background fluorescence is of a similar magnitude to the fluorescence of diffusing fluorophores, then the small number of fluorophores that do reach the center of the focus stream may appear to contribute more to the intensity profile.

Third, the magnitude of the intensity is greater than the 2D model. The PSF may also be an explanation for this observation as the out of focus fluorophores could contribute fluorescence intensity to the center of the focus stream even though fluorophores are not present.

In the 3D model (Figure 6.6b), there are further discrepancies between the experimental results. For φ = 10, 20, and 30, the numerical model has a higher maximum normalized concentration than the experimental maximum normalized fluorescence intensity. Additionally, the slope of the numerical model curve appears to be steeper than the experimental curve for these values of φ. However, for φ = 2 and 5, the opposite trend is observed for the maximum concentration and intensity, as well as the steepness of the slope. The PSF could be an issue for the lower values of φ as described in the 2D model discussion, but the higher values require a separate explanation. One possible explanation is due to the coarseness of the 3D mesh. As seen in Figure 6.7, the coarseness of the mesh plays a role in d_{mix}, with coarser meshes (e.g. the black dashed line) reaching d_{mix} sooner than finer meshes (e.g. the green dashed line), and the maximum normalized concentration also decreases with increasing mesh quality. A finer mesh takes smaller steps when calculating the convection-diffusion equation (Equation 6.1), and thus yields a result that should be in better agreement with experimental results. However, the computational power and time required to calculate an increasingly fine 3D mesh places practical limits on the mesh quality that can be studied. Thus, the coarseness of the mesh used for the 3D numerical studies may partially explain the discrepancy between the numerical model and the experimental results.

A second explanation to explain the decreased maximum normalized fluorescence intensity could be related to how the channel is visualized. As mentioned previously, the entire height of the channel is visualized during fluorescence microscopy data acquisition. For normalizing the fluorescence intensity (Equation 6.3), I_{max} is taken with the entire channel filled with fluorophore. Since the hydrodynamic focusing is only from the sides of the center stream (no focusing occurs on the ceiling and floor), the vertical cross section of the outlet channel concentration profile has an

hourglass-like shape, with a higher concentration at the center of the hourglass. As less fluorescence intensity would be present above and below the center region, the normalized fluorescence intensity along the center line may be less than the numerical model.

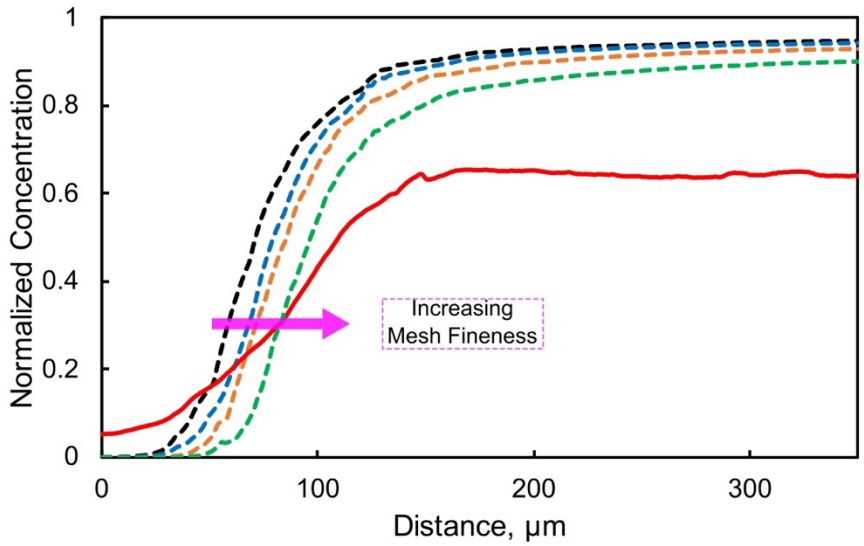

Figure 6.7 Plot of the center normalized concentration curves from a 3D numerical model (dashed lines) and the normalized fluorescence intensity curve from a corresponding experimental condition. For both numerical model and experimental conditions, the channels were square (120 x 120 μm^2) and the flow conditions were Q_c = 10 μL/min and φ = 20. The black curve was solved using a relatively coarse mesh: the fluid dynamics preset "normal" mesh. The blue curve was solved with an incrementally finer mesh (the fluid dynamics preset "fine" mesh), the orange curve was solved with a finer mesh than the blue curve (the fluid dynamics preset "finer" mesh), and the green curve was solved with a finer mesh than the orange curve (the fluid dynamics preset "extra fine").

The 3D model is also different than the 2D model, with higher maximum fluorescence intensities and earlier increased fluorescence intensity. The differences between the models can likely be attributed to the coarser mesh required for the 3D model to compute in a reasonable amount of time, as mentioned previously. While one would expect the finer mesh of the 2D model to be more accurate, the 3D model may be more reflective of experimental conditions due to the added dimension for

diffusion. Additionally, the 3D model appears to have a wider w_f (Figure 6.8), possibly due to the coarser mesh with the 3D model. Differences in the concentration profile between 3D models using square and cylindrical channels (Figure 6.8), likely attributed to the flow profile differences in the two geometries.

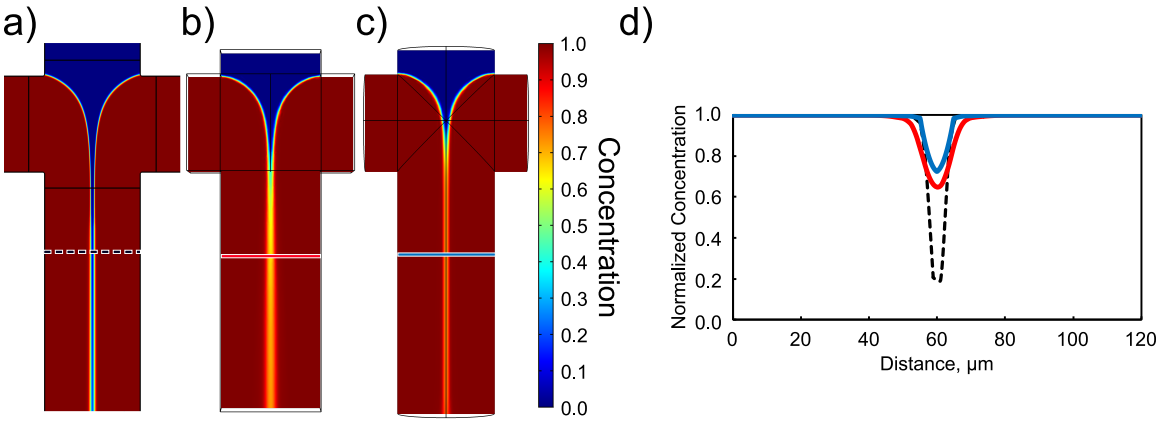

Figure 6.8 Comparison of (a) 2D and (b,c) 3D concentration surface plots calculated with the numerical model. (a) The 2D channels are square and the mesh is set to extremely fine. (b) The 3D channels are square and the mesh is set to normal. (c) The channels are cylindrical, and the mesh is set to normal. (d) Plot of the normalized concentration extracted from the horizontal cut lines in (a-c). The black dashed curve, red solid curve, and blue solid curve correspond to the similarly colored horizontal cut lines in (a), (b), and (c), respectively. The flow rate conditions for (a-c) are: Q_c = 4 μL/min, Q_{sides} = 32 μL/min, Q_{tot} = 68 μL/min. Channel widths are 120 μm.

In order to solve these problems and achieve a concentration profile that better agrees with the numerical models, there are adjustments that can be made. First, the concentration of fluorophore could be increased. As Alexa Fluor 488 does not form dimers like Rhodamine B does and the detector is not saturated, a higher concentration could reduce the early increase in fluorescence intensity. Next, confocal fluorescence microscopy could alleviate some of the PSF error as confocal setups visualize one plane at a time, reducing the influence that out of focus fluorophores will contribute. A turn-on fluorescence experiment could be performed where a non-fluorescing solution from the center inlet is focused by a solution from

the side inlets that triggers the fluorescence from the center species. As there would be much less fluorescence except where the two solutions have mixed, the contributions from PSF of out of focus fluorophores would also be decreased. Lastly, the influence the lack of hydrodynamic focusing on the ceiling and floor of the mixer (i.e. the aforementioned hourglass concentration profile) has on the numerical model and how this relates to the experimental fluorescence profile can be assessed. For instance, at a specified x-position in the mixer outlet (Figure 2.6) of the numerical model, a z-axis cut line of the concentration profile can be extracted. The average concentration from this cut line can be determined and compared with the experimental fluorescence intensity at a corresponding downstream x-position. The determined average concentration from the numerical may be lower than extracted concentration from the center x-axis cut line (Figure 2.6) at the same downstream x-position, and thus the 3D numerical model may be in better agreement with the fluorescence experiment.

6.4.4 Additional Mixer Designs

There are four main 3D printed designs for MISC. The first was a CCM designed for long t_r on the order of seconds and consists of a 3D printed mixer (Figure 6.1c) coupled to an injector by a long (>20 cm) fused silica capillary. This long CCM device was utilized to identify the Pr intermediate of the cytochrome c oxidase oxidation reaction at t_r = 8 s.[57]

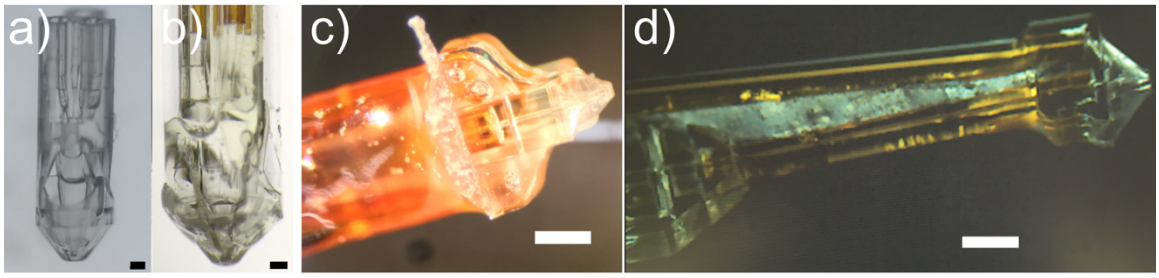

Figure 6.9 Mixing devices for various reaction time points. An (a) unassembled and (b) assembled first-generation hybrid mixing device. In (b) the device is epoxied onto a glass tube that supplies the GDVN focusing gas. (c) Assembled second-generation hybrid mixing device. (d) Second-generation capillary-coupled mixer connected by a short fused-silica capillary to a 3D printed GDVN. Scale bars in (a,b) are 200 μm, and (b,c) are 0.5 mm.

Another design aimed to reach shorter t_r on the order of 100s of ms. To accomplish this, the injector was built into the 3D printed mixer for the first-generation hybrid device (Figure 6.9a,b) At the required flow rates, the protein crystal and substrate solution were fully mixed after the first couple hundred micrometers. However, d_{delay} for the necessary flow rates was too long for printing with the Nanoscribe. In order to reach t_r ~ 10^1 - 10^2 ms a portion of the outlet had an increased diameter to facilitate a decreased u_{max} and thus decrease d_{delay}. The diameter then decreased at the transition from the mixer outlet to the nozzle geometry to enable jetting injection.

There were a few challenging aspects to the assembly of the first-generation hybrid mixer device. Removing the unexposed photoresist in the large portion of the outlet during the development step was difficult as the small inner diameter channels prevented much of the developing solution from reaching the delay region of the outlet. This frequently resulted in a blocked outlet, and thus an unusable device. To allow more developer solution to reach the channel, a hole was built into the delay region of the outlet. After development was complete, the hole was sealed with a thin layer of epoxy during assembly. Sealing the hole with epoxy was a challenging

step as too much epoxy would result in epoxy filling the outlet, yielding an unusable device, and too little epoxy would result in a leaking device which would also be unusable. Assembly was further complicated by the nonplanar arrangement of the inlets and the cylindrical shape of the device. Furthermore, due to the nozzle design,[90] the hybrid device required a delicate assembly with an additional steel rod for the focusing gas.

The second-generation hybrid device aimed to address the shortcomings of the first-generation hybrid device and study shorter reaction intermediates, t_r ~ 10^0 - 10^1 ms. As seen in Figure 6.9c, the arrangement of the three liquid inlets is planar. The nozzle geometry was updated (designed by Reza Nazari, results unpublished), and the gas inlet was integrated into the hybrid device directly above the liquid inlets, simplifying the capillary assembly. Additionally, with a shorter t_r in mind, the outlet was a uniform diameter throughout the device, and the unexposed photoresist could be removed by the developer solution without the need for holes. This design was utilized in a solution scattering experiment at the CXI end station of LCLS to study guanosine 5'-O-[gamma-thio]triphosphate (GTPγS) binding to resistance to inhibitors of cholinesterase A (Ric-8A) proteins complexed with G-protein alpha subunits (Gai). In order to reach t_r ~ 10^1 - 10^2 ms without the challenging device construction associated with the first-generation hybrid device, a second-iteration of the CCM with a shorter outlet capillary was developed (Figure 6.9d). This design requires a 3D printed GDVN with updated geometry from the second-generation hybrid device in order to connect a short capillary (≥ 1 mm) directly from the outlet of the mixer to the inlet of the nozzle. Difficulty of assembly increases with decreasing connecting capillary length, but the variability in the capillary length, and even capillary inner diameter, permit a wide range of t_r to be achievable with this short CCM design.

6.5 Conclusions

The sample delivery requirements are a key component for MISC experiments at an XFEL. Here is described the efforts towards designing 3D printed mixing devices for millisecond mixing by diffusion. Numerical models were developed to calculate t_{mix} of the mixing device, and fluorescence microscopy experiments were performed to verify the models. Although the models and fluorescence experiments have not agreed, explanations for the discrepancies were suggested. These include the PSF of the out of focus fluorophores and low fluorophore concentration. Additionally, some solutions to these problems were proposed, such as working with higher fluorophore concentrations, using confocal microscopy, and performing turn-on fluorescence experiments. Four mixing designs, two CCM and two hybrid devices, were illustrated for achieving a wide range of t_r from 10^0 – 10^3 ms. Moving forward, the proposed solutions to the fluorescence mixing experiments will be performed. Additionally, the mixing devices have been proposed to be used during MISC experiments at an XFEL to study shorter t_r for the oxidation of cytochrome *c* oxidase.

CHAPTER 7

FURTHER APPLICATIONS OF REDUCED SAMPLE CONSUMPTION FOR SFX

7.1 Introduction

In addition to the works in the previous chapters, additional experiments that involve sample delivery for SFX have been accomplished. The results of these experiments have either been published as conference proceedings or are accepted for publication in journal articles. This chapter details the abstracts of which are listed in Chapter 7.2-7.5.

7.2 Biphasic Droplet-Based Sample Delivery of Protein Crystals for Serial Femtosecond Crystallography with an X-ray Free Electron Laser[71]

7.2.1 Abstract

Serial femtosecond crystallography (SFX) laser pulses facilitate the structure determination of smaller crystals than can generally be studied by traditional synchrotron crystallographic methods. One limiting factor of SFX is the large volume of crystal suspension needed to obtain a full data set allowing structure determination. The current method of continuous sample stream injection into an X-ray free electron laser (XFEL) requires milliliters of sample and wastes the majority of the protein crystals grown under time consuming conditions. We propose the utilization of aqueous droplets as an efficient method for protein crystal delivery into an XFEL for structure determination by SFX.

7.2.2 Introduction

Traditionally, protein structure has been determined by X-ray crystallography performed at a synchrotron. Membrane proteins have been difficult to analyze by traditional crystallographic methods for several reasons: growing large enough crystals to withstand long, high-intensity X-ray pulses is time consuming, if not impossible for certain proteins, and smaller crystals that are easier to grow are destroyed before diffraction patterns can be collected.[19] Serial femtosecond X-ray crystallography (SFX) utilizes a high-intensity X-ray free electron laser (XFEL) with extremely short pulses to obtain diffraction patterns of small protein crystals before they are destroyed.[19]

Currently, a continuous stream of crystal suspension is injected into the XFEL.[132] Since the femtosecond laser operates at a frequency of 120 Hz, the time between the pulses results in unused sample injected. The unused sample cannot be recovered and therefore becomes waste. The process to crystallize even a small amount of large protein complexes is resource intensive, so a suitable method of sample conservation is necessary. To accomplish this goal, we aim to generate aqueous sample-containing droplets in an oil carrier phase and synchronize these droplets to the pulses of the laser. This method would effectively replace the wasted crystals with non-precious oil when the laser is off, and we show the first experimental evidence of coupling a microfluidic device to the injector used in an SFX experiment.

7.2.3 Experimental

Microchips made from polydimethylsiloxane (PDMS) with a flow-focusing channel geometry[94] were fabricated using traditional photolithography and soft lithography methods.[270] A 2 cm piece of fused silica capillary (100 μm inner diameter) was

inserted into the outlet channel between two oxygen plasma treated PDMS pieces. A PEEK cross-connection fitting (150 μm inner diameter) (IDEX, USA) was used as another method of droplet generation. Reservoirs and GP1 pressure regulators (Proportion-Air, USA) were used to supply liquids and pressure, respectively. The droplet generator was connected to a gas dynamic virtual nozzle (GDVN)[132] by a fused silica capillary (100 μm inner diameter). The GDVN was connected to a helium gas tank by a separate fused silica capillary and was sealed into a vacuum chamber during the experiments. Imaging was accomplished *via* a high-speed camera (Fastcam SA4, Photron, USA). An Elveflow pressure pump was used to control the applied pressure, and flow-check valves were installed on the oil lines to prevent backflow for experiments at the LCLS beam line.

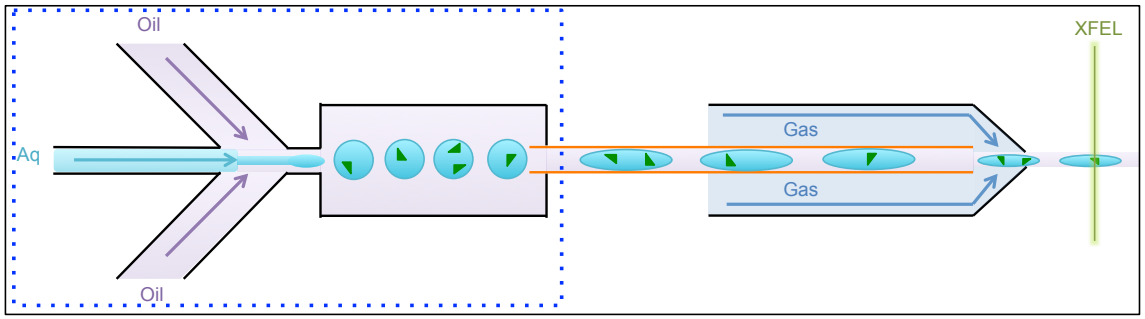

Figure 7.1 Schematic of droplet generation on-chip (inside the blue dotted rectangle) and off-chip interfaced with the XFEL instrument. Left: droplet generation in the PDMS microfluidic device. Middle: Transfer of crystal suspension droplets to a silica capillary (orange indicates the coupled silica capillary). Right: The silica capillary is used as the inner portion of the GDVN injecting a liquid stream into the XFEL chamber. (Figure not to scale.)

7.2.4. Results and Discussion

The droplet generator has two oil-phase inlets and one aqueous-phase inlet meeting at a cross-shaped intersection by pressure-driven flow (Figure 7.1). Due to opposing intermolecular forces, the aqueous dispersed phase does not mix with the oil carrier phase at the intersection and, under certain parameters, will form spherical droplets

of dispersed phase in carrier phase. The droplets and carrier oil are then pushed along by the bulk flow through the outlet and into an interfaced injector. The currently employed SFX injector, a GDVN, uses a fast-flowing sheath gas to jet the liquid stream at the nozzle tip.[132] From there, the liquid stream travels a few micrometers before the X-rays strike the stream.

Initial proof of concept experiments used a PDMS microchip in which aqueous droplets in an oil carrier phase were generated and successfully sent into a fused silica capillary. Figure 7.2 shows (a) droplet generation, (b) transfer to the capillary, and (c) successful droplet generation with crystals of the membrane protein photosystem I.

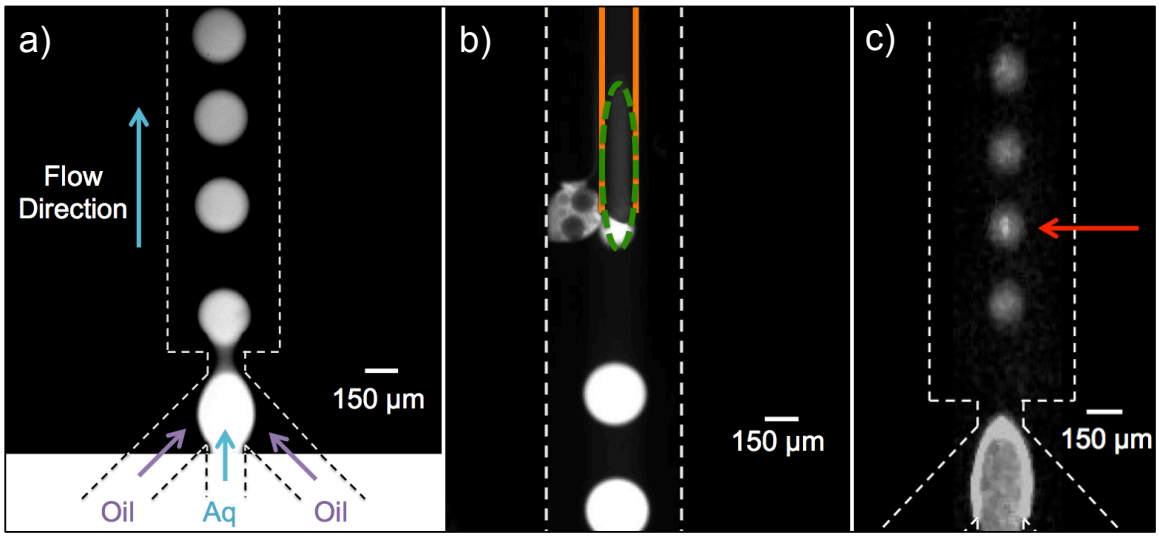

Figure 7.2 (a) Fluorescein droplets generated on-chip. (b) Fluorescein droplets entering a capillary (orange) for downstream injector coupling. The entering droplet is outlined in green. (c) Droplets generated with a photosystem I crystal suspension. The arrow indicates a crystal within the droplet. All images were captured using fluorescence microscopy, and dashed white lines outline the microchannels.

Furthermore, using a PEEK cross connected to a GDVN, droplets were generated at a frequency of 9 Hz and injected (Figure 7.3a) using pressures of 69.6 psi for a representative protein crystal buffer and 70.3 psi for the oil phase, resulting in a

sample flow rate of 21 µL min^{-1}. A pressure of 100 psi was applied to the GDVN to facilitate sheath gas flow, and the liquid was jetted into a vacuum chamber (Figure 7.3b,c).

At the LCLS beam line, droplets containing granulo virus were also generated using the PEEK microfluidic cross fitting. Droplets were generated (Figure 7.3d,e) and injected into the beam line chamber *via* a GDVN. Pressures of 35.9 psi for the crystal buffer, 58.0 psi for the oil phase, and 100 psi for the sheath gas were applied. The droplet frequency was 9 Hz and the sample flow rate was 5.5 µL min^{-1}, a notable reduction compared to the typical 10-15 µL min^{-1} of the GDVN alone.

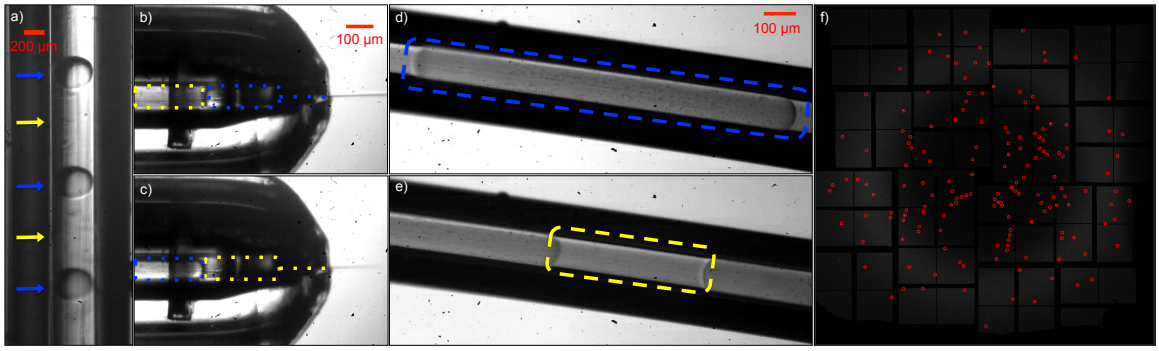

Figure 7.3 (a) In PEEK tubing, droplets of crystal buffer in an oil carrier phase. Crystal suspension and oil are indicated by blue and yellow, respectively. (b-c) High-speed brightfield images of droplets injected through a GDVN. Droplets of crystal suspension jetting (b), shown by the darker line leaving the nozzle, and oil sputtering (c), shown by the blurry line. (d-e) Hydrophobically-treated fused silica capillary (100 µm inner diameter) containing aqueous droplets of granulo virus in an oil carrier phase. A single droplet (d) and the oil between two droplets (e) are shown. (f) Diffraction pattern of granulo virus recorded during droplet generation. Red circles mark peaks determined by Cheetah analysis software. Hit rate was ~ 1 % with a resolution up to 2.6 Å.

7.2.5 Conclusion

In summary, we show that droplets of crystal suspension can be jetted into the XFEL with a 45% decreased sample flow rate and can yield high resolution diffraction patterns (Figure 7.3f). Further optimizations of droplet generation flow rate and

synchronization with XFEL pulses will further reduce sample consumption. Overall, microfluidic droplets are a promising method of sample reduction for SFX.

7.2.6 Acknowledgements

This work was supported by the STC Program of the National Science Foundation through BioXFEL under Agreement No. 1231306 and the National Institutes of Health Award No. R01GM095583. Portions of this research were carried out at the Linac Coherent Light Source (LCLS) at the SLAC National Accelerator Laboratory. LCLS is an Office of Science User Facility operated for the U.S. Department of Energy Office of Science by Stanford University. We thank Andrew Aquila, Mark Hunter, and Sébastien Boutet for support during data collection at the Coherent X-ray Imaging (CXI) instrument at LCLS.

7.3 Sample Consumption Reduction for Serial Crystallography Using Water-In-Oil Droplets[271]

7.3.1 Abstract

Serial femtosecond crystallography with an X-ray free electron laser (XFEL) wastes up to 99% of the continuously injected sample due to the XFEL pulse structure. To reduce sample waste, we utilize a 3D printed microfluidic droplet generator coupled to an injection nozzle to deliver a segmented flow containing droplets of aqueous crystal suspension within an oil carrier. The structure of 3-deoxy-D-*manno*-octulosonate 8-phosphate synthase (KDO8PS) was determined and sample waste reduced significantly.

7.3.2 Introduction

Serial femtosecond crystallography (SFX) has enabled protein structure determination from small crystals at ambient temperatures including time-resolved studies of their reaction dynamics.[20] In SFX, randomly-oriented crystals are continuously injected into the path of a pulsed XFEL beam. Each crystal hit yields one diffraction pattern before destruction by the extremely intense pulse, and thousands of patterns are merged to solve a structure.

The European XFEL (EuXFEL) pulse structure is unique, as trains of MHz X-ray pulses repeat at 10 Hz.[47] The fast repetition rates within a pulse train require large jet velocities (> 50 m/s) for liquid injection methods to replenish the sample, which can be achieved with gas dynamic virtual nozzles (GDVNs). However, > 99% of the sample injected between pulse trains is wasted.[20] Previously used methods for sample conservation such as viscous media injection, electrospinning, acoustic droplet ejection, and fixed-target approaches[23] either cannot achieve suitable jet velocities for MHz pulses or require large alterations to the sample delivery setup. To significantly reduce sample waste, we have proposed water-in-oil droplets for crystal sample delivery when the X-ray is "on" and oil delivery between pulses.[71] Here, we present the application of this approach for sample delivery at the EuXFEL, report on ~ 50% sample waste reduction during the first run of the EuXFEL user-commissioning experiments, and compare diffraction quality of the water-in-oil droplets to continuous injection.

7.3.3 Experimental

Aqueous sample and fluorinated oil (perfluorodecalin/1H,1H,2H,2H-perfluorooctanol, 10:1 v/v) are delivered into a 3D printed T-junction where they form pL-sized droplets (Figure 7.4b,c). The T-junction is interfaced *via* capillaries to a downstream

GDVN[71] for droplet delivery to the X-ray beam (Figure 7.4a). Droplets containing KDO8PS crystals were generated and injected at the EuXFEL with aqueous flow rates between 3 – 12 µL/min. Droplet frequency was monitored in real time using an inline optical droplet detector (Figure 7.5a,b).

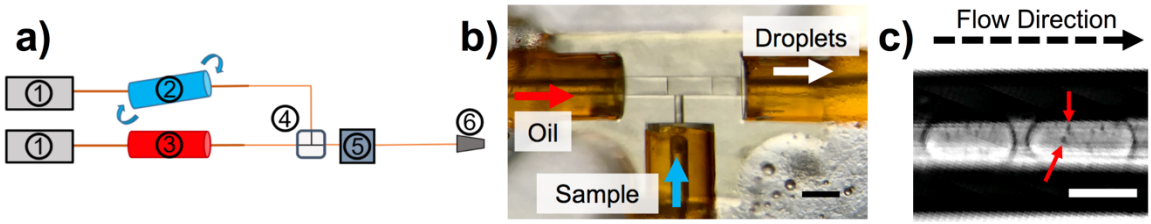

Figure 7.4 (a) Schematic of droplet injection set-up: 1) HPLC pump, 2) protein crystal suspension reservoir on anti-settler, 3) oil reservoir, droplet generator (4), detector (5) and 6) GDVN. (b) Image of 3D printed T-junction with assembled capillaries. (c) Micrograph of droplets in the outlet capillary. Arrows denote crystals in a droplet. Scale bars are 100 µm in (b) & (c).

7.3.4 Results and Discussion

We compared the quality of KDO8PS crystals delivered *via* droplets and continuous sample injection (no oil present). Both droplet and continuous injections were performed for 26 min with 110 µL injected for droplets and 260 µL in continuous mode. The total number of hits was determined as 735 (droplets) and 577 (continuous), resulting in an average of 6.6 and 2.2 hits per µL, respectively. Thus, droplets reduced sample consumption by a factor of two. The diffraction quality was similar for the two methods, with 45% and 54% of hits indexed, an average of 21 ± 14 and 17 ± 10 peaks per pattern, and an average resolution of 4.4 and 4.1 Å for droplet and continuous injection, respectfully. A structure for KDO8PS was solved from all data collected during droplet injection with an average resolution of 4.0 Å (Figure 7.5c).

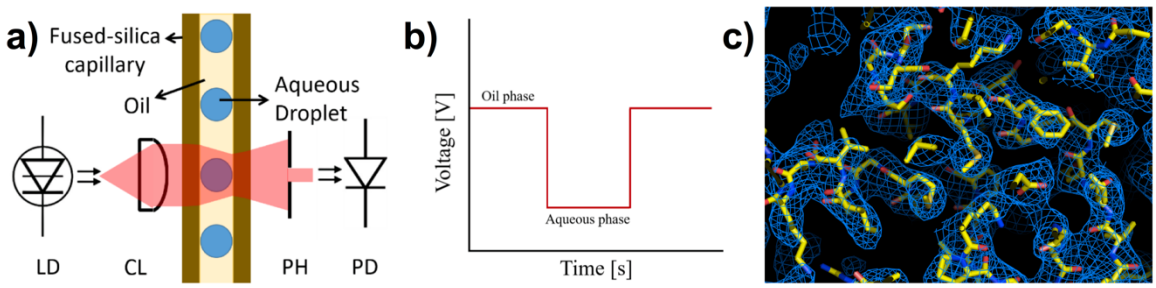

Figure 7.5 (a) Schematic of the droplet detector system. (b) Droplet detector output illustrating the transmittance of the oil and aqueous phases. (c) Preliminary KDO8PS electron density map obtained from the data collected with droplet injection.

7.3.5 Conclusion

We have demonstrated crystal-laden water-in-oil droplets with real-time droplet monitoring for ~ 50% reduced sample waste between pulse trains at the EuXFEL. This approach is compatible with current EuXFEL sample delivery setups and can be employed at any XFEL facility by tuning the droplet frequency accordingly.

7.3.6 Acknowledgements

The work was financially supported by the STC Program of the National Science Foundation through BioXFEL under Agreement No. 1231306 and the National Institutes of Health Award No. R01GM095583.

7.4 Membrane Protein Megahertz Crystallography at the European XFEL[106]

The world's first superconducting megahertz repetition rate hard X-ray free-electron laser (XFEL), the European XFEL, began operation in 2017, featuring a unique pulse train structure with 886 ns between pulses. With its rapid pulse rate, the European XFEL may alleviate some of the increasing demand for XFEL beamtime, particularly for membrane protein serial femtosecond crystallography (SFX), leveraging orders-of-magnitude faster data collection. Here, we report the first membrane protein megahertz SFX experiment, where we determined a 2.9 Å-resolution SFX structure

of the large membrane protein complex, Photosystem I, a >1 MDa complex containing 36 protein subunits and 381 cofactors. We address challenges to megahertz SFX for membrane protein complexes, including growth of large quantities of crystals and the large molecular and unit cell size that influence data collection and analysis. The results imply that megahertz crystallography could have an important impact on structure determination of large protein complexes with XFELs.

7.5 Time-Resolved Serial Femtosecond Crystallography at the European XFEL[107]

The European XFEL (EuXFEL) is a 3.4 km long X-ray source, which produces femtosecond, ultra-brilliant and spatially coherent X-ray pulses at megahertz repetition rates. This X-ray source has been designed to enable the observation of ultrafast processes with near-atomic spatial resolution. Time-resolved crystallographic investigations on biological reactions constitute a particularly important class of experiments with biomedical and health related implications. Due to the unusual X-ray pulse structure, such an experiment is challenging. Here we demonstrate how a biological reaction can be followed on ultrafast time scales at the EuXFEL. We investigate the picosecond time range in the photocycle of photoactive yellow protein (PYP) with MHz X-ray pulse rates. We show that difference electron density maps of excellent quality can be obtained. Results connect the previously explored femtosecond PYP dynamics to time scales accessible at synchrotrons. This opens the door to a wide range of time resolved studies at the EuXFEL.

CHAPTER 8

CONCLUDING REMARKS

8.1 Dissertation Summary

As new XFEL facilities like the EuXFEL are emerging, new sample delivery methods that meet their unique requirements must also be developed. For instance, the EuXFEL currently requires a high velocity jet to replenish crystal sample between MHz X-ray pulses, but the 10 Hz pulse train structure results in ~99% of the injected sample being wasted. To overcome this challenge, a 3D printed T-junction droplet generator has been developed. The principle is based on droplets of crystal sample being segmented by immiscible oil such that crystal sample is in the path of the X-ray during the "on" time of a pulse train and oil is present during the "off" time.

In the development of this 3D printed droplet generator, the surface properties of the IP-S device were characterized. In order to generate aqueous-in-oil droplets, hydrophobic channel walls were required, but the IP-S device was hydrophilic. To create uniformly hydrophobic walls, Novec 1720 was used to coat the walls which remained stable for extended periods of time (hours). To further characterize the 3D printed droplet generator, a relationship between device parameters (e.g. channel width), operating parameters (e.g. aqueous, oil, and total velocities), and the resulting droplet frequency was developed (Figure 5.2). With the frequency characterization and the real time inline droplet detector developed in the Ros lab (Figure 4.4 and Figure 5.1d,e), droplet generation frequency can be adjusted in real time during an SFX experiment as both the droplet detector readout and the pumps that control the aqueous and oil flow rate can be viewed and operated remotely.

To verify that segmented sample delivery is viable for SFX, the 3D printed droplet generators (connected to a glass GDVN) were then utilized for sample delivery of PSI

protein crystals at the MFX chamber of LCLS. While a structure for PSI was not determined, crystal diffraction was observed within the injected aqueous-in-oil droplets, and a relationship between hit rate and water volume fraction was observed, with higher volume fraction resulting in a higher crystal hit rate.

The 3D printed droplet generator coupled to a glass GDVN was utilized at EuXFEL to reduce the amount of sample required to determine a structure of KDO8PS. To this end, a comparison between the volume of sample injected during continuous (no droplets) and segmented sample (with droplets) injection was made. During an equivalent data collection time, the segmented sample required ~60% less sample volume to collect the same quantity and quality of data as continuous injection. Additionally, a crystal structure for KDO8PS was determined up to 2.8 Å using data from only the segmented sample injection, revealing structural details in an unstructured loop region between residues 246 through 251. As the droplet generation was not synchronized with the EuXFEL pulses, the results from this study are promising that further sample consumption reduction can be achieved when the droplets are synchronized.[105]

The 3D printed droplet generator was also employed during another SFX project to reduce sample consumption. However, instead of generating unsynchronized droplets, the two-phase flow was operated in the jetting regime (Chapter 2). By simultaneously flowing aqueous and oil phases, a co-flow was generated. At the EuXFEL, this co-flow reduced the crystal sample flow rate while maintaining the high total flow rate necessary for replenishing crystal sample between X-ray pulses. Using this sample delivery method, a TR-SFX study of PYP at the EuXFEL was accomplished, and intermediate structures of PYP were determined.

Time-resolved SFX is one of the most exciting applications for XFELs as crystal structures of protein reaction intermediates at time scales of hundreds of

femtoseconds or greater can be determined. To date, most TR-SFX has solved structures of photoactivated proteins; however, as detailed in Chapter 1, many protein reactions are not triggered by light. For these non-photoactivated reactions, MISC is used to determine structures of reaction intermediates with time resolution of milliseconds or greater. Current sample delivery methods for MISC either have a simple design (T-junction) with slow time resolution (seconds) or complex fabrication and assembly[49] with fast time resolution (milliseconds). To ease device fabrication and assembly complexity while maintaining the potential for fast time resolution, 3D printed hydrodynamic focusing mixers have been developed. These mixers function by shortening the mixing distance required for a substrate molecule to diffuse through in order to meet and interact with the protein crystal.

During the design of the mixing devices, 2D and 3D numerical models were used to characterize the concentration and velocity profiles within the device. The resulting profiles were then utilized to calculate t_{mix}, and the outlet velocity was used to determine the distance between the mixer and the injection nozzle for a desired t_r. The results from the 2D and 3D models varied significantly, which may be due to the fineness of the mesh and the differences in diffusion properties of the 3D model compared to the 2D model. Future 3D modeling with improved mesh should permit a better understanding of the concentration profile within the device.

In order to verify that the models reflect experimental conditions, fluorescence microscopy mixing experiments were conducted. Device fabrication was automated with 3D printing, and assembly requires insertion of capillaries and permanent affixing of the capillaries with epoxy. The IP-S photoresist that was initially used suffered from high autofluorescence, so the devices were then made from a custom-designed PETA photoresist which has about two orders of magnitude less autofluorescence. As of yet the concentration profiles of the numerical model (both

2D and 3D) have not agreed with the experimental normalized fluorescence intensity curves (Figure 6.6). Furthermore, there are discrepancies between the 2D model and 3D model (e.g. the maximum normalized concentration is greater in the 3D model compared to the 2D model at the same φ). A detailed explanation of what may be causing the discrepancies between experiment and models, as well as the variation between 2D and 3D models, is explained in Chapter 6.

To verify that the mixing device is suitable for MISC, the first iteration of the CCM device (~80 cm capillary between the mixer and nozzle) was utilized at the MFX end station of LCLS to mix an anaerobic suspension of CcO crystals with a CcO buffer solution saturated with oxygen. With d_{delay} ~ 80 cm connecting the mixer to the injection nozzle, t_r = 8 s. At this t_r, the structure for the Pr intermediate of CcO during oxidation was determined.

As mentioned earlier, the ideal t_r for MISC is on the millisecond time scale. To achieve these short t_r, a short t_{mix} (on the order of <10 ms) is required. Additional iterations of the mixing device were subsequently developed in order to reach t_r on time scales of 10^0 – 10^3 ms. These devices included the second iteration of the CCM (≥ 1 mm capillary between the mixer and 3D printed nozzle) and two generations of hybrid devices. Benefits of this 3D printed mixer method include automated fabrication of the mixer (and the nozzle for hybrid devices) and a simpler device construction than previous methods.[51] With a lower fabrication and assembly barrier while maintaining short t_{mix}, these 3D printed MISC sample delivery devices with variable t_r may open the door for additional proteins to be characterized by SFX.

8.2 Future Directions

Looking towards the future, there are several areas of continued study. There are a few limitations of the droplet generator from Chapters 4 and 5. First, the T-junction

geometry was designed with the LCLS X-ray pulse frequency of 120 Hz in mind. However, this geometry is not ideal for achieving the 10 Hz frequency required for the pulse trains structure at the EuXEFL – it requires either working at a low Q_{tot} incompatible with jetting or a high Q_{oil} that is compatible with jetting conditions and a low Q_{aq} (on the order of 10^{-1} µL/min) that can cause crystal settling within the capillary between the sample reservoir and the droplet generator. A larger continuous phase channel geometry would be advantageous for achieving 10 Hz droplet generation frequency with Q_{aq} that avoid crystal settling and Q_{oil} that is compatible with jetting. Second, the aqueous inlet had a diameter of 50 µm which sometimes resulted in crystal clogging when working with large crystals or crystals that have a propensity for forming agglomerates. An increased aqueous phase channel diameter would thus alleviate this clogging concern. For simplification, a square continuous phase channel with a width of 200 µm and a dispersed phase channel with equal width and height to the continuous phase can be employed. Using the same oil and aqueous crystal suspension as in Chapter 5, from Equation 5.1 the necessary Q_{aq} for jetting conditions can be estimated to be ~4 µL/min. This consumes less sample than current continuous injection methods,[47] avoids settling in the capillary between the reservoir and the droplet generator, and decreases the likelihood of crystals clogging in the aqueous channel.

The main drawback of the droplet generator in Chapters 4 and 5 is its inability to control the phase of the droplets. This means crystal-containing droplets generated at the same frequency as the XFEL pulses or pulse trains could be out of phase, resulting in fewer or no crystals being probed by the X-ray beam. In these cases, the droplets were generated with a frequency that did not match the XFEL, so droplets would intersect with X-ray pulses in an unsynchronized manner. To address this deficiency, electrodes have been added to the droplet generator to facilitate electrical

control of droplet generation.[105] The inline droplet detector that has been developed (Chapter 5) can provide information in real time on the phase and frequency of the droplets, and a feedback loop can be established with the appropriate software connecting the droplet detector and the electrode's power supply. The next steps would be to integrate the electrode approach with the larger channel geometry suggested above and to apply this synchronization approach at an SFX experiment. This synchronization work is being spearheaded by Daihyun Kim, Diandra Doppler, and Sahir Gandhi in the Alexandra Ros group.

As discussed in Chapter 6, there is room for improvement in the fluorescence mixing experiments for the mixing device. First, the concentration of the Alexa Fluor 488 dye can be increased in order to rule out low concentration as a cause for the early fluorescence intensity increase. Next, instead of simply mixing a fluorescent solution with non-fluorescent solution, a reaction where fluorescence is triggered could be performed. In this fluorescence reaction, a solution containing a non-fluorescing fluorophore would be mixed together with a solution containing a trigger for the fluorophore. The trigger molecules would react with the fluorophore and initiate fluorescence. With this kind of fluorescence reaction there would be fewer out of focus fluorescing fluorophores for errors related to the PSF. Lastly, a confocal microscopy setup could be utilized to visualize only one plane of the channel, eliminating any PSF errors. If the resulting fluorescence intensity profile from these experiments matches the numerical model's concentration profile, then the model, as well as the calculated mixing times, can be verified.

Another area for improvement in regard to the 3D printed MISC devices is the hydrodynamic focusing. Currently, the device focuses in one-dimension; the ceiling and floor of the device are not focused, thus increasing the uncertainty in t_r. By designing a coaxial device, the substrate solution can focus the crystal suspension in

360°, extending the focusing to two-dimensions (Figure 8.1). Since the device operates in a laminar flow proceeding to the outlet, it is not feasible to focus in three-dimensions. I have performed 3D numerical models with this coaxial design, and focusing in two-dimensions decreases t_{mix} by ~2x and reduces the uncertainty in t_r to < 10%. What remains is to experimentally verify the numerical models, which faces the same challenges described in Chapter 6 and can thus be overcome in the ways listed above. With this updated coaxial design, achieving a shorter t_r to obtain reaction intermediates for the oxidation of cytochrome c oxidase should be feasible. For instance, an A intermediate is present between the reduced state (R) and the Pr state of cytochrome c oxidase during its oxidation, and this A state can be a target for MISC.

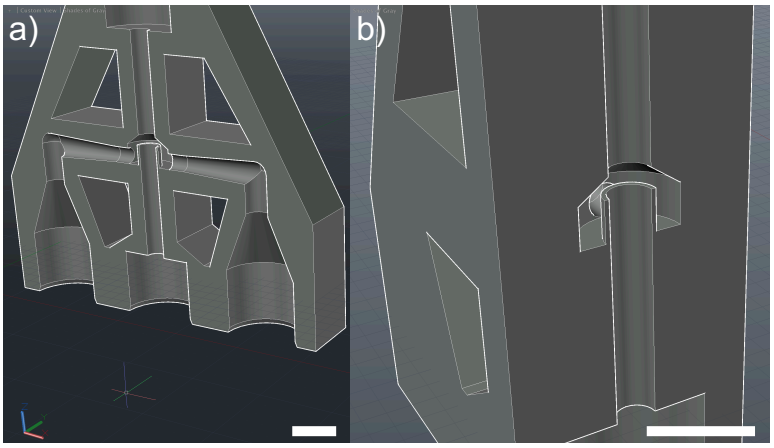

Figure 8.1 CAD drawings of a proposed 3D printed coaxial mixer. In both images the device is sliced in half to view the channel geometry. (a) XZ-plane slice, and (b) YZ-plane slice. The solution from the side inlets can fully surround the center inlet before interacting with the center solution.

Finally, a device that integrates the droplet generator with the mixer would permit reduced sample consumption with MISC. This can be with either a CCM or a hybrid device. The question then becomes should the droplet generator be upstream of the

mixer, or vice versa? To take advantage of the hydrodynamic focusing, the mixer would need to be present upstream of the droplet generator. A challenge for a downstream droplet generator would be the high dispersed phase flow rate required as Q_{tot} for the mixer would become Q_{aq} for the droplet generator. Thus, an adjusted droplet generator geometry would be necessary. Alternatively, the droplet generator could be in the jetting regime as a co-flow device. For a mixer downstream of a droplet generator, an alternative mixing method would be required. There are methods for mixing within a droplet[63, 272] that utilize the flow fields within a droplet and channel geometry for chaotic advection to achieve t_{mix} on the order of milliseconds or sub-milliseconds. With this mixing in a droplet approach, one would need to take ensure the channel geometry does not result in crystals clogging the device.

Printing all three components in one device would be a challenge due to the limited z-axis range of the Nanoscribe. Current iterations of the hybrid device are printed vertically: the fluidic and gas inlets flush with the ITO-coated glass substrate and printing layer-by-layer until ending with the nozzle tip. This is due to the liquid line of the nozzle needing to be free-standing for coaxial gas focusing but also connected to the device during printing. Inserting a droplet generator between the mixer and nozzle may be outside of the height that the Nanoscribe can print in its current setup. As such, a capillary connecting either a mixer to a hybrid droplet generator with an integrated nozzle or a mixer with an integrated droplet generator to a 3D printed nozzle could be employed.

Serial crystallography with XFELs has enabled great strides for structural biology, with more promise on the horizon. To facilitate these future breakthroughs, improvements with sample delivery methods are key. By using 3D printed devices for droplet generation, the amount of sample required to solve a protein structure

can be reduced, easing the crystallization bottleneck. Additionally, the automation and simple fabrication of 3D printed hydrodynamic focusing mixers has the potential to lower the barrier of entry for MISC. As such, the 3D printed sample delivery methods presented here will serve as the building blocks for the structural discoveries of tomorrow.

REFERENCES

1. Dobson, C. M., Biophysical Techniques in Structural Biology. *Annu Rev Biochem* **2019,** *88* (1), 25-33.

2. Garman, E. F., Developments in x-ray crystallographic structure determination of biological macromolecules. *Science* **2014,** *343* (6175), 1102-8.

3. Berman, H. M.; Westbrook, J.; Feng, Z.; Gilliland, G.; Bhat, T. N.; Weissig, H.; Shindyalov, I. N.; Bourne, P. E., The Protein Data Bank. *Nucleic Acids Res* **2000,** *28* (1), 235-42.

4. Bragg, W. H.; Bragg, W. L., The Reflection of X-rays by Crystals. *Proc. R. Soc. Lond. A.* **1913,** *88* (605), 428-438.

5. Drenth, J., *Principles of Protein X-Ray Crystallography*. 3rd ed.; Springer: New York, NY, 2007.

6. Rupp, B., *Biomolecular crystallography: principles, practice, and application to structural biology*. Garland Science: 2009.

7. Smyth, M. S.; Martin, J. H., x ray crystallography. *Mol Pathol* **2000,** *53* (1), 8-14.

8. Garman, E. F., Radiation damage in macromolecular crystallography: what is it and why should we care? *Acta Crystallogr D Biol Crystallogr* **2010,** *66* (Pt 4), 339-51.

9. Ravelli, R. B. G.; McSweeney, S. M., The 'fingerprint' that X-rays can leave on structures. *Structure* **2000,** *8* (3), 315-328.

10. Ravelli, R. B.; Garman, E. F., Radiation damage in macromolecular cryocrystallography. *Curr Opin Struct Biol* **2006,** *16* (5), 624-9.

11. Jones, G. D.; Lea, J. S.; Symons, M. C.; Taiwo, F. A., Structure and mobility of electron gain and loss centres in proteins. *Nature* **1987,** *330* (6150), 772-3.

12. Smith, J. L.; Fischetti, R. F.; Yamamoto, M., Micro-crystallography comes of age. *Curr Opin Struct Biol* **2012,** *22* (5), 602-12.

13. Carter, C. W.; Sweet, R. M., *Macromolecular crystallography. Part A.* Academic Press: New York, 1997; Vol. 276.

14. Martin-Garcia, J. M.; Conrad, C. E.; Coe, J.; Roy-Chowdhury, S.; Fromme, P., Serial femtosecond crystallography: A revolution in structural biology. *Arch Biochem Biophys* **2016,** *602*, 32-47.

15. Wuthrich, K., The way to NMR structures of proteins. *Nat Struct Biol* **2001,** *8* (11), 923-5.

16. Sugiki, T.; Kobayashi, N.; Fujiwara, T., Modern Technologies of Solution Nuclear Magnetic Resonance Spectroscopy for Three-dimensional Structure Determination of Proteins Open Avenues for Life Scientists. *Comput Struct Biotechnol J* **2017,** *15*, 328-339.

17. Murata, K.; Wolf, M., Cryo-electron microscopy for structural analysis of dynamic biological macromolecules. *Biochim Biophys Acta Gen Subj* **2018,** *1862* (2), 324-334.

18. Emma, P.; Akre, R.; Arthur, J.; Bionta, R.; Bostedt, C.; Bozek, J.; Brachmann, A.; Bucksbaum, P.; Coffee, R.; Decker, F. J.; Ding, Y.; Dowell, D.; Edstrom, S.; Fisher, A.; Frisch, J.; Gilevich, S.; Hastings, J.; Hays, G.; Hering, P.; Huang, Z.; Iverson, R.; Loos, H.; Messerschmidt, M.; Miahnahri, A.; Moeller, S.; Nuhn, H. D.; Pile, G.; Ratner, D.; Rzepiela, J.; Schultz, D.; Smith, T.; Stefan, P.; Tompkins, H.; Turner, J.; Welch, J.; White, W.; Wu, J.; Yocky, G.; Galayda, J., First lasing and operation of an angstrom-wavelength free-electron laser. *Nature Photonics* **2010,** *4* (9), 641-647.

19. Chapman, H. N.; Fromme, P.; Barty, A.; White, T. A.; Kirian, R. A.; Aquila, A.; Hunter, M. S.; Schulz, J.; DePonte, D. P.; Weierstall, U.; Doak, R. B.; Maia, F. R.; Martin, A. V.; Schlichting, I.; Lomb, L.; Coppola, N.; Shoeman, R. L.; Epp, S. W.; Hartmann, R.; Rolles, D.; Rudenko, A.; Foucar, L.; Kimmel, N.; Weidenspointner, G.; Holl, P.; Liang, M.; Barthelmess, M.; Caleman, C.; Boutet, S.; Bogan, M. J.; Krzywinski, J.; Bostedt, C.; Bajt, S.; Gumprecht, L.; Rudek, B.; Erk, B.; Schmidt, C.; Homke, A.; Reich, C.; Pietschner, D.; Struder, L.; Hauser, G.; Gorke, H.; Ullrich, J.; Herrmann, S.; Schaller, G.; Schopper, F.; Soltau, H.; Kuhnel, K. U.; Messerschmidt, M.; Bozek, J. D.; Hau-Riege, S. P.; Frank, M.; Hampton, C. Y.; Sierra, R. G.; Starodub, D.; Williams, G. J.; Hajdu, J.; Timneanu, N.; Seibert, M. M.; Andreasson, J.; Rocker, A.; Jonsson, O.; Svenda, M.; Stern, S.; Nass, K.; Andritschke, R.; Schroter, C. D.; Krasniqi, F.; Bott, M.; Schmidt, K. E.; Wang, X.; Grotjohann, I.; Holton, J. M.; Barends, T. R.; Neutze, R.; Marchesini, S.; Fromme, R.; Schorb, S.; Rupp, D.; Adolph, M.; Gorkhover, T.; Andersson, I.; Hirsemann, H.; Potdevin, G.; Graafsma, H.; Nilsson, B.; Spence, J. C., Femtosecond X-ray protein nanocrystallography. *Nature* **2011,** *470* (7332), 73-7.

20. Chapman, H. N., X-Ray Free-Electron Lasers for the Structure and Dynamics of Macromolecules. *Annu Rev Biochem* **2019,** *88* (1), 35-58.

21. Neutze, R.; Wouts, R.; van der Spoel, D.; Weckert, E.; Hajdu, J., Potential for biomolecular imaging with femtosecond X-ray pulses. *Nature* **2000,** *406* (6797), 752-7.

22. Schlichting, I., Serial femtosecond crystallography: the first five years. *IUCrJ* **2015,** *2* (Pt 2), 246-55.

23. Echelmeier, A.; Sonker, M.; Ros, A., Microfluidic sample delivery for serial crystallography using XFELs. *Anal Bioanal Chem* **2019,** *411* (25), 6535-6547.

24. Liu, H.; Spence, J. C. H., XFEL data analysis for structural biology. *Quant. Biol.* **2016,** *4* (3), 159-176.

25. Standfuss, J., Membrane protein dynamics studied by X-ray lasers - or why only time will tell. *Curr Opin Struct Biol* **2019,** *57*, 63-71.

26. Weierstall, U.; James, D.; Wang, C.; White, T. A.; Wang, D.; Liu, W.; Spence, J. C.; Bruce Doak, R.; Nelson, G.; Fromme, P.; Fromme, R.; Grotjohann, I.; Kupitz, C.; Zatsepin, N. A.; Liu, H.; Basu, S.; Wacker, D.; Han, G. W.; Katritch, V.; Boutet, S.; Messerschmidt, M.; Williams, G. J.; Koglin, J. E.; Marvin Seibert, M.; Klinker, M.; Gati, C.; Shoeman, R. L.; Barty, A.; Chapman, H. N.; Kirian, R. A.; Beyerlein, K. R.; Stevens, R. C.; Li, D.; Shah, S. T.; Howe, N.; Caffrey, M.; Cherezov, V., Lipidic cubic phase injector facilitates membrane protein serial femtosecond crystallography. *Nat Commun* **2014,** *5* (1), 3309.

27. Liu, W.; Ishchenko, A.; Cherezov, V., Preparation of microcrystals in lipidic cubic phase for serial femtosecond crystallography. *Nat Protoc* **2014,** *9* (9), 2123-34.

28. Liu, W.; Wacker, D.; Gati, C.; Han, G. W.; James, D.; Wang, D.; Nelson, G.; Weierstall, U.; Katritch, V.; Barty, A.; Zatsepin, N. A.; Li, D.; Messerschmidt, M.; Boutet, S.; Williams, G. J.; Koglin, J. E.; Seibert, M. M.; Wang, C.; Shah, S. T.; Basu, S.; Fromme, R.; Kupitz, C.; Rendek, K. N.; Grotjohann, I.; Fromme, P.; Kirian, R. A.; Beyerlein, K. R.; White, T. A.; Chapman, H. N.; Caffrey, M.; Spence, J. C.; Stevens, R. C.; Cherezov, V., Serial femtosecond crystallography of G protein-coupled receptors. *Science* **2013,** *342* (6165), 1521-4.

29. Liu, W.; Wacker, D.; Wang, C.; Abola, E.; Cherezov, V., Femtosecond crystallography of membrane proteins in the lipidic cubic phase. *Philos Trans R Soc Lond B Biol Sci* **2014,** *369* (1647), 20130314.

30. Fraser, J. S.; van den Bedem, H.; Samelson, A. J.; Lang, P. T.; Holton, J. M.; Echols, N.; Alber, T., Accessing protein conformational ensembles using room-temperature X-ray crystallography. *Proc Natl Acad Sci U S A* **2011,** *108* (39), 16247-52.

31. Keedy, D. A.; van den Bedem, H.; Sivak, D. A.; Petsko, G. A.; Ringe, D.; Wilson, M. A.; Fraser, J. S., Crystal cryocooling distorts conformational heterogeneity in a model Michaelis complex of DHFR. *Structure* **2014,** *22* (6), 899-910.

32. Schmidt, M., Mix and Inject: Reaction Initiation by Diffusion for Time-Resolved Macromolecular Crystallography. *Advances in Condensed Matter Physics* **2013,** *2013*, 1--10.

33. Stagno, J. R.; Liu, Y.; Bhandari, Y. R.; Conrad, C. E.; Panja, S.; Swain, M.; Fan, L.; Nelson, G.; Li, C.; Wendel, D. R.; White, T. A.; Coe, J. D.; Wiedorn, M. O.; Knoska, J.; Oberthuer, D.; Tuckey, R. A.; Yu, P.; Dyba, M.; Tarasov, S. G.; Weierstall, U.; Grant, T. D.; Schwieters, C. D.; Zhang, J.; Ferre-D'Amare, A. R.; Fromme, P.; Draper, D. E.; Liang, M.; Hunter,

M. S.; Boutet, S.; Tan, K.; Zuo, X.; Ji, X.; Barty, A.; Zatsepin, N. A.; Chapman, H. N.; Spence, J. C.; Woodson, S. A.; Wang, Y. X., Structures of riboswitch RNA reaction states by mix-and-inject XFEL serial crystallography. *Nature* **2017,** *541* (7636), 242-246.

34. Spence, J. C. H., XFELs for structure and dynamics in biology. *IUCrJ* **2017,** *4* (Pt 4), 322-339.

35. Levantino, M.; Yorke, B. A.; Monteiro, D. C.; Cammarata, M.; Pearson, A. R., Using synchrotrons and XFELs for time-resolved X-ray crystallography and solution scattering experiments on biomolecules. *Curr Opin Struct Biol* **2015,** *35*, 41-8.

36. Johansson, L. C.; Stauch, B.; Ishchenko, A.; Cherezov, V., A Bright Future for Serial Femtosecond Crystallography with XFELs. *Trends Biochem Sci* **2017,** *42* (9), 749-762.

37. Porter, G.-N.; Norrish, R. G. W., Flash photolysis and spectroscopy. A new method for the study of free radical reactions. *Proc. R. Soc. A* **1950,** *200* (1061), 284-300.

38. Tenboer, J.; Basu, S.; Zatsepin, N.; Pande, K.; Milathianaki, D.; Frank, M.; Hunter, M.; Boutet, S.; Williams, G. J.; Koglin, J. E.; Oberthuer, D.; Heymann, M.; Kupitz, C.; Conrad, C.; Coe, J.; Roy-Chowdhury, S.; Weierstall, U.; James, D.; Wang, D.; Grant, T.; Barty, A.; Yefanov, O.; Scales, J.; Gati, C.; Seuring, C.; Srajer, V.; Henning, R.; Schwander, P.; Fromme, R.; Ourmazd, A.; Moffat, K.; Van Thor, J. J.; Spence, J. C.; Fromme, P.; Chapman, H. N.; Schmidt, M., Time-resolved serial crystallography captures high-resolution intermediates of photoactive yellow protein. *Science* **2014,** *346* (6214), 1242-6.

39. Moffat, K., Time-resolved crystallography and protein design: signalling photoreceptors and optogenetics. *Philos Trans R Soc Lond B Biol Sci* **2014,** *369* (1647), 20130568.

40. Wang, D.; Weierstall, U.; Pollack, L.; Spence, J., Double-focusing mixing jet for XFEL study of chemical kinetics. *J Synchrotron Radiat* **2014,** *21* (Pt 6), 1364-6.

41. Stoddard, B. L.; Cohen, B. E.; Brubaker, M.; Mesecar, A. D.; Koshland, D. E., Jr., Millisecond Laue structures of an enzyme-product complex using photocaged substrate analogs. *Nat Struct Biol* **1998,** *5* (10), 891-7.

42. Tosha, T.; Nomura, T.; Nishida, T.; Saeki, N.; Okubayashi, K.; Yamagiwa, R.; Sugahara, M.; Nakane, T.; Yamashita, K.; Hirata, K.; Ueno, G.; Kimura, T.; Hisano, T.; Muramoto, K.; Sawai, H.; Takeda, H.; Mizohata, E.; Yamashita, A.; Kanematsu, Y.; Takano, Y.; Nango, E.; Tanaka, R.; Nureki, O.; Shoji, O.; Ikemoto, Y.; Murakami, H.; Owada, S.; Tono, K.; Yabashi, M.; Yamamoto, M.; Ago, H.; Iwata, S.; Sugimoto, H.; Shiro, Y.; Kubo, M., Capturing an initial intermediate during the P450nor enzymatic reaction using time-resolved XFEL crystallography and caged-substrate. *Nat Commun* **2017,** *8* (1), 1585.

43. Ellis-Davies, G. C., Caged compounds: photorelease technology for control of cellular chemistry and physiology. *Nat Methods* **2007,** *4* (8), 619-28.

44. Klan, P.; Solomek, T.; Bochet, C. G.; Blanc, A.; Givens, R.; Rubina, M.; Popik, V.; Kostikov, A.; Wirz, J., Photoremovable protecting groups in chemistry and biology: reaction mechanisms and efficacy. *Chem Rev* **2013,** *113* (1), 119-91.

45. Weierstall, U.; Spence, J. C.; Doak, R. B., Injector for scattering measurements on fully solvated biospecies. *Rev Sci Instrum* **2012,** *83* (3), 035108.

46. Mancuso, A. P.; Aquila, A.; Batchelor, L.; Bean, R. J.; Bielecki, J.; Borchers, G.; Doerner, K.; Giewekemeyer, K.; Graceffa, R.; Kelsey, O. D.; Kim, Y.; Kirkwood, H. J.; Legrand, A.; Letrun, R.; Manning, B.; Lopez Morillo, L.; Messerschmidt, M.; Mills, G.; Raabe, S.; Reimers, N.; Round, A.; Sato, T.; Schulz, J.; Signe Takem, C.; Sikorski, M.; Stern, S.; Thute, P.; Vagovic, P.; Weinhausen, B.; Tschentscher, T., The Single Particles, Clusters and Biomolecules and Serial Femtosecond Crystallography instrument of the European XFEL: initial installation. *J Synchrotron Radiat* **2019,** *26* (Pt 3), 660-676.

47. Wiedorn, M. O.; Oberthur, D.; Bean, R.; Schubert, R.; Werner, N.; Abbey, B.; Aepfelbacher, M.; Adriano, L.; Allahgholi, A.; Al-Qudami, N.; Andreasson, J.; Aplin, S.; Awel, S.; Ayyer, K.; Bajt, S.; Barak, I.; Bari, S.; Bielecki, J.; Botha, S.; Boukhelef, D.; Brehm, W.; Brockhauser, S.; Cheviakov, I.; Coleman, M. A.; Cruz-Mazo, F.; Danilevski, C.; Darmanin, C.; Doak, R. B.; Domaracky, M.; Dorner, K.; Du, Y.; Fangohr, H.; Fleckenstein, H.; Frank, M.; Fromme, P.; Ganan-Calvo, A. M.; Gevorkov, Y.; Giewekemeyer, K.; Ginn, H. M.; Graafsma, H.; Graceffa, R.; Greiffenberg, D.; Gumprecht, L.; Gottlicher, P.; Hajdu, J.; Hauf, S.; Heymann, M.; Holmes, S.; Horke, D. A.; Hunter, M. S.; Imlau, S.; Kaukher, A.; Kim, Y.; Klyuev, A.; Knoska, J.; Kobe, B.; Kuhn, M.; Kupitz, C.; Kupper, J.; Lahey-Rudolph, J. M.; Laurus, T.; Le Cong, K.; Letrun, R.; Xavier, P. L.; Maia, L.; Maia, F.; Mariani, V.; Messerschmidt, M.; Metz, M.; Mezza, D.; Michelat, T.; Mills, G.; Monteiro, D. C. F.; Morgan, A.; Muhlig, K.; Munke, A.; Munnich, A.; Nette, J.; Nugent, K. A.; Nuguid, T.; Orville, A. M.; Pandey, S.; Pena, G.; Villanueva-Perez, P.; Poehlsen, J.; Previtali, G.; Redecke, L.; Riekehr, W. M.; Rohde, H.; Round, A.; Safenreiter, T.; Sarrou, I.; Sato, T.; Schmidt, M.; Schmitt, B.; Schonherr, R.; Schulz, J.; Sellberg, J. A.; Seibert, M. M.; Seuring, C.; Shelby, M. L.; Shoeman, R. L.; Sikorski, M.; Silenzi, A.; Stan, C. A.; Shi, X.; Stern, S.; Sztuk-Dambietz, J.; Szuba, J.; Tolstikova, A.; Trebbin, M.; Trunk, U.; Vagovic, P.; Ve, T.; Weinhausen, B.; White, T. A.; Wrona, K.; Xu, C.; Yefanov, O.; Zatsepin, N.; Zhang, J.; Perbandt, M.; Mancuso, A. P.; Betzel, C.; Chapman, H.; Barty, A., Megahertz serial crystallography. *Nat Commun* **2018,** *9* (1), 4025.

48. Kupitz, C.; Olmos, J. L., Jr.; Holl, M.; Tremblay, L.; Pande, K.; Pandey, S.; Oberthur, D.; Hunter, M.; Liang, M.; Aquila, A.; Tenboer, J.; Calvey, G.; Katz, A.; Chen, Y.; Wiedorn, M. O.; Knoska, J.; Meents, A.; Majriani, V.; Norwood, T.; Poudyal, I.; Grant, T.; Miller, M. D.; Xu, W.; Tolstikova, A.; Morgan, A.; Metz, M.; Martin-Garcia, J. M.; Zook, J. D.; Roy-Chowdhury,

S.; Coe, J.; Nagaratnam, N.; Meza, D.; Fromme, R.; Basu, S.; Frank, M.; White, T.; Barty, A.; Bajt, S.; Yefanov, O.; Chapman, H. N.; Zatsepin, N.; Nelson, G.; Weierstall, U.; Spence, J.; Schwander, P.; Pollack, L.; Fromme, P.; Ourmazd, A.; Phillips, G. N., Jr.; Schmidt, M., Structural enzymology using X-ray free electron lasers. *Struct Dyn* **2017,** *4* (4), 044003.

49. Calvey, G. D.; Katz, A. M.; Schaffer, C. B.; Pollack, L., Mixing injector enables time-resolved crystallography with high hit rate at X-ray free electron lasers. *Struct Dyn* **2016,** *3* (5), 054301.

50. Olmos, J. L., Jr.; Pandey, S.; Martin-Garcia, J. M.; Calvey, G.; Katz, A.; Knoska, J.; Kupitz, C.; Hunter, M. S.; Liang, M.; Oberthuer, D.; Yefanov, O.; Wiedorn, M.; Heyman, M.; Holl, M.; Pande, K.; Barty, A.; Miller, M. D.; Stern, S.; Roy-Chowdhury, S.; Coe, J.; Nagaratnam, N.; Zook, J.; Verburgt, J.; Norwood, T.; Poudyal, I.; Xu, D.; Koglin, J.; Seaberg, M. H.; Zhao, Y.; Bajt, S.; Grant, T.; Mariani, V.; Nelson, G.; Subramanian, G.; Bae, E.; Fromme, R.; Fung, R.; Schwander, P.; Frank, M.; White, T. A.; Weierstall, U.; Zatsepin, N.; Spence, J.; Fromme, P.; Chapman, H. N.; Pollack, L.; Tremblay, L.; Ourmazd, A.; Phillips, G. N., Jr.; Schmidt, M., Enzyme intermediates captured "on the fly" by mix-and-inject serial crystallography. *BMC Biol* **2018,** *16* (1), 59.

51. Calvey, G. D.; Katz, A. M.; Pollack, L., Microfluidic Mixing Injector Holder Enables Routine Structural Enzymology Measurements with Mix-and-Inject Serial Crystallography Using X-ray Free Electron Lasers. *Anal Chem* **2019,** *91* (11), 7139-7144.

52. Whitesides, G. M., The origins and the future of microfluidics. *Nature* **2006,** *442* (7101), 368-73.

53. Convery, N.; Gadegaard, N., 30 years of microfluidics. *Micro and Nano Engineering* **2019,** *2*, 76-91.

54. Qin, D.; Xia, Y.; Rogers, J. A.; Jackman, R. J.; Zhao, X.-M.; Whitesides, G. M., Microfabrication, Microstructures and Microsystems. In *Microsystem Technology in Chemistry and Life Science*, Manz, A.; Becker, H., Eds. Springer Berlin Heidelberg: Berlin, Heidelberg, 1998; pp 1-20.

55. DePonte, D. P.; Weierstall, U.; Schmidt, K.; Warner, J.; Starodub, D.; Spence, J. C. H.; Doak, R. B., Gas dynamic virtual nozzle for generation of microscopic droplet streams. *Journal of Physics D-Applied Physics* **2008,** *41* (19), 195505.

56. Grunbein, M. L.; Nass Kovacs, G., Sample delivery for serial crystallography at free-electron lasers and synchrotrons. *Acta Crystallogr D Struct Biol* **2019,** *75* (Pt 2), 178-191.

57. Ishigami, I.; Lewis-Ballester, A.; Echelmeier, A.; Brehm, G.; Zatsepin, N. A.; Grant, T. D.; Coe, J. D.; Lisova, S.; Nelson, G.; Zhang, S.; Dobson, Z. F.; Boutet, S.; Sierra, R. G.; Batyuk, A.; Fromme, P.; Fromme, R.; Spence, J. C. H.; Ros, A.; Yeh, S. R.; Rousseau, D. L., Snapshot of an

oxygen intermediate in the catalytic reaction of cytochrome c oxidase. *Proc Natl Acad Sci U S A* **2019,** *116* (9), 3572-3577.

58. Thorsen, T.; Roberts, R. W.; Arnold, F. H.; Quake, S. R., Dynamic pattern formation in a vesicle-generating microfluidic device. *Phys Rev Lett* **2001,** *86* (18), 4163-6.

59. Seemann, R.; Brinkmann, M.; Pfohl, T.; Herminghaus, S., Droplet based microfluidics. *Rep Prog Phys* **2012,** *75* (1), 016601.

60. Zhu, P.; Wang, L., Passive and active droplet generation with microfluidics: a review. *Lab Chip* **2016,** *17* (1), 34-75.

61. Doufene, K.; Tourne-Peteilh, C.; Etienne, P.; Aubert-Pouessel, A., Microfluidic Systems for Droplet Generation in Aqueous Continuous Phases: A Focus Review. *Langmuir* **2019,** *35* (39), 12597-12612.

62. Baroud, C. N.; Gallaire, F.; Dangla, R., Dynamics of microfluidic droplets. *Lab Chip* **2010,** *10* (16), 2032-45.

63. Song, H.; Chen, D. L.; Ismagilov, R. F., Reactions in droplets in microfluidic channels. *Angew Chem Int Ed Engl* **2006,** *45* (44), 7336-56.

64. Bui, M. P.; Li, C. A.; Han, K. N.; Choo, J.; Lee, E. K.; Seong, G. H., Enzyme kinetic measurements using a droplet-based microfluidic system with a concentration gradient. *Anal Chem* **2011,** *83* (5), 1603-8.

65. Hassan, S. U.; Nightingale, A. M.; Niu, X., Continuous measurement of enzymatic kinetics in droplet flow for point-of-care monitoring. *Analyst* **2016,** *141* (11), 3266-73.

66. Ma, J.; Lee, S. M.; Yi, C.; Li, C. W., Controllable synthesis of functional nanoparticles by microfluidic platforms for biomedical applications - a review. *Lab Chip* **2017,** *17* (2), 209-226.

67. Ma, J.; Wang, Y.; Liu, J., Biomaterials Meet Microfluidics: From Synthesis Technologies to Biological Applications. *Micromachines (Basel)* **2017,** *8* (8).

68. Zheng, B.; Roach, L. S.; Ismagilov, R. F., Screening of protein crystallization conditions on a microfluidic chip using nanoliter-size droplets. *J Am Chem Soc* **2003,** *125* (37), 11170-1.

69. Zheng, B.; Tice, J. D.; Roach, L. S.; Ismagilov, R. F., A droplet-based, composite PDMS/glass capillary microfluidic system for evaluating protein crystallization conditions by microbatch and vapor-diffusion methods with on-chip X-ray diffraction. *Angew Chem Int Ed Engl* **2004,** *43* (19), 2508-11.

70. Echelmeier, A.; Kim, D.; Cruz Villarreal, J.; Coe, J.; Quintana, S.; Brehm, G.; Egatz-Gomez, A.; Nazari, R.; Sierra, R. G.; Koglin, J. E.; Batyuk, A.; Hunter, M. S.; Boutet, S.; Zatsepin, N.; Kirian, R. A.; Grant, T. D.; Fromme, P.; Ros, A., 3D printed droplet generation devices for serial

femtosecond crystallography enabled by surface coating. *J Appl Crystallogr* **2019,** *52* (Pt 5), 997-1008.

71. Echelmeier, A.; Nelson, G.; Abdallah, B. G.; James, D.; Tolstikova, A.; Mariani, V.; Kirian, R. A.; Oberther, D.; Dorner, K.; Fromme, P.; Chapman, H. N.; Weierstall, U.; Spence, J. C. H.; Ros, A., Biphasic Droplet-Based Sample Delivery of Protein Crystals for Serial Femtosecond Crystallography With an X-Ray Free Electron Laser. *Int. Conf. Miniaturized Syst. Chem. Life Sci., 19th* **2015,** *19*, 1374-1376.

72. Reynolds, O., XXIX. An experimental investigation of the circumstances which determine whether the motion of water shall be direct or sinuous, and of the law of resistance in parallel channels. *Philos Trans R Soc London* **1883,** *174*, 935-982.

73. Sharp, K. V.; Adrian, R. J., Transition from laminar to turbulent flow in liquid filled microtubes. *Exp Fluids* **2004,** *36* (5), 741-747.

74. Nguyen, N.-T.; Wereley, S. T., *Fundamentals and Applications of Microfluidics*. Second ed.; Artech House: Norwood, UNITED STATES, 2006.

75. Tabeling, P.; Cheng, S., *Introduction to Microfluidics*. Oxford University Press, Incorporated: Oxford, UNITED KINGDOM, 2006.

76. Berg, H. C., *Random walks in biology*. Princeton University Press: Princeton, New Jersey, 1993.

77. Suh, Y. K.; Kang, S., A Review on Mixing in Microfluidics. *Micromachines* **2010,** *1* (3), 82-111.

78. Lee, C. Y.; Chang, C. L.; Wang, Y. N.; Fu, L. M., Microfluidic mixing: a review. *Int J Mol Sci* **2011,** *12* (5), 3263-87.

79. Cai, G.; Xue, L.; Zhang, H.; Lin, J., A Review on Micromixers. *Micromachines (Basel)* **2017,** *8* (9), 274.

80. Liu, R. H.; Stremler, M. A.; Sharp, K. V.; Olsen, M. G.; Santiago, J. G.; Adrian, R. J.; Aref, H.; Beebe, D. J., Passive mixing in a three-dimensional serpentine microchannel. *Journal of Microelectromechanical Systems* **2000,** *9* (2), 190-197.

81. Xia, H. M.; Wan, S. Y.; Shu, C.; Chew, Y. T., Chaotic micromixers using two-layer crossing channels to exhibit fast mixing at low Reynolds numbers. *Lab Chip* **2005,** *5* (7), 748-55.

82. Yang, J. T.; Fang, W. F.; Tung, K. Y., Fluids mixing in devices with connected-groove channels. *Chemical Engineering Science* **2008,** *63* (7), 1871-1881.

83. Heo, H. S.; Suh, Y. K., Enhancement of stirring in a straight channel at low Reynolds-numbers with various block-arrangement. *Journal of Mechanical Science and Technology* **2005,** *19* (1), 199-208.

84. Iliescu, C.; Taylor, H.; Avram, M.; Miao, J.; Franssila, S., A practical guide for the fabrication of microfluidic devices using glass and silicon. *Biomicrofluidics* **2012,** *6* (1), 16505-1650516.

85. Zhao, X. M.; Xia, Y. N.; Whitesides, G. M., Soft lithographic methods for nano-fabrication. *J Mater Chem* **1997,** *7* (7), 1069-1074.

86. Xia, Y.; Whitesides, G. M., Soft Lithography. *Angew Chem Int Ed Engl* **1998,** *37* (5), 550-575.

87. Sugioka, K.; Cheng, Y., Femtosecond laser three-dimensional micro- and nanofabrication. *Applied Physics Reviews* **2014,** *1* (4), 041303.

88. Waheed, S.; Cabot, J. M.; Macdonald, N. P.; Lewis, T.; Guijt, R. M.; Paull, B.; Breadmore, M. C., 3D printed microfluidic devices: enablers and barriers. *Lab Chip* **2016,** *16* (11), 1993-2013.

89. Maruo, S.; Nakamura, O.; Kawata, S., Three-dimensional microfabrication with two-photon-absorbed photopolymerization. *Opt Lett* **1997,** *22* (2), 132-4.

90. Nelson, G.; Kirian, R. A.; Weierstall, U.; Zatsepin, N. A.; Farago, T.; Baumbach, T.; Wilde, F.; Niesler, F. B.; Zimmer, B.; Ishigami, I.; Hikita, M.; Bajt, S.; Yeh, S. R.; Rousseau, D. L.; Chapman, H. N.; Spence, J. C.; Heymann, M., Three-dimensional-printed gas dynamic virtual nozzles for x-ray laser sample delivery. *Opt Express* **2016,** *24* (11), 11515-30.

91. So, P. T.; Dong, C. Y.; Masters, B. R.; Berland, K. M., Two-photon excitation fluorescence microscopy. *Annu Rev Biomed Eng* **2000,** *2* (1), 399-429.

92. Durisova, J.; Pudis, D.; Goraus, M.; Gaso, P., IP-Dip photoresist surfaces for photonic applications prepared by laser lithography and studied by AFM. *Applied Surface Science* **2018,** *461*, 108-112.

93. Teh, S. Y.; Lin, R.; Hung, L. H.; Lee, A. P., Droplet microfluidics. *Lab Chip* **2008,** *8* (2), 198-220.

94. Anna, S. L.; Bontoux, N.; Stone, H. A., Formation of dispersions using "flow focusing" in microchannels. *Applied Physics Letters* **2003,** *82* (3), 364-366.

95. Dreyfus, R.; Tabeling, P.; Willaime, H., Ordered and disordered patterns in two-phase flows in microchannels. *Phys Rev Lett* **2003,** *90* (14), 144505.

96. Cramer, C.; Fischer, P.; Windhab, E. J., Drop formation in a co-flowing ambient fluid. *Chemical Engineering Science* **2004,** *59* (15), 3045-3058.

97. Rapp, B. E., *Microfluidics: Modeling, Mechanics and Mathematics*. Elsevier: Oxford, 2017.

98. Xu, J. H.; Li, S. W.; Tan, J.; Luo, G. S., Correlations of droplet formation in T-junction microfluidic devices: from squeezing to dripping. *Microfluidics and Nanofluidics* **2008,** *5* (6), 711-717.

99. Christopher, G. F.; Noharuddin, N. N.; Taylor, J. A.; Anna, S. L., Experimental observations of the squeezing-to-dripping transition in T-shaped microfluidic junctions. *Phys Rev E Stat Nonlin Soft Matter Phys* **2008,** *78* (3 Pt 2), 036317.

100. De Menech, M.; Garstecki, P.; Jousse, F.; Stone, H. A., Transition from squeezing to dripping in a microfluidic T-shaped junction. *Journal of Fluid Mechanics* **2008,** *595*, 141-161.

101. Wehking, J. D.; Gabany, M.; Chew, L.; Kumar, R., Effects of viscosity, interfacial tension, and flow geometry on droplet formation in a microfluidic T-junction. *Microfluidics and Nanofluidics* **2014,** *16* (3), 441-453.

102. Zhang, S. H.; Guivier-Curien, C.; Veesler, S.; Candoni, N., Prediction of sizes and frequencies of nanoliter-sized droplets in cylindrical T-junction microfluidics. *Chemical Engineering Science* **2015,** *138*, 128-139.

103. Garstecki, P.; Fuerstman, M. J.; Stone, H. A.; Whitesides, G. M., Formation of droplets and bubbles in a microfluidic T-junction-scaling and mechanism of break-up. *Lab Chip* **2006,** *6* (3), 437-46.

104. Utada, A. S.; Fernandez-Nieves, A.; Stone, H. A.; Weitz, D. A., Dripping to jetting transitions in coflowing liquid streams. *Phys Rev Lett* **2007,** *99* (9), 094502.

105. Kim, D.; Echelmeier, A.; Cruz Villarreal, J.; Gandhi, S.; Quintana, S.; Egatz-Gomez, A.; Ros, A., Electric Triggering for Enhanced Control of Droplet Generation. *Anal Chem* **2019,** *91* (15), 9792-9799.

106. Gisriel, C.; Coe, J.; Letrun, R.; Yefanov, O.; Luna-Chavez, C.; Stander, N.; Lisova, S.; Mariani, V.; Kuhn, M.; Aplin, S.; Grant, T.; Dorner, K.; Sato, T.; Echelmeier, A.; Cruz Villarreal, J.; Hunter, M. S.; Wiedorn, M. O.; Knoska, J.; Mazalova, V.; Roy-Chowdhury, S.; Yang, J.-H.; Jones, A.; Bean, R.; Bielecki, J.; Kim, Y.; Mills, G.; Weinhausen, B.; Meza, J.; Al-Qudami, N.; Bajt, S.; Brehm, G.; Botha, S.; Boukhelef, D.; Brockhauser, S.; Bruce, B.; Coleman, M.; Danilevski, C.; Discianno, E.; Dobson, Z.; Fangohr, H.; Martin-Garcia, J. M.; Gevorkov, Y.; Hauf, S.; Hosseinizadeh, A.; Januschek, F.; Ketawala, G.; Kupitz, C.; Maia, L.; Manetti, M.; Messerschmidt, M.; Michelat, T.; Mondal, J.; Ourmazd, A.; Previtali, G.; Sarrou, I.; Schon, S.; Schwander, P.; Shelby, M.; Silenzi, A.; Sztuk-Dambietz, J.; Szuba, J.; Turcato, M.; White, T. A.; Wrona, K.; Xu, C.; Abdellatif, M.; Zook, J.; Spence, J. C. H.; Chapman, H. N.; Barty, A.; Kirian, R. A.; Frank, M.; Ros, A.; Schmidt, M.; Fromme, R.; Mancuso, A. P.; Fromme, P., Membrane Protein Megahertz Crystallography at the European XFEL. *Nat Commun* **2019**, *Accepted*.

107. Pandey, S.; Bean, R.; Sato, T.; Poudyal, I.; Bielecki, J.; Cruz Villarreal, J.; Yefanov, O.; Mariani, V.; White, T. A.; Kupitz, C.; Hunter, M. S.; Abdellatif, M.; Bajt, S.; Bondar, V.; Echelmeier, A.; Doppler, D.; Emons, M.; Frank, M.; Fromme, R.; Gevorkov, Y.; Giovanetti, G.; Jiang, M.; Kim, D.; Kim, Y.; Kirkwood, H. J.; Klimovskaia, A.; Knoska, J.; Koua, F.; Letrun, R.; Lisova, S.; Maia, L.; Mazalova, V.; Meza, D.; Michelat, T.;

Ourmazd, A.; Palmer, G.; Ramilli, M.; Schubert, R.; Schwander, P.; Silenzi, A.; Sztuk-Dambietz, J.; Tolstikova, A.; Chapman, H. N.; Ros, A.; Barty, A.; Fromme, P.; Mancuso, A. P.; Schmidt, M., Time-Resolved Serial Femtosecond Crystallography at the European XFEL. *Nat Methods* **2019**, *Accepted*.

108. Stone, H. A., Introduction to Fluid Dynamics for Microfluidic Flows. In *CMOS Biotechnology*, Lee, H.; Westervelt, R. M.; Ham, D., Eds. Springer US: Boston, MA, 2007; pp 5-30.

109. Fick, A., V. On liquid diffusion. *The London, Edinburgh, and Dublin Philosophical Magazine and Journal of Science* **1885,** *10* (63), 30-39.

110. Capretto, L.; Cheng, W.; Hill, M.; Zhang, X., Micromixing within microfluidic devices. *Top Curr Chem* **2011,** *304*, 27-68.

111. Knight, J. B.; Vishwanath, A.; Brody, J. P.; Austin, R. H., Hydrodynamic focusing on a silicon chip: Mixing nanoliters in microseconds. *Physical Review Letters* **1998,** *80* (17), 3863-3866.

112. Park, H. Y.; Qiu, X.; Rhoades, E.; Korlach, J.; Kwok, L. W.; Zipfel, W. R.; Webb, W. W.; Pollack, L., Achieving uniform mixing in a microfluidic device: hydrodynamic focusing prior to mixing. *Anal Chem* **2006,** *78* (13), 4465-73.

113. Lee, G. B.; Chang, C. C.; Huang, S. B.; Yang, R. J., The hydrodynamic focusing effect inside rectangular microchannels. *Journal of Micromechanics and Microengineering* **2006,** *16* (5), 1024-1032.

114. Kirby, B., *Micro- and Nanoscale Fluid Mechanics*. Cambridge University Press: Cambridge, 2010.

115. Sadeghi, A., Analytical solutions for mass transport in hydrodynamic focusing by considering different diffusivities for sample and sheath flows. *J Fluid Mech* **2019,** *862*, 517-551.

116. Wu, Z. G.; Nguyen, N. T., Hydrodynamic focusing in microchannels under consideration of diffusive dispersion: theories and experiments. *Sensors and Actuators B-Chemical* **2005,** *107* (2), 965-974.

117. Abdallah, B. G.; Zatsepin, N. A.; Roy-Chowdhury, S.; Coe, J.; Conrad, C. E.; Dorner, K.; Sierra, R. G.; Stevenson, H. P.; Camacho-Alanis, F.; Grant, T. D.; Nelson, G.; James, D.; Calero, G.; Wachter, R. M.; Spence, J. C.; Weierstall, U.; Fromme, P.; Ros, A., Microfluidic sorting of protein nanocrystals by size for X-ray free-electron laser diffraction. *Struct Dyn* **2015,** *2* (4), 041719.

118. Lee, G. B.; Hung, C. I.; Ke, B. J.; Huang, G. R.; Hwei, B. H.; Lai, H. F., Hydrodynamic focusing for a micromachined flow cytometer. *Journal of Fluids Engineering-Transactions of the Asme* **2001,** *123* (3), 672-679.

119. Matthews, B. W., Solvent content of protein crystals. *J Mol Biol* **1968,** *33* (2), 491-7.

120. Boutet, S.; Lomb, L.; Williams, G. J.; Barends, T. R.; Aquila, A.; Doak, R. B.; Weierstall, U.; DePonte, D. P.; Steinbrener, J.; Shoeman, R. L.; Messerschmidt, M.; Barty, A.; White, T. A.; Kassemeyer, S.; Kirian, R. A.; Seibert, M. M.; Montanez, P. A.; Kenney, C.; Herbst, R.; Hart, P.; Pines, J.; Haller, G.; Gruner, S. M.; Philipp, H. T.; Tate, M. W.; Hromalik, M.; Koerner, L. J.; van Bakel, N.; Morse, J.; Ghonsalves, W.; Arnlund, D.; Bogan, M. J.; Caleman, C.; Fromme, R.; Hampton, C. Y.; Hunter, M. S.; Johansson, L. C.; Katona, G.; Kupitz, C.; Liang, M.; Martin, A. V.; Nass, K.; Redecke, L.; Stellato, F.; Timneanu, N.; Wang, D.; Zatsepin, N. A.; Schafer, D.; Defever, J.; Neutze, R.; Fromme, P.; Spence, J. C.; Chapman, H. N.; Schlichting, I., High-resolution protein structure determination by serial femtosecond crystallography. *Science* **2012,** *337* (6092), 362-4.

121. Hunter, M. S.; Segelke, B.; Messerschmidt, M.; Williams, G. J.; Zatsepin, N. A.; Barty, A.; Benner, W. H.; Carlson, D. B.; Coleman, M.; Graf, A.; Hau-Riege, S. P.; Pardini, T.; Seibert, M. M.; Evans, J.; Boutet, S.; Frank, M., Fixed-target protein serial microcrystallography with an x-ray free electron laser. *Sci Rep* **2014,** *4*, 6026.

122. Barty, A.; Kirian, R. A.; Maia, F. R.; Hantke, M.; Yoon, C. H.; White, T. A.; Chapman, H., Cheetah: software for high-throughput reduction and analysis of serial femtosecond X-ray diffraction data. *J Appl Crystallogr* **2014,** *47* (Pt 3), 1118-1131.

123. White, T. A.; Kirian, R. A.; Martin, A. V.; Aquila, A.; Nass, K.; Barty, A.; Chapman, H. N., CrystFEL: a software suite for snapshot serial crystallography. *J Appl Crystallogr* **2012,** *45* (2), 335-341.

124. White, T. A., Processing serial crystallography data with CrystFEL: a step-by-step guide. *Acta Crystallogr D Struct Biol* **2019,** *75* (Pt 2), 219-233.

125. Spence, J. C.; Doak, R. B., Single molecule diffraction. *Phys Rev Lett* **2004,** *92* (19), 198102.

126. Bogan, M. J.; Benner, W. H.; Boutet, S.; Rohner, U.; Frank, M.; Barty, A.; Seibert, M. M.; Maia, F.; Marchesini, S.; Bajt, S.; Woods, B.; Riot, V.; Hau-Riege, S. P.; Svenda, M.; Marklund, E.; Spiller, E.; Hajdu, J.; Chapman, H. N., Single particle X-ray diffractive imaging. *Nano Lett* **2008,** *8* (1), 310-6.

127. Barty, A.; Kupper, J.; Chapman, H. N., Molecular imaging using X-ray free-electron lasers. *Annu Rev Phys Chem* **2013,** *64* (1), 415-35.

128. Lee, J.-h.; Zatsepin, N. A.; Kim, K. H., Time-resolved serial femtosecond X-ray crystallography. *BioDesign* **2018,** *6* (1), 15-22.

129. Altarelli, M.; Mancuso, A. P., Structural biology at the European X-ray free-electron laser facility. *Philos Trans R Soc Lond B Biol Sci* **2014,** *369* (1647), 20130311.

130. Martiel, I.; Muller-Werkmeister, H. M.; Cohen, A. E., Strategies for sample delivery for femtosecond crystallography. *Acta Crystallogr D Struct Biol* **2019,** *75* (Pt 2), 160-177.

131. Oberthuer, D.; Knoska, J.; Wiedorn, M. O.; Beyerlein, K. R.; Bushnell, D. A.; Kovaleva, E. G.; Heymann, M.; Gumprecht, L.; Kirian, R. A.; Barty, A.; Mariani, V.; Tolstikova, A.; Adriano, L.; Awel, S.; Barthelmess, M.; Dorner, K.; Xavier, P. L.; Yefanov, O.; James, D. R.; Nelson, G.; Wang, D.; Calvey, G.; Chen, Y.; Schmidt, A.; Szczepek, M.; Frielingsdorf, S.; Lenz, O.; Snell, E.; Robinson, P. J.; Sarler, B.; Belsak, G.; Macek, M.; Wilde, F.; Aquila, A.; Boutet, S.; Liang, M.; Hunter, M. S.; Scheerer, P.; Lipscomb, J. D.; Weierstall, U.; Kornberg, R. D.; Spence, J. C.; Pollack, L.; Chapman, H. N.; Bajt, S., Double-flow focused liquid injector for efficient serial femtosecond crystallography. *Sci Rep* **2017,** *7* (March), 44628.

132. Weierstall, U., Liquid sample delivery techniques for serial femtosecond crystallography. *Philos Trans R Soc Lond B Biol Sci* **2014,** *369* (1647), 20130337.

133. Lomb, L.; Steinbrener, J.; Bari, S.; Beisel, D.; Berndt, D.; Kieser, C.; Lukat, M.; Neef, N.; Shoeman, R. L., An anti-settling sample delivery instrument for serial femtosecond crystallography. *J Appl Crystallogr* **2012,** *45* (4), 674-678.

134. Hutchison, C. D. M.; Cordon-Preciado, V.; Morgan, R. M. L.; Nakane, T.; Ferreira, J.; Dorlhiac, G.; Sanchez-Gonzalez, A.; Johnson, A. S.; Fitzpatrick, A.; Fare, C.; Marangos, J. P.; Yoon, C. H.; Hunter, M. S.; DePonte, D. P.; Boutet, S.; Owada, S.; Tanaka, R.; Tono, K.; Iwata, S.; van Thor, J. J., X-ray Free Electron Laser Determination of Crystal Structures of Dark and Light States of a Reversibly Photoswitching Fluorescent Protein at Room Temperature. *Int J Mol Sci* **2017,** *18* (9), 1918.

135. Beyerlein, K. R.; Adriano, L.; Heymann, M.; Kirian, R.; Knoska, J.; Wilde, F.; Chapman, H. N.; Bajt, S., Ceramic micro-injection molded nozzles for serial femtosecond crystallography sample delivery. *Rev Sci Instrum* **2015,** *86* (12), 125104.

136. Wojtas, D. H.; Ayyer, K.; Liang, M.; Mossou, E.; Romoli, F.; Seuring, C.; Beyerlein, K. R.; Bean, R. J.; Morgan, A. J.; Oberthuer, D.; Fleckenstein, H.; Heymann, M.; Gati, C.; Yefanov, O.; Barthelmess, M.; Ornithopoulou, E.; Galli, L.; Xavier, P. L.; Ling, W. L.; Frank, M.; Yoon, C. H.; White, T. A.; Bajt, S.; Mitraki, A.; Boutet, S.; Aquila, A.; Barty, A.; Forsyth, V. T.; Chapman, H. N.; Millane, R. P., Analysis of XFEL serial diffraction data from individual crystalline fibrils. *IUCrJ* **2017,** *4* (Pt 6), 795-811.

137. Piotter, V.; Klein, A.; Plewa, K.; Beyerlein, K. R.; Chapman, H. N.; Bajt, S., Development of a ceramic injection molding process for liquid jet nozzles to be applied for X-ray free-electron lasers. *Microsystem Technologies-Micro-and Nanosystems-Information Storage and Processing Systems* **2018,** *24* (2), 1247-1252.

138. Trebbin, M.; Kruger, K.; DePonte, D.; Roth, S. V.; Chapman, H. N.; Forster, S., Microfluidic liquid jet system with compatibility for atmospheric and high-vacuum conditions. *Lab Chip* **2014,** *14* (10), 1733-45.

139. Sia, S. K.; Whitesides, G. M., Microfluidic devices fabricated in poly(dimethylsiloxane) for biological studies. *Electrophoresis* **2003,** *24* (21), 3563-76.

140. Nguyen, N. T.; Hejazian, M.; Ooi, C. H.; Kashaninejad, N., Recent Advances and Future Perspectives on Microfluidic Liquid Handling. *Micromachines* **2017,** *8* (6), 186.

141. Bohne, S.; Heymann, M.; Chapman, H. N.; Trieu, H. K.; Bajt, S., 3D printed nozzles on a silicon fluidic chip. *Rev Sci Instrum* **2019,** *90* (3), 035108.

142. Mafune, F.; Miyajima, K.; Tono, K.; Takeda, Y.; Kohno, J. Y.; Miyauchi, N.; Kobayashi, J.; Joti, Y.; Nango, E.; Iwata, S.; Yabashi, M., Microcrystal delivery by pulsed liquid droplet for serial femtosecond crystallography. *Acta Crystallogr D Struct Biol* **2016,** *72* (Pt 4), 520-3.

143. Roessler, C. G.; Agarwal, R.; Allaire, M.; Alonso-Mori, R.; Andi, B.; Bachega, J. F. R.; Bommer, M.; Brewster, A. S.; Browne, M. C.; Chatterjee, R.; Cho, E.; Cohen, A. E.; Cowan, M.; Datwani, S.; Davidson, V. L.; Defever, J.; Eaton, B.; Ellson, R.; Feng, Y.; Ghislain, L. P.; Glownia, J. M.; Han, G.; Hattne, J.; Hellmich, J.; Heroux, A.; Ibrahim, M.; Kern, J.; Kuczewski, A.; Lemke, H. T.; Liu, P.; Majlof, L.; McClintock, W. M.; Myers, S.; Nelsen, S.; Olechno, J.; Orville, A. M.; Sauter, N. K.; Soares, A. S.; Soltis, S. M.; Song, H.; Stearns, R. G.; Tran, R.; Tsai, Y.; Uervirojnangkoorn, M.; Wilmot, C. M.; Yachandra, V.; Yano, J.; Yukl, E. T.; Zhu, D.; Zouni, A., Acoustic Injectors for Drop-On-Demand Serial Femtosecond Crystallography. *Structure* **2016,** *24* (4), 631-640.

144. Fuller, F. D.; Gul, S.; Chatterjee, R.; Burgie, E. S.; Young, I. D.; Lebrette, H.; Srinivas, V.; Brewster, A. S.; Michels-Clark, T.; Clinger, J. A.; Andi, B.; Ibrahim, M.; Pastor, E.; de Lichtenberg, C.; Hussein, R.; Pollock, C. J.; Zhang, M.; Stan, C. A.; Kroll, T.; Fransson, T.; Weninger, C.; Kubin, M.; Aller, P.; Lassalle, L.; Brauer, P.; Miller, M. D.; Amin, M.; Koroidov, S.; Roessler, C. G.; Allaire, M.; Sierra, R. G.; Docker, P. T.; Glownia, J. M.; Nelson, S.; Koglin, J. E.; Zhu, D.; Chollet, M.; Song, S.; Lemke, H.; Liang, M.; Sokaras, D.; Alonso-Mori, R.; Zouni, A.; Messinger, J.; Bergmann, U.; Boal, A. K.; Bollinger, J. M., Jr.; Krebs, C.; Hogbom, M.; Phillips, G. N., Jr.; Vierstra, R. D.; Sauter, N. K.; Orville, A. M.; Kern, J.; Yachandra, V. K.; Yano, J., Drop-on-demand sample delivery for studying biocatalysts in action at X-ray free-electron lasers. *Nat Methods* **2017,** *14* (4), 443-449.

145. Kubo, M.; Nango, E.; Tono, K.; Kimura, T.; Owada, S.; Song, C.; Mafune, F.; Miyajima, K.; Takeda, Y.; Kohno, J. Y.; Miyauchi, N.; Nakane, T.; Tanaka, T.; Nomura, T.; Davidsson, J.; Tanaka, R.; Murata, M.; Kameshima, T.; Hatsui, T.; Joti, Y.; Neutze, R.; Yabashi, M.; Iwata, S., Nanosecond pump-probe device for time-resolved serial femtosecond

crystallography developed at SACLA. *J Synchrotron Radiat* **2017,** *24* (Pt 5), 1086-1091.

146. Young, I. D.; Ibrahim, M.; Chatterjee, R.; Gul, S.; Fuller, F.; Koroidov, S.; Brewster, A. S.; Tran, R.; Alonso-Mori, R.; Kroll, T.; Michels-Clark, T.; Laksmono, H.; Sierra, R. G.; Stan, C. A.; Hussein, R.; Zhang, M.; Douthit, L.; Kubin, M.; de Lichtenberg, C.; Long Vo, P.; Nilsson, H.; Cheah, M. H.; Shevela, D.; Saracini, C.; Bean, M. A.; Seuffert, I.; Sokaras, D.; Weng, T. C.; Pastor, E.; Weninger, C.; Fransson, T.; Lassalle, L.; Brauer, P.; Aller, P.; Docker, P. T.; Andi, B.; Orville, A. M.; Glownia, J. M.; Nelson, S.; Sikorski, M.; Zhu, D.; Hunter, M. S.; Lane, T. J.; Aquila, A.; Koglin, J. E.; Robinson, J.; Liang, M.; Boutet, S.; Lyubimov, A. Y.; Uervirojnangkoorn, M.; Moriarty, N. W.; Liebschner, D.; Afonine, P. V.; Waterman, D. G.; Evans, G.; Wernet, P.; Dobbek, H.; Weis, W. I.; Brunger, A. T.; Zwart, P. H.; Adams, P. D.; Zouni, A.; Messinger, J.; Bergmann, U.; Sauter, N. K.; Kern, J.; Yachandra, V. K.; Yano, J., Structure of photosystem II and substrate binding at room temperature. *Nature* **2016,** *540* (7633), 453-457.

147. Sierra, R. G.; Gati, C.; Laksmono, H.; Dao, E. H.; Gul, S.; Fuller, F.; Kern, J.; Chatterjee, R.; Ibrahim, M.; Brewster, A. S.; Young, I. D.; Michels-Clark, T.; Aquila, A.; Liang, M.; Hunter, M. S.; Koglin, J. E.; Boutet, S.; Junco, E. A.; Hayes, B.; Bogan, M. J.; Hampton, C. Y.; Puglisi, E. V.; Sauter, N. K.; Stan, C. A.; Zouni, A.; Yano, J.; Yachandra, V. K.; Soltis, S. M.; Puglisi, J. D.; DeMirci, H., Concentric-flow electrokinetic injector enables serial crystallography of ribosome and photosystem II. *Nat Methods* **2016,** *13* (1), 59-62.

148. Ganan-Calvo, A. M.; Montanero, J. M., Revision of capillary cone-jet physics: electrospray and flow focusing. *Phys Rev E Stat Nonlin Soft Matter Phys* **2009,** *79* (6 Pt 2), 066305.

149. Sierra, R. G.; Laksmono, H.; Kern, J.; Tran, R.; Hattne, J.; Alonso-Mori, R.; Lassalle-Kaiser, B.; Glockner, C.; Hellmich, J.; Schafer, D. W.; Echols, N.; Gildea, R. J.; Grosse-Kunstleve, R. W.; Sellberg, J.; McQueen, T. A.; Fry, A. R.; Messerschmidt, M. M.; Miahnahri, A.; Seibert, M. M.; Hampton, C. Y.; Starodub, D.; Loh, N. D.; Sokaras, D.; Weng, T. C.; Zwart, P. H.; Glatzel, P.; Milathianaki, D.; White, W. E.; Adams, P. D.; Williams, G. J.; Boutet, S.; Zouni, A.; Messinger, J.; Sauter, N. K.; Bergmann, U.; Yano, J.; Yachandra, V. K.; Bogan, M. J., Nanoflow electrospinning serial femtosecond crystallography. *Acta Crystallogr D Biol Crystallogr* **2012,** *68* (Pt 11), 1584-7.

150. Dao, E. H.; Poitevin, F.; Sierra, R. G.; Gati, C.; Rao, Y.; Ciftci, H. I.; Aksit, F.; McGurk, A.; Obrinski, T.; Mgbam, P.; Hayes, B.; De Lichtenberg, C.; Pardo-Avila, F.; Corsepius, N.; Zhang, L.; Seaberg, M. H.; Hunter, M. S.; Liang, M.; Koglin, J. E.; Wakatsuki, S.; Demirci, H., Structure of the 30S ribosomal decoding complex at ambient temperature. *RNA* **2018,** *24* (12), 1667-1676.

151. O'Sullivan, M. E.; Poitevin, F.; Sierra, R. G.; Gati, C.; Dao, E. H.; Rao, Y.; Aksit, F.; Ciftci, H.; Corsepius, N.; Greenhouse, R.; Hayes, B.; Hunter, M. S.; Liang, M.; McGurk, A.; Mbgam, P.; Obrinsky, T.; Pardo-Avila, F.;

Seaberg, M. H.; Cheng, A. G.; Ricci, A. J.; DeMirci, H., Aminoglycoside ribosome interactions reveal novel conformational states at ambient temperature. *Nucleic Acids Res* **2018,** *46* (18), 9793-9804.

152. Kern, J.; Alonso-Mori, R.; Tran, R.; Hattne, J.; Gildea, R. J.; Echols, N.; Glockner, C.; Hellmich, J.; Laksmono, H.; Sierra, R. G.; Lassalle-Kaiser, B.; Koroidov, S.; Lampe, A.; Han, G.; Gul, S.; Difiore, D.; Milathianaki, D.; Fry, A. R.; Miahnahri, A.; Schafer, D. W.; Messerschmidt, M.; Seibert, M. M.; Koglin, J. E.; Sokaras, D.; Weng, T. C.; Sellberg, J.; Latimer, M. J.; Grosse-Kunstleve, R. W.; Zwart, P. H.; White, W. E.; Glatzel, P.; Adams, P. D.; Bogan, M. J.; Williams, G. J.; Boutet, S.; Messinger, J.; Zouni, A.; Sauter, N. K.; Yachandra, V. K.; Bergmann, U.; Yano, J., Simultaneous femtosecond X-ray spectroscopy and diffraction of photosystem II at room temperature. *Science* **2013,** *340* (6131), 491-5.

153. Landau, E. M.; Rosenbusch, J. P., Lipidic cubic phases: a novel concept for the crystallization of membrane proteins. *Proc Natl Acad Sci U S A* **1996,** *93* (25), 14532-5.

154. Cherezov, V., Lipidic cubic phase technologies for membrane protein structural studies. *Curr Opin Struct Biol* **2011,** *21* (4), 559-66.

155. Stauch, B.; Cherezov, V., Serial Femtosecond Crystallography of G Protein-Coupled Receptors. *Annu Rev Biophys* **2018,** *47* (1), 377-397.

156. Ishchenko, A.; Gati, C.; Cherezov, V., Structural biology of G protein-coupled receptors: new opportunities from XFELs and cryoEM. *Curr Opin Struct Biol* **2018,** *51*, 44-52.

157. Sugahara, M.; Mizohata, E.; Nango, E.; Suzuki, M.; Tanaka, T.; Masuda, T.; Tanaka, R.; Shimamura, T.; Tanaka, Y.; Suno, C.; Ihara, K.; Pan, D.; Kakinouchi, K.; Sugiyama, S.; Murata, M.; Inoue, T.; Tono, K.; Song, C.; Park, J.; Kameshima, T.; Hatsui, T.; Joti, Y.; Yabashi, M.; Iwata, S., Grease matrix as a versatile carrier of proteins for serial crystallography. *Nat Methods* **2015,** *12* (1), 61-3.

158. Sugahara, M.; Song, C.; Suzuki, M.; Masuda, T.; Inoue, S.; Nakane, T.; Yumoto, F.; Nango, E.; Tanaka, R.; Tono, K.; Joti, Y.; Kameshima, T.; Hatsui, T.; Yabashi, M.; Nureki, O.; Numata, K.; Iwata, S., Oil-free hyaluronic acid matrix for serial femtosecond crystallography. *Sci Rep* **2016,** *6* (1), 24484.

159. Conrad, C. E.; Basu, S.; James, D.; Wang, D.; Schaffer, A.; Roy-Chowdhury, S.; Zatsepin, N. A.; Aquila, A.; Coe, J.; Gati, C.; Hunter, M. S.; Koglin, J. E.; Kupitz, C.; Nelson, G.; Subramanian, G.; White, T. A.; Zhao, Y.; Zook, J.; Boutet, S.; Cherezov, V.; Spence, J. C.; Fromme, R.; Weierstall, U.; Fromme, P., A novel inert crystal delivery medium for serial femtosecond crystallography. *IUCrJ* **2015,** *2* (Pt 4), 421-30.

160. Park, J.; Park, S.; Kim, J.; Park, G.; Cho, Y.; Nam, K. H., Polyacrylamide injection matrix for serial femtosecond crystallography. *Sci Rep* **2019,** *9* (1), 2525.

161. Nogly, P.; Panneels, V.; Nelson, G.; Gati, C.; Kimura, T.; Milne, C.; Milathianaki, D.; Kubo, M.; Wu, W.; Conrad, C.; Coe, J.; Bean, R.; Zhao, Y.; Bath, P.; Dods, R.; Harimoorthy, R.; Beyerlein, K. R.; Rheinberger, J.; James, D.; DePonte, D.; Li, C.; Sala, L.; Williams, G. J.; Hunter, M. S.; Koglin, J. E.; Berntsen, P.; Nango, E.; Iwata, S.; Chapman, H. N.; Fromme, P.; Frank, M.; Abela, R.; Boutet, S.; Barty, A.; White, T. A.; Weierstall, U.; Spence, J.; Neutze, R.; Schertler, G.; Standfuss, J., Lipidic cubic phase injector is a viable crystal delivery system for time-resolved serial crystallography. *Nat Commun* **2016,** *7* (1), 12314.

162. Nango, E.; Royant, A.; Kubo, M.; Nakane, T.; Wickstrand, C.; Kimura, T.; Tanaka, T.; Tono, K.; Song, C.; Tanaka, R.; Arima, T.; Yamashita, A.; Kobayashi, J.; Hosaka, T.; Mizohata, E.; Nogly, P.; Sugahara, M.; Nam, D.; Nomura, T.; Shimamura, T.; Im, D.; Fujiwara, T.; Yamanaka, Y.; Jeon, B.; Nishizawa, T.; Oda, K.; Fukuda, M.; Andersson, R.; Bath, P.; Dods, R.; Davidsson, J.; Matsuoka, S.; Kawatake, S.; Murata, M.; Nureki, O.; Owada, S.; Kameshima, T.; Hatsui, T.; Joti, Y.; Schertler, G.; Yabashi, M.; Bondar, A. N.; Standfuss, J.; Neutze, R.; Iwata, S., A three-dimensional movie of structural changes in bacteriorhodopsin. *Science* **2016,** *354* (6319), 1552-1557.

163. Nogly, P.; Weinert, T.; James, D.; Carbajo, S.; Ozerov, D.; Furrer, A.; Gashi, D.; Borin, V.; Skopintsev, P.; Jaeger, K.; Nass, K.; Bath, P.; Bosman, R.; Koglin, J.; Seaberg, M.; Lane, T.; Kekilli, D.; Brunle, S.; Tanaka, T.; Wu, W.; Milne, C.; White, T.; Barty, A.; Weierstall, U.; Panneels, V.; Nango, E.; Iwata, S.; Hunter, M.; Schapiro, I.; Schertler, G.; Neutze, R.; Standfuss, J., Retinal isomerization in bacteriorhodopsin captured by a femtosecond x-ray laser. *Science* **2018,** *361* (6398), eaat0094.

164. Suga, M.; Akita, F.; Sugahara, M.; Kubo, M.; Nakajima, Y.; Nakane, T.; Yamashita, K.; Umena, Y.; Nakabayashi, M.; Yamane, T.; Nakano, T.; Suzuki, M.; Masuda, T.; Inoue, S.; Kimura, T.; Nomura, T.; Yonekura, S.; Yu, L. J.; Sakamoto, T.; Motomura, T.; Chen, J. H.; Kato, Y.; Noguchi, T.; Tono, K.; Joti, Y.; Kameshima, T.; Hatsui, T.; Nango, E.; Tanaka, R.; Naitow, H.; Matsuura, Y.; Yamashita, A.; Yamamoto, M.; Nureki, O.; Yabashi, M.; Ishikawa, T.; Iwata, S.; Shen, J. R., Light-induced structural changes and the site of O=O bond formation in PSII caught by XFEL. *Nature* **2017,** *543* (7643), 131-135.

165. Seibert, M. M.; Ekeberg, T.; Maia, F. R.; Svenda, M.; Andreasson, J.; Jonsson, O.; Odic, D.; Iwan, B.; Rocker, A.; Westphal, D.; Hantke, M.; DePonte, D. P.; Barty, A.; Schulz, J.; Gumprecht, L.; Coppola, N.; Aquila, A.; Liang, M.; White, T. A.; Martin, A.; Caleman, C.; Stern, S.; Abergel, C.; Seltzer, V.; Claverie, J. M.; Bostedt, C.; Bozek, J. D.; Boutet, S.; Miahnahri, A. A.; Messerschmidt, M.; Krzywinski, J.; Williams, G.; Hodgson, K. O.; Bogan, M. J.; Hampton, C. Y.; Sierra, R. G.; Starodub, D.; Andersson, I.; Bajt, S.; Barthelmess, M.; Spence, J. C.; Fromme, P.; Weierstall, U.; Kirian, R.; Hunter, M.; Doak, R. B.; Marchesini, S.; Hau-Riege, S. P.; Frank, M.; Shoeman, R. L.; Lomb, L.; Epp, S. W.; Hartmann, R.; Rolles, D.; Rudenko, A.; Schmidt, C.; Foucar, L.; Kimmel, N.; Holl, P.; Rudek, B.; Erk, B.; Homke, A.; Reich, C.; Pietschner, D.; Weidenspointner, G.; Struder, L.; Hauser, G.; Gorke, H.; Ullrich, J.;

Schlichting, I.; Herrmann, S.; Schaller, G.; Schopper, F.; Soltau, H.; Kuhnel, K. U.; Andritschke, R.; Schroter, C. D.; Krasniqi, F.; Bott, M.; Schorb, S.; Rupp, D.; Adolph, M.; Gorkhover, T.; Hirsemann, H.; Potdevin, G.; Graafsma, H.; Nilsson, B.; Chapman, H. N.; Hajdu, J., Single mimivirus particles intercepted and imaged with an X-ray laser. *Nature* **2011,** *470* (7332), 78-81.

166. Chavas, L. M.; Gumprecht, L.; Chapman, H. N., Possibilities for serial femtosecond crystallography sample delivery at future light sources. *Struct Dyn* **2015,** *2* (4), 041709.

167. Hantke, M. F.; Hasse, D.; Maia, F. R. N. C.; Ekeberg, T.; John, K.; Svenda, M.; Loh, N. D.; Martin, A. V.; Timneanu, N.; Larsson, D. S. D.; van der Schot, G.; Carlsson, G. H.; Ingelman, M.; Andreasson, J.; Westphal, D.; Liang, M. N.; Stellato, F.; DePonte, D. P.; Hartmann, R.; Kimmel, N.; Kirian, R. A.; Seibert, M. M.; Muhlig, K.; Schorb, S.; Ferguson, K.; Bostedt, C.; Carron, S.; Bozek, J. D.; Rolles, D.; Rudenko, A.; Epp, S.; Chapman, H. N.; Barty, A.; Hajdu, J.; Andersson, I., High-throughput imaging of heterogeneous cell organelles with an X-ray laser. *Nature Photonics* **2014,** *8* (12), 943-949.

168. Hantke, M. F.; Hasse, D.; Ekeberg, T.; John, K.; Svenda, M.; Loh, D.; Martin, A. V.; Timneanu, N.; Larsson, D. S.; van der Schot, G.; Carlsson, G. H.; Ingelman, M.; Andreasson, J.; Westphal, D.; Iwan, B.; Uetrecht, C.; Bielecki, J.; Liang, M.; Stellato, F.; DePonte, D. P.; Bari, S.; Hartmann, R.; Kimmel, N.; Kirian, R. A.; Seibert, M. M.; Muhlig, K.; Schorb, S.; Ferguson, K.; Bostedt, C.; Carron, S.; Bozek, J. D.; Rolles, D.; Rudenko, A.; Foucar, L.; Epp, S. W.; Chapman, H. N.; Barty, A.; Andersson, I.; Hajdu, J.; Maia, F. R., A data set from flash X-ray imaging of carboxysomes. *Sci Data* **2016,** *3*, 160061.

169. Kirian, R. A.; Awel, S.; Eckerskorn, N.; Fleckenstein, H.; Wiedorn, M.; Adriano, L.; Bajt, S.; Barthelmess, M.; Bean, R.; Beyerlein, K. R.; Chavas, L. M.; Domaracky, M.; Heymann, M.; Horke, D. A.; Knoska, J.; Metz, M.; Morgan, A.; Oberthuer, D.; Roth, N.; Sato, T.; Xavier, P. L.; Yefanov, O.; Rode, A. V.; Kupper, J.; Chapman, H. N., Simple convergent-nozzle aerosol injector for single-particle diffractive imaging with X-ray free-electron lasers. *Struct Dyn* **2015,** *2* (4), 041717.

170. Awel, S.; Kirian, R. A.; Wiedorn, M. O.; Beyerlein, K. R.; Roth, N.; Horke, D. A.; Oberthur, D.; Knoska, J.; Mariani, V.; Morgan, A.; Adriano, L.; Tolstikova, A.; Xavier, P. L.; Yefanov, O.; Aquila, A.; Barty, A.; Roy-Chowdhury, S.; Hunter, M. S.; James, D.; Robinson, J. S.; Weierstall, U.; Rode, A. V.; Bajt, S.; Kupper, J.; Chapman, H. N., Femtosecond X-ray diffraction from an aerosolized beam of protein nanocrystals. *J Appl Crystallogr* **2018,** *51* (Pt 1), 133-139.

171. Schulz, E. C.; Kaub, J.; Busse, F.; Mehrabi, P.; Muller-Werkmeister, H. M.; Pai, E. F.; Robertson, W. D.; Miller, R. J. D., Protein crystals IR laser ablated from aqueous solution at high speed retain their diffractive properties: applications in high-speed serial crystallography. *J Appl Crystallogr* **2017,** *50* (6), 1773-1781.

172. Ghazal, A.; Lafleur, J. P.; Mortensen, K.; Kutter, J. P.; Arleth, L.; Jensen, G. V., Recent advances in X-ray compatible microfluidics for applications in soft materials and life sciences. *Lab Chip* **2016,** *16* (22), 4263-4295.

173. Murray, T. D.; Lyubimov, A. Y.; Ogata, C. M.; Vo, H.; Uervirojnangkoorn, M.; Brunger, A. T.; Berger, J. M., A high-transparency, micro-patternable chip for X-ray diffraction analysis of microcrystals under native growth conditions. *Acta Crystallogr D Biol Crystallogr* **2015,** *71* (Pt 10), 1987-97.

174. Mueller, C.; Marx, A.; Epp, S. W.; Zhong, Y.; Kuo, A.; Balo, A. R.; Soman, J.; Schotte, F.; Lemke, H. T.; Owen, R. L.; Pai, E. F.; Pearson, A. R.; Olson, J. S.; Anfinrud, P. A.; Ernst, O. P.; Dwayne Miller, R. J., Fixed target matrix for femtosecond time-resolved and in situ serial micro-crystallography. *Struct Dyn* **2015,** *2* (5), 054302.

175. Roedig, P.; Ginn, H. M.; Pakendorf, T.; Sutton, G.; Harlos, K.; Walter, T. S.; Meyer, J.; Fischer, P.; Duman, R.; Vartiainen, I.; Reime, B.; Warmer, M.; Brewster, A. S.; Young, I. D.; Michels-Clark, T.; Sauter, N. K.; Kotecha, A.; Kelly, J.; Rowlands, D. J.; Sikorsky, M.; Nelson, S.; Damiani, D. S.; Alonso-Mori, R.; Ren, J.; Fry, E. E.; David, C.; Stuart, D. I.; Wagner, A.; Meents, A., High-speed fixed-target serial virus crystallography. *Nat Methods* **2017,** *14* (8), 805-810.

176. Lyubimov, A. Y.; Murray, T. D.; Koehl, A.; Araci, I. E.; Uervirojnangkoorn, M.; Zeldin, O. B.; Cohen, A. E.; Soltis, S. M.; Baxter, E. L.; Brewster, A. S.; Sauter, N. K.; Brunger, A. T.; Berger, J. M., Capture and X-ray diffraction studies of protein microcrystals in a microfluidic trap array. *Acta Crystallogr D Biol Crystallogr* **2015,** *71* (Pt 4), 928-40.

177. Mathews, II; Allison, K.; Robbins, T.; Lyubimov, A. Y.; Uervirojnangkoorn, M.; Brunger, A. T.; Khosla, C.; DeMirci, H.; McPhillips, S. E.; Hollenbeck, M.; Soltis, M.; Cohen, A. E., The Conformational Flexibility of the Acyltransferase from the Disorazole Polyketide Synthase Is Revealed by an X-ray Free-Electron Laser Using a Room-Temperature Sample Delivery Method for Serial Crystallography. *Biochemistry* **2017,** *56* (36), 4751-4756.

178. Oghbaey, S.; Sarracini, A.; Ginn, H. M.; Pare-Labrosse, O.; Kuo, A.; Marx, A.; Epp, S. W.; Sherrell, D. A.; Eger, B. T.; Zhong, Y.; Loch, R.; Mariani, V.; Alonso-Mori, R.; Nelson, S.; Lemke, H. T.; Owen, R. L.; Pearson, A. R.; Stuart, D. I.; Ernst, O. P.; Mueller-Werkmeister, H. M.; Miller, R. J., Fixed target combined with spectral mapping: approaching 100% hit rates for serial crystallography. *Acta Crystallogr D Struct Biol* **2016,** *72* (Pt 8), 944-55.

179. Nam, D.; Kim, C.; Kim, Y.; Ebisu, T.; Gallagher-Jones, M.; Park, J.; Kim, S.; Kim, S.; Tono, K.; Noh, D. Y.; Yabashi, M.; Ishikawa, T.; Song, C., Fixed target single-shot imaging of nanostructures using thin solid membranes at SACLA. *Journal of Physics B-Atomic Molecular and Optical Physics* **2016,** *49* (3), 034008.

180. Górzny, M. Ł.; Opara, N. L.; Guzenko, V. A.; Cadarso, V. J.; Schift, H.; Li, X. D.; Padeste, C., Microfabricated silicon chip as lipid membrane sample

holder for serial protein crystallography. *Micro and Nano Engineering* **2019,** *3*, 31-36.

181. Schieferstein, J. M.; Pawate, A. S.; Varel, M. J.; Guha, S.; Astrauskaite, I.; Gennis, R. B.; Kenis, P. J. A., X-ray transparent microfluidic platforms for membrane protein crystallization with microseeds. *Lab Chip* **2018,** *18* (6), 944-954.

182. Denz, M.; Brehm, G.; Hemonnot, C. Y. J.; Spears, H.; Wittmeier, A.; Cassini, C.; Saldanha, O.; Perego, E.; Diaz, A.; Burghammer, M.; Koster, S., Cyclic olefin copolymer as an X-ray compatible material for microfluidic devices. *Lab Chip* **2017,** *18* (1), 171-178.

183. Doak, R. B.; Nass Kovacs, G.; Gorel, A.; Foucar, L.; Barends, T. R. M.; Grunbein, M. L.; Hilpert, M.; Kloos, M.; Roome, C. M.; Shoeman, R. L.; Stricker, M.; Tono, K.; You, D.; Ueda, K.; Sherrell, D. A.; Owen, R. L.; Schlichting, I., Crystallography on a chip - without the chip: sheet-on-sheet sandwich. *Acta Crystallogr D Struct Biol* **2018,** *74* (Pt 10), 1000-1007.

184. Doak, R.; DePonte, D.; Nelson, G.; Camacho-Alanis, F.; Ros, A.; Spence, J.; Weierstall, U. Microscopic linear liquid streams in vacuum: Injection of solvated biological samples into X-ray free electron lasers. *Proceedings of AIP Conference Proceedings*, AIP: 2012; pp 1314-1323.

185. Seddon, E. A.; Clarke, J. A.; Dunning, D. J.; Masciovecchio, C.; Milne, C. J.; Parmigiani, F.; Rugg, D.; Spence, J. C. H.; Thompson, N. R.; Ueda, K.; Vinko, S. M.; Wark, J. S.; Wurth, W., Short-wavelength free-electron laser sources and science: a review. *Rep Prog Phys* **2017,** *80* (11), 115901.

186. Heymann, M.; Opthalage, A.; Wierman, J. L.; Akella, S.; Szebenyi, D. M.; Gruner, S. M.; Fraden, S., Room-temperature serial crystallography using a kinetically optimized microfluidic device for protein crystallization and on-chip X-ray diffraction. *IUCrJ* **2014,** *1* (Pt 5), 349-60.

187. Hunter, M. S.; Sublett, B. Sample Delivery Methods. https://lcls.slac.stanford.edu/sed/methods (accessed September 5, 2019).

188. Tono, K.; Nango, E.; Sugahara, M.; Song, C.; Park, J.; Tanaka, T.; Tanaka, R.; Joti, Y.; Kameshima, T.; Ono, S.; Hatsui, T.; Mizohata, E.; Suzuki, M.; Shimamura, T.; Tanaka, Y.; Iwata, S.; Yabashi, M., Diverse application platform for hard X-ray diffraction in SACLA (DAPHNIS): application to serial protein crystallography using an X-ray free-electron laser. *J Synchrotron Radiat* **2015,** *22* (3), 532-7.

189. Tono, K., Fluid sample injectors for x-ray free electron laser at SACLA. *High Power Laser Science and Engineering* **2017,** *5*, e7.

190. Maeki, M.; Yamaguchi, H.; Tokeshi, M.; Miyazaki, M., Microfluidic Approaches for Protein Crystal Structure Analysis. *Anal Sci* **2016,** *32* (1), 3-9.

191. Abdallah, B. G.; Chao, T. C.; Kupitz, C.; Fromme, P.; Ros, A., Dielectrophoretic sorting of membrane protein nanocrystals. *ACS Nano* **2013,** *7* (10), 9129-37.

192. Lee, K. S.; Kim, R. H.; Yang, D. Y.; Park, S. H., Advances in 3D nano/microfabrication using two-photon initiated polymerization. *Progress in Polymer Science* **2008,** *33* (6), 631-681.

193. Nisisako, T.; Torii, T.; Higuchi, T., Droplet formation in a microchannel network. *Lab Chip* **2002,** *2* (1), 24-6.

194. Song, H.; Ismagilov, R. F., Millisecond kinetics on a microfluidic chip using nanoliters of reagents. *J Am Chem Soc* **2003,** *125* (47), 14613-9.

195. Song, H.; Tice, J. D.; Ismagilov, R. F., A microfluidic system for controlling reaction networks in time. *Angew Chem Int Ed Engl* **2003,** *42* (7), 768-72.

196. Li, L.; Ismagilov, R. F., Protein crystallization using microfluidic technologies based on valves, droplets, and SlipChip. *Annu Rev Biophys* **2010,** *39* (1), 139-58.

197. Husny, J.; Cooper-White, J. J., The effect of elasticity on drop creation in T-shaped microchannels. *Journal of Non-Newtonian Fluid Mechanics* **2006,** *137* (1-3), 121-136.

198. Ferreira, J.; Castro, F.; Rocha, F.; Kuhn, S., Protein crystallization in a droplet-based microfluidic device: Hydrodynamic analysis and study of the phase behaviour. *Chemical Engineering Science* **2018,** *191*, 232-244.

199. Ho, C. M.; Ng, S. H.; Li, K. H.; Yoon, Y. J., 3D printed microfluidics for biological applications. *Lab Chip* **2015,** *15* (18), 3627-37.

200. Wong, I.; Ho, C. M., Surface molecular property modifications for poly(dimethylsiloxane) (PDMS) based microfluidic devices. *Microfluid Nanofluidics* **2009,** *7* (3), 291-306.

201. Fadeev, A. Y.; Kazakevich, Y. V., Covalently attached monolayers of oligo(dimethylsiloxane)s on silica: A siloxane chemistry approach for surface modification. *Langmuir* **2002,** *18* (7), 2665-2672.

202. Aghvami, S. A.; Opathalage, A.; Zhang, Z. K.; Ludwig, M.; Heymann, M.; Norton, M.; Wilkins, N.; Fraden, S., Rapid prototyping of cyclic olefin copolymer (COC) microfluidic devices. *Sensors and Actuators B-Chemical* **2017,** *247*, 940-949.

203. Campo, A. d.; Greiner, C., SU-8: a photoresist for high-aspect-ratio and 3D submicron lithography. *Journal of Micromechanics and Microengineering* **2007,** *17* (6), R81-R95.

204. Huang, T. Y.; Sakar, M. S.; Mao, A.; Petruska, A. J.; Qiu, F.; Chen, X. B.; Kennedy, S.; Mooney, D.; Nelson, B. J., 3D Printed Microtransporters:

Compound Micromachines for Spatiotemporally Controlled Delivery of Therapeutic Agents. *Adv Mater* **2015,** *27* (42), 6644-50.

205. Ligon, S. C.; Liska, R.; Stampfl, J.; Gurr, M.; Mulhaupt, R., Polymers for 3D Printing and Customized Additive Manufacturing. *Chem Rev* **2017,** *117* (15), 10212-10290.

206. Duong, T. T.; Kim, G.; Ros, R.; Streek, M.; Schmid, F.; Brugger, J.; Anselmetti, D.; Ros, A., Size-dependent free solution DNA electrophoresis in structured microfluidic systems. *Microelectronic Engineering* **2003,** *67-8*, 905-912.

207. Hunter, M. S.; Fromme, P., Toward structure determination using membrane-protein nanocrystals and microcrystals. *Methods* **2011,** *55* (4), 387-404.

208. Sierra, R. G.; Batyuk, A.; Sun, Z.; Aquila, A.; Hunter, M. S.; Lane, T. J.; Liang, M.; Yoon, C. H.; Alonso-Mori, R.; Armenta, R.; Castagna, J. C.; Hollenbeck, M.; Osier, T. O.; Hayes, M.; Aldrich, J.; Curtis, R.; Koglin, J. E.; Rendahl, T.; Rodriguez, E.; Carbajo, S.; Guillet, S.; Paul, R.; Hart, P.; Nakahara, K.; Carini, G.; DeMirci, H.; Dao, E. H.; Hayes, B. M.; Rao, Y. P.; Chollet, M.; Feng, Y.; Fuller, F. D.; Kupitz, C.; Sato, T.; Seaberg, M. H.; Song, S.; van Driel, T. B.; Yavas, H.; Zhu, D.; Cohen, A. E.; Wakatsuki, S.; Boutet, S., The Macromolecular Femtosecond Crystallography Instrument at the Linac Coherent Light Source. *J Synchrotron Radiat* **2019,** *26* (Pt 2), 346-357.

209. Mariani, V.; Morgan, A.; Yoon, C. H.; Lane, T. J.; White, T. A.; O'Grady, C.; Kuhn, M.; Aplin, S.; Koglin, J.; Barty, A.; Chapman, H. N., OnDA: online data analysis and feedback for serial X-ray imaging. *J Appl Crystallogr* **2016,** *49* (Pt 3), 1073-1080.

210. Boutet, S.; Cohen, A.; Wakatsuki, S., The New Macromolecular Femtosecond Crystallography (MFX) Instrument at LCLS. *Synchrotron Radiat News* **2016,** *29* (1), 23-28.

211. Chae, S. K.; Lee, C. H.; Lee, S. H.; Kim, T. S.; Kang, J. Y., Oil droplet generation in PDMS microchannel using an amphiphilic continuous phase. *Lab Chip* **2009,** *9* (13), 1957-61.

212. Nge, P. N.; Rogers, C. I.; Woolley, A. T., Advances in microfluidic materials, functions, integration, and applications. *Chem Rev* **2013,** *113* (4), 2550-83.

213. Martinelli, E.; Agostini, S.; Galli, G.; Chiellini, E.; Glisenti, A.; Pettitt, M. E.; Callow, M. E.; Callow, J. A.; Graf, K.; Bartels, F. W., Nanostructured films of amphiphilic fluorinated block copolymers for fouling release application. *Langmuir* **2008,** *24* (22), 13138-47.

214. Sarvothaman, M. K.; Kim, K. S.; Seale, B.; Brodersen, P. M.; Walker, G. C.; Wheeler, A. R., Dynamic Fluoroalkyl Polyethylene Glycol Co-Polymers: A New Strategy for Reducing Protein Adhesion in Lab-on-a-Chip Devices. *Advanced Functional Materials* **2015,** *25* (4), 506-515.

215. Riche, C. T.; Zhang, C.; Gupta, M.; Malmstadt, N., Fluoropolymer surface coatings to control droplets in microfluidic devices. *Lab Chip* **2014,** *14* (11), 1834-41.

216. Kuhn, S.; Hartman, R. L.; Sultana, M.; Nagy, K. D.; Marre, S.; Jensen, K. F., Teflon-coated silicon microreactors: impact on segmented liquid-liquid multiphase flows. *Langmuir* **2011,** *27* (10), 6519-27.

217. Tullis, J.; Park, C. L.; Abbyad, P., Selective fusion of anchored droplets via changes in surfactant concentration. *Lab Chip* **2014,** *14* (17), 3285-9.

218. Scheler, O.; Kaminski, T. S.; Ruszczak, A.; Garstecki, P., Dodecylresorufin (C12R) Outperforms Resorufin in Microdroplet Bacterial Assays. *ACS Appl Mater Interfaces* **2016,** *8* (18), 11318-25.

219. Guzowski, J.; Gizynski, K.; Gorecki, J.; Garstecki, P., Microfluidic platform for reproducible self-assembly of chemically communicating droplet networks with predesigned number and type of the communicating compartments. *Lab Chip* **2016,** *16* (4), 764-72.

220. Saini, G.; Sautter, K.; Hild, F. E.; Pauley, J.; Linford, M. R., Two-silane chemical vapor deposition treatment of polymer (nylon) and oxide surfaces that yields hydrophobic (and superhydrophobic), abrasion-resistant thin films. *Journal of Vacuum Science & Technology A: Vacuum, Surfaces, and Films* **2008,** *26* (5), 1224-1234.

221. Kirchner, R.; Chidambaram, N.; Altana, M.; Schift, H. How post-processing by selective thermal reflow can reduce the roughness of 3D lithography in micro-optical lenses. *Proceedings of SPIE LASE*, San Francisco, SPIE: San Francisco, 2017.

222. Quéré, D., Wetting and Roughness. *Annual Review of Materials Research* **2008,** *38* (1), 71-99.

223. Yang, F. C.; Chen, X. P.; Yue, P. T., Surface roughness effects on contact line motion with small capillary number. *Physics of Fluids* **2018,** *30* (1), 012106.

224. Yang, C.; Tartaglino, U.; Persson, B. N., Nanodroplets on rough hydrophilic and hydrophobic surfaces. *Eur Phys J E Soft Matter* **2008,** *25* (2), 139-52.

225. White, T. A.; Mariani, V.; Brehm, W.; Yefanov, O.; Barty, A.; Beyerlein, K. R.; Chervinskii, F.; Galli, L.; Gati, C.; Nakane, T.; Tolstikova, A.; Yamashita, K.; Yoon, C. H.; Diederichs, K.; Chapman, H. N., Recent developments in CrystFEL. *J Appl Crystallogr* **2016,** *49* (Pt 2), 680-689.

226. Bowman, S. E.; Bridwell-Rabb, J.; Drennan, C. L., Metalloprotein Crystallography: More than a Structure. *Acc Chem Res* **2016,** *49* (4), 695-702.

227. Andersson, R.; Safari, C.; Dods, R.; Nango, E.; Tanaka, R.; Yamashita, A.; Nakane, T.; Tono, K.; Joti, Y.; Bath, P.; Dunevall, E.; Bosman, R.; Nureki, O.; Iwata, S.; Neutze, R.; Branden, G., Serial femtosecond crystallography

structure of cytochrome c oxidase at room temperature. *Sci Rep* **2017,** *7* (1), 4518.

228. Pande, K.; Hutchison, C. D.; Groenhof, G.; Aquila, A.; Robinson, J. S.; Tenboer, J.; Basu, S.; Boutet, S.; DePonte, D. P.; Liang, M.; White, T. A.; Zatsepin, N. A.; Yefanov, O.; Morozov, D.; Oberthuer, D.; Gati, C.; Subramanian, G.; James, D.; Zhao, Y.; Koralek, J.; Brayshaw, J.; Kupitz, C.; Conrad, C.; Roy-Chowdhury, S.; Coe, J. D.; Metz, M.; Xavier, P. L.; Grant, T. D.; Koglin, J. E.; Ketawala, G.; Fromme, R.; Srajer, V.; Henning, R.; Spence, J. C.; Ourmazd, A.; Schwander, P.; Weierstall, U.; Frank, M.; Fromme, P.; Barty, A.; Chapman, H. N.; Moffat, K.; van Thor, J. J.; Schmidt, M., Femtosecond structural dynamics drives the trans/cis isomerization in photoactive yellow protein. *Science* **2016,** *352* (6286), 725-9.

229. Coquelle, N.; Sliwa, M.; Woodhouse, J.; Schiro, G.; Adam, V.; Aquila, A.; Barends, T. R. M.; Boutet, S.; Byrdin, M.; Carbajo, S.; De la Mora, E.; Doak, R. B.; Feliks, M.; Fieschi, F.; Foucar, L.; Guillon, V.; Hilpert, M.; Hunter, M. S.; Jakobs, S.; Koglin, J. E.; Kovacsova, G.; Lane, T. J.; Levy, B.; Liang, M.; Nass, K.; Ridard, J.; Robinson, J. S.; Roome, C. M.; Ruckebusch, C.; Seaberg, M.; Thepaut, M.; Cammarata, M.; Demachy, I.; Field, M.; Shoeman, R. L.; Bourgeois, D.; Colletier, J. P.; Schlichting, I.; Weik, M., Chromophore twisting in the excited state of a photoswitchable fluorescent protein captured by time-resolved serial femtosecond crystallography. *Nat Chem* **2018,** *10* (1), 31-37.

230. Barends, T. R.; Foucar, L.; Ardevol, A.; Nass, K.; Aquila, A.; Botha, S.; Doak, R. B.; Falahati, K.; Hartmann, E.; Hilpert, M.; Heinz, M.; Hoffmann, M. C.; Kofinger, J.; Koglin, J. E.; Kovacsova, G.; Liang, M.; Milathianaki, D.; Lemke, H. T.; Reinstein, J.; Roome, C. M.; Shoeman, R. L.; Williams, G. J.; Burghardt, I.; Hummer, G.; Boutet, S.; Schlichting, I., Direct observation of ultrafast collective motions in CO myoglobin upon ligand dissociation. *Science* **2015,** *350* (6259), 445-50.

231. Wiedorn, M. O.; Awel, S.; Morgan, A. J.; Ayyer, K.; Gevorkov, Y.; Fleckenstein, H.; Roth, N.; Adriano, L.; Bean, R.; Beyerlein, K. R.; Chen, J.; Coe, J.; Cruz-Mazo, F.; Ekeberg, T.; Graceffa, R.; Heymann, M.; Horke, D. A.; Knoska, J.; Mariani, V.; Nazari, R.; Oberthur, D.; Samanta, A. K.; Sierra, R. G.; Stan, C. A.; Yefanov, O.; Rompotis, D.; Correa, J.; Erk, B.; Treusch, R.; Schulz, J.; Hogue, B. G.; Ganan-Calvo, A. M.; Fromme, P.; Kupper, J.; Rode, A. V.; Bajt, S.; Kirian, R. A.; Chapman, H. N., Rapid sample delivery for megahertz serial crystallography at X-ray FELs. *IUCrJ* **2018,** *5* (Pt 5), 574-584.

232. Srajer, V.; Schmidt, M., Watching Proteins Function with Time-resolved X-ray Crystallography. *J Phys D Appl Phys* **2017,** *50* (37), 373001.

233. Tono, K.; Togashi, T.; Inubushi, Y.; Sato, T.; Katayama, T.; Ogawa, K.; Ohashi, H.; Kimura, H.; Takahashi, S.; Takeshita, K.; Tomizawa, H.; Goto, S.; Ishikawa, T.; Yabashi, M., Beamline, experimental stations and photon beam diagnostics for the hard x-ray free electron laser of SACLA. *New J Phys* **2013,** *15*.

234. Park, J.; Kim, S.; Nam, K. H.; Kim, B.; Ko, I. S., Current status of the CXI beamline at the PAL-XFEL. *J Korean Phys Soc* **2016,** *69* (6), 1089-1093.

235. Milne, C. J.; Schietinger, T.; Aiba, M.; Alarcon, A.; Alex, J.; Anghel, A.; Arsov, V.; Beard, C.; Beaud, P.; Bettoni, S.; Bopp, M.; Brands, H.; Bronnimann, M.; Brunnenkant, I.; Calvi, M.; Citterio, A.; Craievich, P.; Csatari Divall, M.; Dallenbach, M.; D'Amico, M.; Dax, A.; Deng, Y. P.; Dietrich, A.; Dinapoli, R.; Divall, E.; Dordevic, S.; Ebner, S.; Erny, C.; Fitze, H.; Flechsig, U.; Follath, R.; Frei, F.; Gartner, F.; Ganter, R.; Garvey, T.; Geng, Z.; Gorgisyan, I.; Gough, C.; Hauff, A.; Hauri, C. P.; Hiller, N.; Humar, T.; Hunziker, S.; Ingold, G.; Ischebeck, R.; Janousch, M.; Juranic, P.; Jurcevic, M.; Kaiser, M.; Kalantari, B.; Kalt, R.; Keil, B.; Kittel, C.; Knopp, G.; Koprek, W.; Lemke, H. T.; Lippuner, T.; Llorente Sancho, D.; Lohl, F.; Lopez-Cuenca, C.; Marki, F.; Marcellini, F.; Marinkovic, G.; Martiel, I.; Menzel, R.; Mozzanica, A.; Nass, K.; Orlandi, G. L.; Ozkan Loch, C.; Panepucci, E.; Paraliev, M.; Patterson, B.; Pedrini, B.; Pedrozzi, M.; Pollet, P.; Pradervand, C.; Prat, E.; Radi, P.; Raguin, J. Y.; Redford, S.; Rehanek, J.; Rehault, J.; Reiche, S.; Ringele, M.; Rittmann, J.; Rivkin, L.; Romann, A.; Ruat, M.; Ruder, C.; Sala, L.; Schebacher, L.; Schilcher, T.; Schlott, V.; Schmidt, T.; Schmitt, B.; Shi, X.; Stadler, M.; Stingelin, L.; Sturzenegger, W.; Szlachetko, J.; Thattil, D.; Treyer, D. M.; Trisorio, A.; Tron, W.; Vetter, S.; Vicario, C.; Voulot, D.; Wang, M.; Zamofing, T.; Zellweger, C.; Zennaro, R.; Zimoch, E.; Abela, R.; Patthey, L.; Braun, H. H., SwissFEL: The Swiss X-ray Free Electron Laser. *Applied Sciences-Basel* **2017,** *7* (7), 720.

236. Conrad, C. E. Overcoming Barriers in Structural Biology Through Method Development of Serial Crystallography. PhD Thesis, Arizona State University, 2016.

237. Coe, J. Life In Motion: Visualizing Biomacromolecules By Time-Resolved Serial Femtosecond Crystallography. PhD Thesis, Arizona State University, 2018.

238. Kupitz, C.; Grotjohann, I.; Conrad, C. E.; Roy-Chowdhury, S.; Fromme, R.; Fromme, P., Microcrystallization techniques for serial femtosecond crystallography using photosystem II from Thermosynechococcus elongatus as a model system. *Philos Trans R Soc Lond B Biol Sci* **2014,** *369* (1647), 20130316.

239. Geloni, G.; Saldin, E.; Samoylova, L.; Schneidmiller, E.; Sinn, H.; Tschentscher, T.; Yurkov, M., Coherence properties of the European XFEL. *New J Phys* **2010,** *12* (3), 035021.

240. Allahgholi, A.; Becker, J.; Delfs, A.; Dinapoli, R.; Goettlicher, P.; Greiffenberg, D.; Henrich, B.; Hirsemann, H.; Kuhn, M.; Klanner, R.; Klyuev, A.; Krueger, H.; Lange, S.; Laurus, T.; Marras, A.; Mezza, D.; Mozzanica, A.; Niemann, M.; Poehlsen, J.; Schwandt, J.; Sheviakov, I.; Shi, X.; Smoljanin, S.; Steffen, L.; Sztuk-Dambietz, J.; Trunk, U.; Xia, Q.; Zeribi, M.; Zhang, J.; Zimmer, M.; Schmitt, B.; Graafsma, H., The Adaptive Gain Integrating Pixel Detector at the European XFEL. *J Synchrotron Radiat* **2019,** *26* (Pt 1), 74-82.

241. Boukhelef, D.; Szuba, J.; Wrona, K.; Youngman, C. Software development for high speed data recording and processing. *Proceedings of ICALEPCS2013*, San Francisco, CA, USA, San Francisco, CA, USA, 2013; pp 665-668.

242. Fangohr, H.; Beg, M.; Bondar, V.; Boukhelef, D.; Brockhauser, S.; Danilevski, C.; Ehsan, W.; Esenov, S. G.; Flucke, G.; Giovanetti, G.; Göries, D.; Hauf, S.; Heisen, B.; Hickin, D. G.; Khakhulin, D.; Klimovskaia, A.; Kuster, M.; Lang, P. M.; Maia, L.; Mekinda, L.; Michelat, T.; Parenti, A.; Previtali, G.; Santos, H.; Silenzi, A.; Sztuk-Dambietz, J.; Szuba, J.; Teichmann, M.; Weger, K.; Wiggins, J.; Wrona, K.; Xu, C.; Aplin, S.; Barty, A.; Kuhn, M.; Mariani, V.; Kluyver, T. Data Analysis support in Karabo at European XFEL. *Proceedings of 16th Int. Conf. on Accelerator and Large Experimental Control Systems*, Barcelona, Spain, JACoW Publishing: Barcelona, Spain, 2017; pp 245-252.

243. Gevorkov, Y.; Yefanov, O.; Barty, A.; White, T. A.; Mariani, V.; Brehm, W.; Tolstikova, A.; Grigat, R. R.; Chapman, H. N., XGANDALF - extended gradient descent algorithm for lattice finding. *Acta Crystallogr A Found Adv* **2019,** *75* (Pt 5), 694-704.

244. Duisenberg, A. J. M., Indexing in Single-Crystal Diffractometry with an Obstinate List of Reflections. *J Appl Crystallogr* **1992,** *25* (2), 92-96.

245. Powell, H. R.; Johnson, O.; Leslie, A. G., Autoindexing diffraction images with iMosflm. *Acta Crystallogr D Biol Crystallogr* **2013,** *69* (Pt 7), 1195-203.

246. Kabsch, W., Xds. *Acta Crystallogr D Biol Crystallogr* **2010,** *66* (Pt 2), 125-32.

247. Winn, M. D.; Ballard, C. C.; Cowtan, K. D.; Dodson, E. J.; Emsley, P.; Evans, P. R.; Keegan, R. M.; Krissinel, E. B.; Leslie, A. G.; McCoy, A.; McNicholas, S. J.; Murshudov, G. N.; Pannu, N. S.; Potterton, E. A.; Powell, H. R.; Read, R. J.; Vagin, A.; Wilson, K. S., Overview of the CCP4 suite and current developments. *Acta Crystallogr D Biol Crystallogr* **2011,** *67* (Pt 4), 235-42.

248. McCoy, A. J.; Grosse-Kunstleve, R. W.; Adams, P. D.; Winn, M. D.; Storoni, L. C.; Read, R. J., Phaser crystallographic software. *J Appl Crystallogr* **2007,** *40* (Pt 4), 658-674.

249. Vainer, R.; Belakhov, V.; Rabkin, E.; Baasov, T.; Adir, N., Crystal structures of Escherichia coli KDO8P synthase complexes reveal the source of catalytic irreversibility. *J Mol Biol* **2005,** *351* (3), 641-52.

250. Murshudov, G. N.; Skubak, P.; Lebedev, A. A.; Pannu, N. S.; Steiner, R. A.; Nicholls, R. A.; Winn, M. D.; Long, F.; Vagin, A. A., REFMAC5 for the refinement of macromolecular crystal structures. *Acta Crystallogr D Biol Crystallogr* **2011,** *67* (Pt 4), 355-67.

251. Emsley, P.; Lohkamp, B.; Scott, W. G.; Cowtan, K., Features and development of Coot. *Acta Crystallogr D Biol Crystallogr* **2010,** *66* (Pt 4), 486-501.

252. Joosten, R. P.; Long, F.; Murshudov, G. N.; Perrakis, A., The PDB_REDO server for macromolecular structure model optimization. *IUCrJ* **2014,** *1* (Pt 4), 213-20.

253. Joosten, R. P.; Joosten, K.; Murshudov, G. N.; Perrakis, A., PDB_REDO: constructive validation, more than just looking for errors. *Acta Crystallogr D Biol Crystallogr* **2012,** *68* (Pt 4), 484-96.

254. Schrödinger, L. L. C., The PyMOL Molecular Graphics System, Version~1.8. **Nov-2015**.

255. Schulz, J.; Bielecki, J.; Doak, R. B.; Dorner, K.; Graceffa, R.; Shoeman, R. L.; Sikorski, M.; Thute, P.; Westphal, D.; Mancuso, A. P., A versatile liquid-jet setup for the European XFEL. *J Synchrotron Radiat* **2019,** *26* (Pt 2), 339-345.

256. Gupta, A.; Kumar, R., Flow regime transition at high capillary numbers in a microfluidic T-junction: Viscosity contrast and geometry effect. *Physics of Fluids* **2010,** *22* (12), 122001.

257. Gañán-Calvo, A. M., Generation of Steady Liquid Microthreads and Micron-Sized Monodisperse Sprays in Gas Streams. *Physical Review Letters* **1998,** *80* (2), 285-288.

258. Jonsson, H. O.; Caleman, C.; Andreasson, J.; Timneanu, N., Hit detection in serial femtosecond crystallography using X-ray spectroscopy of plasma emission. *IUCrJ* **2017,** *4* (Pt 6), 778-784.

259. Grunbein, M. L.; Bielecki, J.; Gorel, A.; Stricker, M.; Bean, R.; Cammarata, M.; Dorner, K.; Frohlich, L.; Hartmann, E.; Hauf, S.; Hilpert, M.; Kim, Y.; Kloos, M.; Letrun, R.; Messerschmidt, M.; Mills, G.; Nass Kovacs, G.; Ramilli, M.; Roome, C. M.; Sato, T.; Scholz, M.; Sliwa, M.; Sztuk-Dambietz, J.; Weik, M.; Weinhausen, B.; Al-Qudami, N.; Boukhelef, D.; Brockhauser, S.; Ehsan, W.; Emons, M.; Esenov, S.; Fangohr, H.; Kaukher, A.; Kluyver, T.; Lederer, M.; Maia, L.; Manetti, M.; Michelat, T.; Munnich, A.; Pallas, F.; Palmer, G.; Previtali, G.; Raab, N.; Silenzi, A.; Szuba, J.; Venkatesan, S.; Wrona, K.; Zhu, J.; Doak, R. B.; Shoeman, R. L.; Foucar, L.; Colletier, J. P.; Mancuso, A. P.; Barends, T. R. M.; Stan, C. A.; Schlichting, I., Megahertz data collection from protein microcrystals at an X-ray free-electron laser. *Nat Commun* **2018,** *9* (1), 3487.

260. Radaev, S.; Dastidar, P.; Patel, M.; Woodard, R. W.; Gatti, D. L., Structure and mechanism of 3-deoxy-D-manno-octulosonate 8-phosphate synthase. *J Biol Chem* **2000,** *275* (13), 9476-84.

261. Li, Z.; Sau, A. K.; Furdui, C. M.; Anderson, K. S., Probing the role of tightly bound phosphoenolpyruvate in Escherichia coli 3-deoxy-d-manno-octulosonate 8-phosphate synthase catalysis using quantitative time-resolved electrospray ionization mass spectrometry in the millisecond time range. *Anal Biochem* **2005,** *343* (1), 35-47.

262. Mayer, F.; Richter, S.; Hubner, P.; Jabbour, T.; Wegener, M., 3D Fluorescence-Based Security Features by 3D Laser Lithography. *Advanced Materials Technologies* **2017,** *2* (11), 1700212.

263. Buch-Manson, N.; Spangenberg, A.; Gomez, L. P. C.; Malval, J. P.; Soppera, O.; Martinez, K. L., Rapid Prototyping of Polymeric Nanopillars by 3D Direct Laser Writing for Controlling Cell Behavior. *Sci Rep* **2017,** *7* (1), 9247.

264. Zhang, W.; Tullier, M. P.; Patel, K.; Carranza, A.; Pojman, J. A.; Radadia, A. D., Microfluidics using a thiol-acrylate resin for fluorescence-based pathogen detection assays. *Lab Chip* **2015,** *15* (21), 4227-31.

265. Heyman, N. S.; Burt, J. M., Hindered diffusion through an aqueous pore describes invariant dye selectivity of Cx43 junctions. *Biophys J* **2008,** *94* (3), 840-54.

266. Culbertson, C. T.; Jacobson, S. C.; Michael Ramsey, J., Diffusion coefficient measurements in microfluidic devices. *Talanta* **2002,** *56* (2), 365-73.

267. Gendron, P. O.; Avaltroni, F.; Wilkinson, K. J., Diffusion coefficients of several rhodamine derivatives as determined by pulsed field gradient-nuclear magnetic resonance and fluorescence correlation spectroscopy. *J Fluoresc* **2008,** *18* (6), 1093-101.

268. Moreno-Villoslada, I.; Jofre, M.; Miranda, V.; Gonzalez, R.; Sotelo, T.; Hess, S.; Rivas, B. L., pH dependence of the interaction between rhodamine B and the water-soluble poly(sodium 4-styrenesulfonate). *J Phys Chem B* **2006,** *110* (24), 11809-12.

269. Donaphon, B. M. Interchromophoric Interactions Between TMR, Alexa, and BODIPY Fluorophores. PhD Thesis, Arizona State University, 2018.

270. Abdallah, B. G.; Roy-Chowdhury, S.; Coe, J.; Fromme, P.; Ros, A., High throughput protein nanocrystal fractionation in a microfluidic sorter. *Anal Chem* **2015,** *87* (8), 4159-67.

271. Echelmeier , A.; Cruz Villarreal, J.; Kim , D.; Gandhi, S.; Egatz-Gomez, A.; Thifault, D.; Coe, J. D.; Brehm, G.; Madsen, C.; Quintana, S.; Bajt, S.; Messerschmidt, M.; Meza, D.; Oberther, D.; Wiedorn, M. O.; Fleckenstein, H.; Botha, S.; Mendez, D.; Knoska, J.; Martin-Garcia, J. M.; Hu, H.; Lisova, S.; Allahgholi, A.; Gevorkov, Y.; Ayyer, K.; Aplin, S.; Ginn, H. M.; Graafsma, H.; Morgan, A.; Greiffenberg, D.; Klujev, A.; Laurus, T.; Poehlsen, J.; Trunk, U.; Maia, F. R.; Mezza, D.; Fromme, R.; Weinhausen, B.; Mills, G.; Vagovic, P.; Barty, A.; Mancuso, A. P.; Weierstall, U.; Spence, J. C. H.; Chapman, H. N.; Zatsepin, N. A.; Fromme, P.; Kirian, R. A.; Ros, A. Sample Consumption Reduction for Serial Crystallography Using Water-in-Oil Droplets. *Proceedings of Int. Conf. Miniaturized Syst. Chem. Life Sci., 23rd*, Basel, Switzerland, µTAS 2019: Basel, Switzerland, 2019.

272. Tice, J. D.; Song, H.; Lyon, A. D.; Ismagilov, R. F., Formation of droplets and mixing in multiphase microfluidics at low values of the Reynolds and the capillary numbers. *Langmuir* **2003,** *19* (22), 9127-9133.

APPENDIX A

[SUPPLEMENTAL MATERIAL FOR CHAPTER 4]

This Appendix contains Figure A.1, referring to contact angle measurements for the studied surfaces and coatings, and Figure A.2, showing additional diffraction images for PSI crystals.

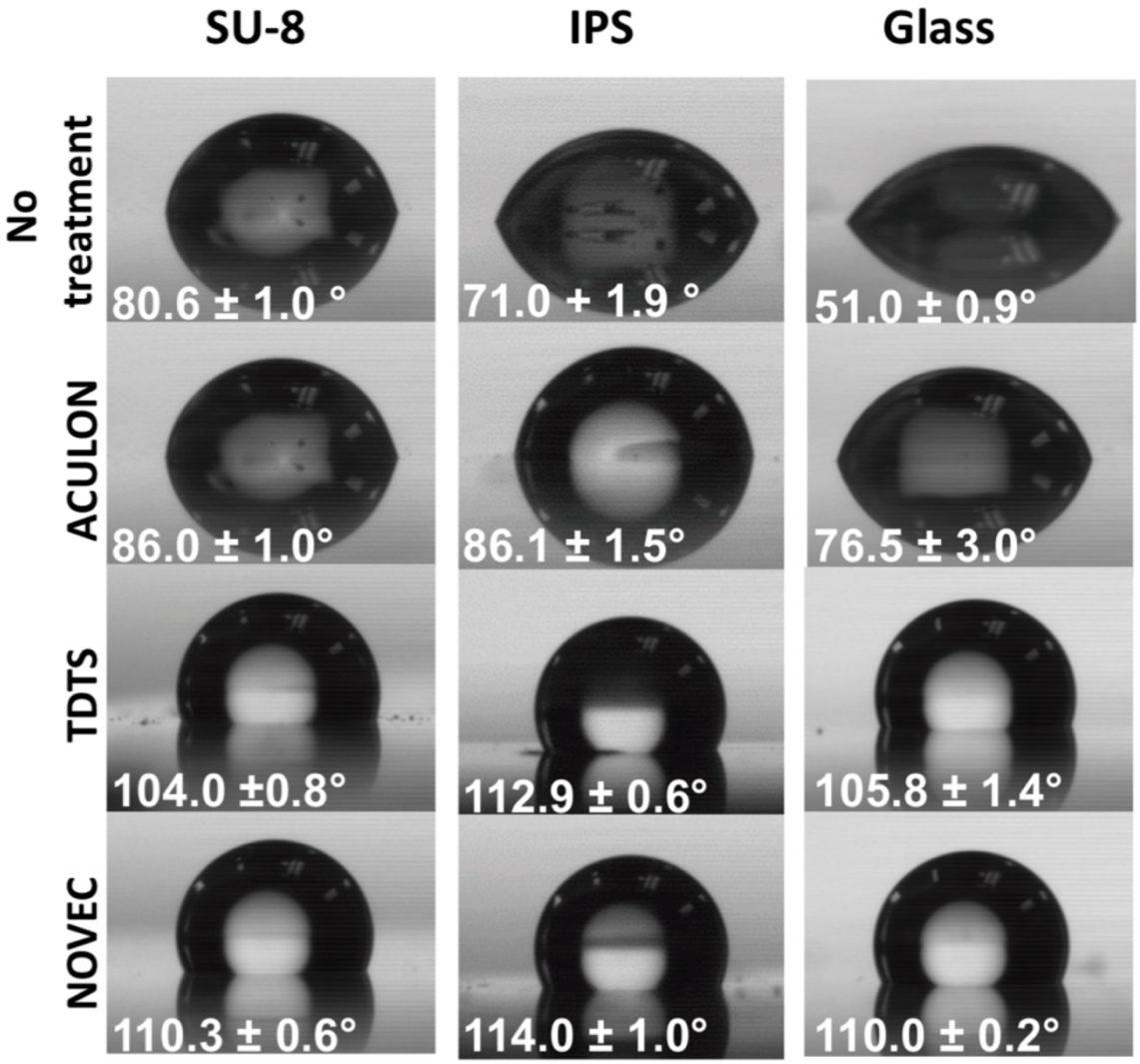

Figure A.1 Static water contact angle (θ) measurements. Images of a 2 μL water-in-air droplet on SU-8, IP-S and glass, before and after treatment with the three fluorinated chemicals.

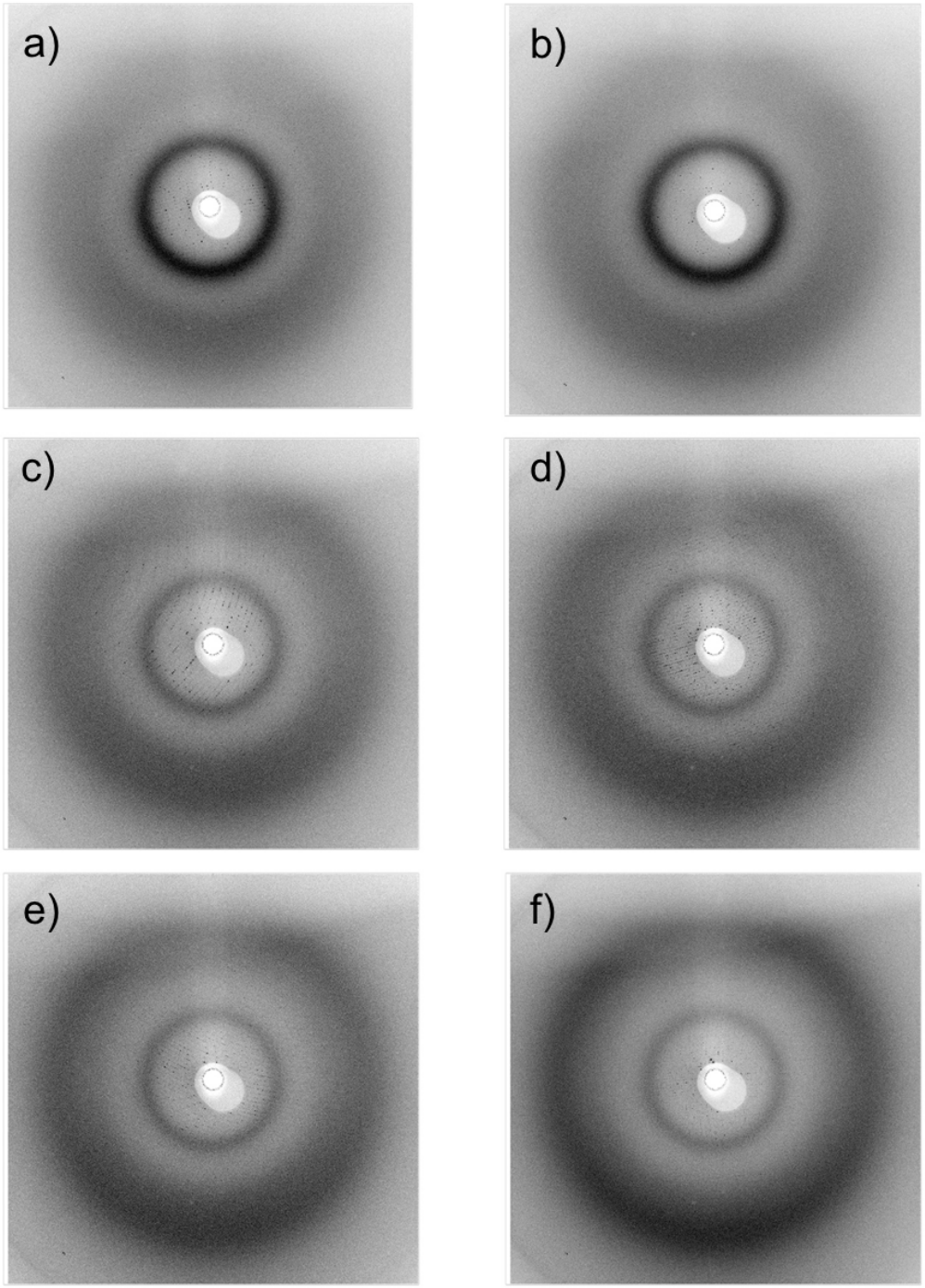

Figure A.2 PSI Diffraction Images. Examples of diffraction images with a high volume fraction of oil, noted by the intense oil ring at low resolution, are shown on the top (a,b). Diffraction images with higher volume fraction of water are shown in (c-f), noted by the more intense water ring at higher resolution.

APPENDIX B

[SUPPLEMENTAL MATERIAL FOR CHAPTER 5]

This Appendix contains Table B.1, listing the data collection statistics, and Table B.2, detailing the structure solution and refinement. It also contains: Figure B.1, showing aqueous-in-oil droplets containing photosystem I (PSI) crystals; Figure B.2, illustrating an oil injection jet; Figure B.3, depicting the unit cell size distribution for KDO8PS; Figure B.4, showing the L-test result; and Figure B.5, illustrating a representative diffraction pattern of one KDO8PS microcrystal.

Table B.1 Data Collection Statistics

Diffraction source	European XFEL, SPB/SFX
Wavelength (Å)	1.33316
Temperature (K)	293 K
Detector	AGIPD
Crystal-detector distance (mm)	173.5
No. of indexed crystal patterns	15 777
Exposure time per image (fs)	100
Space group	I23
a, *b*, *c* (Å)	118.4, 118.4, 118.4
α, β, γ (°)	90.0, 90.0, 90.0
Resolution range (Å)	48.0-2.80 (2.90-2.80)
Total No. of reflections	1 268 974 (99319)
No. of unique reflections	6 888 (674)
Completeness (%)	100 (100)
Multiplicity	184.2 (147.4)
$\langle I/\sigma(I) \rangle$ #	4.61 (0.95) #
CC*	0.9953 (0.7003)
R_{split}	14.3 (121.2)
Overall *B* factor from Wilson plot ($Å^2$)	84.6

Values for the outer shell are given in parentheses.
It is common practice in serially collected diffraction data to include data down to a CC* of 0.5, which commonly gives an $I/\sigma(I)<2.0$ in the highest resolution shell. Due to the partiality of reflections in serially collected data, $I/\sigma(I)$ is understood to be severely underestimated.

Table B.2 Structure solution and refinement

Resolution range (Å)	48.0-2.8
Completeness (%)	100
No. of reflections, working set	6384
No. of reflections, test set	494
Final R_{cryst}	19.3
Final R_{free}	26.1
No. of non-H atoms	
Protein	2100
Ion	0
Ligand	0
Water	2
Total	2102
R.m.s. deviations	
Bonds (Å)	0.002
Angles (°)	0.94
Average *B* factors (Å^2)	
Protein	90.8
Water	67.1
Ramachandran plot	
Most favored (%)	92.6
Allowed (%)	6.0

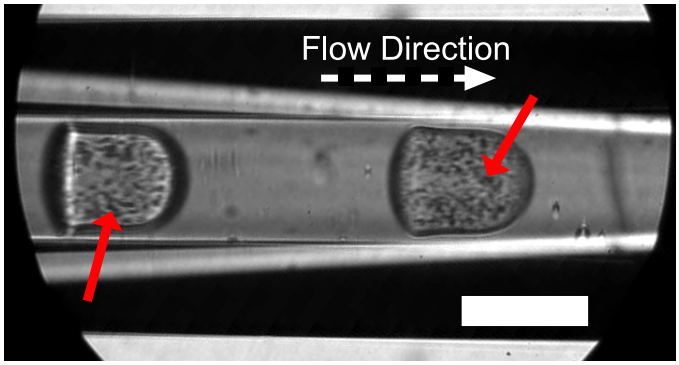

Figure B.1 Representative image of PSI crystals within droplets of mother liquor segmented by the oil phase. Droplets were generated at Q_{aq} = 4.5 µL/min and Q_{oil} = 12 µL/min and imaged in the capillary after the droplet generator. Dark dots in droplets, emphasized by red arrows, indicate crystals. For demonstration purposes, PSI crystals were used as they provide a high contrast for imaging. PSI crystals were prepared and grown as described previously.[191] Scale bar is 100 µm.

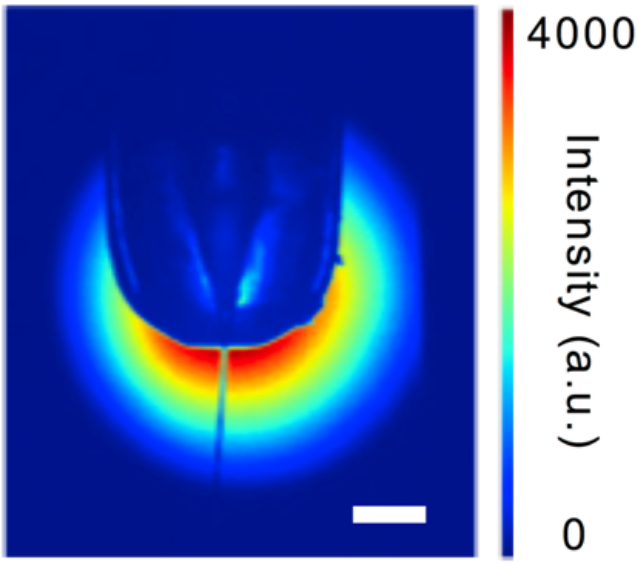

Figure B.2 False color image of a jet from a surface treated GDVN in the SPB/SFX vacuum chamber during oil injection. Scale bar is 300 µm. The laser illumination is in-line with the camera as seen by the high intensity rings.

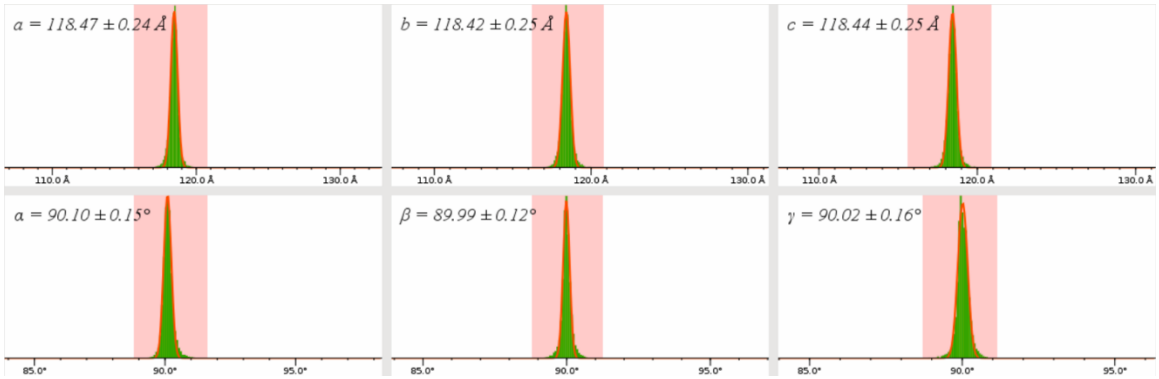

Figure B.3 Unit cell size distribution for the 15,777 indexed and integrated diffraction patterns. A Gaussian function was fit to each distribution and the mean calculated using cell_explorer from the CrystFEL software package.

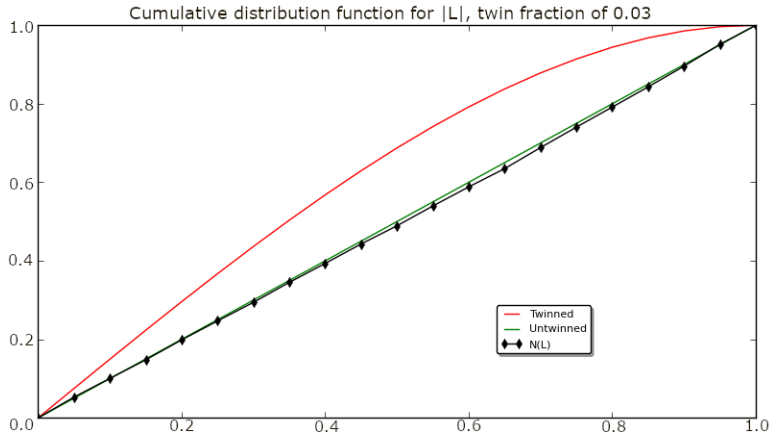

Figure B.4 L-test result showing that the data is de-twinned and the indexing ambiguity associated with the cubic I23 spacegroup has been resolved.

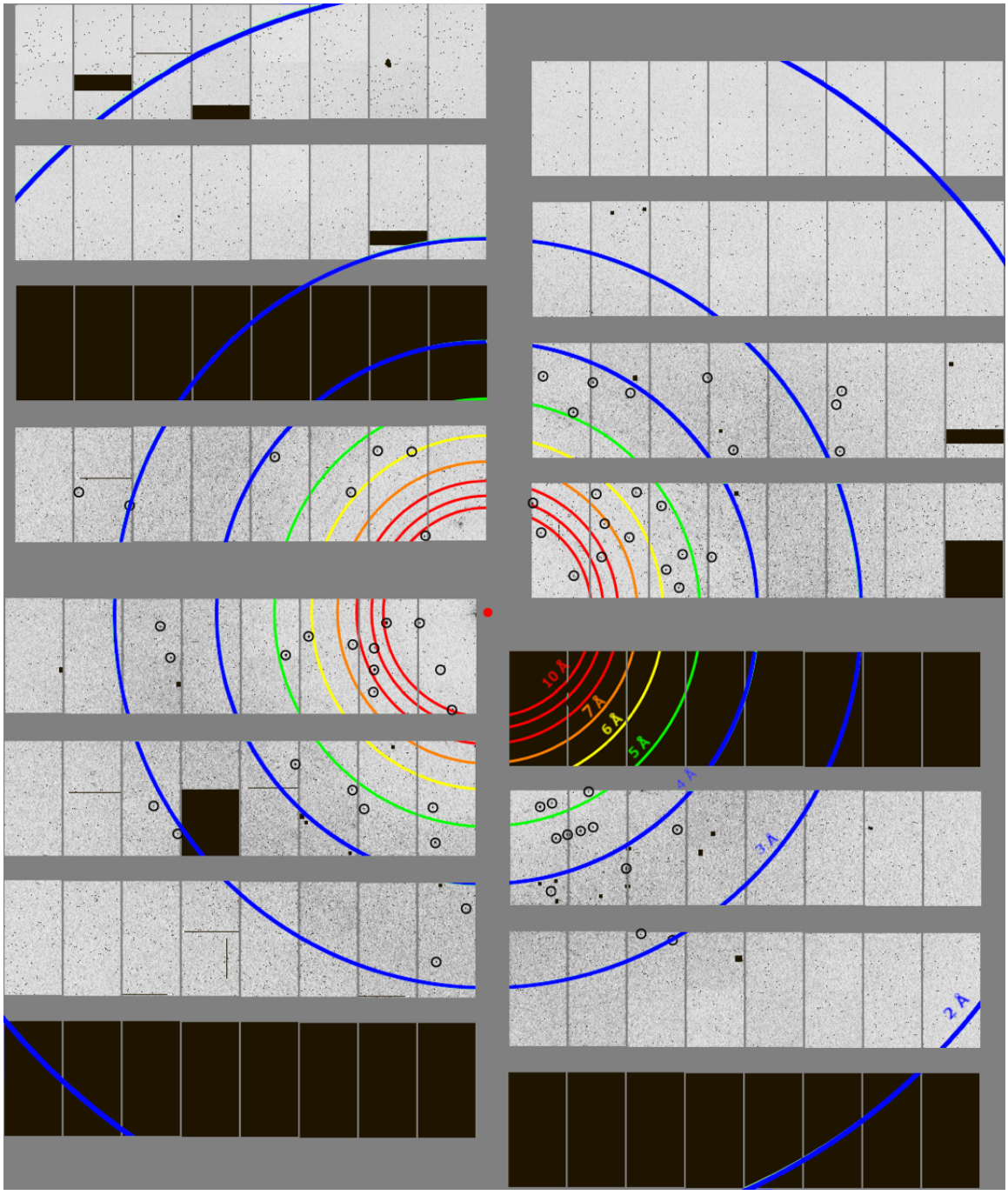

Figure B.5 Representative diffraction pattern of a single KDO8PS microcrystal with resolution up to 2.80 Å. Found peaks are highlighted with black circles as determined by Cheetah. Larger black regions and spots are masked out areas on the detector.

APPENDIX C

[SUPPLEMENTAL MATERIAL FOR CHAPTER 6]

This Appendix contains the detailed printing parameters for Chapter 6 and Figure C.1, showing a velocity profile from a 2D numerical model.

Detailed 3D Printing Settings

The 3D printed mixer (printed in the PETA photoresist, Figure 6.4b,c) was designed in AutoCAD (AutoDesk, USA) and the resulting .stl file was imported into DeScribe (version 2.5.1, Nanoscribe, Germany) to build a printing file usable with the Photonic Professional GT (Nanoscribe, Germany). The structure was printed in solid mode. The slicing distance was fixed at 1 μm with a base slice count of 2. The hatching distance was 0.5 μm. The contour count was set to 12 with a distance of 0.2 μm. A rectangular block size of 285x285x100 μm^3 was chosen, although the z-direction can increase to 150 μm without problem. The block shear angle was set to 20° with a block and layer overlap of 5 μm and 1 μm, respectively. Blocks were printed in lexical mode, with flying blocks avoided, neighboring blocks grouped, and backlash corrected. The galvo scanner stage was used for fast translation in the x- and y-axes, and the z-axis was controlled by the piezo scanner for fine translation. Blocks were offset to minimize the number of stitching lines within a channel, specifically the mixing cross intersection. The piezo settling time and galvo acceleration were adjusted to 20 ms and 5 μm/s, respectively. The stage correction function in DeScribe was utilized to correct for uneven stitching. The contour laser power and scan speed were set to 85% and 100,000 μm/s, respectively. The solid laser power and scan speed were set to 100% and 80,000 μm/s, respectively. These laser power and scan speeds were used to avoid overexposure of the photoresist (which causes bubbling during exposure) and to maximize printing speed.

Before each print job, the microscope objective was cleaned with isopropyl alcohol and allowed to dry. A small drop of the PETA photoresist was deposited onto the

conductive side of a clean ITO-coated glass slide and loaded into the Photonic Professional GT. The print file developed in DeScribe was loaded into the NanoWrite software (Nanoscribe, Germany). Using a 25x objective with the magnification ring on the DiLL setting, the objective automatically approached the photoresist and autofocused on the refractive index change between the ITO-coated glass slide and the photoresist. Printing proceeded as stated in the printing file. Printing time took approximately 16 hours with the above printing conditions. For printing in IP-S, the default IP-S solid recipe in DeScribe provides suitable conditions and was utilized to print the device in Figure 6.4a without adjustment.

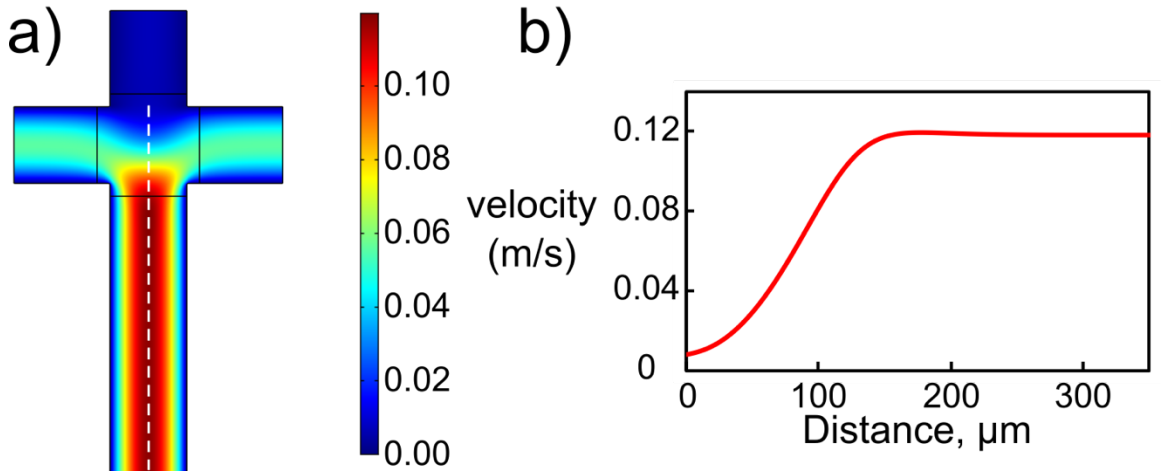

Figure C.1 (a) Velocity surface plot for the 2D numerical model of the following flow rate condition: Q_c = 4 μL/min, Q_{sides} = 32 μL/min, Q_{tot} = 68 μL/min. (b) Corresponding line plot of the velocity profile taken from the center white dashed cut line in (a). With Equation 6.2, this velocity profile, used in conjunction with a corresponding concentration profile (Figure 6.2) obtained from the same cut line, can be used to determine t_{mix}. Channel widths in (a) are 120 μm.

APPENDIX D

[SUPPLEMENTAL VIDEOS]

[Consult Attached Files]

This Appendix contains the descriptions of the supplementary video for Chapter 4.

Supplementary Video D.1 Droplet formation in a 3D printed droplet generator

Droplets of PSI buffer ($Q_{PSI\ buffer}$ = 0.5 µL min^{-1}) generated in oil (Q_{oil} = 6 µL min^{-1}) with a 3D printed droplet generator that has been surface treated with Novec. The video is slowed by 100x. This video corresponds to Chapter 4.

APPENDIX E

[COPYRIGHT PERMISSIONS]

The following chapters of this dissertation have been published and are used with permission from all co-authors:

Chapter 3: Reprinted with permission from Echelmeier, A.; Sonker, M.; Ros, A., Microfluidic sample delivery for serial crystallography using XFELs. *Anal Bioanal Chem* **2019**, *411* (25), 6535-6547.

Chapter 4: Reprinted with permission from Echelmeier, A.; Kim, D.; Cruz Villarreal, J.; Coe, J.; Quintana, S.; Brehm, G.; Egatz-Gomez, A.; Nazari, R.; Sierra, R. G.; Koglin, J. E.; Batyuk, A.; Hunter, M. S.; Boutet, S.; Zatsepin, N.; Kirian, R. A.; Grant, T. D.; Fromme, P.; Ros, A., 3D printed droplet generation devices for serial femtosecond crystallography enabled by surface coating. *J Appl Crystallogr* **2019**, *52* (5).

Chapter 7.2: Reprinted with permission from Echelmeier, A.; Nelson, G.; Abdallah, B. G.; James, D.; Tolstikova, A.; Mariani, V.; Kirian, R. A.; Oberther, D.; Dorner, K.; Fromme, P.; Chapman, H. N.; Weierstall, U.; Spence, J. C. H.; Ros, A., Biphasic Droplet-Based Sample Delivery of Protein Crystals for Serial Femtosecond Crystallography With an X-Ray Free Electron Laser. *Int. Conf. Miniaturized Syst. Chem. Life Sci.*, *19th* **2015**, *19*, 1374-1376.

Chapter 7.3: Reprinted with permission from Echelmeier, A.; Cruz Villarreal, J.; Kim, D.; Gandhi, S.; Egatz-Gomez, A.; Thifault, D.; Coe, J. D.; Brehm, G.; Madsen, C.; Quintana, S.; Bajt, S.; Messerschmidt, M.; Meza, D.; Oberther, D.; Wiedorn, M. O.; Fleckenstein, H.; Botha, S.; Mendez, D.; Knoska, J.; Martin-Garcia, J. M.; Hu, H.; Lisova, S.; Allahgholi, A.; Gevorkov, Y.; Ayyer, K.; Aplin, S.; Ginn, H. M.; Graafsma, H.; Morgan, A.; Greiffenberg, D.; Klujev, A.; Laurus, T.; Poehlsen, J.; Trunk, U.;

Maia, F. R.; Mezza, D.; Fromme, R.; Weinhausen, B.; Mills, G.; Vagovic, P.; Barty, A.; Mancuso, A. P.; Weierstall, U.; Spence, J. C. H.; Chapman, H. N.; Zatsepin, N. A.; Fromme, P.; Kirian, R. A.; Ros, A. Sample Consumption Reduction for Serial Crystallography Using Water-in-Oil Droplets. *Proceedings of Int. Conf. Miniaturized Syst. Chem. Life Sci., 23rd*, Basel, Switzerland, μTAS 2019: Basel, Switzerland, 2019.